Cluster Ambitions: From Simple Structures to Extended Cluster Networks in Niobium and Tantalum Chalcohalides

Dissertation

der Mathematisch-Naturwissenschaftlichen Fakultät

der Eberhard Karls Universität Tübingen

zur Erlangung des Grades eines

Doktors der Naturwissenschaften

(Dr. rer. nat.)

vorgelegt von

M.Sc. Fabian Grahlow

aus Stuttgart

Tübingen

2025

Gedruckt mit Genehmigung der Mathematisch-Naturwissenschaftlichen Fakultät
der Eberhard Karls Universität Tübingen.

Tag der mündlichen Qualifikation:	17.12.2025
Dekan:	Prof. Dr. Thilo Stehle
1. Berichterstatter:	Prof. Dr. Hans-Jürgen Meyer
2. Berichterstatter:	Prof. Dr. Eberhard Schweda

Acknowledgment

Am Ende dieser Arbeit möchte ich all jenen danken, die mich auf dem Weg zu dieser Dissertation begleitet und unterstützt haben.
Mein besonderer Dank gilt Herrn Prof. Dr. H.-Jürgen Meyer für die Möglichkeit, diese Arbeit in seinem Arbeitskreis durchzuführen, sowie für seine fachliche Begleitung und die stets offenen Türen für Rückfragen und Diskussionen.
Dr. Markus Ströbele danke ich herzlich für seine kristallographische Hilfe und seine große, fachliche Expertise.
Ebenso danke ich Dr. Carl Romao für die theoretischen Berechnungen und die Erklärungen zu unerwarteten physikalischen Eigenschaften.
Mein ausdrücklicher Dank gilt außerdem Prof. Dr. Marcus Scheele, Dr. Fabian Strauß und Mario Martin für die Unterstützung durch die Durchführung der Leitfähigkeitsmessungen und für die vielen Momente, in denen ungewöhnliche Messreihen zu kleinen Abenteuern wurden.
Für die Durchführung der XPS-Messungen danke ich Eric Juriatti, ebenso Elke Nadler für die von Gesprächen begleiteten REM-Aufnahmen.
Mein herzlicher Dank gilt auch Jan Beitlberger, Dr. Florian Pachel, Patrick Schmidt, Albert Schwarz, Melena Groß und Dr. Elaheh Bayat für die schöne Zeit im Labor, das gemeinsame Lachen, das Durchhalten in stressigen und kräftezehrenden Phasen und all die spaßigen Momente. Insbesondere jene abseits der Forschung, bei denen wir uns zwischen Abzug, Werkbank und Pflanzentopf wiedergefunden haben.
Außerdem bedanke ich mich bei Dr. Jochen Glaser für die Unterstützung bei der Interpretationen von magnetischen Messungen und für die anregenden Gespräche.
Dem gesamten Arbeitskreis danke ich für die tolle Atmosphäre, die Hilfsbereitschaft, das offene Miteinander und viele inspirierende Gespräche.
Nicht zuletzt gilt mein Dank meiner Familie, die mir im Hintergrund stets den Rücken gestärkt hat.

Contents

List of Abbreviations

eV	electron volt
EDX	energy dispersive X-ray spectroscopy
SEM	scanning electron microscopy
DFT	density functional theory
DFPT	density functional perturbation theory
E_f	fermi energy
PXRD	powder X-ray diffraction
SC-XRD	single-crystal X-ray diffraction
vdW	van der Waals
DRIFTS	diffuse reflectance infrared fourier transform spectroscopy
HT	high temperature
LT	low temperature
XPS	X-ray photoelectron spectroscopy
NMR	nuclear magnetic resonance
TXRF	total reflection X-ray fluorescence
UHV	ultra-high vacuum
VEC	valence electron count
Li-NMC	$Li(Ni,Mn,Co)O_2$
NMC 622	$LiNi_{0.6}Mn_{0.2}Co_{0.2}O_2$
ELF	electron localisation function
2c2e	two-centre two-electron

Summary

In the course of this thesis, niobium and tantalum chalcohalide cluster networks were synthesised and investigated with regard to their structural and physical properties.

$A\mathrm{Nb_3SBr_7}$ (A = Rb, Cs) crystallises in strands of one-dimensionally connected $[\mathrm{Nb_3SBr_7}]^-$ units, which contain trigonal $\mathrm{Nb_3}$ clusters with seven cluster electrons. While six electrons can be assigned to three two-centre two-electron (2c2e) bonds, an additional, unpaired electron per cluster is present, which is responsible for unusual physical properties. The temperature-dependent conductivity does not exhibit classical semiconducting behaviour but instead follows a power-law dependence. Additionally, strong electron correlations were confirmed by density functional theory (DFT) calculations, which revealed significant electron density between clusters along the chain, with intra-chain hopping being strongly favored over inter-chain hopping. This behaviour indicates that the electrons in this material do not act like a conventional Fermi liquid, but rather resemble a Tomonaga–Luttinger liquid, where strongly correlated electrons are confined to one dimension.

Analogously, $\mathrm{Ta_4SBr_{11}}$ is also a system with seven cluster electrons. It consists of μ_4-S capped $\mathrm{Ta_4}$ butterfly-clusters arranged in corrugated, two-dimensional layers, forming a van der Waals (vdW) material. Due to the possible lateral displacement of the layers, intrinsic disorder arises, resulting in a single-crystal X-ray diffraction (SC-XRD) structure solution that shows a superposition of several possible cluster arrangements. Conductivity measurements showed semiconducting behaviour, indicating a certain mobility of the electrons. The distribution of the seven cluster electrons is non-trivial; however, magnetic measurements revealed antiferromagnetic interactions of unpaired electrons, and DFT calculations also indicated electronic correlations between unpaired electrons on neighboring clusters.

Another example of a system with seven cluster electrons is the binary compound $\mathrm{Nb_3}X_8$ (X = Cl, Br, I), which undergoes a magnetic-to-nonmagnetic phase transition upon cooling from high temperature (HT) phase to a low temperature (LT) phase, with the transition temperature depending on the halide. A Hubbard dimerisation of unpaired electrons of adjacent layers plays a central role in this magnetostructural transition. As part of this work and in support of a theoretical study, $\mathrm{Nb_3Cl_8}$ and $\mathrm{Nb_3Cl_4Br_4}$ were synthesised, and their structures were analysed above and below

the phase transition temperature using SC-XRD. Additionally, optical band gaps, temperature-dependent conductivities, and magnetic properties of $Nb_3Cl_4Br_4$ were measured to gain a better understanding of the electronic structure and the role of the unpaired electron in the transition.

Furthermore, different synthetic pathways toward novel cluster networks were explored. Using an unconventional reduction with Li_2CN_2, several $M_5O_4I_{11}$ (M = Nb, Ta) compounds were synthesised and characterised within a heterogeneous system. For M = Ta, the three networks o-$Ta_5O_4I_{11}$ (o = orthorhombic), m-$Ta_5O_4I_{11}$ (m = monoclinic), and $Ta_5O_4I_{11}(TaI_5)$ were obtained. All three feature a similar pentanuclear cluster core in the form of a distorted square pyramid, composed of one central Ta atom at the apex and four outer Ta atoms at the base corners. The four oxygen atoms are positioned along the edges of the base and coordinate three Ta atoms each. These clusters are connected via iodide ligands to form corrugated layers. X-ray photoelectron spectroscopy (XPS) measurements revealed a Ta(IV):Ta(III) ratio of 4:1, suggesting the presence of a reduced Ta^{3+} centre at the pyramid apex and four Ta^{4+} atoms at the base corners. o-$Ta_5O_4I_{11}$ and m-$Ta_5O_4I_{11}$ exhibit semiconducting behaviour with small activation energies of 0.1 eV and 0.4 eV, respectively. In the case of $Ta_5O_4I_{11}(TaI_5)$, stronger layer corrugation was observed, accompanied by intercalation of molecular TaI_5 units between the cluster layers.

These results demonstrate how variation of cluster size, dimensionality, and electron count enables the realisation of interesting physical properties. In particular, systems with an odd number of cluster electrons often host unpaired electrons in correlated states, show magnetic transitions, or support low-dimensional charge transport. The structural flexibility and the synthetic versatility of chalcohalide cluster chemistry therefore opens up broad opportunities for the design of functional materials with exceptional physical properties.

Zusammenfassung

Im Rahmen dieser Arbeit wurden Niob- und Tantal Chalkohalogenid-Cluster-Netzwerke synthetisiert und ihre strukturellen sowie physikalischen Eigenschaften untersucht.
$A\mathrm{Nb_3SBr_7}$ (A = Rb, Cs) kristallisiert in Strängen aus eindimensional verknüpften $[\mathrm{Nb_3SBr_7}]^-$-Einheiten, in denen trigonale $\mathrm{Nb_3}$-Cluster mit sieben Cluster-Elektronen vorliegen. Während sechs Elektronen drei 2c2e-Bindungen zugeordnet werden können, ist ein zusätzliches, ungepaartes Elektron pro Cluster vorhanden, das für außergewöhnliche physikalische Eigenschaften verantwortlich ist. Die temperaturabhängige Leitfähigkeit zeigt kein klassisches halbleitendes Verhalten, sondern stattdessen eine Potenzgesetz-Abhängigkeit mit der Temperatur. Zusätzlich wurden in DFT-Berechnungen starke Wechselwirkungen der Elektronen bestätigt, die eine ausgeprägte Elektronendichte zwischen den Clustern innerhalb einer Kette zeigten, mit einer deutlichen Bevorzugung der Elektronenbeweglichkeit innerhalb der Kette. Dies deutet auf ein Verhalten der Elektronen wie in einer Tomonaga-Luttinger-Flüssigkeit hin. Abweichend von dem klassischen Verhalten als Fermi-Flüssigkeit liegt hierbei eine eindimensionale Kette aus stark korrelierten Elektronen vor.
Analog dazu ist auch die Verbindung $\mathrm{Ta_4SBr_{11}}$ ein System mit sieben Cluster-Elektronen. Hierbei handelt es sich um $\mathrm{Ta_4}$-Cluster, die in gewellten, zweidimensionalen Schichten angeordnet sind und ein van der Waals Material bilden. Aufgrund der möglichen Verschiebbarkeit der Schichten gegeneinander ergibt sich eine intrinsische Unordnung, sodass in der Einkristallstrukturanalyse nur ein gemitteltes Bild mehrerer möglicher Cluster-Anordnungen sichtbar ist. Leitfähigkeitsmessungen zeigen ein halbleitendes Verhalten, was auf eine gewisse Mobilität der Elektronen hinweist. Die Verteilung der sieben Cluster-Elektronen ist nicht trivial, allerdings konnten in magnetischen Messungen antiferromagnetische Wechselwirkungen ungepaarter Elektronen festgestellt werden, und auch in den DFT-Berechnungen war eine elektronische Korrelation von ungepaarten Elektronen in benachbarten Clustern zu erkennen.
Ein weiteres Beispiel für ein System mit sieben Cluster-Elektronen ist die binäre Verbindung $\mathrm{Nb_3}X_8$ (X = Cl, Br, I). Diese zeigt beim Abkühlen einen Phasenübergang von einer magnetischen HT-Phase zu einer nichtmagnetischen LT-Phase, wobei die Übergangstemperatur Halogenid-abhängig ist. Die Bildung von Hubbard-Dimeren aus ungepaarten Elektronen von Clustern benachbarter Schichten spielt eine zentrale

Rolle für diesen magnetostrukturellen Übergang. Im Rahmen dieser Arbeit wurden als Ergänzung zu einer theoretischen Untersuchung Nb_3Cl_8 und $Nb_3Cl_4Br_4$ synthetisiert und deren Strukturen oberhalb und unterhalb der Phasenumwandlungstemperatur anhand von Einkristallen untersucht. Zusätzlich wurden die optischen Bandlücken bestimmt, sowie temperaturabhängige Leitfähigkeiten und magnetische Eigenschaften gemessen, um ein besseres Verständnis für die elektronische Struktur und die Rolle des ungepaarten Elektrons bei der Phasenumwandlung zu gewinnen.

Darüber hinaus wurden im Rahmen dieser Arbeit verschiedene Wege zur Synthese neuartiger Cluster-Netzwerke untersucht. In einer unkonventionellen Reduktion mit Li_2CN_2 konnten in einem heterogenen System mehrere $M_5O_4I_{11}$-Verbindungen (M = Nb, Ta) synthetisiert und charakterisiert werden. Für M = Ta wurden die drei Netzwerke *o*-$Ta_5O_4I_{11}$ (orthorhombisch), *m*-$Ta_5O_4I_{11}$ (monoklin) und $Ta_5O_4I_{11}(TaI_5)$ erhalten. Alle drei enthalten denselben pentanuklearen Cluster-Kern in Form einer verzerrt-quadratischen Pyramide, bestehend aus einem zentralen Ta-Atom an der Spitze und vier äußeren Ta-Atomen an den Basisecken. Die vier Sauerstoffatome befinden sich an den Kanten der Basisebene und koordinieren jeweils drei Tantalatome. Die Cluster sind durch Iodid-Liganden zu gewellten Schichten verknüpft. XPS-Messungen weisen auf ein Ta(IV):Ta(III)-Verhältnis von 4:1 hin, was auf ein reduziertes Ta^{3+} an der Pyramidenspitze und vier Ta^{4+} an den Ecken der Basis schließen lässt. *o*-$Ta_5O_4I_{11}$ und *m*-$Ta_5O_4I_{11}$ zeigen halbleitendes Verhalten mit kleinen Aktivierungsenergien von 0,1 eV bzw. 0,4 eV. Im Fall von $Ta_5O_4I_{11}(TaI_5)$ wurde eine stärkere Wellung der Schichten beobachtet, begleitet von einer Einlagerung molekularer TaI_5-Einheiten zwischen den Cluster-Schichten.

Insgesamt zeigen diese Ergebnisse, wie sich durch gezielte Variation von Clustergröße und Elektronenzahl neuartige, physikalische Eigenschaften erschließen lassen. Besonders Systeme mit ungerader Anzahl an Cluster-Elektronen, die ungepaarte Elektronen in korrelierten Zuständen aufweisen, zeigen ungewöhnliche, magnetische Übergänge oder einen nieder-dimensionalen Ladungstransport. Die strukturelle Flexibilität und synthetische Variabilität der Chalkohalogenid-Cluster-Chemie eröffnet damit vielseitige Perspektiven für die gezielte Entwicklung funktionaler Materialien mit außergewöhnlichen physikalischen Eigenschaften.

List of Publications and Manuscripts

Publication 1:

Electronic Structure and Transport in the Potential Luttinger Liquids $CsNb_3SBr_7$ and $RbNb_3SBr_7$

Fabian Grahlow, Fabian Strauß, Marcus Scheele, Markus Ströbele, Alberto Carta, Sophie F. Weber, Scott Kroeker, Carl P. Romao, H.-Jürgen Meyer

Phys. Chem. Chem. Phys., **2024**, 26, 11789

Publication 2:

Ta_4SBr_{11}: A Cluster Mott Insulator with a Corrugated, Van der Waals Layered Structure

Fabian Grahlow, Fabian Strauß, Patrick Schmidt, Jaroslav Valenta, Markus Ströbele, Marcus Scheele, Carl P. Romao, H.-Jürgen Meyer

Inorg. Chem., **2024**, 63, 19717-19727

Publication 3:

Hubbard Dimer Physics and the Magnetostructural Transition in the Correlated Cluster Material Nb_3Cl_8

Alberto Carta, Peter Mlkvik, Fabian Grahlow, Markus Ströbele, H.-Jürgen Meyer, Carl P. Romao, Nicola A. Spaldin, Claude Ederer

arXiv:2509.03988, **2025**, DOI: 10.48550/arXiv.2509.03988

Publication 4:

Structural Modifications of $M_5O_4I_{11}$ (M = Nb, Ta) Cluster Networks from Heterogeneous Solid-State Reactions

Fabian Grahlow, Jan Beitlberger, Mario Martin, Eric Juriatti, Heiko Peisert, Marcus Scheele, Markus Ströbele, Carl P. Romao and H.-Jürgen Meyer

Dalton Trans., **2025**, 54, 16593-16604

Manuscript 1:

A Complete Cathode Recovery Cycle of an Exhausted and Dismantled Lithium Battery Material

Fabian Grahlow, Patrick Schmidt, H.-Jürgen Meyer

Scientific Contribution

Publication 1:

Electronic Structure and Transport in the Potential Luttinger Liquids $CsNb_3SBr_7$ and $RbNb_3SBr_7$

The manuscript was prepared in collaboration with Prof. H.-J. Meyer, Dr. C. P. Romao, Dr. F. Strauß and Prof. S. Kroeker. I synthesised the material, selected and contacted the crystals, and carried out the conductivity measurements together with Dr. F. Strauß, who evaluated the data and co-wrote the corresponding section with Prof. M. Scheele. Dr. M. Ströbele performed the SC-XRD measurements and carried out the structure refinement. Dr. A. Carta, S. F. Weber and Dr. C. P. Romao conducted the theoretical calculations and wrote the respective part of the manuscript. Prof. S. Kroeker was responsible for the nuclear magnetic resonance (NMR) spectroscopy.

Publication 2:

Ta_4SBr_{11}: A Cluster Mott Insulator with a Corrugated, Van der Waals Layered Structure

The manuscript was written by me in collaboration with Prof. H.-J. Meyer. I designed and carried out the synthesis and performed the SC-XRD measurements. Dr. M. Ströbele was responsible for the structure refinement. I conducted and evaluated the total reflection X-ray fluorescence (TXRF) measurements, and E. Nadler performed the energy dispersive X-ray spectroscopy (EDX) and scanning electron microscopy (SEM) analyses. P. Schmidt carried out the diffuse reflectance infrared fourier transform spectroscopy (DRIFTS) measurement and wrote the corresponding section. I performed the conductivity measurements together with Dr. F. Strauß, who also wrote that part in the manuscript. Prof. M. Scheele edited the manuscript. Dr. C. P. Romao performed the theoretical calculations and contributed the respective text. J. Valenta conducted the magnetic measurements and wrote that section.

Publication 3:

Hubbard Dimer Physics and the Magnetostructural Transition in the Correlated Cluster Material Nb_3Cl_8

The theoretical part was performed and written by Dr. A. Carta, P. Mlkvik, Dr. C. P. Romao, Prof. N. A. Spaldin and Prof. C. Ederer. I planned and conducted the experimental work and wrote the corresponding section in collaboration with Prof. H.-J. Meyer. Dr. C. P. Romao edited this part of the manuscript. I performed the DRIFTS and SC-XRD measurements, and Dr. M. Ströbele carried out the structure refinements. The conductivity measurements were performed and analysed in collaboration with Dr. F. Strauß. Dr. J. Glaser carried out the magnetic measurements and I evaluated the data in collaboration with him and I wrote this section.

Publication 4:

Structural Modifications of $M_5O_4I_{11}$ *(M = Nb, Ta) Cluster Networks from Heterogeneous Solid-State Reactions*

The manuscript was written in collaboration with J. Beitlberger and Prof. H.-J. Meyer. I planned and conducted the experimental syntheses and preparations of the tantalum compounds, while J. Beitlberger synthesised and measured the niobium compound. I prepared the conductivity measurements and carried them out together with M. Martin, who evaluated the data and co-wrote that section with Prof. M. Scheele. The DRIFTS measurements were performed in collaboration with J. Beitlberger. I prepared the samples for the XPS measurements, which were performed by E. Juriatti, who co-wrote that part with Prof. H. Peisert. Dr. M. Ströbele carried out the structure refinements. Dr. C. P. Romao performed the calculations and wrote the corresponding section.

Manuscript 1:

A Complete Cathode Recovery Cycle of an Exhausted and Dismantled Lithium Battery Material

The manuscript was written in collaboration with P. Schmidt and Prof. H.-J. Meyer. P. Schmidt and I planned and performed all experimental procedures together.

1 Introduction

1.1 Binary Niobium and Tantalum Halides

Niobium and tantalum halides MX_5 (M = Nb, Ta; X = halide) in their highest oxidation state usually contain octahedrally coordinated metal centres, typically forming M_2X_{10} dimers.[1–8] The reduction of these compounds leads to the formation of metal-rich metal halides with metal–metal interactions. The Peierls distorted MX_4 forms one-dimensional strands of M–M dimers,[8–11] while NbI_3 forms chains of equidistant Nb–Nb bonds.[12,13]

The research on metal-rich compounds of niobium and tantalum halides is dominated by cluster compounds that are predominantly synthesised through high-temperature solid-state reactions. A prominent structural motif is the octahedral M_6 (M = Nb, Ta) cluster core which is commonly found in the $M_6X^i_{12}X^a_6$-structure type with 12 edge-bridging (^{i} = inner) halides and 6 outer (^{a} = outer) halides (Figure 1, right) or in the $M_6X^i_8X^a_6$-structure type, with 8 inner, face capping halides (Figure 1, left), which is favoured for when smaller metals are paired with larger halides.[14–20]

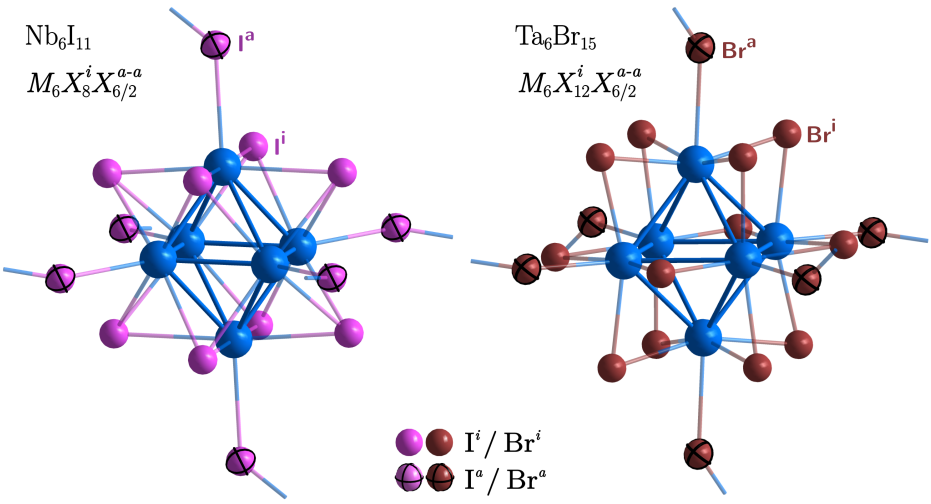

Figure 1: Comparison of the $[M_6X_8]$-cluster type in Nb_6I_{11}[21] (left) and the $[M_6X_{12}]$-cluster type in Ta_6Br_{15}[18] (right).

These octahedral clusters – especially the corresponding molybdenum and tungsten clusters – are intensively studied in terms of their photoactivity, showing bright red to orange luminescence.[22] In presence of oxygen, they show an energy transfer of excited triplet states onto molecular oxygen to form singlet oxygen, which makes $[M_6X_8]$-cluster

compounds interesting for several applications like surface disinfection or localised photodynamic therapy in cancer treatment.[22–25] Due to the spatial separation of adjacent clusters by the terminal ligands, extended cluster networks of these octahedral clusters are semiconductors with poor electrical conductivity.[26] Typically, M_6 clusters are considered electron precise with all skeletal electrons residing in the metal-to-metal bonds of the clusters.

Another cluster compound that has been extensively studied is the M_3 cluster core (Figure 2, left), which is found for M = Nb in Nb_3X_8 (X = Cl, Br, I).[27–30] In the Nb_3X_8 structure, the niobium atoms in each layer are displaced from the centres of their coordination octahedra, forming trigonal clusters that are interconnected into extended two-dimensional vdW layers (Figure 2, left). Each of the trigonal clusters contains seven skeletal electrons with one lone cluster electron. Upon cooling, Nb_3X_8 undergoes a magnetic-to-nonmagnetic phase transition accompanied by a significant change in the stacking order, resulting in different modifications being reported for the high and low temperature phases.[31,32] Several theoretical studies have reported some sort of "dimerisation" of nearest neighbour trimers along the stacking direction. However the exact mechanism is still under debate.[32–36]

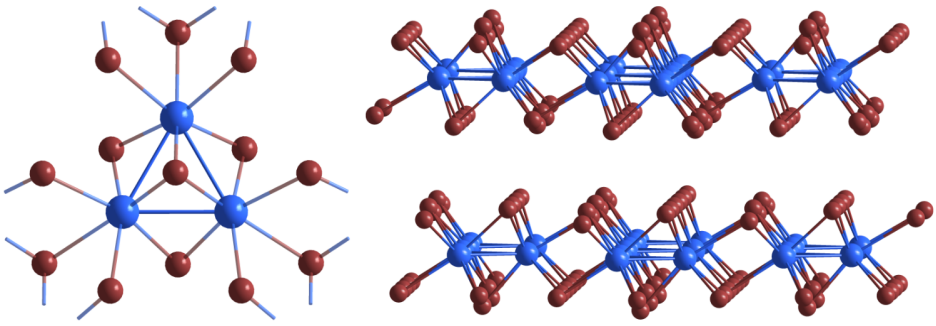

Figure 2: M_3 cluster core (left) and vdW stacking of 2D layers (right) in Nb_3Br_8.[27,28]

In this structure, the capping halide above the trigonal cluster can be substituted by a chalcogenide to form the structure family M_3ChX_7 (M = Nb, Ta; Ch = S, Se, Te; X = Br, I).[30] This substitution reduces the number of cluster electrons from seven to six, yielding a diamagnetic compound with electron precise clusters.

1.2 Introduction of Chalcogenides to the Niobium and Tantalum Halide System

The introduction of chalcogenides as heteroanions significantly expands the diversity of the *M*–*Ch*–*X* family (*M* = Nb, Ta; *Ch* = chalcogenide; *X* = halide). Some of these structures adopt salt-like structures, in which the fully oxidised metal centres are typically coordinated by both chalcogen and halogen anions in well-separated coordination environments. $(Nb_4Se_{15}I_2)I_2$, for example, forms 1D chains of niobium atoms with bridging Se^{2-} and Se_2^- (Figure 3, left). Two of the iodide ions are directly bonded to Nb^{5+} and the other two separate the chains and are only loosely bound.[37] Compounds of the type MO_2X (*M* = Nb, Ta; *X* = F, Cl, Br, I) form two-dimensional vdW materials with double layers composed of $[MO_5I_2]$ pentagonal bipyramids that are connected via their apical oxygen atoms (Figure 3, middle). In these structures, the metal atoms are seven-coordinated.[38–41] M_3O_7X (*M* = Nb, Ta; *X* = F, Cl) compounds form a 3D networks consisting of distorted edge-sharing $[MO_5X]$ and corner-sharing $[MO_6]$ octahedra (Figure 3, right).[42–46]

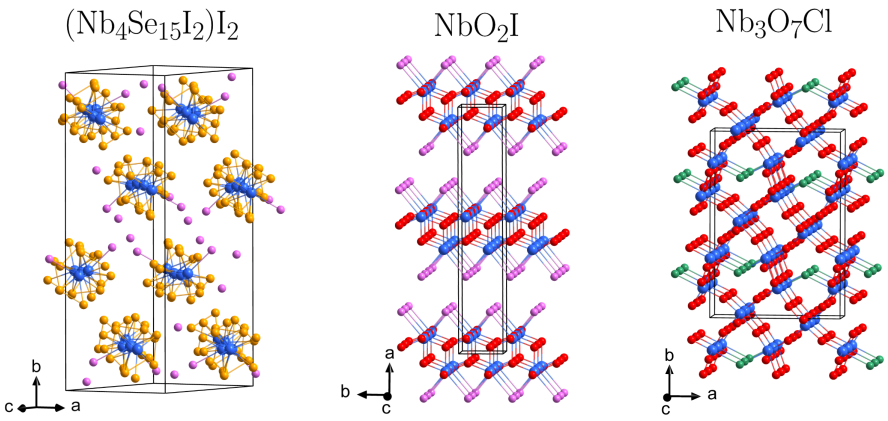

Figure 3: Sections of the crystal structures of $(Nb_4Se_{15}I_2)I_2$ (left),[37] NbO_2I (middle),[47] and Nb_3O_7Cl (right).[48] Nb: blue, Se: yellow, O: red, Cl: green, I: pink.

More typically, the introduction of a heteroanion leads to a reduction of the metal centres to M^{4+} with a d^1 configuration, which often leads to a Peierls distortion and therefore a formation of dimers arranged in one-dimensional chains or layered structures. The compound $[(TaSe_4)_3]I$ illustrates the energetic complexity of such one-dimensional systems: the sequence of shorter and longer *M*–*M* distances changes upon cooling through a centrosymmetric-to-noncentrosymmetric phase transition.[49]

1.3 Cluster Formation in the Niobium and Tantalum Chalcohalide System

Depending on the definition of metal atom cluster compounds, simple dimeric M_2 species are not readily classified as clusters. According to Cotton (1966) cluster compounds can be defined as "those containing a finite group of metal atoms which are held together entirely, mainly, or at least to a significant extent, by bonds directly between the metal atoms even though some non-metal atoms may be associated intimately with the cluster", a definition that explicitly includes metal dimers.[50] As the formation of metal–metal bonds is a fundamental aspect of reduced-metal atom cluster formation and these are already present in compounds containing dimers, such species will be included in the scope of this chapter.

Although the number of crystallographically identified niobium and tantalum chalcohalide cluster compounds has steadily increased since the initial discovery and definition of metal atom cluster, the diversity of structural motifs has remained relatively limited. Table 1 summarises the most relevant structurally characterised cluster motifs.

A reoccurring feature in many of these compounds is their low-dimensional connectivity with metal atoms in octahedral coordination environments. These are typically bridged by halide (X^-), chalcogenide (Ch^{2-}) or dichalcogenide (Ch_2^{2-}) ligands, giving rise to a range of different 1D and 2D networks. M_2-clusters commonly form linear chains, in with the metal dimers are extended through various halide and chalcogenide ligands. In $Nb_2Ch_2X_6$ and $Nb_3Se_5X_7$, the chalcogenides are bridging the short M–M bond, while the bridging halides connect these dimers into chains.[51,52]

M_3-cluster represent an extension of the dimer motif to form either linear or trigonal M_3 cluster cores. In case of the latter, both chalcogen and halogen atoms can be μ_3-capping the trigonal cluster or bridging the edges of the cluster. Additionally, Nb_3SI_7 forms three topologically different layered structures, where the same cluster core is connected in different ways, depending on the chosen temperatures for synthesis.[53] The presence of alkali cations enables further structural variation. In $CsNb_3SBr_7$, trigonal M_3 clusters form quasi one-dimensional strands.[54] This highlights the diversity of different networks containing the same cluster core, which in turn modifies the physical properties.

Table 1: Typical niobium and tantalum chalcohalide cluster motifs.

	cluster core		references
M_2	$Nb_2Se_2I_6$ 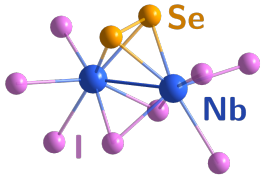	$Nb_3Se_5Cl_7$ 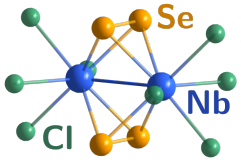	$Nb_2Ch_2X_6$ (Ch = Se, Te; X = Br, I)[51] $Nb_3Se_5X_7$ (X = Cl, Br, I)[55]
M_3	$Nb_6Se_{20}Br_6$ 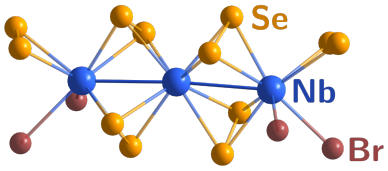		$Nb_3Se_{10}X_2$ (X = Cl, Br)[56,57] $Nb_6Se_{20}Br_6$[58]
	Nb_3SBr_7 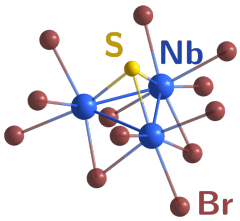	$Nb_3O_2Cl_5$ 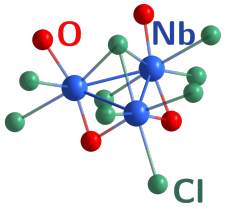	M_3ChX_7 (M = Nb, Ta; Ch = S, Se; X = Br, I)[59–63] $Nb_3O_2Cl_5$[64]
M_4	$Ta_4S_9Br_8$ 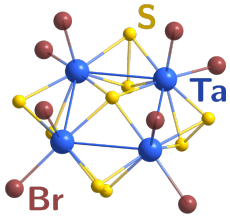	$Nb_4Se_4I_4$ 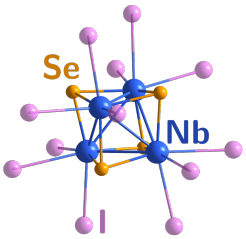	$Ta_4S_9X_8$ (X = Br, I)[65] $Nb_4Se_4I_4$[66]
M_6	Nb_6SI_9 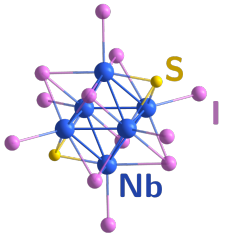	$Nb_{10}O_7Cl_{16}$ 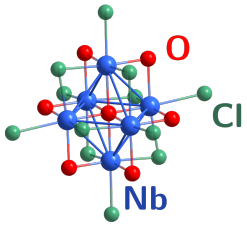	Nb_6SI_9[67] $Nb_{10}O_7Cl_{16}$[68]
	$Rb_3Nb_6SBr_{17}$ 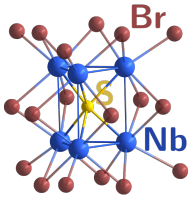		$Rb_3Nb_6SBr_{17}$[69]

In case of Ta_4SI_{11}, trigonal M_3-clusters with isolated Ta^{4+} atoms in octahedral iodide coordination have been postulated.[70] However, the structure exhibits intrinsic disorder so the exact connectivity remains ambiguous. With the given site occupation, a butterfly-type structure is also feasible as is found in Nb_4PnX_{11} (Pn = N, P; X = Cl, Br, I), having the same composition with a capping pnictide instead of chalcogenide, forming a μ_4-Pn capped M_4 cluster core.[71]

Other M_4 cluster geometries include the tetrahedral $Nb_4Se_4I_4$ cluster, where each face is capped by a selenide ion,[66] and a tetragonal planar $Ta_4S_9X_8$ (X = Br, I) cluster which incorporates a central S^{2-} anion and four S_2^{2-} anions at the edges.[65]

While M_5 have not yet been reported for niobium or tantalum chalcohalide systems, several structurally divers examples for M_6 clusters are known. The metal clusters in Nb_6SI_9 are based on M_6X_{11}, however two halide ligands are replaced by face-capping sulphides, which leads to a connection of octahedral clusters into extended one-dimensional strands.[67] In $Nb_{10}O_7Cl_{16}$, chains of $Nb_6O_6^iCl_6^iCl_6^a$ and double chains of $Nb_2(\mu_2\text{-}Cl)_2Cl_4O_4$ form extended vdW layers through shared oxygen and chlorine ligands.[68] These examples highlight the flexibility of chalcogenide coordination: In case of the sulphur compound, the chalcogenide acts as a face-capping ligand and in the oxygen compound, the chalcogenide ligands are edge-capping and in the centre of the octahedron. Another M_6 motif is observed in $Rb_3[Nb_6SBr_{17}]$, in which a central sulphide anion is surrounded by a trigonal prismatic Nb_6 core. These clusters are connected via shared outer iodide ligands.[69]

The examples discussed above illustrate how chalcogenide ligands expand the structural variety of niobium and tantalum halide-based cluster chemistry. Although the number of known compounds remains limited, the presence of metal–metal bonding, diverse ligand coordination, and low-dimensional connectivity already gives rise to a wide range of distinct cluster motifs. The specific choice and position of chalcogen and halogen atoms strongly influences cluster nuclearity, oxidation state, and connectivity. This structural and chemical flexibility offers a promising foundation for exploring more complex cluster topologies. Building on this understanding, the following section focuses on how such compounds can be synthesised. Because cluster compounds require reduced metal centres in specific geometries, careful control over temperature, reduction conditions, and reaction pathways is essential.

1.4 Synthetic Pathways to Cluster Formation

Typically, cluster compounds of niobium and tantalum are synthesised at elevated temperatures above 600 °C, either directly from the elements ($M + X_2 + Ch$) or via metallothermic reduction reactions ($M'X_5 + M'' + Ch$). In cases where M' and M'' are the same metal in different oxidation states, such reactions proceed through a comproportionation mechanism. A mixed alkali halide (AX) melt is often employed to enhance ion mobility, thereby improving crystallinity. However, these conventional synthetic pathways often require prolonged reaction durations and high temperatures, making it difficult to isolate thermally labile compounds with intermediate oxidation states. As an alternative, main group and transition metals can serve as unconventional reducing agents, as demonstrated by the gradual reduction of WCl_6 with M (M = Bi, Hg, Fe), which results in the formation for W_6Cl_{12} and intermediate M–W–Cl phases.[72–74] Hereby, the use of M enables milder reduction conditions at lower temperatures.

Reactions between metals and halides often involve transport through the gas phase. Especially under heterogeneous conditions involving both solid and gaseous components, reaction pathways become highly complex and extremely sensitive to thermal gradients. The control of such synthetic conditions is essential for the targeted preparation of new compounds.

In the course of this work, several reaction strategies have been explored to synthesise both known and novel chalcohalide cluster compounds, which have subsequently been investigated in terms of their structures and physical properties.

2 Objective

Since the first niobium and tantalum cluster compounds were reported, the rate of discovering genuinely new cluster networks in these systems has slowed. Classical high-temperature routes such as reactions from the elements ($M + X_2 + Ch$), reactions in an alkali halide flux (AX) and halide transport reactions (X_2) tend to reproduce a limited set of cluster motifs, especially compared with the richer tungsten (chalco)halide chemistry. This work therefore set out to broaden the structural diversity of niobium and tantalum chalcohalides and to link new structures to their electronic behaviour.

For this purpose, both classical pathways and unconventional heterogeneous reductions were explored to stabilise intermediate oxidation states and new connectivities, to determine the resulting crystal structures, and to relate low dimensionality and electron count to electrical transport and magnetism. In addition to synthesising new structures with novel motifs, known compounds were reinvestigated with respect to their physical properties, particularly $CsNb_3SBr_7$ and Nb_3X_8 (X = Cl, Br, I), both trigonal seven-electron clusters that have attracted attention due to unusual electronic and magnetic behaviour.

Experimentally, the work combined targeted solid-state syntheses, SC-XRD and powder X-ray diffraction (PXRD) for structure determination, and electrical transport, magnetic, and optical measurements, complemented by electronic calculations through collaboration, to analyse the synthesised materials.

Overall, this work aimed to establish synthetic routes to cluster networks and to clarify the links between structural connectivity, dimensionality, electron count, and their resulting properties.

3 Summary of the Main Results

Methods

Single-Crystal X-Ray Diffraction (SC-XRD)

The crystal structures of the compounds $CsNb_3SBr_7$ (CCDC: 2048757),[75] $RbNb_3SBr_7$ (CCDC: 2048759),[75] Ta_4SBr_{11} at 80 K (CCDC: 2352652 at 80 K; CCDC: 2181179 at 150 K),[76] Cs_2TaBr_6 (CCDC: 2327955),[76] $Nb_3Cl_4Br_4$ (CCDC: 2365009 at 100 K; CCDC: 2364410 at 270 K), $Ta_2O_3I_4$ (CCDC: 2389419), $LiTa_3O_2I_{12}$ (CCDC: 2390289), $Nb_5O_4I_{11}$ (CCDC: 2400835), *o*-$Ta_5O_4I_{11}$ (CCDC: 2380271), *m*-$Ta_5O_4I_{11}$ (CCDC: 2424946), $Ta_5O_4I_{11}(TaI_5)$ (CCDC: 2351105), and $KTiBr_4$ (CCDC: 2179182) were obtained from SC-XRD. Therefore, single crystals were selected and mounted on the tip of a microloop for intensity measurements. Data collection was performed using a Rigaku XtaLAB Synergy-S single-crystal X-ray diffractometer equipped with a HyPix 6000E detector and monochromated Mo-K_α ($\lambda = 0.71073$ Å) or Cu-K_α ($\lambda = 1.54070$ Å) radiation at different temperatures using N_2-cooling. The reflection intensities were corrected for absorption with an analytical method using CrysAlisPro 1.71.42.121a (Rigaku Oxford Diffraction, 2024). The structure was solved by direct methods (SHELXT), and full-matrix least-square structure refinements were performed with SHELXL-2019/3[77] as implemented in Olex2-1.5.[78]

Powder X-Ray Diffraction (PXRD)

All reaction products were investigated by PXRD using a StadiP diffractometer (Stoe, Darmstadt) with germanium-monochromated Cu-$K_{\alpha 1}$ radiation ($\lambda = 1.54070$ Å) and a Mythen1 detector. Ground powder was sandwiched between two pieces of Mylar foil using high vacuum grease and measured in a 2Θ range of 5° to 120°, if not otherwise reported. Qualitative analysis of the obtained PXRD data was done using the program Match! (3.14.238, Crystal Impact) in combination with the Crystallography Open Database (COD), Powder Diffraction File (PDF-2004) and selected Inorganic Crystal Structure Database (ICSD) entries. The graphical representations were created with Match! and the Affinity Suite (2.6.3).

Scanning Electron Microscopy (SEM) and Energy-Dispersive X-Ray Spectroscopy (EDX)

EDX measurements were performed using a HITACHI SU8030 SEM and a Bruker QUANTAX 6G EDX detector. Single crystals and powdered samples were hereby mounted onto carbon tape. For inert transfer, a home made vacuum transfer device was developed. It consists of a steel lid with an O-ring seal (Figure 4 a). The lid is placed on top of the sample holder and evacuated within the glove box airlock. It is then rapidly flooded with argon to create a reduced-pressure environment (10^{-3} mbar), ensuring an airtight seal via the O-ring (Figure 4 b and c). Once inserted into the SEM transfer chamber and evacuated, the internal pressure becomes slightly higher than the external pressure. This allows the magnetic lid to be lifted using neodymium magnets from outside the chamber (Figure 4 d).

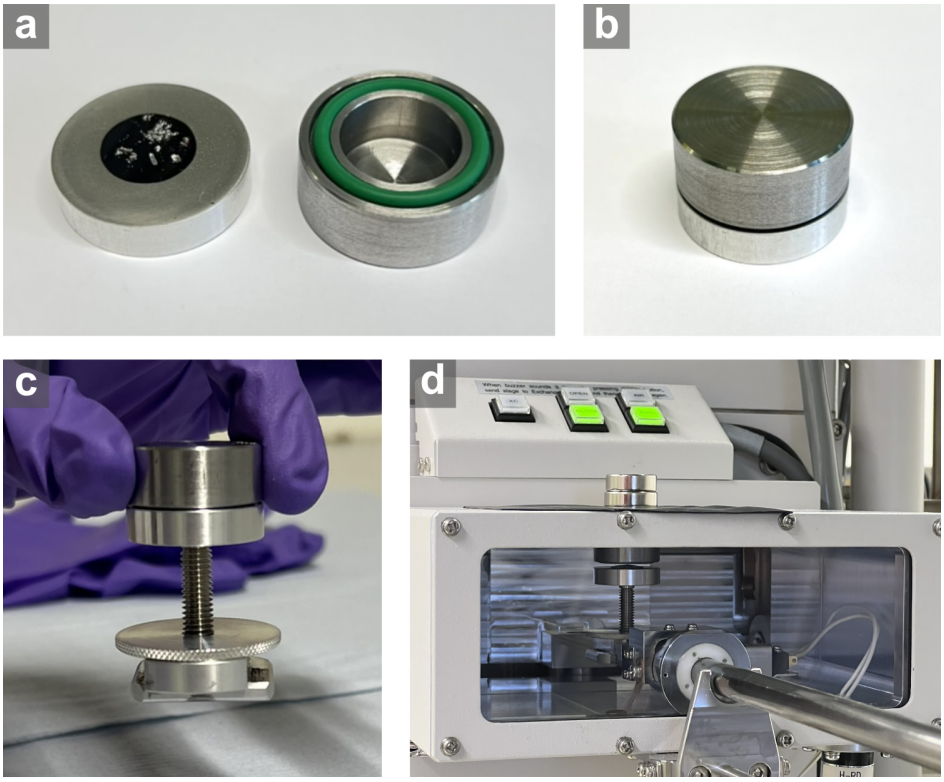

Figure 4: Procedure for inert transfer of samples into the scanning electron microscope. (a) Sample is fixed onto the sample holder using carbon tape. (b) The lid is placed on top of the sample holder, evacuated within the glovebox airlock, and then rapidly flooded with argon to ensure airtight seal. (c) The sealed assembly is mounted on the transfer stage and introduced into the SEM airlock, while the reduced-pressure environment maintains the seal. (d) Once the SEM chamber is evacuated, the transfer chamber lid can be lifted using an external magnet. Reproduced from Publication 4.[88]

X-Ray Photoelectron Spectroscopy (XPS)

XPS measurements were performed under ultra-high vacuum (UHV) conditions ($8 \cdot 10^{-10}$ mbar) using an XR50 Al-K_α standard source equipped with a PHOIBOS 100 hemispherical analyser (SPECS GmbH, Berlin, Germany). To avoid exposure to air and prevent oxidation, the synthesised samples were mounted on a double-sided conductive carbon tape under argon atmosphere. For inert transfer into the spectrometer, a custom-built vacuum transfer device was employed. This device consists of an aluminium lid with an O-ring that seals the sample holder under reduced pressure within the glovebox airlock (Figure 5). Upon evacuation of the XPS transfer chamber, the external pressure drops below the internal pressure, causing the lid to detach and fall off, thereby revealing the sample without contact to air. The chamber is then further evacuated to UHV before transferring the sample into the measurement chamber. Peak fitting of XPS spectra was performed using the software Unifit 2018 (Unifit Scientific Software GmbH, Leipzig, Germany).

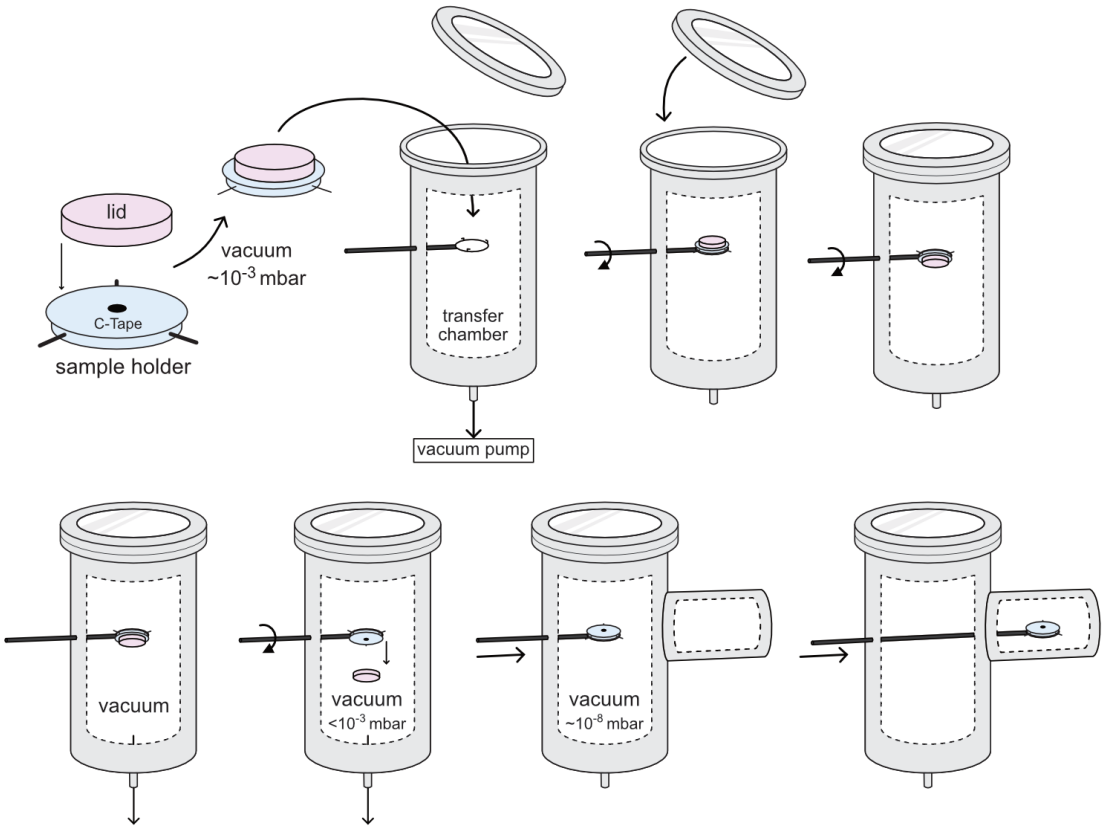

Figure 5: Schematic illustration of the inert transfer procedure for XPS measurements. Reproduced from Publication 4.[88]

Electrical Conductivity

Conductivity measurements were performed in a Lake ShoreCryotronics CRX-6.5K probe station with a Keithley 2636B source meter unit. Single crystals were contacted on a silicon substrate with a 770 nm oxide layer using silver paste and transferred into the measuring chamber under protective Argon atmosphere. The conductive silver pads at each end of the crystals were connected to the circuit with gold coated tungsten tips (Figure 6). The chamber was kept under vacuum ($< 5 \cdot 10^{-5}$ mbar) and the temperature was varied between 10 K and 350 K. Two-point conductivity measurements were performed by varying the applied source-drain voltage from -2 V to 2 V and -200 mV to 200 mV while detecting the current. For time-resolved photocurrent measurements, using a picosecond pulsed laser driver (Taiko PDL M1, PicoQuant) together with a laser head 779 nm (pulse length $<$ 500 ps), the crystals were illuminated at 55 mW/cm^2 laser output power using the continuous wave mode under a constant bias of 1 V.[75]

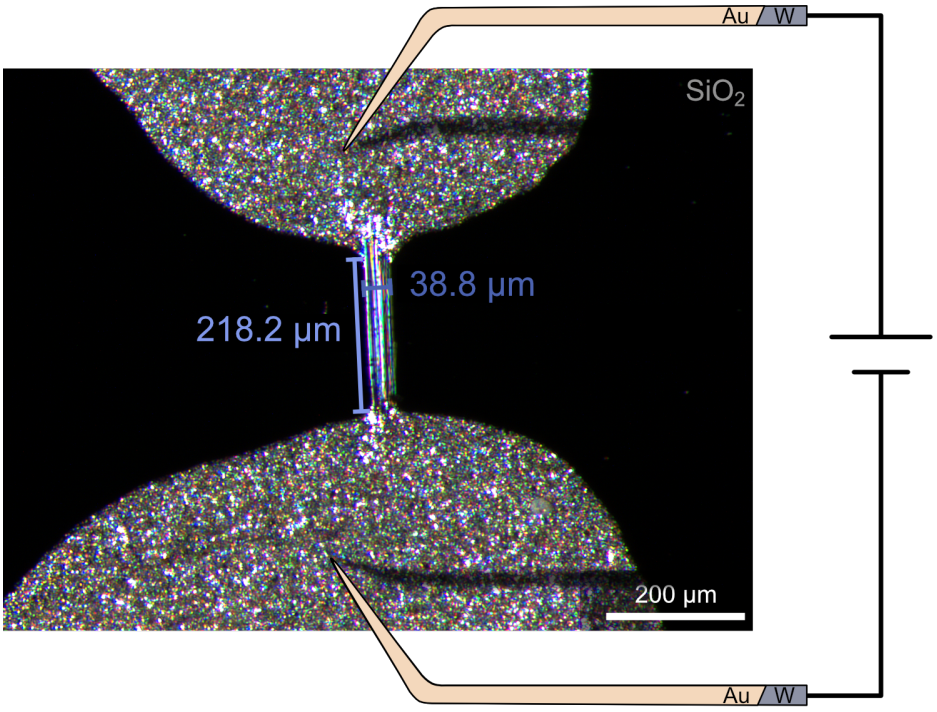

Figure 6: Experimental setup for the electrical conductivity measurements. A single crystal of $CsNb_3SBr_7$ is contacted with conductive silver paste. Gold coated tungsten tips are used to close the circuit.

3.1 Electronic Structure and Transport in the Potential Luttinger Liquids $CsNb_3SBr_7$ and $RbNb_3SBr_7$ (Publication 1)[75]

As shown in the introduction, trigonal M_3 clusters are known as Nb_3X_8 and Nb_3SBr_7, showing their electronic flexibility, with a valence electron count (VEC) of seven and six, respectively. While Nb_3SBr_7 is typically synthesised in a reaction of niobium pentabromide with elemental niobium and sulphur, the stoichiometric addition of ABr (A = Rb, Cs) to the reaction mixture leads to the formation of ANb_3SBr_7 (A = Rb, Cs).[54,75] Due to the VEC of seven, interesting electronic and magnetic properties are to be expected, as six electrons can be assigned to Nb–Nb bonding within the Nb_3 cluster with another unpaired electron, as has been reported for Nb_3X_8.[54,79]
Instead of forming vdW layers, however, the crystal structures of ANb_3SBr_7 (A = Rb, Cs) contain face-capped $[Nb_3S]$ clusters that are connected to chains along the a-axis. The $[Nb_3SBr_7]$ cluster units are linked into one-dimensional chains by three inner (^{i}) edge capping bromides, six shared ($^6/_2$) outer ($^{a\text{-}a}$) bromides, and one terminal outer (^{a}) bromide, forming the $[Nb_3SBr_3^iBr_{6/2}^{a\text{-}a}Br^a]^-$ structural unit (Figure 7).

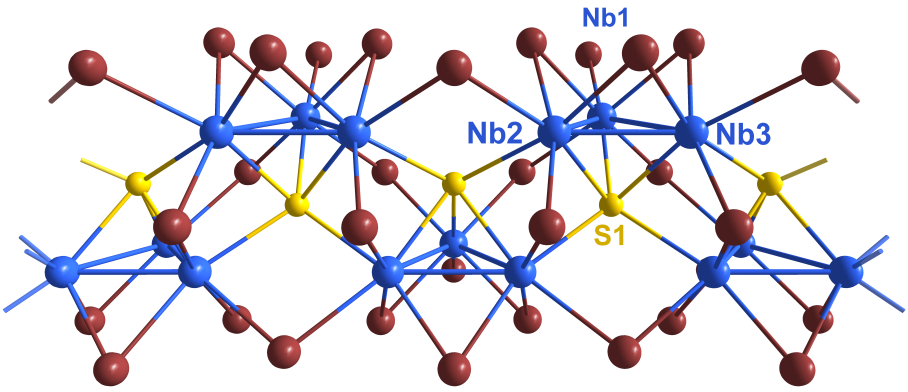

Figure 7: Section of a single chain in the structure of $CsNb_3SBr_7$ along the crystallographic c-direction. Niobium atoms are shown blue, sulphur yellow, and bromide atoms brown.

These chains are packed in a hexagonal manner, where the alkali metal cations separate the chains from each another (Figure 8). The difference between the crystal structures with A = Rb and Cs is reflected in the orthorhombic ($Pmc2_1$) and monoclinic ($P2_1/c$) space group symmetries, respectively. This results from the different radii and coordination patterns of the alkali ions. In the Cs compound, the ion is located in a nearly regular cuboctahedral bromide coordination, whereas in the Rb compound it

is surrounded by an irregular twelvefold bromide arrangement. As these bromide ions are also connected to the niobium clusters, the different coordination causes shifts of adjacent clusters along the one-dimensional chains (Figure 9).

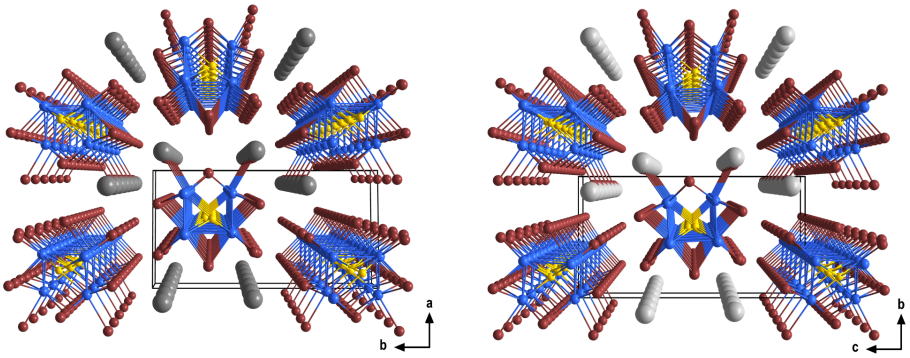

Figure 8: Comparison of crystal structures of $CsNb_3SBr_7$ ($P2_1/c$, left) $RbNb_3SBr_7$ ($Pmc2_1$, right) with their unit cells. Nb (blue), S (yellow), Br (brown), Cs (dark grey) and Rb (light grey) atoms are shown. Modified from publication 1.[75] (Rearrangement of figures)

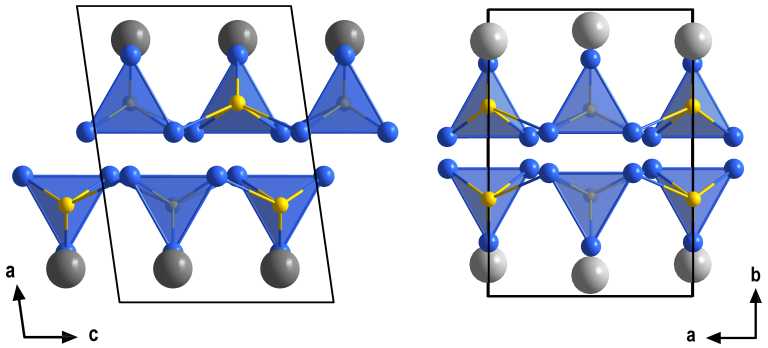

Figure 9: Comparison of crystal structures of $CsNb_3SBr_7$ ($P2_1/c$, left) and $RbNb_3SBr_7$ ($Pmc2_1$, right) with their unit cells. Bromides are omitted in the drawings for better clarity. Cs (dark grey) and Rb (light grey) atoms are shown.

This one-dimensionality of the crystal structure also becomes apparent in the morphology of the synthesised crystals. The SEM images in Figure 10 show needle-like crystals of $CsNb_3SBr_7$, show a fraying behaviour indicating weaker forces along the crystallographic a and b directions then along the c-axis. This was verified using density functional perturbation theory (DFPT) calculations, which reveal highly anisotropic behaviour, with the c-axis being the stiffest direction. However, the a- and b-directions make non-negligible contributions, indicating significant bonding interactions involving Cs^+. The anisotropy is therefore pronounced, but not strictly one-dimensional.

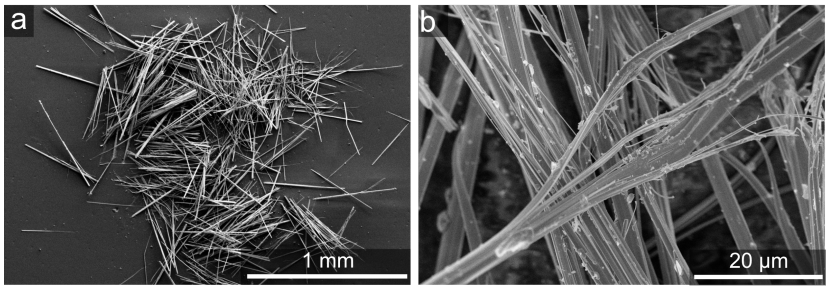

Figure 10: SEM micrographs of (a) $CsNb_3SBr_7$ crystals, showing their pronounced needle-like morphology, (b) fraying of a rod of $CsNb_3SBr_7$. Modified from publication 1.[75] (Sub-picture c removed)

In order to examine the impact of the low dimensionality on the physical properties, the electrical conductivity and the theoretical electronic band structure were investigated. Both compounds exhibit ohmic behaviour in the temperature range of 20 K to 300 K. The temperature-dependent conductivity indicate temperature-activated behaviour (Figure 11, inset), however the general trend does not fit typical semi conductivity. Instead, the electrical conductivity (σ) as a function of temperature can be fitted to a power law dependence ($\sigma(T) \propto c \cdot T^{\alpha}$), and is therefore consistent with a Luttinger liquid.[80,81] Below 30 K to 50 K, the curve is deviating from the fit and cannot be described by an Arrhenius curve, indicating either a Peierls distortion or Mott insulating phase.

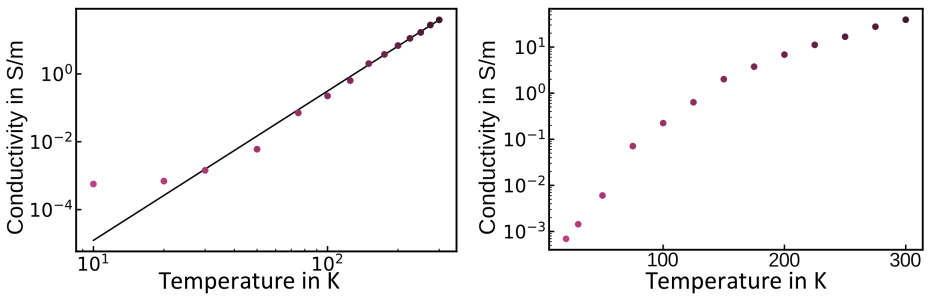

Figure 11: Double logarithmic plot of the electrical conductivity of $CsNb_3SBr_7$ versus set temperature in a range of 20 K to 300 K with a power law fit (black) following $\sigma(T) = cT^{\alpha}$ with $\alpha = 4.4$ (left). Electrical conductivity of $CsNb_3SBr_7$ versus temperature in a range of 20 K to 300 K (right). Modified from publication 1.[75] (Separate inset)

This behaviour implies, that the electrons in ANb_3SBr_7 (A = Rb, Cs) do not behave as a classical fermi liquid of independent quasi particles, but instead as a strongly correlated one-dimensional chain of electrons. The exponent $\alpha = 4.4$ of the power-law suggests repulsive interactions between the electrons.[82,83]

To gain more insight into the electronic structure, DFT calculations were performed (Figure 12). The results show zero band gap semimetallicity with crossings of the Fermi level near the B and A points of the Brillouin zone and extremely small band gaps ($< 0.1\,\mathrm{eV}$) between B and D, and between A and E. Maximally localised Wannier functions near the Fermi level reveal electron density between the clusters of a chain and indicate that nearest-neighbour intra-chain hopping is significantly favoured over inter-chain hopping.

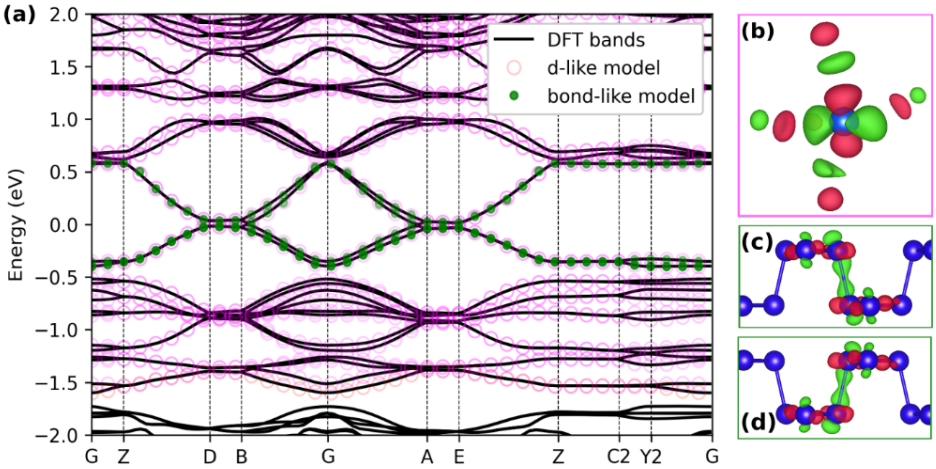

Figure 12: The calculated electronic band structure of nonmagnetic $CsNb_3SBr_7$ (a), and corresponding atom-centred (b) and bond-centred (c and d) maximally localised Wannier functions (shown at G). Blue spheres represent Nb atoms. Special points in and paths through the Brillouin zone were chosen following literature.[84]

The combination of a one-dimensional metallic structure, temperature-dependent conductivity, and short ^{133}Cs and ^{93}Nb NMR T_1 relaxation times supports the conclusion that $A\mathrm{Nb_3SBr_7}$ behaves as a Luttinger liquid above approximately 30 K. This behaviour is intrinsically linked to the one-dimensional arrangement of connected trigonal [Nb_3S] cluster cores, each hosting a single unpaired electron. Such an electronic state could present opportunities for future applications in low-dimensional quantum materials.
The observation of Luttinger liquid behaviour in $A\mathrm{Nb_3SBr_7}$ (A = Rb, Cs) demonstrates the variety of unconventional physical properties that can emerge from low-dimensional cluster networks. This emphasises the relevance of investigating further niobium and tantalum chalcohalide systems, aiming to identify new types of cluster connectivity and to study how these structural variations influence their electronic and magnetic properties.

3.2 Ta_4SBr_{11}: A Cluster Mott Insulator with a Corrugated, Van der Waals Layered Structure (Publication 2)[76]

Given the close similarities between niobium and tantalum arising from the lanthanide contraction, it appeared reasonable to explore whether reactions analogous to those used for $A Nb_3SBr_7$ could also yield related chalcohalide cluster compounds in the tantalum system. While the ionic radii of Nb and Ta are nearly identical,[85] their chemistry differs considerably in metal-rich compositions. In this case, Ta_4SBr_{11} was obtained through a comproportionation reaction in a molten CsBr flux, which served both as a reactant to form Cs_2TaBr_6 intermediately and as a medium to promote crystal growth by increasing ion mobility:

$$1.8\,\mathrm{Ta} + 2.2\,\mathrm{TaBr_5} + \mathrm{S} \xrightarrow[3\ \mathrm{d}]{400\ ^\circ\mathrm{C},\ \mathrm{CsBr}} \mathrm{Ta_4SBr_{11}}$$

The reaction yielded Ta_4SBr_{11} as platelet-like crystals, as observed in SEM images (Figure 13), reflecting the layered character of the crystal structure.

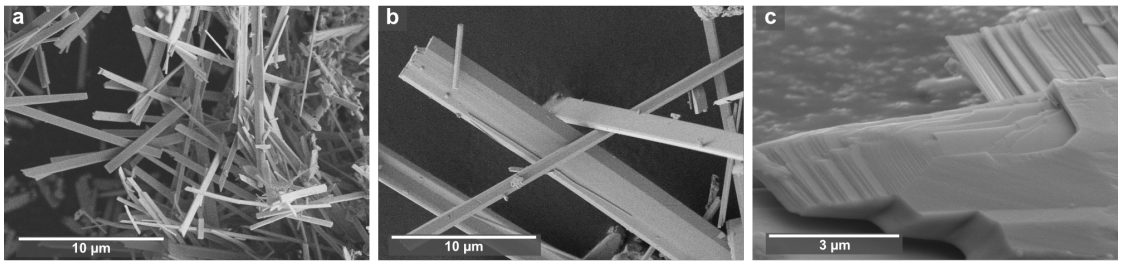

Figure 13: Scanning electron micrographs of Ta_4SBr_{11} crystals obtained from the direct synthesis (a) and grown from a flux of CsBr (b and c). Modified from publication 2.[76] (Rearrangement of figures)

The structure consists of characteristic butterfly-shaped [$Ta_4(\mu_4$-S)] clusters (Figure 14, left), in which four tantalum atoms are bridged by a central sulphur atom. Each cluster contains a total of seven cluster electrons, analogous to $A Nb_3SBr_7$, which results in one unpaired electron per cluster. The [Ta_4S] units are linked into chains along the a-axis via four bridging bromido ligands (Br3 and Br4). Additional bromides (Br2) connect the clusters along the b-axis, giving rise to corrugated vdW layers (Figure 14, right). These layers can shift relative to one another along the a-direction, leading to a superposition of several stacking arrangements in the SC-XRD data. The refined

average structure is shown in Figure 15. This crystal structure was first described in my master's thesis[86] and is closely related to the butterfly-type $[M_4(\mu_3\text{-}Pn)]$cluster cores reported for Nb_4PnX_{11}(Pn = N, P; X = Cl, Br, I),[71] where the capping sulphur atom is replaced by a pnictide.

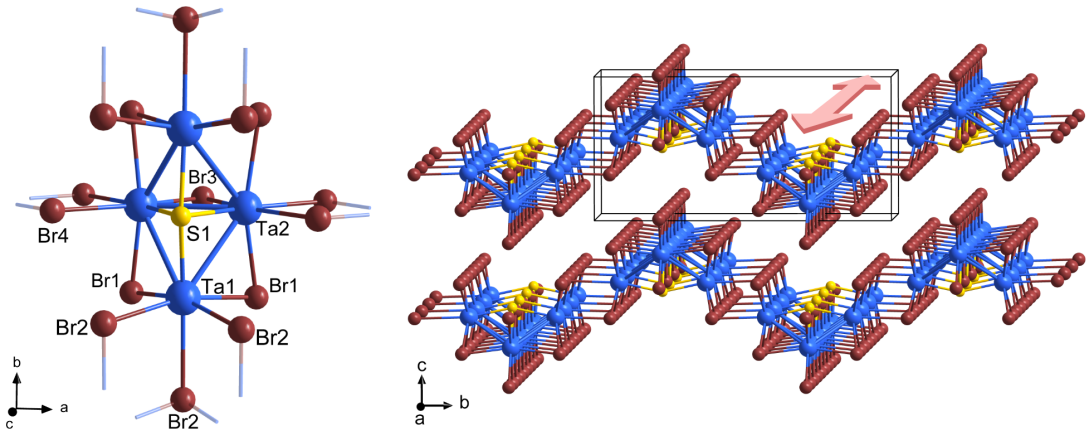

Figure 14: Characteristic $[Ta_4(\mu_4S)]$ butterfly cluster in the structure of Ta_4SBr_{11} with its connectivity pattern implied by broken-off bonds (left). Corrugated layer structure of Ta_4SBr_{11}, the red arrow highlights the shearing direction of the layers (right). Modified from publication 2.[76] (Two separate figures combined to one)

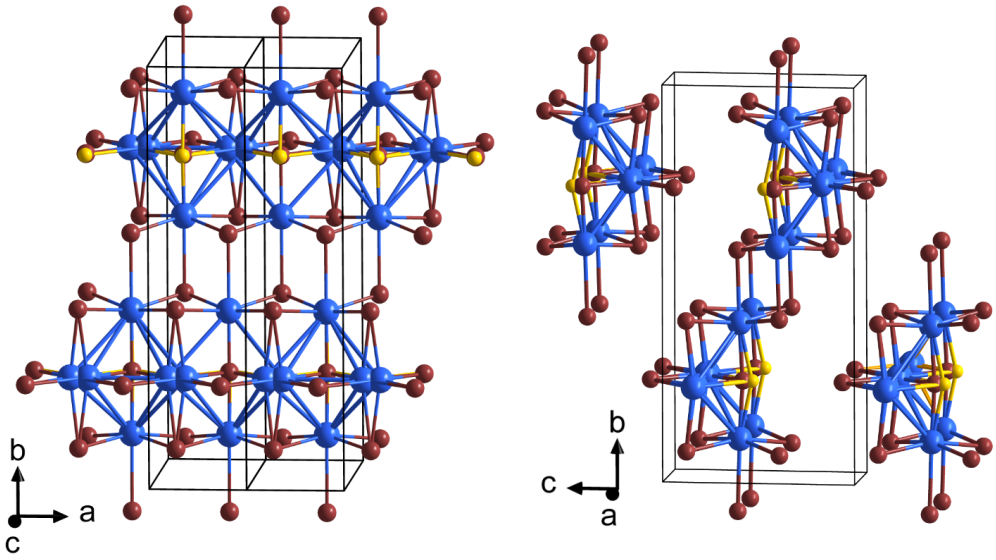

Figure 15: Refined average structure of Ta_4SBr_{11} in two projections. Tantalum atoms are depicted in blue, bromine in brown and sulphur in yellow. Modified from publication 2.[76] (Rearrangement of figures)

Electrical conductivity measurements reveal semiconducting behaviour with two distinct linear regimes in the Arrhenius plot (Figure 16). No structural phase transition was detected upon cooling to 80 K, i.e. below the temperature associated with the change in slope.

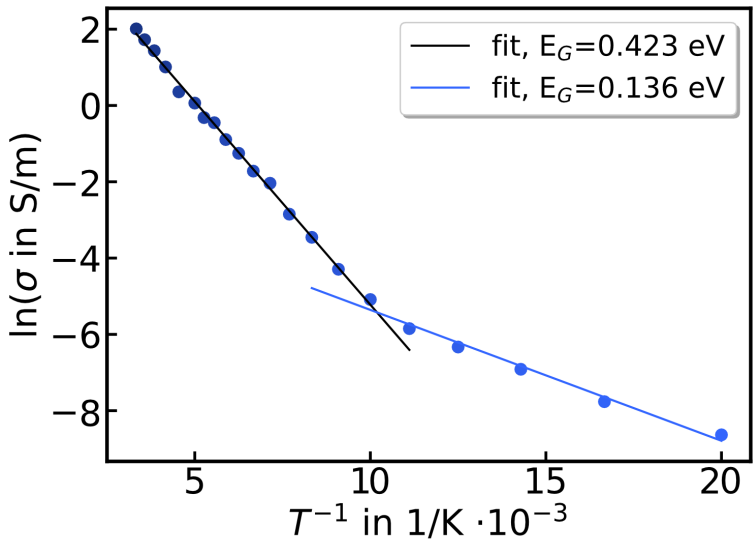

Figure 16: Arrhenius-plot of the temperature-dependent conductivity. Two regimes can be identified and fitted linearly to determine the electronic band gap.

Magnetic measurements show antiferromagnetic coupling between clusters, consistent with the presence of seven cluster electrons and thus one unpaired electron per Ta_4 unit, similar to the situation in ANb$_3$SBr$_7$. DFT calculations confirm that antiferromagnetic ordering between neighbouring clusters leads to a small band gap opening, with electronic states near the Fermi level, dominated by the cluster-based orbitals.
In summary, the combination of low-dimensional connectivity, unpaired electron content, and magnetic correlations defines the electronic behaviour of Ta_4SBr_{11}. As another example of a seven-electron cluster, Ta_4SBr_{11} shares a key feature with compounds such as Nb_3X_8 and $CsNb_3SBr_7$, where the presence of an unpaired electron in each cluster, together with strong electronic correlations, leads to properties beyond the predictions of simple band theory. Electronic structure calculations, supported by experimental data, suggest that Ta_4SBr_{11} is a cluster Mott insulator, similar to monolayer Nb_3Cl_8.[34] If monolayers of Ta_4SBr_{11} could be obtained (exfoliation attempts on Ta_4SBr_{11} single-crystals have not been successful), they might also exhibit interesting emergent phenomena such as flat electronic bands.

3.3 Hubbard Dimer Physics and the Magnetostructural Transition in the Correlated Cluster Material Nb_3Cl_8 (Publication 3)[87]

Nb_3X_8 (X = Cl, Br, I) is a layered cluster material consisting of $Nb_3X_4^iX_{6/2}^{a\text{-}a}X_{3/3}^{a\text{-}a}$ cluster units arranged in a breathing Kagome lattice, where each trimer hosts seven cluster electrons with one lone electron in the $2a_1$ level. This gives rise to narrow a_1 bands near fermi energy (E_f). As discussed above, monolayers behave as 2D Mott insulators, whereas in the bulk additional stacking physics must be considered.

This electronic situation leads to a magnetostructural transition near 100 K. While the HT phase is well established as $P\bar{3}m$ the LT symmetry remains debated ($R\bar{3}M$, $R3$, $C2/m$). Across the magnetic-to-nonmagnetic transition a strong quenching of the trimer moments is observed, but the microscopic mechanism remains under discussion. The aim of this work was to assess the different proposed explanations for its magnetostructural transition, such as charge disproportionation, antiferromagnetic quenching, and interlayer singlet formation, in light of the alternative low-temperature structures. To access the LT structure crystallographically, we examined $Nb_3Cl_4Br_4$, which undergoes a transition from a HT $P\bar{3}m$ phase to a LT $C2/m$ phase (Table 2). Across this transition, symmetry breaking occurs within the trigonal cluster motifs, but the intra-trimer Nb–Nb distances change only slightly. The dominant structural effect is instead a stacking rearrangement, leading to inter-trimer dimerisation between clusters of adjacent layers (Figure 17).

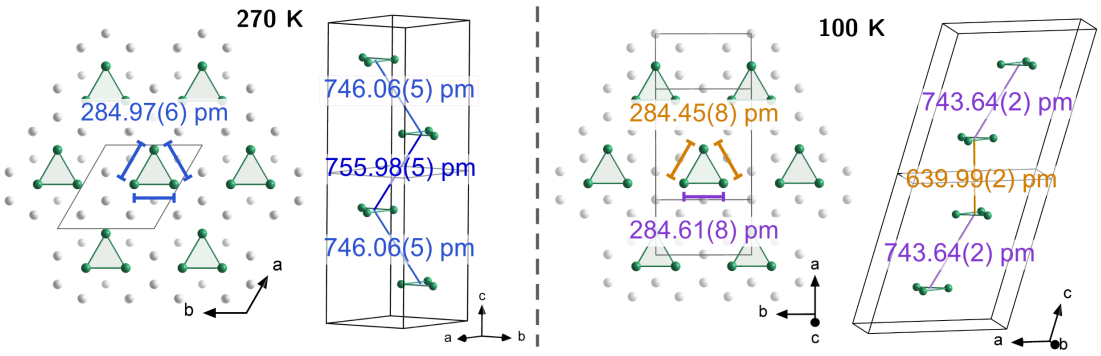

Figure 17: Stacking arrangement and distances of Nb_3 clusters and Nb–Nb distances within Nb_3 clusters in $Nb_3Cl_4Br_4$ as determined from single-crystal X-ray diffraction data at 270 K (left) and 100 K (right). Niobium atoms are depicted in green, chloride and bromide ions are gray. Modified from publication 3.[87] (two figures combined to one)

Table 2: Selected crystallographic data of $Nb_3Br_{4-x}Cl_{4+x}$ above and below the transition temperature.

Formula*	$Nb_3Br_{3.7}Cl_{4.3}$	$Nb_3Br_{3.8}Cl_{4.2}$
CCDC number	2364410	2365009
Temperature	270.0(1) K	100.0(1) K
Crystal system	trigonal	monoclinic
Space group	$P\bar{3}m$	$C2/m$
Wavelength	1.54184 Å	0.71037 Å
Radiation type	Cu-K_α	Mo-K_α
R_1	0.0350	0.0350
wR_2	0.0903	0.0909

*The composition variation is within the synthesis and refinement error margin, and is considered as $Nb_3Br_4Cl_4$.

The temperature-dependent conductivity measurements on single crystals of Nb_3Cl_8 revealed semiconducting behaviour above 100 K in the HT phase. Below this temperature, however, the conductivity dropped below the detection limit without any hysteresis, indicating the absence of mobile charge carriers in the LT phase. This behaviour is consistent with the dimerisation of clusters across adjacent layers, where the unpaired electrons become localised. Both optical band gap measurements on bulk material and the magnetic susceptibility measurements agreed with previously reported data. Importantly, the magnetic-to-nonmagnetic transition was not only observed in single crystals but could also be clearly detected on bulk samples.

On the theoretical side, DFT+U+V and DFT+DMFT calculations rule out charge disproportionation as the primary mechanism for the transition. Instead, the transition is driven by the stacking-induced inter-inter trimer dimerisation, while intra-trimer distortions play only a secondary role. Moreover, Nb_3Cl_8 can be described as a system of weakly coupled Hubbard dimers. Within this picture, the two interpretations discussed in the literature, one describing the compound as a strongly correlated Mott-like state with antiferromagnetic interactions and the other as a singlet-like band insulator are not contradictory, but represent two limits of the same model. The strength of the inter-trimer coupling determines where the material falls between these regimes. In this way, the variations observed between Nb_3Cl_8, $Nb_3Cl_4Br_4$, and related compounds can be understood, since the choice of halide directly influences the degree of inter-trimer interaction and thus shifts the balance between Mott-like and singlet-like behaviour.

3.4 Structural Modifications of $M_5O_4I_{11}$ (M = Nb, Ta) Cluster Networks from Heterogeneous Solid-State Reactions (Publication 4)[88]

Conventional syntheses of reduced niobium and tantalum cluster halides use high-temperature solid-state routes, often in alkali halide melts or under transport conditions. In this study, an unconventional reduction of TaI_5 with Li_2CN_2 in the Ta–O–I system yields three van der Waals-layered cluster networks that share a pentanuclear cluster core: *o*-$Ta_5O_4I_{11}$, *m*-$Ta_5O_4I_{11}$, and $Ta_5O_4I_{11}(TaI_5)$ with embedded TaI_5. All three are built from a common square-pyramidal $[Ta_5O_4]$ cluster core, but they differ in the arrangement of iodide ligands and thus in the connectivity between neighbouring clusters, which produces distinct cluster networks (Figure 18).

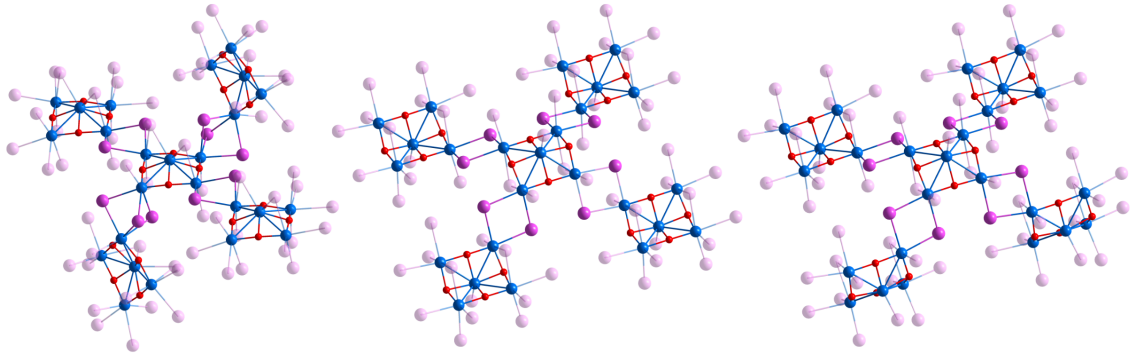

Figure 18: Comparison of the inter cluster connectivity of *o*-$Ta_5O_4I_{11}$, *m*-$Ta_5O_4I_{11}$ and $Ta_5O_4I_{11}(TaI_5)$.

The different iodide environments of the cluster cores can be seen in Figure 19. In *o*-$Ta_5O_4I_{11}$, the ligand environment can be written as $[(Ta_5O_4)I^i_2I^a_4I^{a\text{-}a}_{10/2}]$, i.e. two inner iodides, four terminal outer iodides, and ten outer bridging iodides shared between adjacent clusters (counting as 10/2 per cluster). In *m*-$Ta_5O_4I_{11}$, it is $[(Ta_5O_4)I^i_2I^a_5I^{a\text{-}a}_{8/2}]$, i.e. two inner, five terminal outer, and eight outer bridging iodides (8/2 per cluster). In *o*-$Ta_5O_4I_{11}$ there are three μ_2-bridging iodides along one in-plane direction of the vdW layers and two along the perpendicular direction, whereas *m*-$Ta_5O_4I_{11}$ has two bridges to each of the four adjacent clusters. This leads to shorter inter-cluster distances in one in-plane direction for *o*-$Ta_5O_4I_{11}$ and, overall, to different corrugation patterns of the layers.

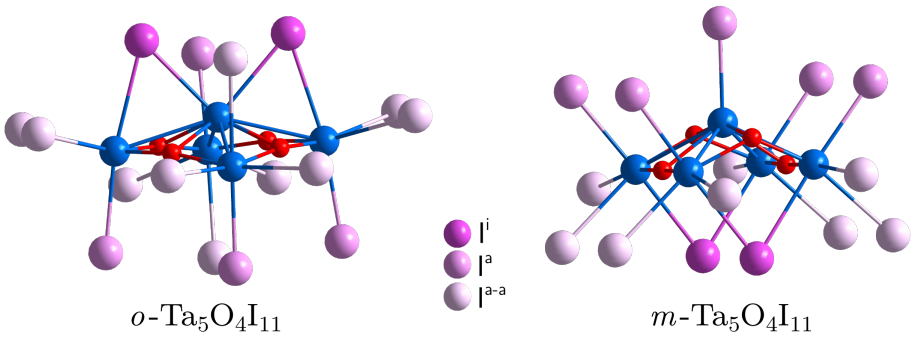

Figure 19: Side view of clusters in o-$Ta_5O_4I_{11}$ (left) and m-$Ta_5O_4I_{11}$ (right), highlighting the different arrangements of iodine atoms and their impact on the distortion of the cluster core.

Figure 20 shows SEM images of crystal agglomerates and surface morphologies for o-$Ta_5O_4I_{11}$ (a–c) and m-$Ta_5O_4I_{11}$ (d–f). The two polymorphs exhibit clearly different crystal habits: o-$Ta_5O_4I_{11}$ often presents well-defined, individually resolvable layers (c), consistent with comparatively weaker interlayer interactions, whereas m-$Ta_5O_4I_{11}$ displays more compact, block-like surfaces (f), pointing to stronger interactions between adjacent layers.

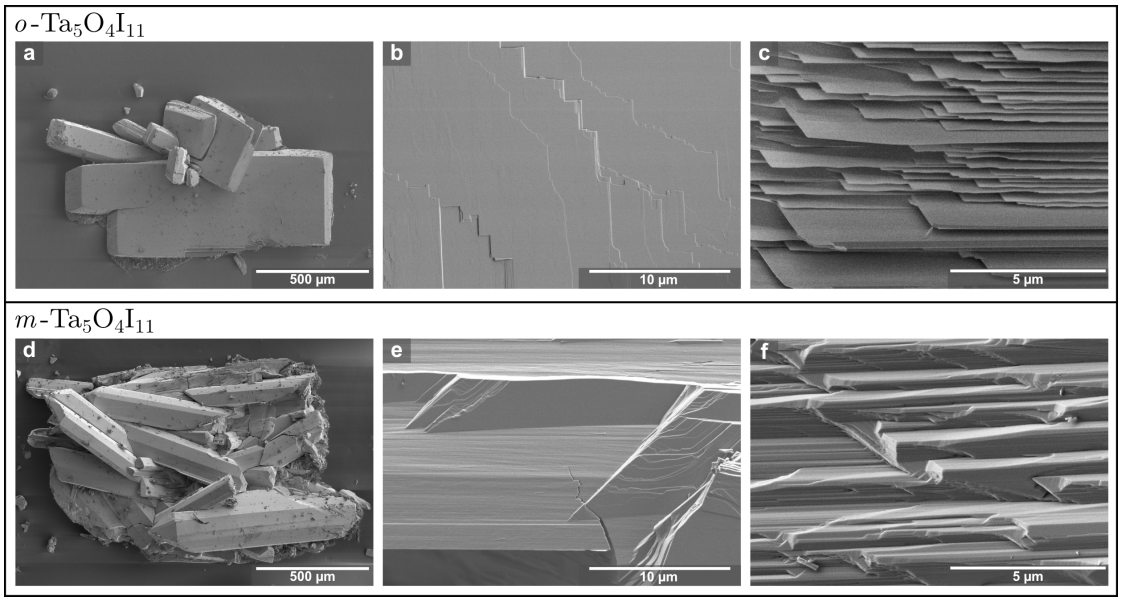

Figure 20: Scanning electron micrographs of o-$Ta_5O_4I_{11}$ crystals (a-c) and m-$Ta_5O_4I_{11}$ crystals (d-f), showing a layered morphology. Modified from publication 4.[88] (Rearrangement of figures)

XPS indicates a mixed-valence configuration with a Ta(IV):Ta(III) ratio of 4.14:1, consistent with a reduced apical Ta^{3+} and four Ta^{4+} at the basal positions of the Ta_5O_4 core. In temperature dependent conductivity measurements, both polymorphs show semiconducting behaviour with Arrhenius-type transport (Figure 21). *o*-$Ta_5O_4I_{11}$ shows the smaller activation energy (∼0.10 eV) and higher conductivity, while *m*-$Ta_5O_4I_{11}$ exhibits a larger activation energy (∼0.40 eV). This is consistent with the shorter inter-cluster separation along the crystallographic *c*-axis in *o*-$Ta_5O_4I_{11}$.

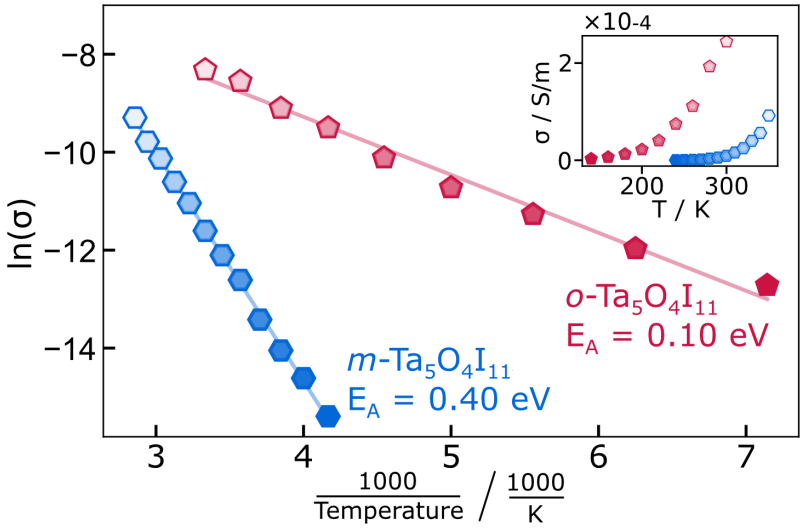

Figure 21: Arrhenius-plot of the temperature-dependent conductivity between 140 K-300 K for *o*-$Ta_5O_4I_{11}$ (red) and 240 K-350 K for *m*-$Ta_5O_4I_{11}$ (blue). The inset shows the linear plot of the conductivity versus temperature.

In DFT calculations, *o*-$Ta_5O_4I_{11}$ and *m*-$Ta_5O_4I_{11}$ show clear differences in electronic structure. In *o*-$Ta_5O_4I_{11}$, the states near E_f are dominated by Ta *d* character and split into distinct band manifolds. The upper manifolds are nearly flat, consistent with localised electrons and a largely ionic picture. In *m*-$Ta_5O_4I_{11}$, pronounced hybridisation near E_f introduces O and I contributions to the Ta states, and a band gap opens in line with increased covalency. The electron localisation function (ELF) calculations support this: *o*-$Ta_5O_4I_{11}$ exhibits mostly spherical ELFs around Ta and O with nodal planes between Ta atoms, indicating ionic bonding, whereas *m*-$Ta_5O_4I_{11}$ shows distorted ELFs and interstitial density between pairs of Ta atoms, corresponding to the formation of Ta–Ta bonds. Overall, *o*-$Ta_5O_4I_{11}$ seems to be more ionic, while *m*-$Ta_5O_4I_{11}$ has a more covalent character.

$Ta_5O_4I_{11}(TaI_5)$ is closely related to *m*-$Ta_5O_4I_{11}$ in terms of cluster connectivity, both retain the same iodide environment, but the additional incorporation of molecular TaI_5 units substantially changes the layer topology (Figure 18). The amplitude of the sinusoidal corrugation is larger in $Ta_5O_4I_{11}(TaI_5)$ than in *m*-$Ta_5O_4I_{11}$, which creates voids that can accommodate and stabilise TaI_5 molecules (Figure 22) that are otherwise only found in the vapour phase but not in solid state structures.

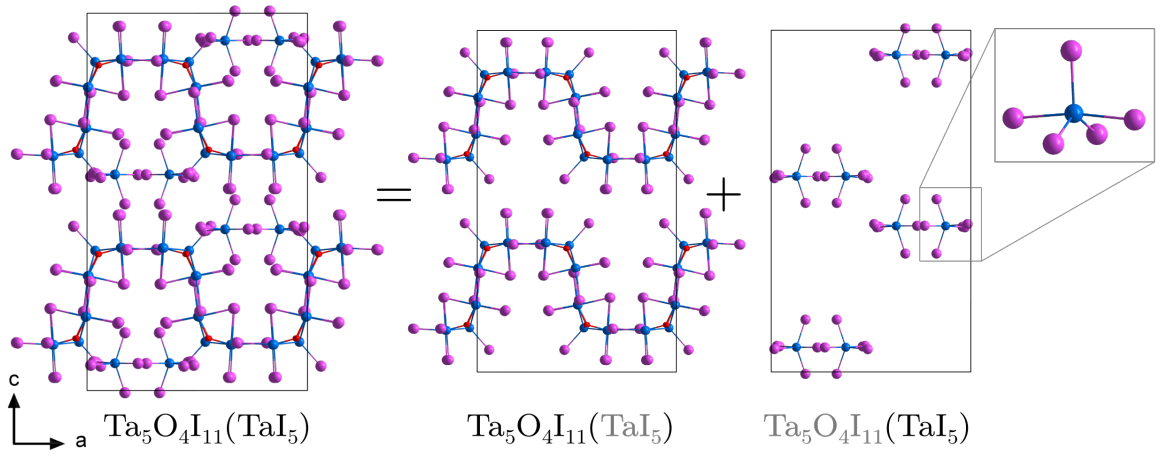

Figure 22: Projected crystal structure of $Ta_5O_4I_{11}(TaI_5)$ (left) and segmentation of the structure into $[Ta_5O_4I_{11}]$ and $[TaI_5]$ (middle), and an additional isolated TaI_5 unit (right). Modified from publication 4.[88] (Rearrangement and combination of figures)

The side-by-side occurrence of all of these different cluster networks highlights the complexity of the reaction conditions and the influence of gas-phase transport and thermal gradients. The $[Ta_5O_4]$ cluster motif combines structural stability with geometric flexibility: it persists across distinct environments and tolerates substantial distortions. Nevertheless, *o*-$Ta_5O_4I_{11}$ and *m*-$Ta_5O_4I_{11}$ are not interconvertible by thermal treatment. Heating beyond $\sim$650 °C leads to decomposition and formation of $TaOI_2$ rather than a phase transition between the two modifications. For *o*-$M_5O_4I_{11}$ (M = Nb, Ta) the niobium and tantalum structures are isotypic, however, no niobium analogues of *m*-$Ta_5O_4I_{11}$ or $Ta_5O_4I_{11}(TaI_5)$ were observed. Instead, niobium forms distinct cluster architectures, reflecting element-specific differences.[89,90]

4 Unpublished Work

4.1 Synthesis and Crystal Structure of $KTiBr_4$

In the titanium halide system, Ti(IV), Ti(III), and Ti(II) oxidation states are common. The Ti(III) ($3d^1$) and Ti(II) ($3d^2$) cases are particularly interesting because they combine unpaired electrons with direct Ti–Ti bonds.[91] While only few titanium cluster compounds are known (e.g., $Na_2Ti_3Cl_8$ with Ti_3 trimers;[92] $K_4[(Ti_4O)I_{12}]$ with Ti_4 square geometry;[93] and $(Ti_6C)Cl_{14}$ with Ti_6 octahedral geometry),[94] most ternary compounds adopt motifs based on isolated or face-sharing TiX_6 octahedra: isolated $[TiX_6]^{3-}$(A_3TiX_6),[95] dimers of face-sharing octahedra ($A_3Ti_2X_9$),[92] linear Ti_3X_{12} trimers ($K_4Ti_3Br_{12}$, $In_4Ti_3Br_{12}$),[96,97] or infinite chains of face-sharing octahedra ($ATiX_3$).[91,98]

Motivated by the limited number of known titanium cluster motifs, I attempted to synthesise new types of clusters in the Ti–X system. However, instead of yielding cluster compounds, the investigated reactions produced several known phases besides $KTiBr_4$, which was obtained in a comproportionation reaction of Ti and $TiBr_4$ with excess titanium powder and KBr. The compound was obtained as black $KTiBr_4$ crystals growing on green needle-like crystals of β-$TiBr_3$[99](Figure 23):

$$1.5\,\mathrm{Ti} + 1.5\,\mathrm{TiBr_5} + 1\,\mathrm{KBr} \xrightarrow[3\ \mathrm{d}]{450\ ^\circ\mathrm{C}} \mathrm{KTiBr_4} + \mathrm{TiBr_3} + \mathrm{Ti}$$

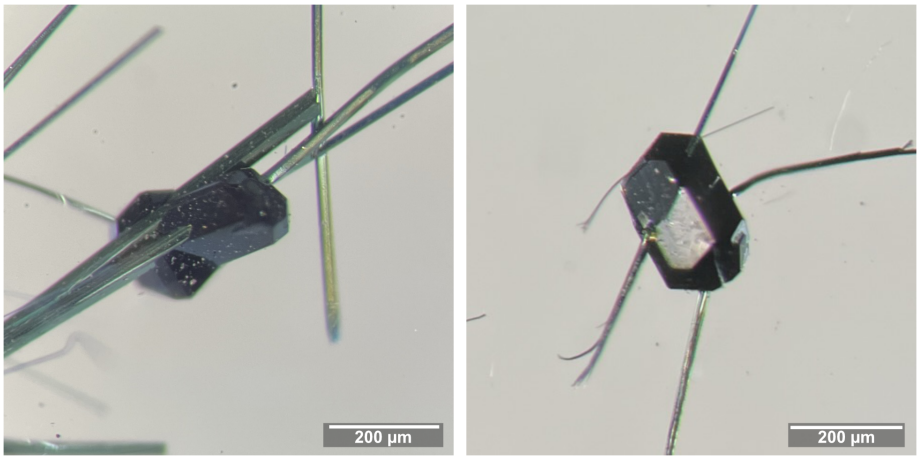

Figure 23: Optical micrographs of black $KTiBr_4$ crystals, growing on green, needle-like crystals of β-$TiBr_3$.

Single-crystal data collected at 100 K show that $KTiBr_4$ crystallises in the trigonal space group $R\bar{3}c$ with $a = b = 12.1280(2)$ Å, and $c = 26.0221(5)$ Å(Table 3).

$KTiBr_4$ adopts a new structure type related to $ATiX_3$, which consists of infinite TiX_3 chains. In $KTiBr_4$, however, the face-sharing octahedral chains are broken into triples: strands of face-sharing $[Ti_3Br_{12}]^{3-}$ units are separated by potassium, resulting in $^1_\infty[K_3Ti_3Br_{12}]$ chains. Three representative views of the crystal structure are shown in Figure 24. The motif of interrupted face-sharing chains (trimers instead of infinite chains) is analogous to the situation in $K_4Ti_3Br_{12}$ and $In_4Ti_3Br_{12}$.[96,97]

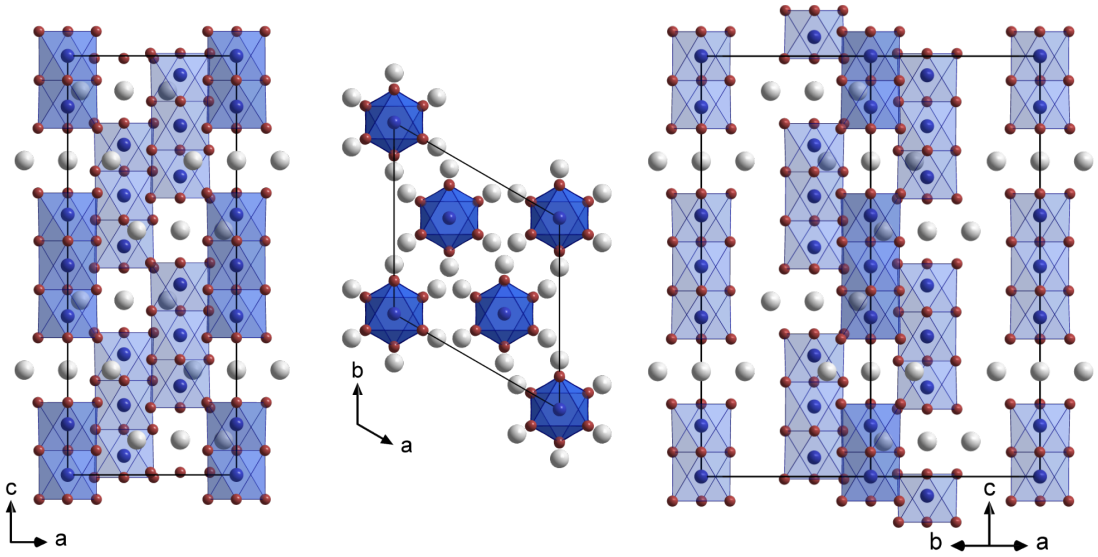

Figure 24: Selected viewing directions of the $KTiBr_4$ crystal structure, the unit cell is outlined. Ti: dark blue, K: grey, Br: brown.

Table 3: Selected crystallographic data of $KTiBr_4$.

Formula	$KTiBr_4$
CCDC number	2179182
Temperature	150 K
Crystal system	trigonal
Space group	$R\bar{3}c$
Wavelength	0.71037 Å
Radiation type	Mo-K_α
R_1	0.0146
wR_2	0.0228

Figure 25 (left) highlights the local environment: each $[Ti_3Br_{12}]^{3-}$ unit is a linear trimer of face-sharing $TiBr_6$ octahedra, with potassium ions located between adjacent trimers along the strand. The interatomic distances (Figure 25, right) are consistent with literature values for face-sharing octahedra, with Ti–Ti distances of about 315.5 pm and Ti–Br distances of 252–263 pm.[91,96,100]

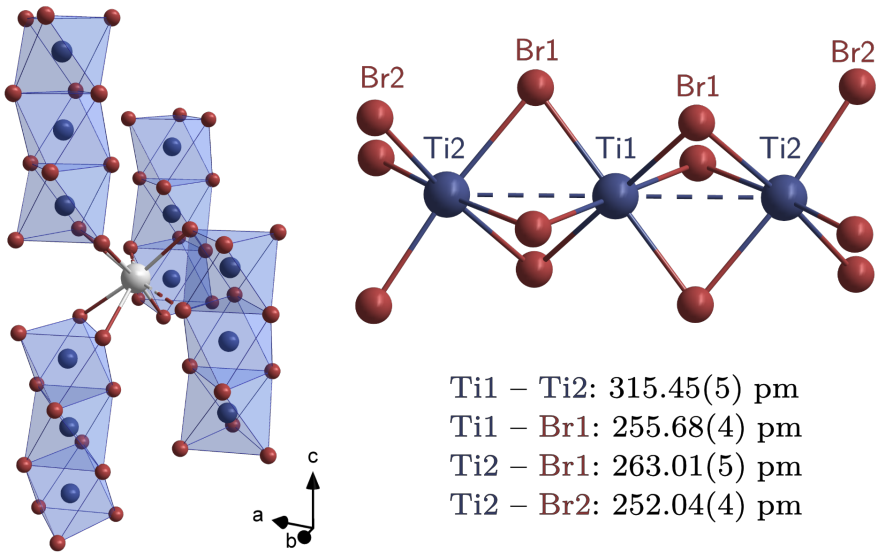

Figure 25: Arrangement of $[Ti_3Br_{12}]^{3-}$ units as a coordination around the potassium cation (left) and isolated $[Ti_3Br_{12}]^{3-}$ unit with some interatomic distances (right).

$KTiBr_4$ extends the *A*-Ti-*X* halide family by introducing a trimer-based, "broken-chain" motif in which infinite face-sharing columns are segmented into linear $[Ti_3Br_{12}]^{3-}$ units separated by potassium. Despite the presence of slightly reduced Ti^{3+}, the interatomic distances do not indicate significant Ti–Ti interactions. The compound is also highly air-sensitive, which limited further characterisation and prevented extended property measurements.

4.2 A Complete Cathode Recovery Cycle of an Exhausted and Dismantled Lithium Battery Material

Beyond the scope of cluster synthesis, a simple and cost-effective recycling process of spent graphitic $Li(Ni,Mn,Co)O_2$ (Li-NMC) battery material was investigated for "black mass", a mixture of anode and cathode powder, obtained from a commercial thermomechanical battery segmentation process. The developed procedure involves a combination of thermal treatment, leaching and electrolysis to remove impurities without altering the NMC starting composition. Fresh $LiNi_{0.6}Mn_{0.2}Co_{0.2}O_2$ (NMC 622) cathode material was synthesised using an aqueous sol-gel method as a proof of concept.

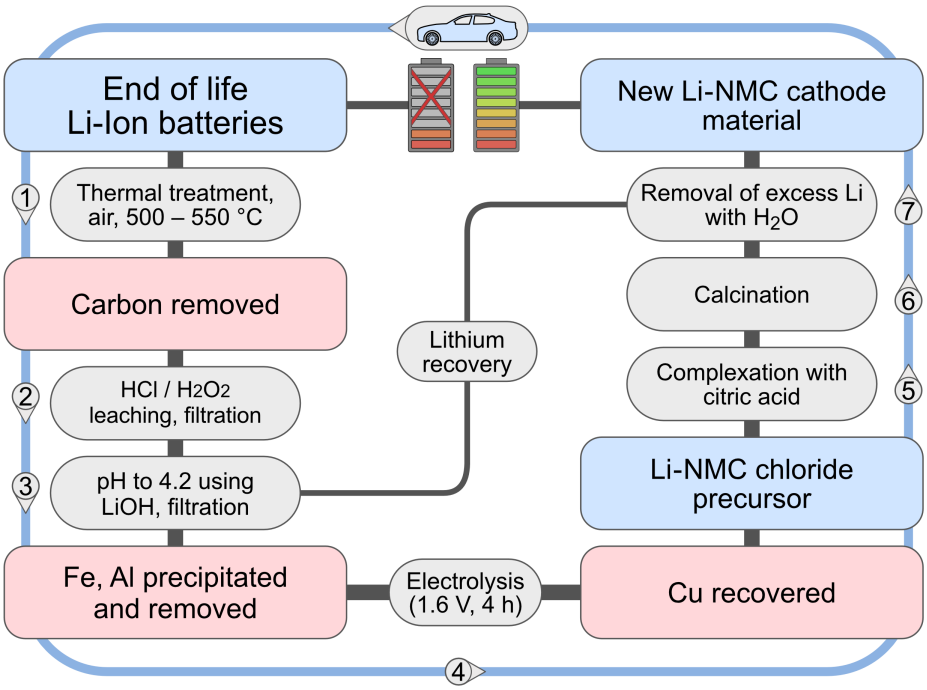

Figure 26: Recycling scheme for end of life lithium battery, departing from heat treatment for the removal of carbon, followed by acid leaching, pH dependent precipitation of impurities and electrolysis, sol-gel synthesis, involving complexation and calcination as structuring procedure for new Li-NMC cathode material.

Figure 26 outlines the seven-step recycling scheme developed in this work. In Step 1, the crude “black mass” is thermally treated at 500–550 °C to remove binders, electrolyte residues, and graphite without altering the layered NMC phase or its composition. Some aluminium- and iron-containing species are formed during this pretreatment and persist as insoluble residues in the subsequent leach. In Step 2, the solid is leached

with 5 M hydrochloric acid (HCl) in the presence of a small amount of H_2O_2. HCl is chosen over nitric acid because HNO_3/H_2O_2 tends to precipitate insoluble MnO_2, which would then require additional sulphuric or hydrochloric acid to re-dissolve. In Step 3, the filtrate acidity is adjusted to pH∼4.3 by adding LiOH. This selectively precipitates the remaining Fe and Al impurities and, at the same time, compensates the lithium deficiency, so that the target Li(Ni,Mn,Co)O_2 stoichiometry can be re-established. In Step 4, copper is quantitatively recovered from solution by electrolysis at 1.6 V for 4 h using a graphite anode and a copper cathode. In Steps 5 and 6, the remaining solution is dried, converted into a citrate gel via an aqueous sol–gel route, and then calcined to produce fresh Li-NMC cathode powder. In Step 7, excess lithium introduced during the pH adjustment is removed by washing the product with water.

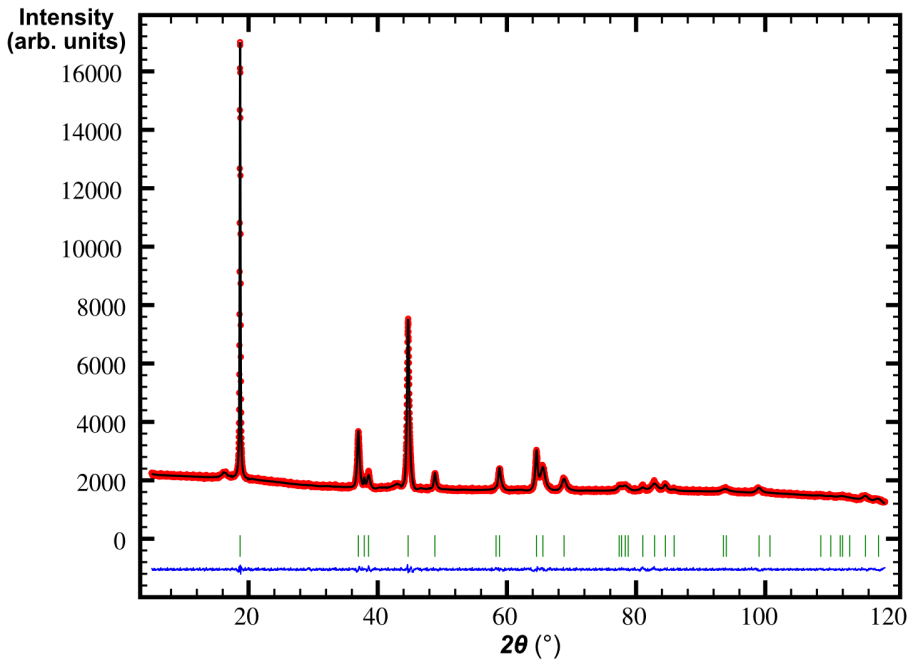

Figure 27: Rietveld fit of the Cu-K_α PXRD pattern of the fresh Li-NMC material. The observed pattern (red dots) is superimposed with the calculated pattern (black line). Green ticks mark the Bragg reflections of the calcined Li-NMC 622 material. The difference curve between the observed and calculated pattern is shown in the lower part of the graph (blue line). Broad reflections at 2Θ values 16.2° and 43.1° emerge from the sample carrier foil.

Rietveld refinement of the recycled powder using $LiNiO_2$ (space group $R\bar{3}m$) as the starting model and fixing Ni:Mn:Co to the TXRF-derived ratios shows excellent agreement between observed and calculated patterns, with no significant side phases (Figure

27). The refinement accounts for small particle size and converges with good residuals; about 5.8 % Ni^{2+} on Li^{+} sites is inferred, which is consistent with the more cubic/octahedral particle habit seen by SEM (50–250 nm). Together, the diffraction and compositional data confirm that Ni, Mn, and Co are fully incorporated in the layered $LiNiO_2$-type structure after resynthesis.

The route closes the loop from mixed "black mass" to phase-pure, composition-controlled Li-NMC (622/532) without element-by-element separation, using only common reagents and unit operations (thermal, HCl/H_2O_2 leach, pH-precipitation with LiOH, electrolytic Cu regeneration, citrate sol-gel).

Before application, the electrochemical performance still needs to be verified. At a minimum, cyclic voltammetry and coin-cell testing should be carried out to confirm reversible (de)intercalation and cycle stability. For industrial use, further development is required to handle variable starting material, scale the process while keeping impurity control (Cu/Al/Fe), implement closed-loop acid and solvent management, and reduce the energy footprint of the thermal step.

5 Conclusion

In this work, several low-dimensional cluster networks were investigated with respect to their crystal structures and electronic behaviour. While $A\mathrm{Nb_3SBr_7}$ (A = Rb, Cs) form one-dimensional chain structures, $\mathrm{Ta_4SBr_{11}}$, $\mathrm{Nb_3}X_8$ (X = Cl, Br, I), and $M_5\mathrm{O_4I_{11}}$ (M = Nb, Ta) adopt two-dimensional vdW layered architectures. This reduction in dimensionality, together with an odd electron count per cluster, gives rise to pronounced electronic correlations: in $A\mathrm{Nb_3SBr_7}$, the temperature dependence of the conductivity is consistent with Luttinger-liquid behaviour; in $\mathrm{Nb_3Cl_8}$ cooling drives the formation of Hubbard dimers between unpaired cluster electrons of adjacent layers, resulting in a magnetostructural transition; and in the intrinsically disordered, corrugated layers of $\mathrm{Ta_4SBr_{11}}$, unpaired electrons in butterfly-type clusters exhibit antiferromagnetic coupling. All three are seven-electron cluster materials whose properties cannot be captured by simple band-structure arguments.

Whereas $A\mathrm{Nb_3SBr_7}$ and $\mathrm{Ta_4SBr_{11}}$ were obtained by classical solid-state comproportionation routes in an alkali halide flux, an unconventional heterogeneous reduction with $\mathrm{Li_2CN_2}$ opened an alternative pathway to new cluster motifs in the Ta–O–I system. In the penta nuclear $M_5\mathrm{O_4I_{11}}$ (M = Nb, Ta) family, three structurally distinct cluster networks were obtained, all based on a closely related $[M_5\mathrm{O_4}]$ core. Although these structures appear similar at first glance, changes in the positions of iodide ligands and in the inter-cluster connectivity markedly affect the electronic behaviour: o-$\mathrm{Ta_5O_4I_{11}}$ exhibits a smaller activation energy than m-$\mathrm{Ta_5O_4I_{11}}$, and electron-localisation-function calculations indicate more ionic connectivity for o-$\mathrm{Ta_5O_4I_{11}}$ and more covalent connectivity for m-$\mathrm{Ta_5O_4I_{11}}$.

These results point to a practical route to new cluster motifs via unconventional reduction. The physical properties of the studied networks show that low dimensionality and specific electron counts generate correlated states with unusual electronic transport and magnetic behaviour. This combination could ultimately enable new types of electronic components and deepen our understanding of electron behaviour in cluster-based materials.

References

[1] S. Rabe, U. Müller, *Z. Kristallogr. - New Cryst. Struct.* **2000**, *215*, 1–2.

[2] S. Tragl, H.-J. Meyer, *Z. Kristallogr. - New Cryst. Struct.* **2007**, *222*, 161–162.

[3] W. Hönle, H.-G. von Schnering, *Z. Kristallogr.* **1990**, *191*, 139–140.

[4] W. Hönle, S. Furuseth, H.-G. von Schnering, *Z. Naturforsch. B* **1990**, *45*, 952–956.

[5] W. Littke, G. Brauer, *Z. Anorg. Allg. Chem.* **1963**, *325*, 122–129.

[6] K. Habermehl, I. Pantenburg, P. Held, G. Meyer, *Z. Anorg. Allg. Chem.* **2008**, *634*, 829–831.

[7] K. Habermehl, I. Pantenburg, G. Meyer, *Acta Crystallogr. Sec. E* **2010**, *66*, i67.

[8] R. W. Berg, *Coordin. Chem. Rev.* **1992**, *113*, 1–130.

[9] R. McCarley, J. Boatman, *Inorg. Chem.* **1963**, *2*, 547–551.

[10] H. Schäfer, L. Grau, *Z. Anorg. Allg. Chem.* **1954**, *275*, 198–209.

[11] G. Meyer, R. Wiglusz, I. Pantenburg, A.-V. Mudring, *Z. Anorg. Allg. Chem.* **2008**, *634*, 825–828.

[12] P. W. Seabaugh, J. D. Corbett, *Inorg. Chem.* **1965**, *4*, 176–181.

[13] F. Hulliger, *Structural chemistry of layer-type phases*, Springer Science, Business Media, **1976**.

[14] H. Imoto, A. Simon, *Inorg. Chem.* **1982**, *21*, 308–319.

[15] A. Simon, H.-G. von Schnering, H. Wöhrle, H. Schäfer, *Z. Anorg. Allg. Chem.* **1965**, *339*, 155–170.

[16] B. Baján, H.-J. Meyer, *Z. Kristallogr. Cryst.* **1995**, *210*, 607–607.

[17] B. Baján, H.-J. Meyer, *Z. Naturforsch. B* **1995**, *50*, 1373–1376.

[18] H.-G. von Schnering, D. Vu, S.-L. Jin, K. Peters, *Z. Kristallogr. - New Cryst. Struct.* **1999**, *214*, 15–16.

[19] D. Bauer, H.-G. von Schnering, *Z. Anorg. Allg. Chem.* **1968**, *361*, 259–276.

[20] H. M. Artelt, G. Meyer, *Z. Kristallogr.* **1993**, *206*, 306–307.

[21] A. Simon, H.-G. von Schnering, H. Schäufer, *Z. Anorg. Allg. Chem.* **1967**, *355*, 295–310.

[22] T. Hummel, D. Dutczak, A. Y. Alekseev, L. S. Adamenko, M. A. Shestopalov, Y. V. Mironov, D. Enseling, T. Jüstel, H.-J. Meyer, *RSC Adv.* **2020**, *10*, 22257–22263.

[23] A. W. Maverick, H. B. Gray, *J. Am. Chem. Soc.* **1981**, *103*, 1298–1300.

[24] F. Pachel, M. Ströbele, C. P. Romao, D. Enseling, T. Jüstel, H.-J. Meyer, *Eur. J. Inorg. Chem.* **2023**, *26*, e202300096.

[25] N. T. K. Nguyen, C. Lebastard, M. Wilmet, N. Dumait, A. Renaud, S. Cordier, N. Ohashi, T. Uchikoshi, F. Grasset, *Sci. Technol. Adv. Mater.* **2022**, *23*, 547–578.

[26] P. J. Kuhn, R. E. McCarley, *Inorg. Chem.* **1965**, *4*, 1482–1486.

[27] A. Simon, H.-G. von Schnering, *J. Less-Common Met.* **1966**, *11*, 31–46.

[28] K. Habermehl, G. Meyer, *Z. Naturforsch. B* **2010**, *65*, 770–772.

[29] M. Ströbele, J. Glaser, A. Lachgar, H.-J. Meyer, *Z. Anorg. Allg. Chem.* **2001**, *627*, 2002–2004.

[30] M. N. Sokolov, V. P. Fedin, *Coordin. Chem. Rev.* **2004**, *248*, 925–944.

[31] C. M. Pasco, I. El Baggari, E. Bianco, L. F. Kourkoutis, T. M. McQueen, *ACS Nano* **2019**, *13*, 9457–9463.

[32] J. P. Sheckelton, K. W. Plumb, B. A. Trump, C. L. Broholm, T. M. McQueen, *Inorg. Chem. Front.* **2017**, *4*, 481–490.

[33] Y. Haraguchi, C. Michioka, M. Ishikawa, Y. Nakano, H. Yamochi, H. Ueda, K. Yoshimura, *Inorg. Chem.* **2017**, *56*, 3483–3488.

[34] S. Grytsiuk, M. I. Katsnelson, E. G. C. P. v. Loon, M. Rösner, *npj Quantum Mater.* **2024**, *9*, 8.

[35] R. Peng, Y. Ma, X. Xu, Z. He, B. Huang, Y. Dai, *Phys. Rev. B* **2020**, *102*, PRB, 035412.

[36] J. Hu, X. Zhang, C. Hu, J. Sun, X. Wang, H.-Q. Lin, G. Li, *Commun. Phys.* **2023**, *6*, 172.

[37] K. Qu, Z. W. Riedel, I. Sánchez-Ramírez, S. Bettler, J. Oh, E. N. Waite, T. J. Woods, N. Mason, P. Abbamonte, F. de Juan, M. G. Vergniory, D. P. Shoemaker, *Inorg. Chem.* **2023**, *62*, 3067–3074.

[38] S. Hartwig, H. Hillebrecht, *Z. Naturforsch. B* **2007**, *62*, 1543–1548.

[39] H. Schäfer, L. Zylka, *Z. Anorg. Allg. Chem.* **1965**, *338*, 309–311.

[40] L. K. Frevel, H. W. Rinn, *Acta Crystallogr.* **1956**, *9*, 626–627.

[41] L. Zylka, Dissertation, **1966**.

[42] J. Kim, Y. Dong, H. Yun, *Acta Crystallogr. Sect. C:Struct. Chem.* **1999**, *55*.

[43] H.-G. von Schnering, W. Beckmann, *Z. Anorg. Allg. Chem.* **1966**, *347*, 231–239.

[44] S. Andersson, *Acta Chem. Scand.* **1964**, *18*.

[45] M. Vlasse, C. Morillière, J.-P. Chaminade, M. Pouchard, *Bull. Soc. Fr. Mineral. Cristallogr.* **1975**, *98*, 325–330.

[46] H. Schäfer, E. Sibbing, R. Gerken, *Z. Anorg. Allg. Chem.* **1961**, *307*, 163–173.

[47] H. Hillebrecht, P. J. Schmidt, H. W. Rotter, G. Thiele, P. Zönnchen, H. Bengel, H. J. Cantow, S. N. Magonov, M. H. Whangbo, *J. Alloy. Compd.* **1997**, *246*, 70–79.

[48] H.-G. von Schnering, W. Mertin, *Naturwissenschaften* **1964**, *51*, 552–552.

[49] A. Bera, S. Rom, S. K. Pradhan, S. Bera, S. Kalimuddin, T. Saha-Dasgupta, M. Mondal, *Phys. Rev. B* **2023**, *108*, PRB, 035112.

[50] F. A. Cotton, *Q. Rev. Chem. Soc.* **1966**, *20*, 389–401.

[51] H. F. Franzen, W. Hönle, H.-G. von Schnering, *Z. Anorg. Allg. Chem.* **1983**, *497*, 13–20.

[52] J. Rijnsdorp, G. J. de Lange, G. A. Wiegers, *J. Solid State Chem.* **1979**, *30*, 365–373.

[53] G. J. Miller, *J. Alloy. Compd.* **1995**, *229*, 93–106.

[54] H.-J. Meyer, *Z. Anorg. Allg. Chem.* **1994**, *620*, 863–866.

[55] J. Rijnsdorp, F. Jellinek, *J. Solid State Chem.* **1979**, *28*, 149–156.

[56] A. Meerschaut, P. Grenouilleau, J. Rouxel, *J. Solid State Chem.* **1986**, *61*, 90–97.

[57] J.-E. Kwak, S.-I. Hahn, H. Yun, *Acta Crystallogr. Sect. E:Crystallogr. Commun.* **2007**, *63*, i27–i29.

[58] A. Meerschaut, P. Grenouilleau, L. Gue´mas, J. Rouxel, *J. Solid State Chem.* **1987**, *70*, 36–47.

[59] G. V. Khvorykh, A. V. Shevelkov, V. A. Dolgikh, B. A. Popovkin, *J. Solid State Chem.* **1995**, *120*, 311–315.

[60] M. D. Smith, G. J. Miller, *J. Solid State Chem.* **1998**, *140*, 226–232.

[61] M. D. Smith, G. J. Miller, *Z. Anorg. Allg. Chem.* **2000**, *626*, 94–102.

[62] M. D. Smith, G. J. Miller, *J. Am. Chem. Soc.* **1996**, *118*, 12238–12239.

[63] P. J. Schmidt, G. Thiele, *Acta Crystallogr. Sec. C* **1997**, *53*, 1743–1745.

[64] F. Gulo, C. Perrin, *Mater. Res. Bull.* **2000**, *35*, 253–262.

[65] M. N. Sokolov, A. L. Gushchin, P. A. Abramov, A. V. Virovets, E. V. Peresypkina, S. G. Kozlova, B. A. Kolesov, C. Vicent, V. P. Fedin, *Inorg. Chem.* **2005**, *44*, 8756–8761.

[66] H. B. Yaich, J. C. Jegaden, M. Potel, M. Sergent, A. K. Rastogi, R. Tournier, *J. Less-Common Met.* **1984**, *102*, 9–22.

[67] H.-J. Meyer, J. D. Corbett, *Inorg. Chem.* **1991**, *30*, 963–967.

[68] S. Cordier, F. Gulo, T. Roisnel, R. Gautier, B. le Guennic, J. F. Halet, C. Perrin, *Inorg. Chem.* **2003**, *42*, 8320–8327.

[69] H. Womelsdorf, H.-J. Meyer, *Angew. Chem* **1994**, *33*, 1943–1944.

[70] M. D. Smith, G. J. Miller, *Inorg. Chem.* **2003**, *42*, 4165–4170.

[71] M. Ströbele, O. Oeckler, M. Thelen, R. F. Fink, A. Krishnamurthy, S. Kroeker, H.-J. Meyer, *Inorg. Chem.* **2022**, *61*, 17599–17608.

[72] V. Kolesnichenko, L. Messerle, *Inorganic chemistry* **1998**, *37*, 3660–3663.

[73] M. Stroebele, H.-J. Meyer, *Constitutional Isomerism of BiW6Cl15:(BiCl)[W6Cl14] and (BiCl2)[W6Cl13]*, **2009**

[74] A. Mos, C. Castro, S. Indris, M. Ströbele, R. F. Fink, H.-J. Meyer, *Inorg. Chem.* **2015**, *54*, 9826–9832.

[75] F. Grahlow, F. Strauß, M. Scheele, M. Ströbele, A. Carta, S. F. Weber, S. Kroeker, C. P. Romao, H.-J. Meyer, *Phys. Chem. Chem. Phys.* **2024**, *26*, 11789–11797.

[76] F. Grahlow, F. Strauß, P. Schmidt, J. Valenta, M. Ströbele, M. Scheele, C. P. Romao, H.-J. Meyer, *Inorg. Chem.* **2024**, *63*, 19717–19727.

[77] G. Sheldrick, *Acta Crystallogr. Sec. C* **2015**, *71*, 3–8.

[78] O. V. Dolomanov, L. J. Bourhis, R. J. Gildea, J. A. Howard, H. Puschmann, *J. Appl. Crystallogr.* **2009**, *42*, 339–341.

[79] H.-J. Meyer, *Z. Anorg. Allg. Chem.* **1994**, *620*, 81–84.

[80] D. Baeriswyl, L. Degiorgi, *Strong interactions in low dimensions*, *Vol. 25*, Springer Science, Business Media, **2007**.

[81] M. Bockrath, D. H. Cobden, J. Lu, A. G. Rinzler, R. E. Smalley, L. Balents, P. L. McEuen, *Nature* **1999**, *397*, 598–601.

[82] F. D. M. Haldane, *J. Phys. C: Solid State Phys.* **1981**, *14*, 2585.

[83] H. Fehske, G. Hager in *Metal-to-Nonmetal Transitions*, (Eds.: R. Redmer, F. Hensel, B. Holst), Springer, Berlin, Heidelberg, **2010**, pp. 1–21.

[84] Y. Hinuma, G. Pizzi, Y. Kumagai, F. Oba, I. Tanaka, *Nato. Sc. S. Ss. Iii. C. S.* **2017**, *128*, 140–184.

[85] R. Shannon, *Acta Crystallogr. A* **1976**, *32*, 751–767.

[86] F. Grahlow, Master's Thesis, **2022**.

[87] A. Carta, P. Mlkvik, F. Grahlow, M. Ströbele, H.-J. Meyer, C. P. Romao, N. A. Spaldin, C. Ederer, *arXiv* **2025**, *2509.03988*.

[88] F. Grahlow, J. Beitlberger, M. Martin, E. Juriatti, H. Peisert, M. Scheele, M. Ströbele, C. P. Romao, H.-J. Meyer, *Dalton Trans.* **2025**, *54*, 16593–16604.

[89] J. Beitlberger, M. Ströbele, F. Strauß, M. Scheele, C. P. Romao, H.-J. Meyer, *Eur. J. Inorg. Chem.* **2024**, *27*, e202400329.

[90] J. Beitlberger, M. Martin, M. Scheele, P. Schmidt, M. Stroebele, H.-J. Meyer, *Dalton Trans.* **2025**.

[91] G. Meyer, T. Gloger, J. Beekhuizen, *Z. Anorg. Allg. Chem.* **2009**, *635*, 1497–1509.

[92] I. I. Kozhina, D. V. Korol'kov, *J. Struct. Chem.* **1965**, *6*, 84–89.

[93] L. Jongen, A.-V. Mudring, A. Möller, G. Meyer, *Angew. Chem. Int. Ed.* **2004**, *43*, 3183–3185.

[94] D. J. Hinz, G. Meyer, *J. Chem. Soc. Chem. Commun.* **1994**, 125–126.

[95] D. Hinz, T. Gloger, G. Meyer, *Z. Anorg. Allg. Chem.* **2000**, *626*, 822–824.

[96] M. Schroeder, S. Hartwig, K. W. Krämer, S. Decurtins, H. Hillebrecht, *Inorg. Chem.* **2012**, *51*, 8385–8393.

[97] L. Jongen, G. Meyer, *Z. Anorg. Allg. Chem.* **2004**, *630*, 1732–1732.

[98] L. Jongen, T. Gloger, J. Beekhuizen, G. Meyer, *Z. Anorg. Allg. Chem.* **2005**, *631*, 582–586.

[99] B. G. Newland, R. A. J. Shelton, *J. Less-Common Met.* **1970**, *22*, 369–372.

[100] J. A. Beekhuizen, Doctoral Thesis, **2006**.

6 Publications

Publication 1

Electronic Structure and Transport in the Potential Luttinger Liquids $CsNb_3Br_7S$ and $RbNb_3Br_7S$

Publication 2

Ta_4SBr_{11}: A Cluster Mott Insulator with a Corrugated, Van der Waals Layered Structure

Publication 3

Hubbard Dimer Physics and the Magnetostructural Transition in the Correlated Cluster Material Nb_3Cl_8

Publication 4

Structural Modifications of $M_5O_4I_{11}$ (M = Nb, Ta) Cluster Networks from Heterogeneous Solid-State Reactions

Publication 1

Electronic Structure and Transport in the Potential Luttinger Liquids
$CsNb_3Br_7S$ and $RbNb_3Br_7S$

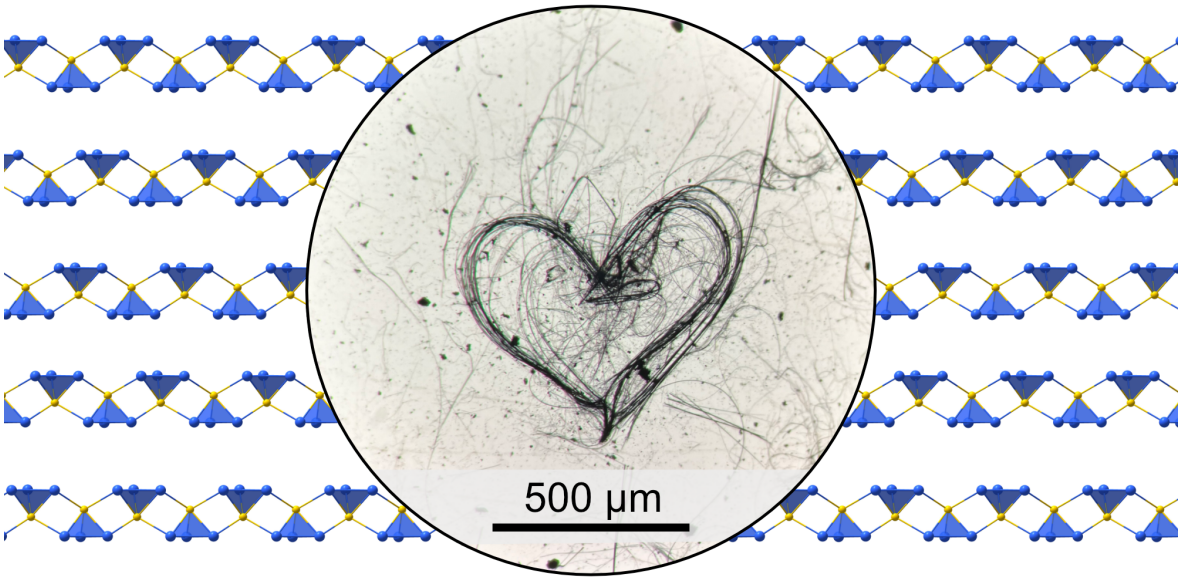

DOI: 10.1039/D4CP00293H
Reproduced from
Phys. Chem. Chem. Phys., **2024**, 26, 11789-11797

PCCP

ROYAL SOCIETY OF CHEMISTRY

PAPER

View Article Online
View Journal | View Issue

Cite this: *Phys. Chem. Chem. Phys.*, 2024, **26**, 11789

Electronic structure and transport in the potential Luttinger liquids $CsNb_3Br_7S$ and $RbNb_3Br_7S$†

Fabian Grahlow,[a] Fabian Strauß,[b] Marcus Scheele,[b] Markus Ströbele,[a] Alberto Carta,[c] Sophie F. Weber,[c] Scott Kroeker,[d] Carl P. Romao *[c] and H.-Jürgen Meyer *[a]

The crystal structures of ANb_3Br_7S (A = Rb and Cs) have been refined by single crystal X-ray diffraction, and are found to form highly anisotropic materials based on chains of the triangular Nb_3 cluster core. The Nb_3 cluster core contains seven valence electrons, six of them being assigned to Nb–Nb bonds within the Nb_3 triangle and one unpaired d electron. The presence of this surplus electron gives rise to the formation of correlated electronic states. The connectivity in the structures is represented by one-dimensional $[Nb_3Br_7S]^-$ chains, containing a sulphur atom capping one face (μ_3) of the triangular niobium cluster, which is believed to induce an important electronic feature. Several types of studies are undertaken to obtain deeper insight into the understanding of this unusual material: the crystal structure, morphology and elastic properties are analysed, as well the (photo-)electrical properties and NMR relaxation. Electronic structure (DFT) calculations are performed in order to understand the electronic structure and transport in these compounds, and, based on the experimental and theoretical results, we propose that the electronic interactions along the Nb chains are sufficiently one-dimensional to give rise to Luttinger liquid (rather than Fermi liquid) behaviour of the metallic electrons.

Received 22nd January 2024,
Accepted 26th March 2024

DOI: 10.1039/d4cp00293h

rsc.li/pccp

Introduction

Metal-rich niobium halides are well known in chemistry, typically appearing with the octahedral Nb_6 cluster core, as in Nb_6X_{14} (X = Cl, Br),[1–3] or with a triangular Nb_3 cluster core in the structure of Nb_3X_8 (X = Cl, Br, I).[4,5] The electronic structure of Nb_6X_{14} is well described with eight metal-centred molecular orbitals (MOs) being occupied by 16 electrons. Nb_3X_8 (X = Cl, Br, I) compounds appear as layered structures based on close-packed halide arrangements in which $\frac{3}{4}$ of the octahedral voids in every second interlayer are occupied by niobium atoms. However, each niobium atom in the crystal structure is displaced away from the centre of its coordination octahedron to form trigonal clusters (shown in Fig. 1), each containing seven electrons in metal-centred states.[6] A magnetic-to-nonmagnetic phase transition has been shown upon cooling in Nb_3Cl_8 with interlayer charge transfer between Nb_3 trimers in adjacent layers,[7] although such charge transfer was not observed in other studies.[8,9]

The valence electron count (VEC) in compounds containing triangular Nb_3 clusters compounds is between 6 and 8; for instance, VEC = 6 for Nb_3Br_7S[10] and $Nb_3O_2Cl_5$,[11] VEC = 7 for Nb_3X_8 (X = Cl, Br, I) and $CsNb_3Br_7S$,[12] and VEC = 8 for $NaNb_3Cl_8$.[9,13,14] The compounds with seven valence electrons

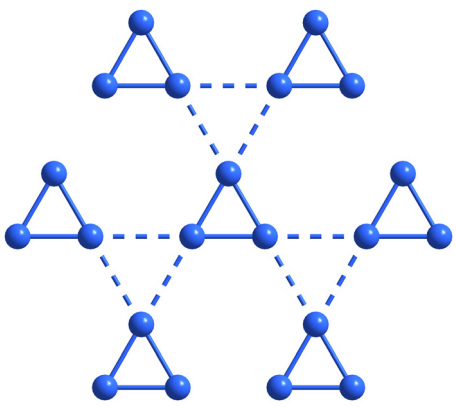

Fig. 1 Projection of arrangement of Nb_3 clusters within one interlayer of the structure of Nb_3X_8.

[a] *Section for Solid State and Theoretical Inorganic Chemistry, Institute of Inorganic Chemistry, Eberhard-Karls-Universität Tübingen, Auf der Morgenstelle 18, 72076 Tübingen, Germany. E-mail: juergen.meyer@uni-tuebingen.de*
[b] *Institute for Physical and Theoretical Chemistry, Eberhard-Karls-Universität Tübingen, Auf der Morgenstelle 18, 72076 Tübingen, Germany*
[c] *Department of Materials, ETH Zurich, Wolfgang-Pauli-Str. 27, 8093 Zürich, Switzerland. E-mail: carl.romao@mat.ethz.ch*
[d] *Department of Chemistry, University of Manitoba, Winnipeg, Manitoba R3T 2N2, Canada*

† Electronic supplementary information (ESI) available. CCDC 2048757 and 2048759. For ESI and crystallographic data in CIF or other electronic format see DOI: https://doi.org/10.1039/d4cp00293h

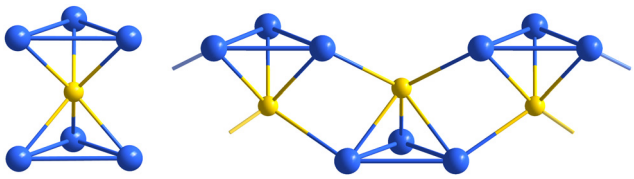

Fig. 2 The $[Nb_6S]$ cluster core in the structure of $A_3[Nb_6SBr_{17}]$ (left), and a section of the infinite $[Nb_3S]$ chain in ANb_3Br_7S (right).

can have interesting magnetic behaviour, especially in combination with the two-dimensional polar Kagome lattice structure of Nb_3X_8.[8,9,15–17] MO calculations on the seven-electron cluster $[Nb_3X_{13}]^{5-}$, adapted from the Nb_3X_8 structure, revealed that six electrons can be assigned to Nb–Nb bonding within the Nb_3 cluster and that the HOMO level is a half-filled $2a_1$ orbital.[6]

Compounds $A_3[Nb_6SBr_{17}]$ with A = Rb, Tl, K, Cs[18,19] contain a sulphur-centred, trigonal prismatic $[Nb_6S]$ core which has been reported to contain only weak Nb–Nb interactions between adjacent Nb_3-triangles (Fig. 2 at left).[18] The chain structure of $CsNb_3SBr_7$ is based on similar $[Nb_3S]$ clusters, shown in Fig. 2 on the right. Both compounds contain seven valence electrons per Nb_3 cluster.

Triangular $[Nb_3]^{8+}$ clusters consisting of an Nb–Nb bonded arrangement are of fundamental interest. In isolation, each cluster has seven valence electrons and thus one unpaired d electron in a $2a_1$ orbital. Such unpaired electrons in Nb clusters have recently become the source of significant research attention due to their formation of various long-range ordered states, for example by charge disproportionation between layers in Nb_3Cl_8,[7] and the formation of a Mott insulating state in $GaNb_4S_8$.[20]

The structure of $CsNb_3Br_7S$ was reported in 1993 to contain $[Nb_3]^{8+}$ clusters, each of which is capped with a (μ_3) sulphur atom to form the motif of a tetrahedron (Fig. 2, right). These clusters are arranged in chains parallel to the *c*-axis, with alternating positions of the clusters above and below the central sulphur chain. The chains have an outer shell of bromide ions, and voids in the crystal structure between the chains are filled by caesium ions. The extended Hückel method was used to predict that $CsNb_3Br_7S$ is a semimetal, with the Nb d orbitals forming bands which cross the Fermi level.[12]

We have revisited this material, which shows an interesting crystal morphology of cleavable rods. The synthesis and crystal structure of $CsNb_3Br_7S$ is revised in order to confirm its structure and electronic properties. In addition, the synthesis and structure of the closely related compound $RbNb_3Br_7S$ is reported for the first time. The elastic properties and NMR relaxation of $CsNb_3Br_7S$ are investigated, electric conductivity measurements along the $[Nb_3S]_n$ chain direction are performed for both compounds, and theoretical investigations of the electronic structure are performed using density functional theory (DFT).

Our studies suggest that $CsNb_3Br_7S$ and $RbNb_3Br_7S$ have conducting electrons which can be described as (Tomonaga–) Luttinger liquids, rather than the more usual Fermi liquids. Luttinger liquids are a type of one-dimensional paramagnetic quantum fluid, characterized by their separate transport of charge density waves (CDWs) and spin density waves (SDWs).[21,22] They can be identified by their characteristic spectral function and by the power-law response of various physical properties as a function of temperature.[21]

Experimental

Synthetic procedures

ANb_3Br_7S compounds with A = Rb and Cs were prepared by solid-state reactions starting from mixtures of ABr (99.0% Merck), $NbBr_5$ (99.9% ABCR GmbH), niobium powder (99.9% ABCR GmbH) and sulphur (99.9% Carl Roth GmbH) in stoichiometric proportions with total masses of 100 to 200 mg per batch. The starting materials were homogenised by grinding under an argon atmosphere and fused in silica tubing. Loaded ampoules were heated at 800 °C for 24 h (heating and cooling rates of 2 K min^{-1}). Short-term reactions and fast cooling rates yielded a furry, crystalline material consisting of fine needle-like crystals. Long-term reactions with slow cooling rates gave longer, rod-shaped crystals. Both compounds ANb_3Br_7S (A = Rb, Cs) appear as black crystals with metallic lustre and are stable in air for weeks, as confirmed by X-ray powder diffraction.

Crystallography

Carefully selected black needle-shaped single-crystals of $RbNb_3Br_7S$ and $CsNb_3Br_7S$ were mounted on a Rigaku XtaLab Synergy-S X-ray diffractometer using Cu-Kα (λ = 1.54184 Å) and Mo-Kα (λ = 0.71073 Å) radiation, respectively. The single crystals were kept under N_2 cooling at 100 K during the data collection. Corrections for absorption effects were applied with CrysAlisPro 171.41.64.93a (Rigaku Oxford Diffraction, 2020). Crystal structures were solved by the integrated space group and crystal-structure determination routine of SHELXT[23] and full-matrix least-squares structure refinements with SHELXL-2014[23] implemented in Olex2 1.3-ac4.[24] The structure of $RbNb_3Br_7S$ was refined as a racemic twin with a Flack parameter 0.50(3).

Details of the crystal structure investigations can be obtained from the joint CCDC/FIZ Karlsruhe online deposition service: https://www.ccdc.cam.ac.uk/structures/by quoting the deposition numbers CCDC 2048759 for $RbNb_3Br_7S$ and CCDC 2048757 for $CsNb_3Br_7S$.†

Electron microscopy

Electron micrographs were recorded on a JEOL 8900 Superprobe spectrometer. The samples were coated with carbon prior to the measurements.

Electrical characterisation

Conductivity measurements were performed in a Lake Shore Cryotronics CRX-6.5K probe station with a Keithley 2636B source meter unit. Rod-shaped crystals of $CsNb_3Br_7S$ and $RbNb_3Br_7S$ were transferred into the chamber under protective gas and contacted with silver paste on a silicon substrate with 770 nm oxide layer. The conductive silver pads at each end of the crystals were connected to the circuit with tungsten tips

(Fig. S1, ESI†). The chamber was kept under vacuum ($<5 \times 10^{-5}$ mbar) and the temperature was varied between 20 K and 300 K. Before each measurement, sufficient time was allowed for the sample to reach the chosen temperature. Two-point conductivity measurements were performed by varying the applied source–drain voltage from −1 V to 1 V while detecting the current. Time-resolved photocurrent measurements used a picosecond pulsed laser driver (Taiko PDL M1, PicoQuant) together with a laser head 779 nm (pulse length <500 ps); the crystals were illuminated at 40 mW laser output power using the continuous wave mode under a constant bias of 1 V.

Nuclear magnetic resonance spectroscopy

^{133}Cs NMR data were collected at 65.5 MHz (B_0 = 11.7 T) and 52.4 MHz (B_0 = 9.4 T) using Bruker Avance III spectrometers. The ^{133}Cs magic-angle spinning (MAS) spectra were acquired on a polycrystalline sample at 11.7 T by Bloch decay, using a 2.5 mm MAS probe with spinning rates of 10.00, 20.00 and 30.00 kHz. The chemical shift is referenced to external 0.1 M CsCl(aq) at 0.0 ppm. T_1 relaxation times were measured by fitting inversion-recovery data to a mono-exponential decay function.

^{93}Nb NMR spectra were acquired at 97.9 MHz (B_0 = 9.4 T) on a Bruker Avance III 400 using a 4 mm MAS probe. The wideband uniform-rate smooth-truncation (WURST) quadrupolar Carr–Purcell–Meiboom–Gill (QCPMG) pulse sequence was used to acquire six individual spectra on a non-spinning sample at variable transmitter offsets, which were subsequently assembled into the 1.8 MHz spectrum. All NMR spectra were acquired at ambient temperature without temperature regulation.

Computational methods

Density functional theory (DFT) calculations were performed using the software packages Abinit (v. 9)[25] and Quantum Espresso. Calculations of the elastic tensor and Γ-point phonon frequencies were performed in Abinit using norm-conserving pseudopotentials from the Abinit library, a 4 × 4 × 4 Monkhorst–Pack grid of k-points,[26] a 34 Ha plane-wave basis set energy cutoff, and the PBE exchange–correlation functional.[27]

Calculations of the electronic band structure with antiferromagnetic ordering and a Hubbard U term[28] (U = 5 eV and J = 0.2 eV on the Nb sites)[29] and with spin–orbit coupling were performed in Abinit using the projector-augmented wave (PAW) method[30] with pseudopotentials from the GBRV library,[31] a Monkhorst–Pack grid of k-points with real-space basis vectors [0 2 4] [4 0 4] and [4 2 0],[26] a 128 Ha plane-wave basis set energy cutoff within the PAW spheres and a 24 Ha cutoff outside.

We also performed calculations without spin polarization to construct a tight-binding model based on Wannier functions. For these calculations we employed Wannier90[32] and Quantum Espresso[33] using ultrasoft pseudopotentials also from the GBRV library[33] with a 4 × 2 × 6 Monkhorst–Pack grid, and a plane-wave energy and density cutoff of 72 Ry and 864 Ry, respectively.

All the calculations stated above were performed with PBE exchange–correlation functional[27] with the DFT-D3 dispersion correction,[34] and Methfessel–Paxton cold smearing of the electronic states.[35] Special points in and paths through the Brillouin zone were chosen following Hinuma *et al.*[36] All computational parameters were chosen following convergence studies. The band structures produced by Abinit and by Quantum Espresso with these parameters were compared and found to be essentially identical.

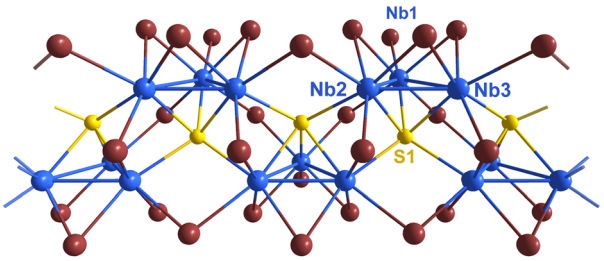

Fig. 3 Section of a single chain in the structure of $CsNb_3Br_7S$ along the crystallographic c-direction. Niobium atoms are shown blue, sulphur yellow, and bromide atoms brown.

Results and discussion

Crystal structures

The crystal structures of ANb_3Br_7S (A = Rb, Cs) were solved and refined from single-crystal X-ray diffraction data. The structure of $CsNb_3Br_7S$ was confirmed to agree with the previously reported data on the same compound with the monoclinic space group $P2_1/c$ (No. 14).[12] The structure of the new compound $RbNb_3Br_7S$ was refined with the orthorhombic space group $Pmc2_1$ (No. 26). Both crystal structures contain the same arrangement of triangular Nb_3 clusters face-capped (μ_3) by sulphur atoms, and linked into chains *via* bromide and sulphide ions along the crystallographic a direction for A = Rb, and along c direction for A = Cs. The $[Nb_3SBr_7]^-$ cluster units in both structures are linked into chains by three inner (i) edge capping bromides, six shared (6/2) outer (a–a) bromides, and one terminal outer (a) bromide, forming the structural unit $[Nb_3SBr_3{}^{i}Br_{6/2}{}^{a-a}Br^{a}]^-$, which can be seen in Fig. 3.

The difference between the two crystal structures with A = Cs and Rb is expressed in the different symmetries of the orthorhombic and monoclinic space groups. This can be explained by the different radii and coordination patterns of alkali ions in the structures. The caesium ion is situated in a nearly regular cube-octahedral environment of bromides, and Rb is surrounded by an irregular twelvefold arrangement of bromide ions. These environments with bromide ions, which are also linked to the niobium clusters, cause shifts of adjacent clusters along the one-dimensional chain of the structure (Fig. 4).

The distances between the three crystallographically distinct niobium atoms are about 290 pm within Nb_3 cluster triangles and about 310 pm between adjacent triangles (see Table 1 for details). Despite the similarity of these interatomic distances, previously reported electronic structure calculations (extended Hückel) on $CsNb_3Br_7S$ had revealed comparable Nb–Nb crystal

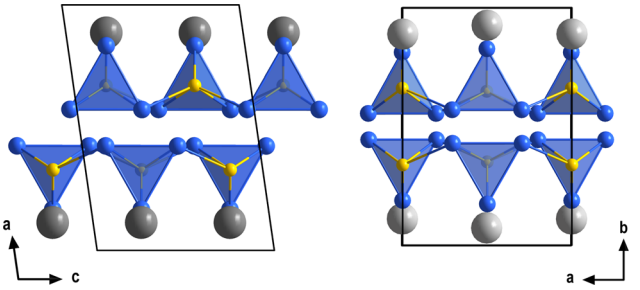

Fig. 4 Comparison of crystal structures of $CsNb_3Br_7S$ ($P2_1/c$, left) and $RbNb_3Br_7S$ ($Pmc2_1$, right) with their unit cells. Bromides are omitted in the drawings for better clarity. Cs (dark grey) and Rb (light grey) atoms are shown.

orbital overlap populations (0.25) within Nb_3 triangles and weak (0.09) overlap populations between adjacent triangles.

The cohesion between adjacent cluster chains in the structure is dominated by ionic (Br–A) bonding, as expressed by the appearance of differently shifted chain arrangements in the crystal structures of ANb_3Br_7S with A = Rb and Cs along the chain directions (Fig. 4). The primary growth direction of needle-shaped crystal rods coincides with the direction of the $[Nb_3SBr_3{}^{i}Br_{6/2}{}^{a-a}Br^{a}]^-$ chains (Fig. 5). This pronounced growth direction suggests a one-dimensional character of the material, as supported by the fraying behaviour of crystal rods shown below, and later quantitatively evaluated by the elastic properties (directional Young's modulus).

Electron microscopy and elastic properties

The morphology of synthesized $CsNb_3Br_7S$ crystals is shown in SEM micrographs in Fig. 6. $CsNb_3Br_7S$ forms rods with fairly uniform dimensions of about 500 μm length and 10 μm diameter. As Fig. 6a shows, each rod could be assumed to be a single crystal, but a magnified view suggests that this is not always clear. This morphology can be readily explained by a highly anisotropic crystal structure, and our XRD studies on single crystals confirm the long axis of the rods to coincide with the crystallographic *c*-axis. Fig. 6b shows fraying of a rod, an interesting feature indicating that the material is at least somewhat flexible, and that the cohesive forces along the a and b

Table 1 Selected interatomic distances (pm) in ANb_3Br_7S (A = Rb, Cs) compounds. The A = Rb compound contains two independent Nb_3 clusters in the structure

Compound	$RbNb_3Br_7S$	$CsNb_3Br_7S$
Nb–Nb Δ[a]	289.3(3), 290.3(3)	290.71(7)
	289.3(3), 290.3(3)	290.01(7)
	281.2(3) 288.6(3)	286.63(7)
Nb–Nb ′[b]	310.2(3)	310.74(5)
Nb–S Δ	238.8(6) 248.4(8)	238.3(2)
	238.8(6) 248.4(8)	246.0(2)
	233.0(8) 250.7(9)	246.1(2)
Nb–S ′	257.2(6)	262.9(2)
	265.6(5)	263.5(2)

[a] Within cluster triangle (Δ). [b] Between cluster triangles (′).

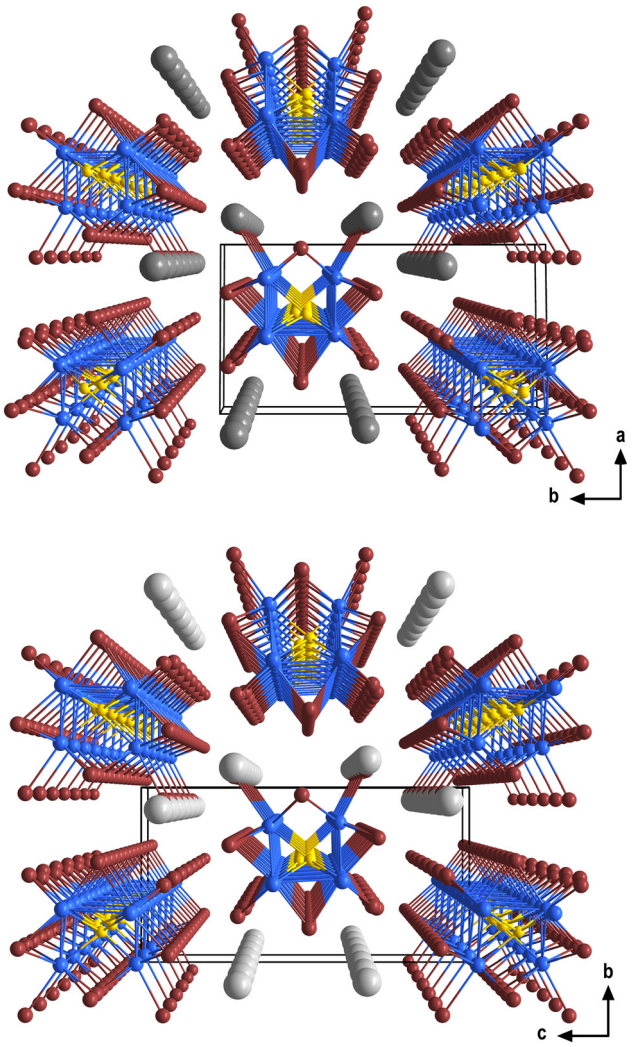

Fig. 5 Comparison of crystal structures of $RbNb_3Br_7S$ ($Pmc2_1$, bottom) and $CsNb_3Br_7S$ ($P2_1/c$, top) with their unit cells. Nb (blue), S (yellow), Br (brown), Cs (dark grey) and Rb (light grey) atoms are shown.

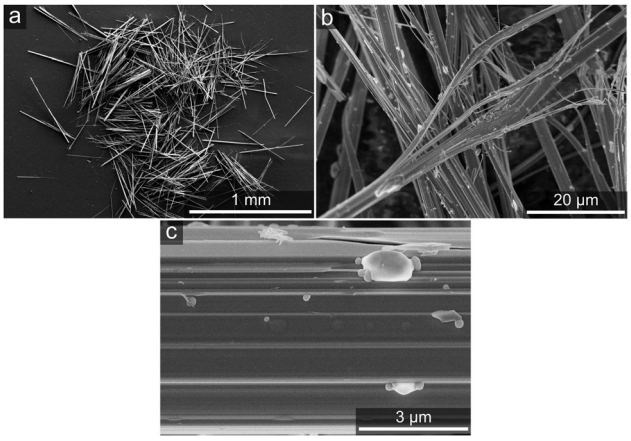

Fig. 6 SEM micrographs of (a) $CsNb_3Br_7S$ crystals, showing their pronounced rod-like morphology, (b) fraying of a rod of $CsNb_3Br_7S$ and (c) their high degree of uniformity on the micron scale.

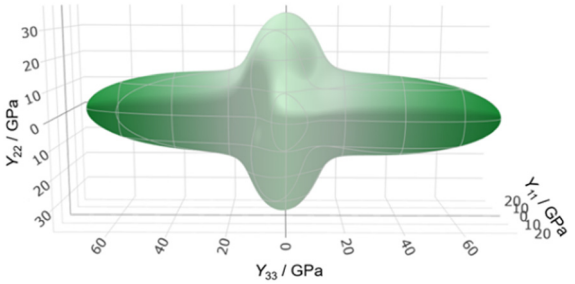

Fig. 7 The calculated directional Young's modulus (Y_{ii}) of $CsNb_3Br_7S$, shown as a green surface. The view is along the *a*-axis (analogous to Fig. 2).

axes might be expected to have van der Waals character; except in this case they are instead ionic interactions between the bromides of the cluster and A cations.

In order to examine the origins of this fraying behaviour further, and to determine to what extent the elastic properties of $CsNb_3Br_7S$ can be considered one-dimensional, its elastic tensor was calculated using DFPT (eqn (S1), ESI†). The vdW-D3 dispersion correction of Grimme was employed to ensure that van der Waals forces would be accounted for in the model. The easiest way to visualize the elastic anisotropy is through the directional Young's modulus (Y_{ii}), which describes the resistance of the material to uniaxial stress in a given direction. This is shown in Fig. 7; $CsNb_3Br_7S$ is found to be stiffest along the *c*-axis, with a directional Young's modulus of 74 GPa. While *c* is the stiffest direction, the Young's modulus also shows significant peaks coinciding with *a* (24 GPa) and *b* (34 GPa), indicating that the mechanical bonding between $[Nb_3Br_7S]^-$ chains through the Cs^+ cations is significant. These results demonstrate that, although $CsNb_3Br_7S$ is highly anisotropic, its elasticity is decidedly not one-dimensional.

Electrical properties

Both $CsNb_3Br_7S$ and $RbNb_3Br_7S$ exhibit ohmic behaviour in the measured temperature range between 20 and 300 K. Fig. 8 shows the dark current obtained at room temperature for two different $CsNb_3Br_7S$ crystals. Conductivities of 0.35 S cm^{-1} for

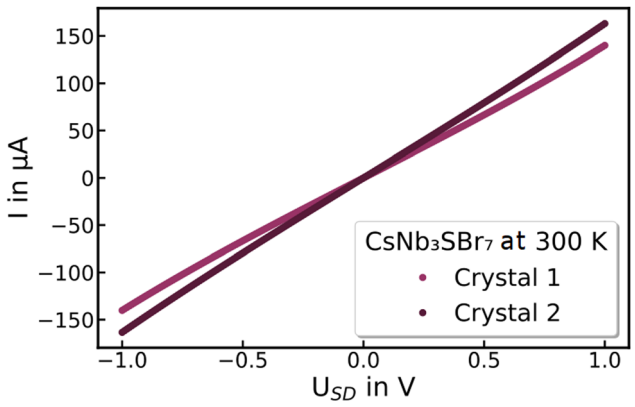

Fig. 8 Dark currents *I* of $CsNb_3Br_7S$ crystals on silicon with 770 nm dioxide layer at 300 K with an applied source–drain voltage U_{SD} of −1 V to 1 V.

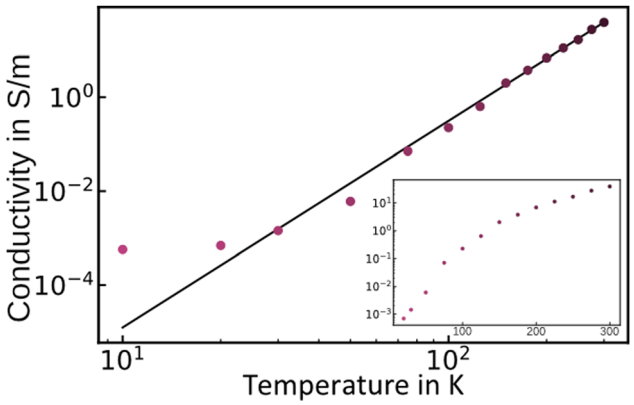

Fig. 9 Double logarithmic plot of the electrical conductivity of $CsNb_3Br_7S$ *versus* set temperature in a range of 20 K to 300 K with a power law fit (black) following $\sigma(T) = cT^{\alpha}$ with $\alpha = 4.4$. In the inset: electrical conductivity of $CsNb_3Br_7S$ *versus* temperature in a range of 20 K to 300 K.

$CsNb_3Br_7S$ and 1.65 S cm^{-1} for $RbNb_3Br_7S$ are measured with a two-point measurement. The inset in Fig. 9 shows the temperature-dependent electrical conductivity in the range of 20 K to 300 K for $CsNb_3Br_7S$, indicating a temperature-activated behaviour. The same trend of a decreasing conductivity with decreasing temperature is observed for $RbNb_3Br_7S$, *cf.* Fig. S2 (ESI†).

The electrical conductivity of $CsNb_3Br_7S$ (Fig. 9, inset) and $RbNb_3Br_7S$ (Fig. S2, right, ESI†) show a general increase with increasing temperature. As shown in Fig. 9, above 50 K ($CsNb_3Br_7S$) and 30 K ($RbNb_3Br_7S$), the electrical conductivity (σ) as a function of temperature can be fitted to a power law ($\sigma(T) = cT^{\alpha}$ for some constants α and *c*), and therefore is consistent with a Luttinger liquid.[21,37] At lower temperatures, the conductivity cannot be fit to an Arrhenius curve, suggesting that it is not a simple semiconductor in that regime.

Photoelectric properties

When the crystals are illuminated with 779 nm CW-laser pulses, both compounds show a photoresponse, see Fig. 10. This photocurrent consists of a steep and fast increase, followed by a slower second component. We attribute the first rise to photoexcited charge carriers, and the second increase to the effect of concomitant heating of the crystal (compare with Fig. 8).

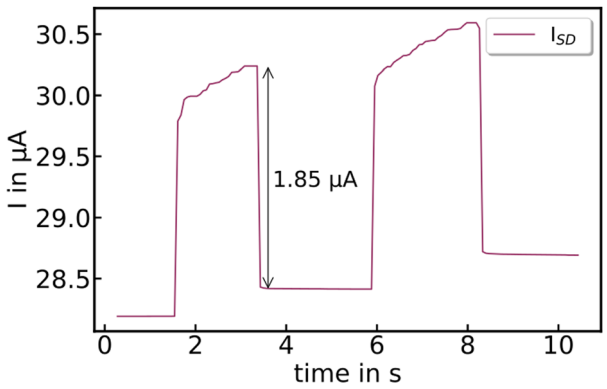

Fig. 10 Photoresponse of a $CsNb_3Br_7S$ crystal to a 779 nm laser at 200 K.

The photocurrent is strongly temperature-activated, ranging from a few nA at 20 K to several tens of μA at room temperature.

Nuclear magnetic resonance

The ^{133}Cs MAS NMR spectrum exhibits a single peak at 330 ppm (Fig. S3, ESI†), near the upper edge of the chemical shift range for diamagnetic samples. The peak position is not far from that of CsBr (258 ppm),[38] consistent with the similar local Cs environment. The narrowness of the central peak indicates a small quadrupolar interaction, and the full extent of the spinning sideband envelope corresponds to a quadrupole coupling constant around 250 kHz, typical for crystalline materials.[39] The spinning sidebands at slower spinning rates are symmetrically distributed about the central peak, implying that there is no appreciable anisotropy in the Cs chemical shielding. No changes were observed in the central peak position or lineshape upon increasing the spinning rate, despite the accompanying temperature increase of about 25 °C.[40] The most unique feature of the ^{133}Cs NMR response is its anomalously short spin–lattice relaxation time: while most insulating and semiconducting solids have ^{133}Cs T_1 values in the range of 30–60 s[41,42] – with values up to 900 s having been reported[43] – the T_1 of $CsNb_3Br_7S$ was measured to be 165 ms at 11.7 T. Such a short relaxation time is often indicative of nuclear interactions with unpaired electron spins, however, no evidence of a contact shift or electron–dipolar coupling is observed. Instead, this may be considered evidence for a Luttinger liquid, which exhibits extremely fast spin–lattice relaxation in certain magnetic field regimes.[44] A second T_1 measurement at 9.4 T yielded similarly rapid relaxation of 185 ms. Attempts to record a ^{93}Nb NMR spectrum were partially successful, yielding a broad signal spanning nearly 1.8 MHz (not shown), reflective of the large quadrupole moment of ^{93}Nb and its asymmetric local environments; however, the ^{93}Nb T_1s are similarly short (<200 ms) and the T_2 value estimated from the echo train is around 2 ms. These observations from NMR support the designation of $CsNb_3Br_7S$ as a Luttinger liquid.

Electronic structure

The electronic structure of $CsNb_3Br_7S$ was examined further using density functional theory (DFT). The results are in qualitative agreement with earlier calculations (both extended Hückel[6] and DFT[45]) showing semimetallicity (specifically, zero band gap semiconductor behaviour) due to crossings of the Fermi level near the B $(0\ 0\ \frac{1}{2})$ and A $(-\frac{1}{2}\ 0\ \frac{1}{2})$ points of the Brillouin zone (Fig. 11 and 12). The band gap remains extremely small (<0.1 eV) between B $(0\ 0\ \frac{1}{2})$ and D $(0\ \frac{1}{2}\ \frac{1}{2})$, and between A $(-\frac{1}{2}\ 0\ \frac{1}{2})$, and E $(-\frac{1}{2}\ \frac{1}{2}\ \frac{1}{2})$.

In order to understand the nature of the electronic states near the Fermi level, we constructed maximally localized Wannier functions[46] from the DFT wavefunctions (Fig. 11) in two ways. We first include all the bands with strong Nb d character (see Fig. S5, ESI†) in the energy window. This way we obtain Wannier functions that have a form like Nb d orbitals (Fig. 11b), with additional of p-orbital tails coming from the hybridization with Br and S (open magenta circles in Fig. 11). In this model, the largest absolute value for the hopping integral inside one trimer is around 1.2 eV, while the largest hopping for contiguous trimers can be as high as 0.7 eV, which underlines a non-negligible contribution of inter-trimer hybridization in the electronic structure.

The importance of considering contiguous trimers is more evident if we include only the 4 states around the Fermi energy in the energy window during the wannierization (full green circles in Fig. 11). Fig. 11(c and d) shows the result of the spread

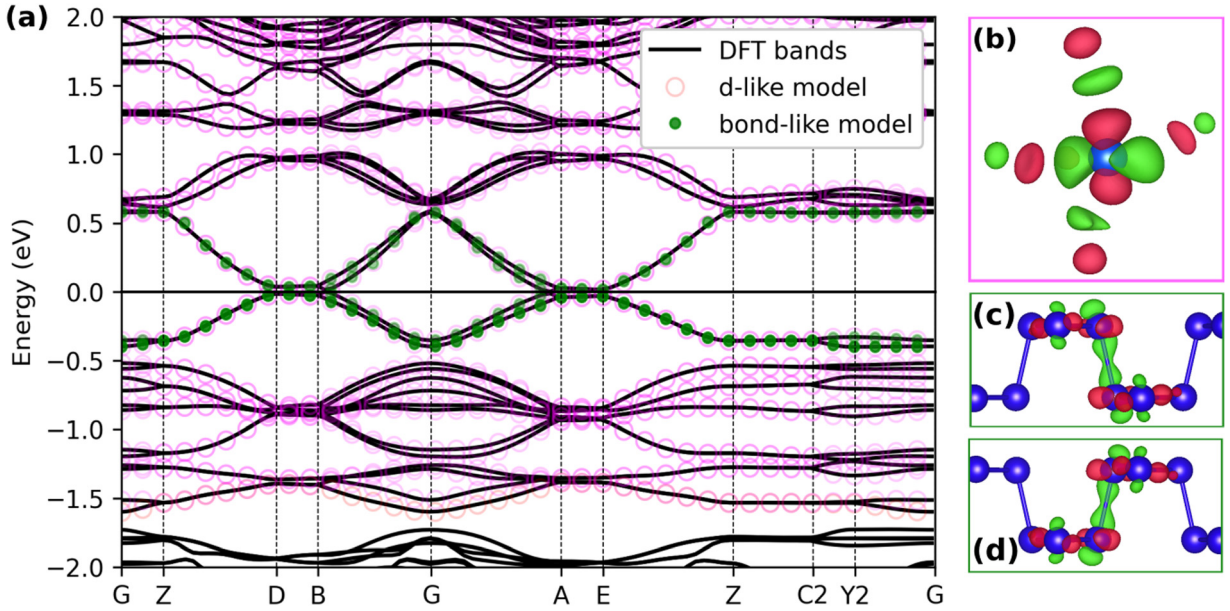

Fig. 11 The calculated electronic band structure of nonmagnetic $CsNb_3Br_7S$ (a), and corresponding atom-centred (b) and bond-centred (c and d) maximally localized Wannier functions (shown at Γ). Blue spheres represent Nb atoms. Special points in and paths through the Brillouin zone were chosen following literature.[36]

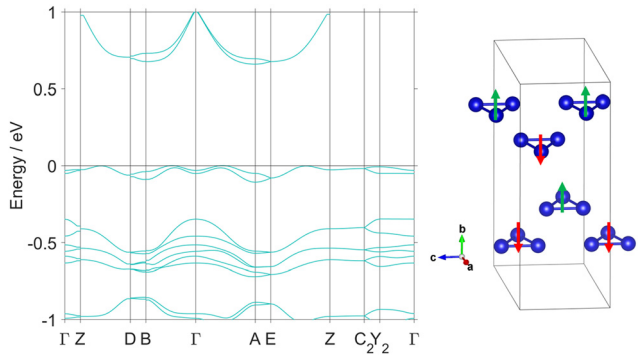

Fig. 12 The calculated electronic band structure of $CsNb_3Br_7S$ with an antiferromagnetic arrangement of magnetic moments on the Nb triangles along each chain (shown at right). Special points in and paths through the Brillouin zone were chosen following literature.[36]

minimization, with the Wannier functions being centered between the Nb trimers. The hopping integrals (t) of the tight-binding model corresponding to the bond-centred Wannier functions (Table S1, ESI†) indicate that nearest-neighbour intra-chain hopping ($t \approx -0.2$ eV) is significantly favored over inter-chain hopping ($t' \approx -0.01$ eV).

The predicted electronic conduction in $CsNb_3Br_7S$ is not unsurprising given the presence of unpaired electrons in each $[Nb_3]^{8+}$ cluster, which leads to each $[Nb_3Br_7S]^-$ chain having one unpaired electron per Nb_3 cluster. However, the measured temperature-activated electrical conductivity is inconsistent with a conventional metal or semimetal, but not with a Luttinger liquid. Together with the power law dependence of the electronic conductivity on temperature and short NMR T_1 relaxation times, our findings indicate that $CsNb_3Br_7S$ is a Luttinger liquid above *ca.* 30 K. The values of the Luttinger parameter α extracted from the electronic conductivity ($\alpha = 4.4$ for $CsNb_3Br_7S$ and $\alpha = 4.2$ for $RbNb_3Br_7S$) indicate that the electron–electron interactions are repulsive in nature, and that the chains contain strong impurities, *i.e.* discontinuities or barriers in the chains which require quantum tunnelling for electronic transport.[47] The presence of strong impurities precludes further modelling of the Luttinger electronic interaction parameters from the available data.

A metallic one-dimensional chain of electrons has several possible mechanisms of gap opening upon cooling. At low temperature, electronic correlations will favour the formation of a charge-ordered singlet (Peierls) or triplet (Mott) insulator, and which state forms depends on the relative energetics.[48] Below 30 K, as the conductivity no longer follows a power law, we expect a gap to have opened in the CDW and SDW continuum corresponding to the Luttinger liquid. We can therefore consider several mechanisms of gap opening in $CsNb_3Br_7S$.

The first is the Peierls distortion, which is a CDW instability that, for example, forms alternating long and short bonds (as in polyacetylene). We would expect this mechanism to lead to variations in the Nb–Nb bond lengths, either within the Nb_3 trimers as has been reported in Nb_3Cl_8[49] or between them.

In our structure refinement (at 100 K) each Nb_3 cluster in $CsNb_3Br_7S$ is crystallographically identical; any Peierls distortion would lower the crystallographic symmetry and would be easily detectable using single-crystal X-ray diffraction. Therefore, we conclude that there is no Peierls distortion or charge disproportionation in $CsNb_3Br_7S$ at 100 K, although there may be at lower temperatures.

Instead of forming bound pairs of electrons in a Peierls insulator, exchange coupling in combination with electronic correlations can create a Mott insulator *via* a SDW instability. Here, a Mott insulator would correspond to a state where each cluster has one localized electron with antiferromagnetic spin alignment with respect its neighbours along the chain (Fig. 12). However, in a Mott insulator, the magnetic susceptibility would be expected to show temperature dependence corresponding to an antiferromagnet or a paramagnet with antiferromagnetic correlations, which is seen only below 30 K in $CsNb_3Br_7S$, and the material could be a Mott insulator below that temperature. Above 30 K, $CsNb_3Br_7S$ shows temperature independent paramagnetic behaviour (TIP), and a magnetic-to-nonmagnetic charge transition seen in Nb_3Cl_8 is absent in $CsNb_3Br_7S$ (Fig. S4, ESI†).

Spin–orbit coupling presents a third mechanism for opening a band gap. Previous studies have shown that, while in the absence of SOC, $CsNb_3Br_7S$ is a topological nodal straight-line semimetal, inclusion of SOC introduces a small gap of *ca.* 5 meV at the crossing points. Note that due to the combination of P and T symmetries, the semimetal state in the absence of SOC has a well-defined, nontrivial Z_2 invariant,[50] and the gapped phase in the presence of SOC is also expected to be topological.[45] Such a gap is small, but still would be expected to lead to semiconducting behaviour for a Fermi liquid at low temperature. However, our calculations indicate that, while there is such a gap near B (0 0 $\frac{1}{2}$), the bands cross the Fermi level near A ($-\frac{1}{2}$ 0 $\frac{1}{2}$) (Fig. 13). There is a small amount of dispersion of the electronic bands along a, which can be attributed to weak interchain interactions, and which leads to the formation of conducting electronic states.

Therefore, the nature of $CsNb_3Br_7S$ at temperatures below 30 K, where the Luttinger liquid state breaks down, cannot be definitively determined from the available data. The calculated phonon energies at Γ (Table S2, ESI†) do not show an instability related to dimerization; the lowest energy phonon which

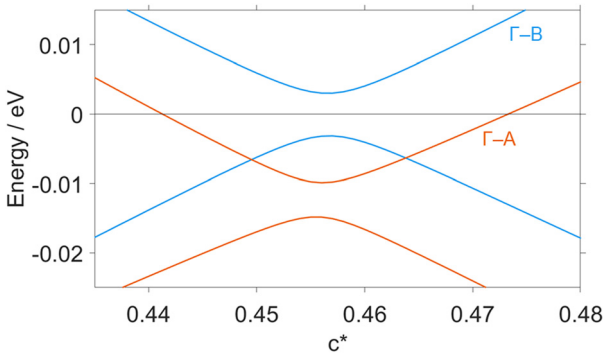

Fig. 13 The calculated electronic band structure of nonmagnetic $CsNb_3Br_7S$, calculated with spin–orbit coupling on a fine grid of k-points along Γ–B (0 0 c^*) (blue) and Γ–A ($-\frac{1}{2}$ 0 c^*) (orange). Special points in and paths through the Brillouin zone were chosen following literature.[36]

involves modulation of the Nb–Nb distances has a frequency of 38.67 cm^{-1} (4.6 meV). This indicates that the rough scale of the energy barrier which the CDW instability would need to overcome in order to create a Peierls distortion is small. The upturn in the magnetic susceptibility at low temperatures (Fig. S4, ESI†) suggests a potential Mott insulating state. Further low-temperature structural and magnetic investigation is therefore required to determine the ground states of $CsNb_3Br_7S$ and $RbNb_3Br_7S$ at temperatures approaching absolute zero.

Conclusions

The previously given crystal structure of $CsNb_3Br_7S$ is confirmed by single crystal X-ray diffraction studies and the new compound $RbNb_3Br_7S$ is reported with a slightly distinct structure. Structure determinations on these compounds are challenging, due to the formation of twins and fraying character of needle-like rods parallel to the direction of infinite $[Nb_3Br_7S]^-$ chains. Crystals of both compounds appear black with metallic lustre but show semiconducting behaviour. Refinement of the crystal structure reveals a one-dimensional nature, due to the presence of $[Nb_3Br_7S]^-$ chains. However, different arrangements of chains in the structure of ANb_3Br_7S with A = Rb, Cs due to different ionic radii of A cations reflect significant ionic (A–Br) interaction between adjacent chains. This is also expressed by the calculated elastic properties (directional Young's modulus) of $CsNb_3Br_7S$ in which the chain direction (*c*-axis) is the stiffest direction (74 GPa), but stiffness maxima also coincide with *a* and *b*, indicating that the ionic bonding between $[Nb_3Br_7S]^-$ chains through Cs cations is significant. Electronic structure calculations indicate that $CsNb_3Br_7S$ is a one-dimensional metal. At temperatures above 30 K, the experimental data indicates that the CDWs and SDWs are fluid, and the material behaves as a Luttinger liquid. The increase in conductivity with temperature in the Luttinger liquid phase indicates repulsive interactions between electrons. Below 30 K, a band gap could open through formation of a Peierls (CDW ordered) or Mott (SDW correlated) insulator.

Conflicts of interest

There are no conflicts to declare.

Acknowledgements

Support of this Research by the German Research Foundation (DFG) through grant ME 914/32-1 and SCHE1905/9-1 (project no. 426008387) is gratefully acknowledged. C. P. R. and S. F. W. were supported by ETH Zurich and by the European Union and Horizon 2020 through a Marie Sklodowska–Curie Fellowship, Grant Agreement No. 101030352 (C. P. R.) and by Grant No. 810451 (S. F. W.). A. C. was supported by ETH Zurich. Computational resources were provided by ETH Zurich, by the Swiss National Supercomputing Center (CSCS) under project IDs s1128 and eth3, and by the state of Baden–Württemberg through bwHPC and the DFG through grant INST 40/575-1 FUGG (JUSTUS 2 cluster). S. K. is supported by grants from the Natural Sciences and Engineering Research Council (NSERC) of Canada, and the Canada Foundation for Innovation (CFI). We thank Dr Arun Krishnamurthy and Mr Mojtaba Abbasi (University of Manitoba) for the solid-state NMR measurements.

Notes and references

1 A. Simon, H. G. Schnering, H. Wöhrle and H. Schäfer, *Z. Anorg. Allg. Chem.*, 1965, **339**, 155–170.
2 R. Allen and J. Sheldon, *Aust. J. Chem.*, 1965, **18**, 277–283.
3 M. B. Robin and N. A. Kuebler, *Inorg. Chem.*, 1965, **4**, 978–985.
4 H. Schäfer and H. G. Schnering, *Angew. Chem.*, 1964, **76**, 833–868.
5 A. Simon and H. G. Von Schnering, *J. Less-Common Met.*, 1966, **11**, 31–46.
6 H.-J. Meyer, *Z. Anorg. Allg. Chem.*, 1994, **620**, 81–84.
7 Y. Haraguchi, C. Michioka, M. Ishikawa, Y. Nakano, H. Yamochi, H. Ueda and K. Yoshimura, *Inorg. Chem.*, 2017, **56**, 3483–3488.
8 J. P. Sheckelton, K. W. Plumb, B. A. Trump, C. L. Broholm and T. M. McQueen, *Inorg. Chem. Front.*, 2017, **4**, 481–490.
9 C. M. Pasco, I. El Baggari, E. Bianco, L. F. Kourkoutis and T. M. McQueen, *ACS Nano*, 2019, **13**, 9457–9463.
10 S. Abrahams, *Acta Crystallogr., Sect. B: Struct. Sci.*, 2008, **64**, 426–437.
11 F. Gulo and C. Perrin, *Mater. Res. Bull.*, 2000, **35**, 253–262.
12 H.-J. Meyer, *Z. Anorg. Allg. Chem.*, 1994, **620**, 863–866.
13 J. R. Kennedy and A. Simon, *Inorg. Chem.*, 1991, **30**, 2564–2567.
14 C. C. Torardi and R. E. McCarley, *Inorg. Chem.*, 1985, **24**, 476–481.
15 Z. Sun, H. Zhou, C. Wang, S. Kumar, D. Geng, S. Yue, X. Han, Y. Haraguchi, K. Shimada, P. Cheng, L. Chen, Y. Shi, K. Wu, S. Meng and B. Feng, *Nano Lett.*, 2022, **22**, 4596–4602.
16 Y. Feng and Q. Yang, *J. Mater. Chem. C*, 2023, **11**, 5762–5769.
17 C.-G. Duan, J. Hong, F. Sui, K. Wang, X. Han, Y. Zheng, W.-Y. Tong, X. Deng, Z. Guan and B. Tian, *Physical Sciences*, 2023, preprint, DOI: **10.21203/rs.3.rs-3457733/v1**.
18 H. Womelsdorf and H.-J. Meyer, *Angew. Chem., Int. Ed. Engl.*, 1994, **33**, 1943–1944.
19 H. Womelsdorf and H.-J. Meyer, *Z. Anorg. Allg. Chem.*, 1996, **622**, 2083–2088.
20 S. Jakob, H. Müller, D. Johrendt, S. Altmannshofer, W. Scherer, S. Rayaprol and R. Pöttgen, *J. Mater. Chem.*, 2007, **17**, 3833–3838.
21 D. Baeriswyl and L. Degiorgi, *Strong interactions in low dimensions*, Springer Science & Business Media, 2007.
22 F. D. M. Haldane, *J. Phys. C: Solid State Phys.*, 1981, **14**, 2585.
23 G. Sheldrick, *Acta Crystallogr., Sect. C: Struct. Chem.*, 2015, **71**, 3–8.
24 O. V. Dolomanov, L. J. Bourhis, R. J. Gildea, J. A. K. Howard and H. Puschmann, *J. Appl. Crystallogr.*, 2009, **42**, 339–341.
25 X. Gonze, B. Amadon, G. Antonius, F. Arnardi, L. Baguet, J.-M. Beuken, J. Bieder, F. Bottin, J. Bouchet, E. Bousquet,

N. Brouwer, F. Bruneval, G. Brunin, T. Cavignac, J.-B. Charraud, W. Chen, M. Côté, S. Cottenier, J. Denier, G. Geneste, P. Ghosez, M. Giantomassi, Y. Gillet, O. Gingras, D. R. Hamann, G. Hautier, X. He, N. Helbig, N. Holzwarth, Y. Jia, F. Jollet, W. Lafargue-Dit-Hauret, K. Lejaeghere, M. A. L. Marques, A. Martin, C. Martins, H. P. C. Miranda, F. Naccarato, K. Persson, G. Petretto, V. Planes, Y. Pouillon, S. Prokhorenko, F. Ricci, G.-M. Rignanese, A. H. Romero, M. M. Schmitt, M. Torrent, M. J. van Setten, B. Van Troeye, M. J. Verstraete, G. Zérah and J. W. Zwanziger, *Comput. Phys. Commun.*, 2020, **248**, 107042.

26 H. J. Monkhorst and J. D. Pack, *Phys. Rev. B: Solid State*, 1976, **13**, 5188.

27 J. P. Perdew, K. Burke and M. Ernzerhof, *Phys. Rev. Lett.*, 1996, **77**, 3865.

28 B. Amadon, F. Jollet and M. Torrent, *Phys. Rev. B: Condens. Matter Mater. Phys.*, 2008, **77**, 155104.

29 D. B. Migas, A. B. Filonov, V. E. Borisenko and N. V. Skorodumova, *J. Alloys Compd.*, 2020, **821**, 153527.

30 M. Torrent, N. A. W. Holzwarth, F. Jollet, D. Harris, N. Lepley and X. Xu, *Comput. Phys. Commun.*, 2010, **181**, 1862–1867.

31 K. F. Garrity, J. W. Bennett, K. M. Rabe and D. Vanderbilt, *Comput. Mater. Sci.*, 2014, **81**, 446–452.

32 G. Pizzi, V. Vitale, R. Arita, S. Blügel, F. Freimuth, G. Géranton, M. Gibertini, D. Gresch, C. Johnson, T. Koretsune, J. Ibañez-Azpiroz, H. Lee, J.-M. Lihm, D. Marchand, A. Marrazzo, Y. Mokrousov, J. I. Mustafa, Y. Nohara, Y. Nomura, L. Paulatto, S. Poncé, T. Ponweiser, J. Qiao, F. Thöle, S. S. Tsirkin, M. Wierzbowska, N. Marzari, D. Vanderbilt, I. Souza, A. A. Mostofi and J. R. Yates, *J. Phys.: Condens. Matter*, 2020, **32**, 165902.

33 P. Giannozzi, O. Andreussi, T. Brumme, O. Bunau, M. Buongiorno Nardelli, M. Calandra, R. Car, C. Cavazzoni, D. Ceresoli, M. Cococcioni, N. Colonna, I. Carnimeo, A. Dal Corso, S. de Gironcoli, P. Delugas, R. A. DiStasio, A. Ferretti, A. Floris, G. Fratesi, G. Fugallo, R. Gebauer, U. Gerstmann, F. Giustino, T. Gorni, J. Jia, M. Kawamura, H. Y. Ko, A. Kokalj, E. Küçükbenli, M. Lazzeri, M. Marsili, N. Marzari, F. Mauri, N. L. Nguyen, H. V. Nguyen, A. Otero-de-la-Roza, L. Paulatto, S. Poncé, D. Rocca, R. Sabatini, B. Santra, M. Schlipf, A. P. Seitsonen, A. Smogunov, I. Timrov, T. Thonhauser, P. Umari, N. Vast, X. Wu and S. Baroni, *J. Phys.: Condens. Matter*, 2017, **29**, 465901.

34 S. Grimme, J. Antony, S. Ehrlich and H. Krieg, *J. Phys. Chem.*, 2010, **132**(15), 154104.

35 M. Methfessel and A. Paxton, *Phys. Rev. B: Condens. Matter Mater. Phys.*, 1989, **40**, 3616.

36 Y. Hinuma, G. Pizzi, Y. Kumagai, F. Oba and I. Tanaka, *Comput. Mater. Sci.*, 2017, **128**, 140–184.

37 M. Bockrath, D. H. Cobden, J. Lu, A. G. Rinzler, R. E. Smalley, L. Balents and P. L. McEuen, *Nature*, 1999, **397**, 598–601.

38 S. Mooibroek, R. E. Wasylishen, R. Dickson, G. Facey and B. A. Pettitt, *J. Magn. Reson.*, 1986, **66**, 542–545.

39 J. E. C. Wren, B. J. Greer, V. K. Michaelis, C. S. Higman and S. Kroeker, *Inorg. Chem.*, 2015, **54**, 9853–9861.

40 K. Levin and S. Kroeker, *Solid State Nucl. Magn. Reson.*, 2019, **101**, 101–109.

41 A. Karmakar, A. Bhattacharya, G. M. Bernard, A. Mar and V. K. Michaelis, *ACS Mater. Lett.*, 2021, **3**, 261–267.

42 A. Karmakar, S. Mukhopadhyay, P. G. B. Gachod, V. A. Mora-Gomez, G. M. Bernard, A. Brown and V. K. Michaelis, *Chem. Mater.*, 2021, **33**, 6078–6090.

43 A. Karmakar, G. M. Bernard, A. Meldrum, A. O. Oliynyk and V. K. Michaelis, *J. Am. Chem. Soc.*, 2020, **142**, 10780–10793.

44 M. Jeong, D. Schmidiger, H. Mayaffre, M. Klanjšek, C. Berthier, W. Knafo, G. Ballon, B. Vignolle, S. Krämer, A. Zheludev and M. Horvatić, *Phys. Rev. Lett.*, 2016, **117**, 106402.

45 Q. Yuan, Z. Wang, Z. Wang, X. Shi and G. Wang, *New J. Phys.*, 2022, **24**, 093033.

46 N. Marzari, A. A. Mostofi, J. R. Yates, I. Souza and D. Vanderbilt, *Rev. Mod. Phys.*, 2012, **84**, 1419–1475.

47 C.-H. Hsu, P. Stano, Y. Sato, S. Matsuo, S. Tarucha and D. Loss, *Phys. Rev. B*, 2019, **100**, 195423.

48 H. Fehske and G. Hager, in *Metal-to-Nonmetal Transitions*, ed. R. Redmer, F. Hensel and B. Holst, Springer Berlin Heidelberg, Berlin, Heidelberg, 2010, pp. 1–21.

49 Y. Haraguchi, C. Michioka, M. Ishikawa, Y. Nakano, H. Yamochi, H. Ueda and K. Yoshimura, *Inorg. Chem.*, 2017, **56**, 3483–3488.

50 Y. Kim, B. J. Wieder, C. L. Kane and A. M. Rappe, *Phys. Rev. Lett.*, 2015, **115**, 036806.

Electronic Supplementary Material (ESI) for Physical Chemistry Chemical Physics.

Supporting Information

Electronic Structure and Transport in the Potential Luttinger Liquids $CsNb_3Br_7S$ and $RbNb_3Br_7S$

Fabian Grahlow[a], Fabian Straußb, Marcus Scheele[b], Markus Ströbele[a], Alberto Carta[c], Sophie F. Weber[c], Scott Kroeker[d], Carl P. Romao*[c] and H.-Jürgen Meyer*[a]

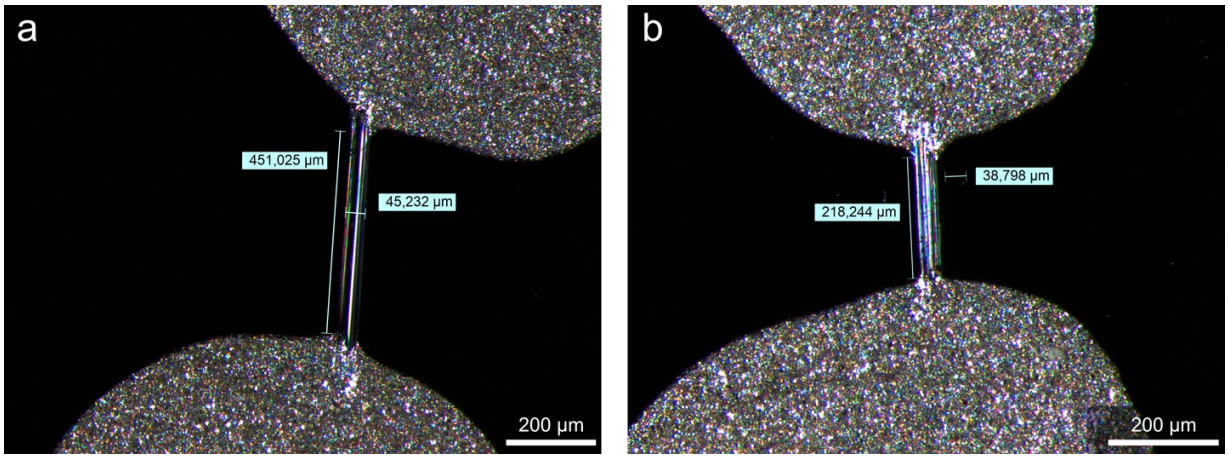

Figure S1: Optical micrographs of a (a) contacted $CsNb_3Br_7S$ crystal and a (b) contacted $RbNb_3Br_7S$ crystal.

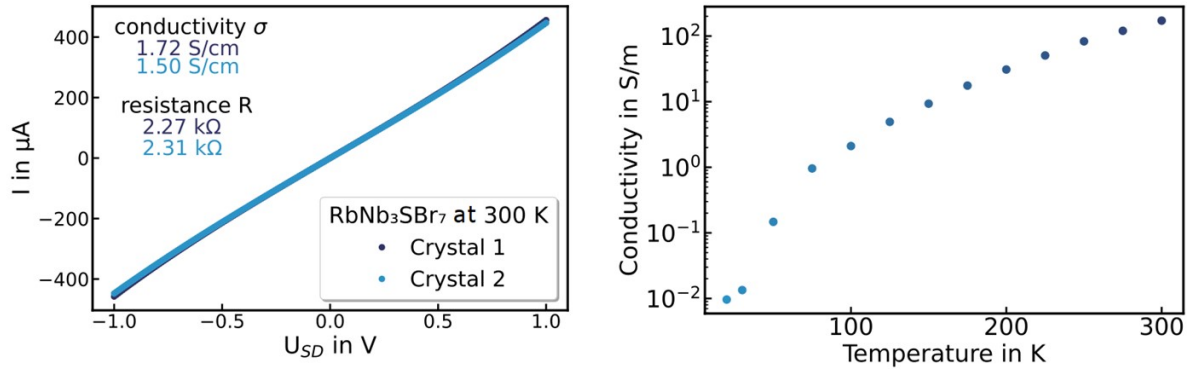

Figure S2: (left)Dark currents of $RbNb_3Br_7S$ Crystals on silicon with 770 nm dioxide layer at 300 K. (Right) Electrical conductivity of $RbNb_3Br_7S$ versus set temperature in a range of 20 K to 300 K.

[a] *Section for Solid State and Theoretical Inorganic Chemistry*
Institute of Inorganic Chemistry
Eberhard-Karls-Universität Tübingen
Auf der Morgenstelle 18, 72076 Tübingen, Germany
[*a] *E-mail: juergen.meyer@uni-tuebingen.de*
[b] *Institute for Physical and Theoretical Chemistry*
Eberhard-Karls-Universität Tübingen
Auf der Morgenstelle 18, 72076 Tübingen, Germany
[c] *Department of Materials, ETH Zurich,*
Wolfgang-Pauli-Str. 27, 8093 Zürich, Switzerland
[*c] *E-mail: carl.romao@mat.ethz.ch*
[d] *Department of Chemistry, University of Manitoba, Winnipeg, Manitoba R3T 2N2, Canada*

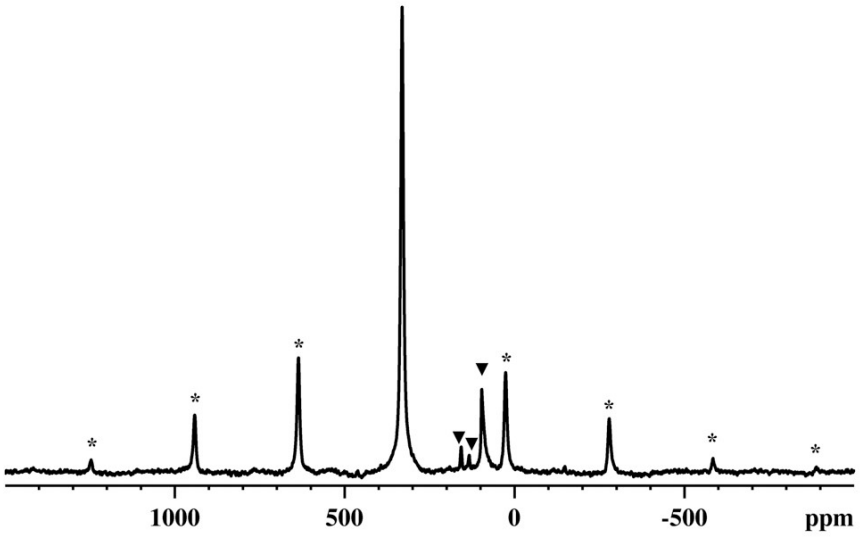

Figure S3: ^{133}Cs MAS NMR spectrum of $CsNb_3Br_7S$ acquired at 65.5 MHz with a spinning rate of 20.000(3) kHz. Spinning sidebands are marked with asterisks; peaks from minor impurities or decomposition products are indicated by arrows.

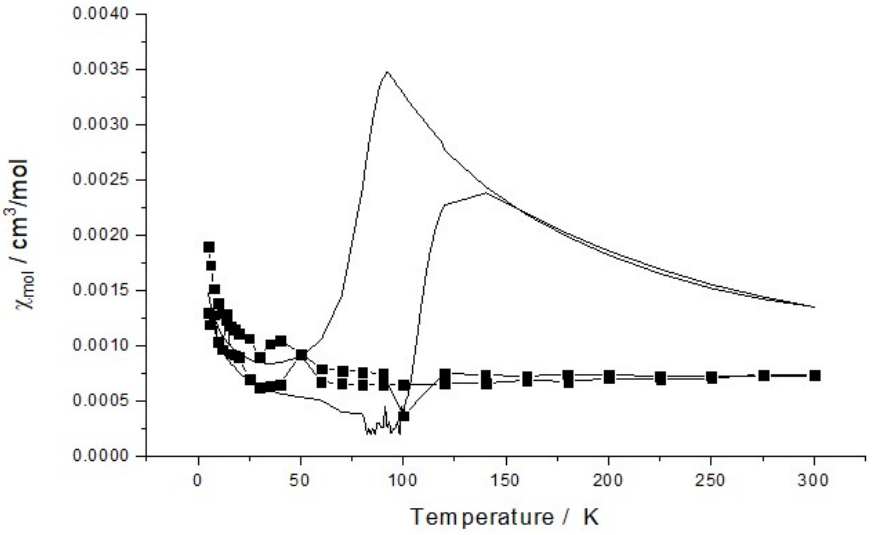

Figure S4: Measured magnetic susceptibility during one heating/cooling cycle at 100 Oe for Nb_3Cl_8 (line) and $CsNb_3Br_7S$ (line with squares).

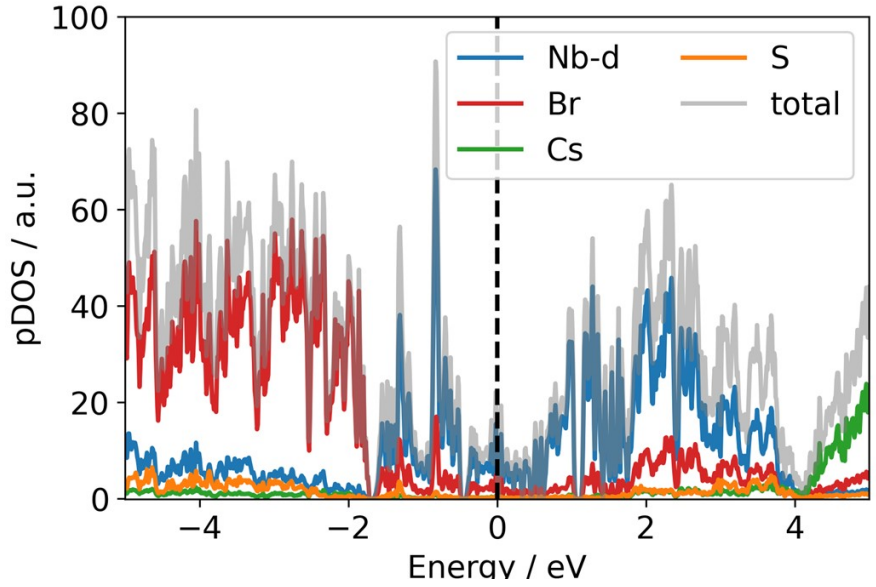

Figure S5: Calculated projected density of electronic states in $CsNb_3Br_7S$. The Fermi energy is shown as a black line.

Table S1: Parameters of the tight-binding model corresponding to the bond-centred Wannier functions of $CsNb_3Br_7S$.

***R* (unit cell translation)**	***t* (hopping integral) / eV**	**Note**
[0 0 0]	7.05	On-site bond energy
[0 0 0]	-0.20	Nearest neighbor intra-chain hopping
[0 0 1]	0.02	Next-nearest intra-chain hopping
[0 0 0]	-0.01	Nearest inter-chain hopping

Table S2: Calculated phonon frequencies at Γ of $CsNb_3Br_7S$.

Phonon frequency / cm^{-1}				
0.00	0.00	0.00	13.82	19.00
22.51	30.40	36.64	38.67	43.39
44.75	45.29	46.37	46.77	48.39
48.87	49.56	52.99	53.70	60.98
61.65	63.65	64.04	64.20	64.22
64.54	71.97	74.61	75.42	76.19
79.48	79.70	81.84	83.49	83.53
83.97	85.83	87.15	87.45	91.20
92.28	92.43	93.26	94.01	96.09
96.48	96.84	99.12	99.95	100.35
103.28	103.46	104.84	105.28	106.97
107.81	108.53	110.47	114.45	115.29
115.87	116.33	120.49	120.61	122.27
122.29	127.94	128.16	129.81	131.58
131.70	131.83	132.11	133.17	134.87
135.14	137.85	138.71	139.79	140.27
144.25	145.04	145.26	146.83	148.07
148.69	150.41	150.49	151.01	152.26
154.77	155.07	167.36	167.92	169.24
170.62	174.51	174.71	191.26	191.41
195.37	195.41	198.30	204.25	210.01
210.04	210.17	212.79	212.86	215.80
216.07	217.71	217.79	219.59	222.61
228.86	229.39	229.53	231.31	232.42
238.55	239.04	243.34	243.73	246.34
250.03	251.19	253.81	255.17	255.42
264.96	266.98	311.65	311.80	329.66
330.67	332.12	332.23	342.05	342.21
389.45	390.98	394.79	395.03	

Publication 2

Ta_4SBr_{11}: A Cluster Mott Insulator with a Corrugated, Van der Waals Layered Structure

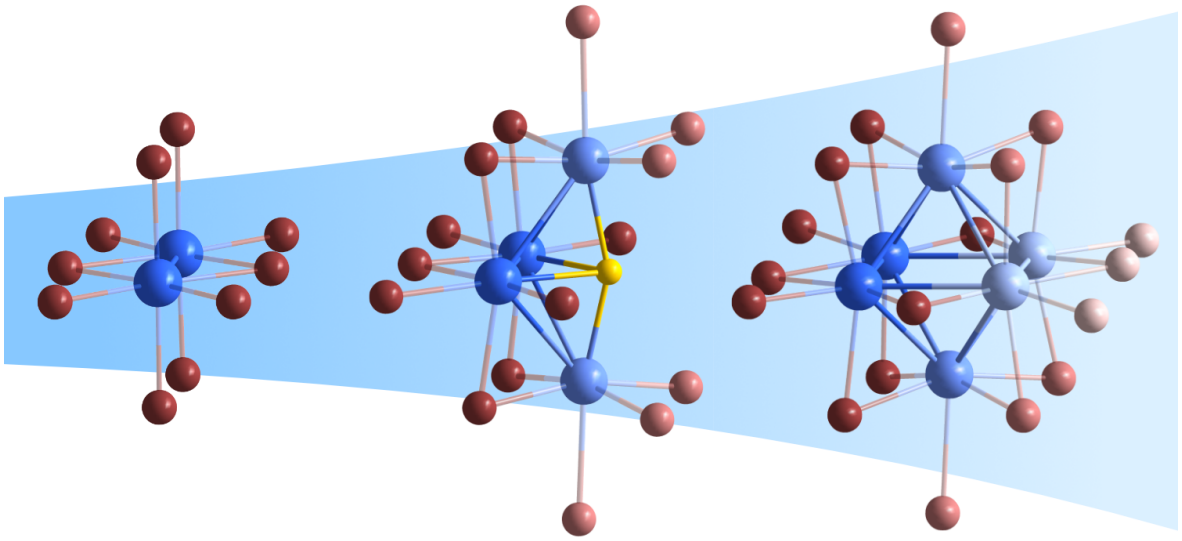

DOI: 10.1021/acs.inorgchem.4c02896

Reprinted with permission from

Inorg. Chem., **2024**, 63, 19717-19727

Inorganic Chemistry

pubs.acs.org/IC Article

Ta_4SBr_{11}: A Cluster Mott Insulator with a Corrugated, Van der Waals Layered Structure

Fabian Grahlow, Fabian Strauß, Patrick Schmidt, Jaroslav Valenta, Markus Ströbele, Marcus Scheele, Carl P. Romao,* and Hans-Jürgen Meyer*

Cite This: *Inorg. Chem.* 2024, 63, 19717−19727 Read Online

ACCESS | Metrics & More | Article Recommendations | Supporting Information

ABSTRACT: The compound Ta_4SBr_{11} was prepared by a comproportionation reaction of tantalum bromide with tantalum and elemental sulfur. The crystal structure, as refined by single-crystal X-ray diffraction, is composed of clusters with Ta_4S cores, arranged in corrugated van der Waals layers. Individual layers appear to be displaced relative to each other along one direction. Successful crystal growth in a melt of CsBr yielded black platelets of Ta_4SBr_{11}, which were used to investigate the electrical properties of the compound. The electronic structure was studied by diffuse reflectance infrared Fourier transform (DRIFT) spectroscopy and by density functional theory (DFT) band structure calculations, revealing this material to be a small-gap semiconductor. DFT results, in combination with magnetic susceptibility measurements, suggest that metallicity originating from the one unpaired Ta d electron per cluster is most likely suppressed by electronic correlations, forming a cluster Mott insulator.

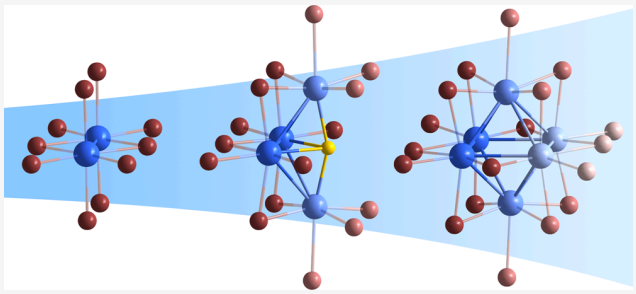

INTRODUCTION

The chemistry of reduced niobium and tantalum halides is dominated by cluster compounds prepared by solid-state synthesis at elevated temperatures. Their structures are characterized by octahedral metal (M = Nb, Ta) cluster cores $M_6X_{12}{}^iX_6{}^a$ with halide ligands (X = F, Cl, Br, and I) in edge-bridged (^{i}) and terminal (^{a}) positions.[1] Average oxidation states in binary tantalum compounds Ta_6X_{14} and Ta_6X_{15} range from +2.33 to +2.5. The electronic structures of such compounds have been studied, revealing that the M_6X_{14} cluster with M = Nb or Ta is considered electron precise with 14 electrons per cluster. These skeletal electrons reside in metal-to-metal bonds of the clusters. As a result of the separation of adjacent clusters via outer (^{a}) ligands, semiconducting behavior with poor electrical conductivity is observed for these crystalline compounds.[2−4]

Another binary species, MX_4 with M = Nb, Ta form infinite chain structures with alternating M-M distances, including bonding between pairs of metal atoms, which can be described by a Peierls distortion. The electrical conductivity of $NbCl_4$ has been reported to increase sharply (by a factor of 10^4−10^5) with increasing temperature (at 533 K), the Nb−Nb distances also tend to equalize, but the temperature dependence remains typical for a semiconductor.[5]

Known tantalum chalcogenide (Ch) halides include one-dimensional compounds of the type $(TaCh_4)_nX$ (Ch = Se, Te; n = 1, 2, 4; X = Br, I)[6−8] and trinuclear niobium and tantalum cluster compounds with the stoichiometry M_3ChX_7 (M = Nb, Ta; Ch = S, Se, Te; X = Cl, Br, I).[9−12] The latter compounds can be derived from the binary Nb_3X_8 (X = Cl, Br, I) structure by substituting the μ_3-capping X atom of the cluster with a chalcogenide (Ch) atom. The structure of Nb_3Cl_8 contains seven skeletal electrons.[13] Recently, an interlayer charge disproportionation has been proposed for Nb_3Cl_8 when lowering the temperature, resulting in a magnetic-to-non-magnetic phase transition and a structural phase transition.[14−17] Monolayer Nb_3Cl_8 has been identified as a cluster Mott insulator, and has been the subject of significant recent interest due to its correlated flat metallic bands and the formation of a quantum spin liquid state due to magnetic frustration.[18]

Trigonal clusters in ANb_3SBr_7 (A = Rb, Cs) also contain seven skeletal electrons, of which six electrons may be assigned for Nb−Nb bonding with one electron per cluster remaining unpaired.[19,20] In their quasi-one-dimensional structure, these circumstances are expected to lead to a Luttinger liquid-like behavior.[20] These observations illustrate the appeal and complexity of heterohalide clusters, with their properties depending on the localized or delocalized distributions of

Received: July 11, 2024
Revised: August 27, 2024
Accepted: September 19, 2024
Published: October 7, 2024

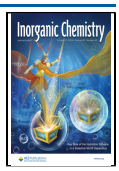

https://doi.org/10.1021/acs.inorgchem.4c02896
Inorg. Chem. 2024, 63, 19717−19727

their cluster electrons. In this context, the field of reduced tantalum halides notably lacks compounds having intermediate oxidation states between +2.5 and +4, which is of interest for the development of novel heterohalide cluster compounds.

Recently we reported niobium pnictide-halides Nb_4PnX_{11}, (Pn = N, P; X = Cl, Br, I) containing the butterfly shaped [Nb_4] niobium cluster, μ_4-capped by a pnictogen (N or P) atom.[21] In our current work, we describe the related compound Ta_4SBr_{11}, containing a butterfly shaped [Ta_4] tantalum cluster compound with a μ_4-capped sulfide atom. Specifically, we report the solid-state synthesis, crystal structure, electrical conductivity, magnetic susceptibility and the calculated band structure of Ta_4SBr_{11}. These results suggest that Ta_4SBr_{11} is a cluster Mott insulator with a van der Waals layered structure. Other Mott insulators containing Ta include the cluster compound $GaTa_4Se_8$[22] and the van der Waals material TaS_2;[23] Ta_4SBr_{11} demonstrates an interesting combination of these two structural features.

RESULTS AND DISCUSSION

Synthesis. Ta_4SBr_{11} was prepared from tantalum, tantalum(V) bromide and sulfur at 400 °C. It is obtained as black, rod-shaped platelets showing metallic luster. The compound was obtained from a high yield reaction, according to the powder XRD pattern (Figure S1). The addition of CsBr to the reaction mixture was found to improve crystal growth. In this process, CsBr and $TaBr_5$ form a eutectic melt allowing the reaction to proceed and promoting the formation of sizable crystals of Ta_4SBr_{11}. Figure 1 shows electron micrographs of Ta_4SBr_{11} crystals from the direct synthesis (a) and significantly larger crystals grown from a CsBr flux (b and c).

The crystal growth process involves the compounds $CsTaBr_6$[24] and Cs_2TaBr_6 as intermediate products or side-phases, whose structures were characterized by means of single-crystal X-ray diffraction techniques. The as-yet unreported compound Cs_2TaBr_6 crystallizes in the space group $Fm\bar{3}m$ with a = 10.6831(2) Å,[25] isostructural to K_2TaCl_6.[26] The structure can be described as a face-centered cubic packing of $[TaBr_6]^{2-}$ octahedra with Cs^+ in cuboctahedral voids formed by bromides (Figure S3).

TXRF, EDX, and SEM. Elemental analysis of crystalline samples of Ta_4SBr_{11} was performed with two techniques. Total reflection X-ray fluorescence (TXRF) measurements revealed a Ta : S : Br ratio of 4.00 : 1.05(4) : 11.08(7). Energy-dispersive X-ray spectroscopy (EDX) measurements on various spots of single crystals resulted in a emission spectrum corresponding to an average Ta : S : Br ratio of 4.00 : 1.2(±0.23) : 11.77(±0.76), verifying the composition determined by single-crystal XRD.

Crystal Structure. The crystal structure of Ta_4SBr_{11}, as refined on the basis of single-crystal XRD data (Table S1) at 150 K, was found to be intrinsically disordered (Table S2 and Figure 2). The average structure was solved and refined in the space group $Pmmn$ and contains two distinct tantalum positions: one tantalum atom in a split position on both sides of a mirror plane and the second position with 50% occupancy. Out of four independent bromides in the structure, one (Br4) shares its position with the sulfur (50% each) in a bridging position.

Using these split positions, refinements resulted in wR_2 values below 4%, yielding a kinked van der Waals type layer structure with stacking orthogonal to the c-axis direction (Figure 2). However, all reasonable structure models require a doubling of the a lattice parameter and thus a superstructure. Close inspection of the diffraction patterns yielded diffuse scattering along a^* rather than sharp superstructure reflections (Figure S2). Assuming a translation period of 2a, the disorder can be resolved and ordered structure models developed in a straightforward manner. A similar average structure was previously reported and decomposed for Nb_4PnX_{11} (Pn = N, P; X = Cl, Br, I).[21]

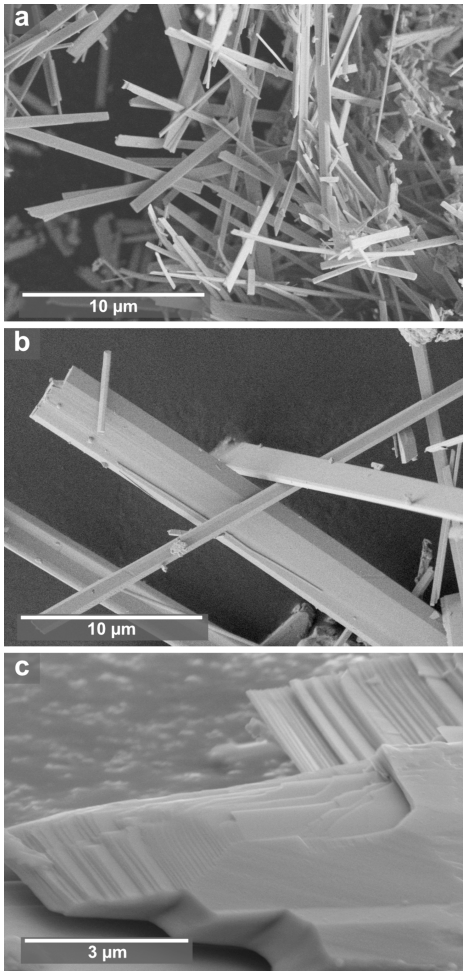

Figure 1. Scanning electron microscope (SEM) micrographs of Ta_4SBr_{11} crystals obtained from the direct synthesis (a) and grown from a flux of CsBr (b and c).

The characteristic motif in the structure of Ta_4SBr_{11} is the butterfly shaped $Ta_4(\mu_4\text{-}S)$ cluster core with a capping sulfur atom (Figure 3). For each cluster, there are four bridging bromido ligands, Br3 and Br4, connecting the cluster into linear chains along [100], that will be compared below with the arrangement of atoms in structure of $TaBr_4$. Furthermore, the bromides Br2 connect the butterfly clusters along [010]. These bridging functionalities together create layers within the a,b plane of the structure.

However, the connection of Ta_4S clusters within one layer of the structure (via Br2) can be accomplished in two different ways, as can be understood from the average structure displayed in Figure S4. This leads to two possible cluster arrangements within layers of the structure, one kinked and one linear, as shown in Figure 4.

The connectivity of clusters via Br2 ligands creates an inversion center between butterfly clusters that can be

https://doi.org/10.1021/acs.inorgchem.4c02896
Inorg. Chem. 2024, 63, 19717−19727

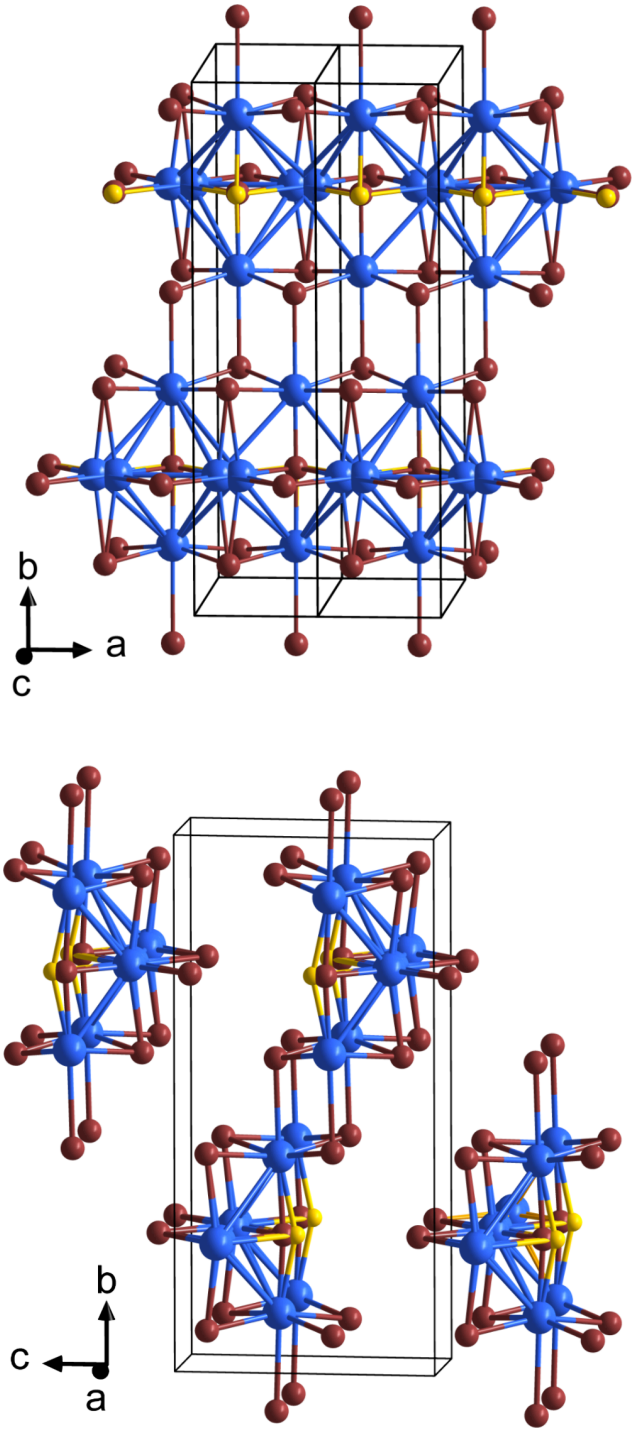

Figure 2. Refined average structure of Ta_4SBr_{11} in two projections. Tantalum atoms are depicted in blue, bromine in brown and sulfur in yellow.

envisioned in Figure 5, thereby creating a sinusoidal pattern within each layer. This arrangement is further expanded in Figure 6, emphasizing the arrangement of corrugated layers in the structure. It is evident that the structure demonstrates van der Waals bonding between layers. In planar van der Waals layer structures, such as graphite or in transition metal dichalcogenides, shearing of layers may occur along different directions.[27−29] Due to the corrugated layer structure of

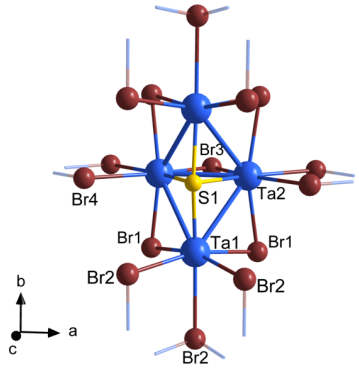

Figure 3. Characteristic $[Ta_4(\mu_4S)]$ butterfly cluster in the structure of Ta_4SBr_{11} with its connectivity pattern implied by broken bonds.

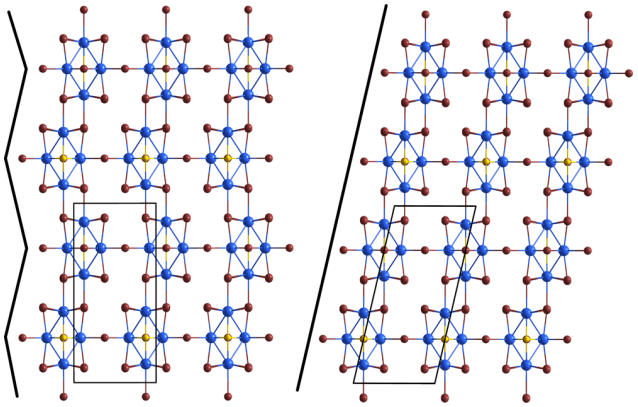

Figure 4. Two possible cluster arrangements, kinked (left) and linear (right) in a single layer of Ta_4SBr_{11}, shown with respective unit cells (black lines) given in Table 1.

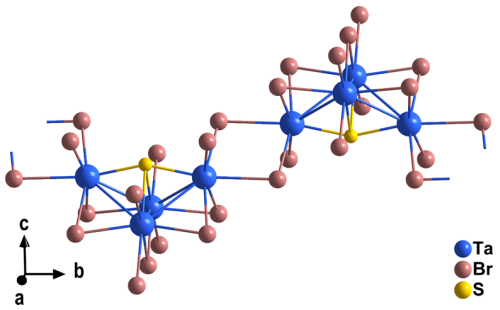

Figure 5. Section of the Ta_4SBr_{11} structure, visualizing the corrugated connectivity of two clusters along the *b*-axis.

Ta_4SBr_{11}, shearing can occur only along one direction, which is along [100] as indicated by the red arrow in Figure 6.

Shearing of layers parallel to [100] results in essentially two different possible arrangements of layers. Figure 7 shows two possible sequences of cluster layers, held together by the van der Waals interactions, in which the stacking of clusters is eclipsed (left) or staggered (right).

In summary, the average structure of Ta_4SBr_{11} (Figure 2 and Figure S4) can be explained as a superposition of in-plane and interplane disorder. Each of these types of disorder can be decomposed into two main arrangements, resulting in four ordered structures with reduced symmetries, which are presented in Table 1. The kinked arrangement of layers can be described with the monoclinic space group $P2_1/m$, with a

https://doi.org/10.1021/acs.inorgchem.4c02896
Inorg. Chem. 2024, 63, 19717−19727

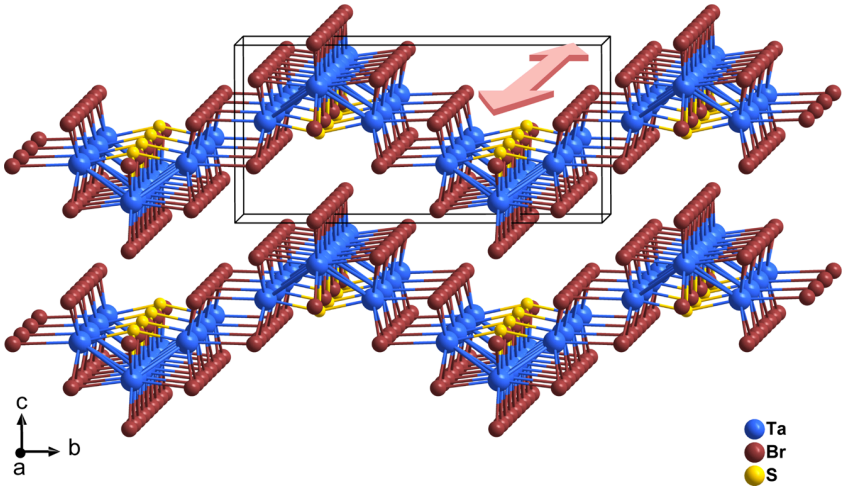

Figure 6. Corrugated layer structure of Ta_4SBr_{11}. The red arrow highlights the shearing direction of the layers.

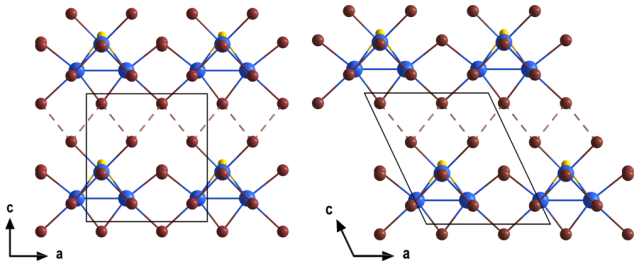

Figure 7. Possible arrangements of two parallel chains hold together by a van der Waals gap (dashed lines). Clusters can be either stacked in an eclipsed (left) or staggered (right) fashion. Relevant crystallographic information for both structures are given in Table 1.

monoclinic angle (β) that is dependent on the stacking of layers (90° in eclipsed and 115.38° in staggered cluster stacking). For the linear arrangement of clusters (Figure 4, right) within layers, the resulting space groups are $P2/c$ (eclipsed) and $C2/c$ (staggered), where the monoclinic angle defines the arrangements of the clusters within the layers. The lattice constant a and the unit cell volume V are doubled, or even quadrupled for the linear arrangement within layers and a staggered arrangement between layers, when compared to the average structure.

Ta−Ta distances along the four edges of the butterfly cluster are equal, with $d_{Ta1-Ta2}$ = 309.14(3) pm, while the connecting edge between the cluster triangles is shorter with $d_{Ta1-Ta1}$ = 291.50(4) pm. The distance between adjacent clusters is $d_{Ta1-Ta1}$ = 418.46(4) pm, and the distances Ta−S are d_{Ta1-S} = 231.0(1) pm and d_{Ta2-S} = 248.5(4) pm. The connectivity of the 1D butterfly cluster chains along [100] is comparable to that of the structure of metal tetrahalides. The Ta−Ta distances within and between the butterfly clusters in Ta_4SBr_{11} are compared with the alternating short and long $M-M$ distances in $TaBr_4$ and WBr_4 in Figure 8.[30,31] The given sections of structures are easily comparable, with the appearance of alternating short and long distances between metal atoms. In $TaBr_4$, the ratio of the short distance to the long distance is 0.764, and for WBr_4 it is 0.691. In Ta_4SBr_{11} this ratio is 0.696. Given that two tantalum atoms in $TaBr_4$ form a two-center-two-electron bond, and tungsten atoms form a two-center-four-electron bond in WBr_4, the ratio in Ta_4SBr_{11} appears to be closer to the double bond character in WBr_4.

With seven skeletal electrons, Ta_4SBr_{11} contains the same number of cluster electrons as Nb_3Br_8 and $CsNb_3Br_7S$, but it is obvious that the electronic structures of these compounds are different. An odd number of electrons can give rise to different kinds of electronic behavior, which are very much dependent on the crystal structure, as outlined through the examples of Nb_3Br_8 and $CsNb_3Br_7S$ in the Introduction. In attempt to analyze the electronic properties of Ta_4SBr_{11}, we performed DRIFT spectroscopy as well as conductivity, magnetic measurements and electronic band structure calculations using density functional theory (DFT).

DRIFT Optical Band Gap Determination. The absorption coefficient F was obtained using Kubelka−Munk analysis following $F(R_\infty) = \frac{\alpha}{S} = \frac{(1-R_\infty)^2}{2R_\infty}$, where $R_\infty = \frac{R_{sample}}{R_{standard}}$ is the

Table 1. Crystallographic Data of the Average Structure of Ta_4SBr_{11} Compared to Those of Ordered Structures

		intralayer arrangement: kinked		intralayer arrangement: linear	
		interlayer arrangement:		interlayer arrangement:	
	average structure	eclipsed	staggered	eclipsed	staggered
space group	$Pmmn$	$P2_1/m$	$P2_1/m$	$P2/c$	$C2/c$
crystal system	orthorhombic	monoclinic	monoclinic	monoclinic	monoclinic
a/pm	355.07(1)	710.1	710.1	710.1	710.1
b/pm	1546.90(4)	1546.9	1546.9	748.42	1496.8
c/pm	748.42(3)	748.4	828.38	1587.13	1587.13
β/Å	90.000	90.000	115.381	102.928	102.928
V/Å^3	411.08(2)	822.15	822.15	822.15	1644.30

https://doi.org/10.1021/acs.inorgchem.4c02896
Inorg. Chem. 2024, 63, 19717−19727

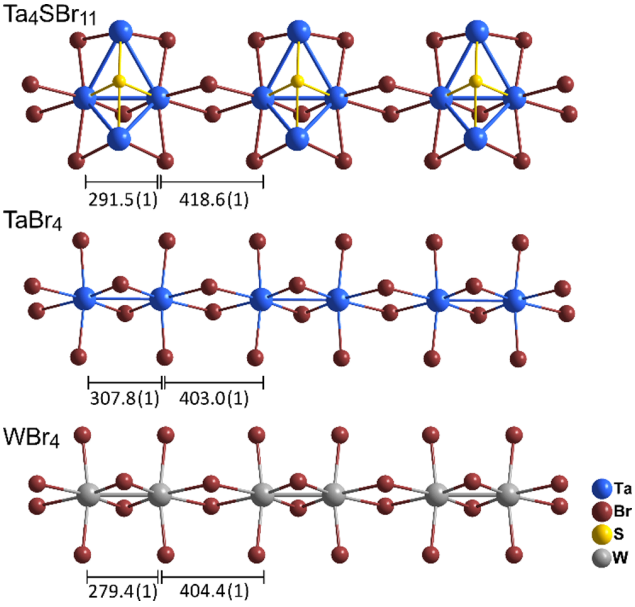

Figure 8. Comparison of 1D strands in the structures of Ta_4SBr_{11}, $TaBr_4$,[30] and WBr_4[31] with metal-to-metal distances given in pm.

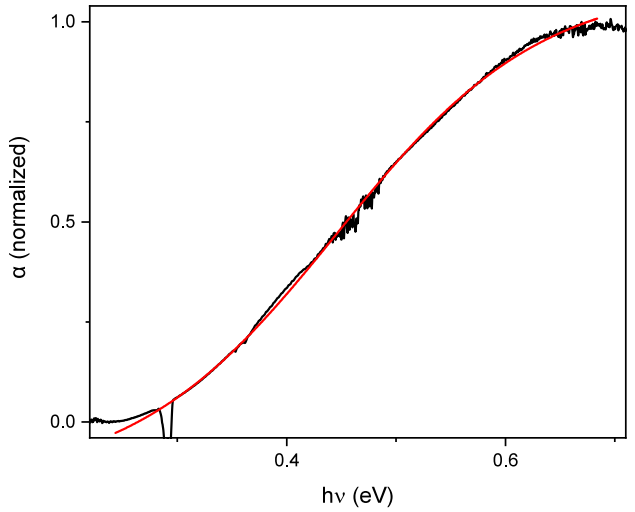

Figure 9. Optical absorption coefficient spectra of Ta_4SBr_{11} with the Boltzmann function used to fit α (normalized) (R^2 = 0.997, χ^2 = 3.01 × 10^{-4}, signals around 0.29 eV can be assigned to atmospheric absorption bands of CO_2).

reflectance of an infinitely thick specimen, α is the absorption and S is the scattering coefficient. For particle sizes greater than the light wavelengths measured, the scattering coefficient is understood to be approximately independent of frequency ($F(R_\infty) \sim \alpha$) and therefore $F(R_\infty)$ could be understood as a "pseudoabsorbance" coefficient.[32−38]

The observed absorption edge in the spectrum is very broad, which causes a high difference between the calculated direct and indirect bandgap. An alternative band gap determination according to Zanata et al. was performed to account for the disordered structure (see Figure 9).[39] The energy is plotted against the absorption coefficient α and fitted with a sigmoid-Boltzmann function:

$$\alpha(E) = \alpha_{\max} + \frac{\alpha_{\min} - \alpha_{\max}}{1 + \exp\left(\frac{E - E_0^{Boltz}}{\delta E}\right)}$$

where α_{min} (α_{max}) stands for the minimum (maximum) absorption coefficient; E_0^{Boltz} is the energy coordinate at which the absorption coefficient is halfway between α_{min} and α_{max}; and δE is associated with the slope of the sigmoid, indicating the energy range over which most optical transitions occur, and gives an idea of the magnitude of the disorder.[39]

The band gap can then be calculated by following equation with n_{dir}^{Boltz} = 0.3 and n_{indir}^{Boltz} = 4.3:

$$E_g^{Boltz} = E_0^{Boltz} - n_{dir/indir}^{Boltz} \cdot \delta E$$

and results with δE = 0.0933(8) eV in a direct $E_g^{Boltz}(direct)$ = 0.4181(3) eV and indirect $E_g^{Boltz}(indirect)$ = 0.044(3) eV bandgap. Since the center of the absorption edge is at about ∼0.45 eV, a direct band gap can be assumed with a very broad slope of δE = 0.0933(8) eV, originating from the disordered structure.

However, the Tauc plot (E_{dir}^{Tauc} = 0.455 eV and E_{indir}^{Tauc} = 0.183 eV with $\alpha \approx F(R_\infty)$) yielded a broad spectrum that made an unambiguous bandgap determination challenging (see Figure S6), which is why the Zanata method was preferred here.[40] We note that these values are somewhat smaller than the DFT-calculated band gap of 0.4 eV (see below). However, the DFT bandgap is dependent on the value of the adjustable phenomenological Hubbard U parameter. Therefore, the difference between the experimental and calculated gap is, in this case, an indicator of the reasonable but not perfect choice of U. Additionally, the effects of disorder are not included in the DFT calculation; disorder in general acts to transform indirect gaps to direct gaps, as indirect band gaps are necessarily reliant on the presence of translational symmetry. Relatively mild structural disorder (e.g., introduction of defects)[41] can be sufficient to cause such a transition.

Electrical Properties. Further information regarding the band gap, as well as the electronic properties was obtained by temperature-dependent conductivity measurements. We performed two-point probe I−V scans (see Figure S7 for a typical measurement) to determine the electrical conductivity in the temperature range between 20 and 300 K (Figure S8 left). For each temperature the current voltage characteristic shows ohmic behavior, as exemplarily shown in Figure S7 left. In addition, an ample and rapid photoresponse to optical excitation at 779 nm was observed (Figure S8 right). Under the assumption of Arrhenius-type temperature-activated hopping transport, two distinct linear regions were obtained in the Arrhenius plots, specifically from 300−100 K and from 100−20 K (Figure 10). Assuming a position of the Fermi level in the middle of the bandgap, we derive the corresponding activation energies for the two domains and relate their values to $E_G/2$. The energy gap in electron volts can be extracted and displayed according to the following approximation:[42−45]

$$E_g = -slope \cdot \ln(10) \cdot 2 \cdot k_B \cdot 6.25 \cdot 10^{18} eV$$

Following this approximation gives $E_{G,1}$ = 0.124 eV and $E_{G,2}$ = 0.424 eV. These values are in reasonable agreement with the indirect and direct band gaps, obtained by the Zanata analysis of the DRIFT spectroscopy data. The sudden change in the temperature-dependent transport data at 100 K may indicate a

https://doi.org/10.1021/acs.inorgchem.4c02896
Inorg. Chem. 2024, 63, 19717−19727

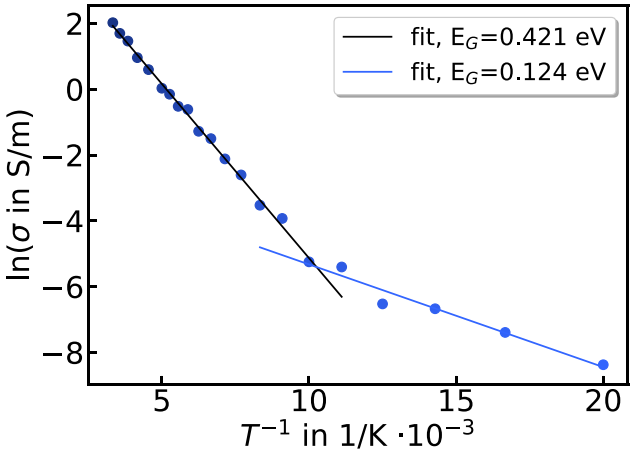

Figure 10. Arrhenius-plot of the temperature-dependent conductivity shown in Figure S8. Two regimes can be identified and fitted linearly to determine the electronic band gap.

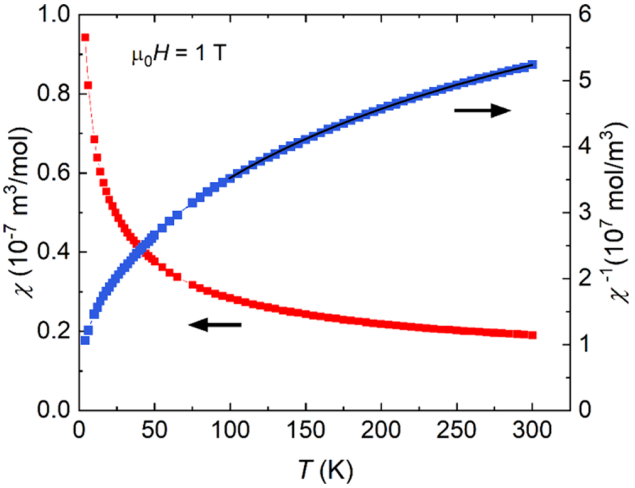

Figure 11. Temperature dependence of magnetic susceptibility (red squares) and inverse magnetic susceptibility (blue squares) with plotted modified Curie–Weiss fit.

phase transition or some other change in the electronic structure.

Crystal Structure Refinement at 80 K. Following the result of two distinct slopes in the temperature-dependent conductivity measurement, we performed another crystal-structure refinement based on a measurement at lower temperature. The crystal structure refinement data at 80 K did not show a phase-transition relative to the previously refined structure at 150 K. A comparison of refined interatomic distances in Ta_4SBr_{11} at 150 and 80 K is given in Table 2.

Table 2. Comparison of Selected Interatomic Distances in Ta_4SBr_{11} at 150 and 80 K

Ta_4SBr_{11} distance (pm)	150 K	80 K
Ta(1)–Ta(2)	309.14(3)	309.30(9)
Ta(2)–Ta(2)	291.50(4)	291.6(1)
	418.64(4)	417.4(1)
Ta(1)–S	231.0(1)	231.1(2)
Ta(2)–S	248.5(4)	248.9(7)

Interatomic distances within the butterfly cluster are almost identical. Only the Ta2–Ta2 distance connecting two short edges of butterfly cluster is decreased by 1.2 pm at 80 K (see Figure 3 for comparison). Although we must consider this change as significant (because it is above the 3σ limit), it is not clear if this change indicates a weaker decay of the electric conductivity (decrease of activation energy) below 100 K. However, a convergence of short and long metal-to-metal distances in the Peierls-distorted structure of $NbCl_4$ has been reported to increase the electrical conductivity, as mentioned in the introduction.[5]

Magnetic Properties. The temperature dependence of the magnetic susceptibility was measured at 1 and 0.5 T and proved the purity of the measured sample with paramagnetic response down to 2 K. The data for measurements at 1 T are depicted in Figure 11, showing a plot of the inverse magnetic susceptibility with a modified Curie–Weiss fit ($\chi(T) = C(T - \theta_p) + \chi_0$ wherein C, θ_p, and χ_0 are the Curie constant, the Weiss temperature, and the temperature-independent susceptibility). The magnetic susceptibility follows Curie–Weiss behavior from 100 K, and a fit to the data gives an effective magnetic moment μ_{eff} = 1.23(1) μ_B per formula unit as well as a Weiss temperature θ_p = −49(1) K, pointing to antiferromagnetic interactions and temperature-independent susceptibility χ_0 = 1.2(5) 10^{-8} m^3/mol. These findings are consistent with the assignment of Ta_4SBr_{11} as a Mott insulator (see DFT results below), specifically as a paramagnet with local antiferromagnetic correlations.[46] The observed value of μ_{eff} is slightly less than the calculated value of one unpaired electron (μ_{eff} = 1.73 μ_B), which could be due to formation of electron pairs (intercluster singlet formation) at defects or domain walls within the disordered crystal.[16]

DFT Calculations. The electronic band structure of Ta_4SBr_{11} was separately calculated for each of the intra- and interlayer arrangements of clusters shown in Table 1, initially without inclusion of any magnetic ordering of the unpaired spins. These calculations resulted, in all cases, in metallic band structures, with two half-occupied Ta d bands at the Fermi energy. As this finding is inconsistent with experimental results showing the material to be a semiconductor, several potential mechanisms of band gap opening were tested theoretically. First, spin–orbit coupling (SOC) was introduced into the calculations (Figure S5), since SOC can open band gaps, for example in topological insulators.[47] However, despite the significant SOC in Ta,[48] its effect on the bands near the Fermi energy was relatively small, and the material remained metallic.

Second, we consider the formation of a Mott insulator, i.e. a state where the combination of strong electronic correlations (specifically electron–electron repulsion) and antiferromagnetic exchange interactions leads to electron localization and the opening of a band gap.[46,49] In order to model such a state using DFT, we combine an antiferromagnetic ordering of the unpaired electron spins, with the Hubbard U correction[50] on the Ta sites, which accounts for electronic correlations. A value of U_{eff} = 4.5 eV was chosen based on the literature.[51] As DFT calculations combining the Hubbard U correction with SOC are computationally intensive, only two combinations of crystallographic and magnetic structure were trialed.

As Figure 12 shows, the combination of the linear intralayer, eclipsed interlayer arrangement with an antiferromagnetic ordering involving alternating cluster magnetic moments along c opened a band gap. This gap has a magnitude of 0.4 eV and is indirect, lying between the valence band maximum at $\mathcal{Z}\left(0\frac{1}{2}0\right)$

https://doi.org/10.1021/acs.inorgchem.4c02896
Inorg. Chem. 2024, 63, 19717–19727

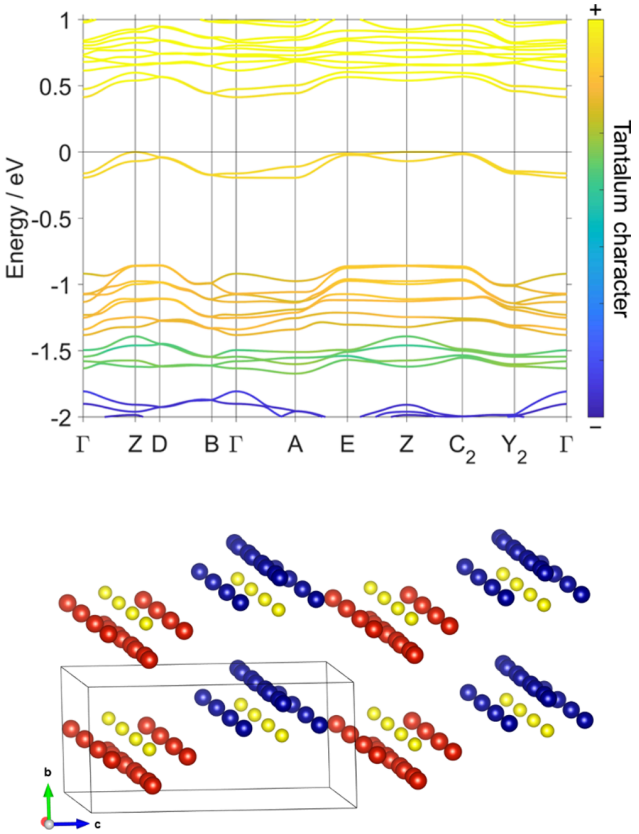

Figure 12. Calculated electronic band structure (top) of eclipsed Ta_4SBr_{11} layers, with a linear intralayer arrangement of clusters and antiferromagnetic ordering of the unpaired spins (bottom), showing the opening of a gap due to strong electronic correlations and the formation of a Mott insulator. Ta atoms with spins oriented in the + *c* direction are colored in red; those with spins oriented in the − *c* direction are colored in blue. Br atoms are not shown for clarity. The magnetic supercell (64 atoms) used for the calculation is shown as a black outline. The bands within 1.75 eV of the Fermi level show Ta d character; the lower bands show significant hybridization with the Br p bands at −2 eV. Special points in and paths through the Brillouin zone were chosen following literature.[52]

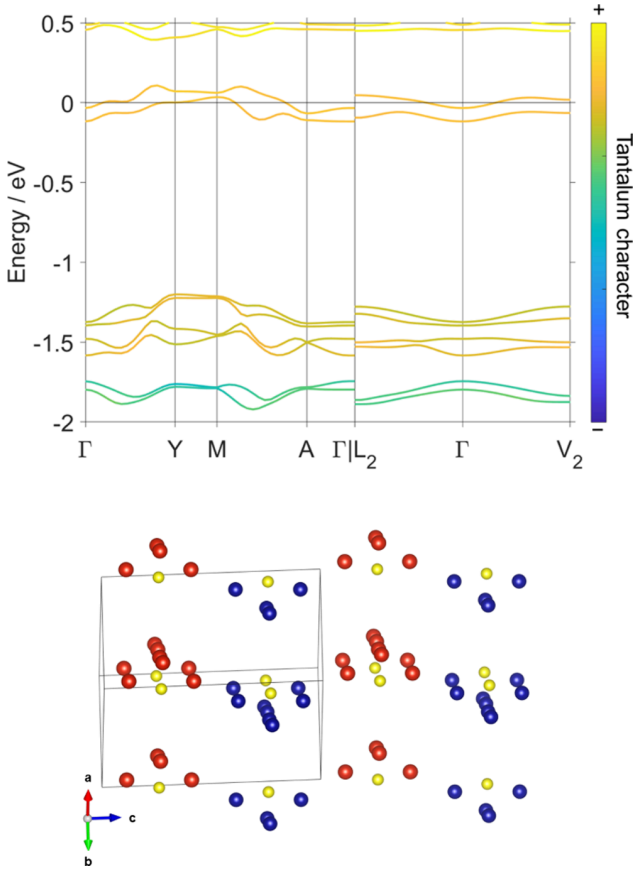

Figure 13. Calculated electronic band structure (top) of staggered Ta_4SBr_{11} layers, with a linear intralayer arrangement of clusters and antiferromagnetic ordering of the unpaired spins (bottom), showing the absence of a band gap. The two magnetic sublattices (with the predominant component of the spin aligned along ± *a*) are colored in red and blue, respectively (bottom). Br atoms are not shown for clarity. The unit cell used for the calculation is shown as a black outline. Special points in and paths through the Brillouin zone were chosen following literature.[52]

and the conduction band minimum at Γ (0 0 0). The DFT-calculated magnetic moments on the Ta atoms corresponded to 0.9 electronic moments per cluster, indicating a high degree of local magnetic polarization of the one unpaired electron per cluster. This polarization, in combination with the emergence of a band gap, corresponds to the formation of a Mott insulating state. The Ta d bands are found to hybridize with the Br p bands, indicating the presence of some covalent character to the Ta−Br bonding.

The second structure tested, which had the same magnetic ordering but a linear intralayer, staggered interlayer crystallographic structure, remained metallic (Figure 13). This can be attributed to the smaller degree of magnetic polarization, with only 0.6 electronic moments per cluster. Whereas in the case shown in Figure 12, the spins were aligned along ± *c* (along the corrugation direction), here the predominant component of the magnetic moment vector lies along ± *a*, i.e. in an interlayer direction. Interestingly, this implies that the interlayer stacking could have a significant impact on the electronic and magnetic structure of the material. The properties of monolayers or bilayers of Ta_4SBr_{11} are therefore an interesting direction for further research, especially since we note that the metallic bands shown in Figure 13 are nearly flat, an interesting phenomenon (related to superconductivity and other quantum properties) shared with monolayer Nb_3Cl_8[17] and twisted bilayer graphene.[53] It is important to note that this result does not by itself demonstrate that the linear, staggered configuration should be metallic, as there are other possible magnetic orderings which were not tested due to the demanding nature of these calculations..

Another mechanism of gap opening, the charge density wave (CDW) instability (the 2-dimensional analogue of the 1-dimensional Peierls instability),[46,49,54] was not investigated in depth, as magnetic susceptibility measurements (see above) are consistent with the Mott insulator hypothesis. However, we note that the calculated Fermi surfaces (Figure S5) show pseudo-2D bands, indicating the possibility of CDW instabilities. Such instabilities could cause structural disorder without leading to the opening of an electronic band gap, as is seen in the van der Waals material WTe_2I.[55]

At first intuition, neither of the disordered arrangements within and between layers seems to be energetically favored. In order to estimate the potential energy landscape related to shearing along the van der Waals layers (see Figure 7), we

https://doi.org/10.1021/acs.inorgchem.4c02896
Inorg. Chem. 2024, 63, 19717−19727

compared the lattice energy (without the inclusion of the Hubbard U or magnetic ordering) of the four arrangements shown in Table 1. The linear, staggered configuration was found to have the lowest energy, with both eclipsed configurations having energies 0.04 eV (4 kJ/mol) higher, and the kinked, staggered configuration having the highest energy at 0.1 eV (9 kJ/mol) above the minimum. These differences are significant, and are large enough that thermal effects at 80−150 K (the temperatures at which the crystal structure was determined) would not be sufficiently large to cause the observed disorder. However, the thermal energy available at the synthesis temperature (673 K), might be sufficiently large to cause disorder, which then could be frozen into the structure upon cooling. In addition, the calculated structures may not reflect the correct energy differences of the full range of possible disordered layered structures, where larger cells with more complex layer disorder would also have to be considered, exponentially increasing the computational time.

CONCLUSIONS

The new material Ta_4SBr_{11} is characterized by bridged $[Ta_4(\mu_4\text{-}S)]$ butterfly clusters, connected by bromides to form a corrugated van der Waals type layer structure. This compound parallels the structure of the previously reported compounds Nb_4PnX_{11} (Pn = N, P; X = Cl, Br, I), which represents a six-electron cluster. Both compounds exhibit complex disordering patterns, indicated by characteristic streaks in their XRD patterns. The structural disorder in Ta_4SBr_{11} can be understood as a combination of in-plane disorder, due to two different cluster connectivities, and interlayer shear along the [100] direction.

The connectivity of the clusters parallels the structure of $NbCl_4$ along one direction, where the alternation of metal-to-metal distances indicates metal−metal bonding with concomitant modification of the electronic structure. The small-gap semiconductor Ta_4SBr_{11} represents another example of a seven-electron cluster, like Nb_3Cl_8 and $CsNb_3Br_7S$. In all of these compounds, the presence of an unpaired electron in each cluster, in combination with strong electronic correlations, leads to unusual properties which cannot be explained by simple band theory. Electronic structure calculations in combination with experimental results lead us to conclude that Ta_4SBr_{11} is likely to be a cluster Mott insulator, like monolayer Nb_3Cl_8. If monolayers of Ta_4SBr_{11} can be prepared, they might also have interesting emergent properties such as flat electronic bands.

EXPERIMENTAL SECTION

Synthesis and Crystal Structure. Manipulations of starting materials, such as charging the silica ampules (estimated volume 5 cm^3) with starting materials were performed in an argon-filled glovebox (MBraun, labmaster 130, O_2 < 1 ppm, H_2O < 1 ppm).

Ta_4SBr_{11} Bulk Synthesis. A mixture of $TaBr_5$ (234.3 mg, 0.40 mmol, Sigma-Aldrich, 99.9%), Ta (59.8 mg, 0.33 mmol, Merck, 98%) and S_8 (5.9 mg, 0.18 mmol, Carl Roth GmbH, 99.9%), fused into an evacuated silica tube, was heated with 2.0 K/min in a Simon-Müller-furnace. After heating at 400 °C (200 h), Ta_4SBr_{11} was obtained as crystalline powder.

Ta_4SBr_{11} Single Crystals. CsBr (39.1 mg, 0.18 mmol, Merck, 99.9%) was added to the reaction mixture as a flux. Hereby, CsBr and $TaBr_5$ (234.3 mg, 0.40 mmol) react to $CsTaBr_6$, and Cs_2TaBr_6 as intermediate reactants, which react with Ta (59.8 mg, 0.33 mmol) and S_8 (5.9 mg, 0.18 mmol). To obtain X-ray pure phases, the powder was resealed in a second hourglass-ampule (length: 14 cm). Unreacted $TaBr_5$ and $TaOBr_2$ were sublimed off in a temperature gradient 400 °C/300 °C. Yield: 55−65%. A PXRD pattern of the product is shown in Figure S1.

Powder X-ray Diffraction. All reaction products were investigated by powder X-ray diffraction (PXRD) using a StadiP diffractometer (Stoe, Darmstadt) with Ge-monochromated Cu−$K_{\alpha1}$ radiation, and a Mythen1 Detector.

Single-Crystal X-ray Diffraction. Data collections were performed on a Rigaku XtaLAB Synergy-S single-crystal X-ray diffractometer equipped with HyPix-6000HE detector and monochromated Mo−K_α radiation (λ = 0.7107 Å) and Cu−K_α radiation (λ = 1.54184 Å) at 150 and 80 K. X-ray intensities were corrected for absorption with a numerical method (crystal faces) using CrysAlisPro 1.171.41.67a (Rigaku Oxford Diffraction, 2020). This software was also used to calculate reconstructed reciprocal space sections. The average structures were solved by direct methods (SHELXS) and refined by full-matrix least-squares methods performed with SHELXL-2014 as implemented in Olex2 1.3-ac4.44.

CCDC 2352652 contains the supplementary crystallographic data for Ta_4SBr_{11} at 80 K; CCDC 2181179 for Ta_4SBr_{11} at 150 K; CCDC 2327955 for Cs_2TaBr_6. These data can be obtained free of charge from The Cambridge Crystallographic Data Centre via www.ccdc.cam.ac.uk/structures.

EDX and SEM. Energy dispersive X-ray spectroscopy (EDX) and Scanning electron microscopy (SEM) were performed on a HITACHI SU8030 scanning electron microscope with a Bruker QUANTAX 6G EDX-detector. For this purpose, single crystals of Ta_4SBr_{11} were fixed on carbon-tapes.

Electrical Conductivity. Conductivity measurements were performed in a Lake ShoreCryotronics CRX-6.5K probe station with a Keithley 2636B source meter unit. Rod-shaped crystals of Ta_4SBr_{11} were contacted with silver paste on a silicon substrate with 770 nm oxide layer and transferred into the chamber under protective gas. The conductive silver pads at each end of the crystals were connected to the circuit with tungsten tips (Figure S7 right). The chamber was kept under vacuum (<5 × 10^{-5} mbar) and the temperature was varied between 20 and 300 K. Before each measurement, sufficient time was allowed for the sample to reach the chosen temperature. Two-point conductivity measurements were performed by varying the applied source-drain voltage from −1 to 1 V while detecting the current. For time-resolved photocurrent measurements, using a picosecond pulsed laser driver (Taiko PDL M1, PicoQuant) together with a laser head 779 nm (pulse length <500 ps) the crystals were illuminated at 40 mW laser output power using the continuous wave mode under a constant bias of 1 V. The measured crystals had the dimensions: 106 μm × 16 μm × 4 μm and 80 μm × 15 μm × 5 μm.

DRIFT (Diffuse Reflectance Infrared Fourier Transformation) Spectroscopy. Samples were measured at room temperature under inert conditions in diffuse reflectance with a Harrick Praying Mantis attachment using a Bruker Vertex 70 infrared spectrophotometer with a deuterated triglycine sulfate (DTGS) detector and KBr beamsplitter. The background spectra were collected using pure dried KBr in powder form.

TXRF (Total Internal Reflection X-ray Fluorescence) Spectroscopy. TXRF studies were performed using a S2 Picofox (Bruker AXS Microanalysis, Berlin, Germany) equipped with a Mo X-ray tube, which was operated at 50 kV and 600 μA. The measurement period for each sample was 1000 s (live time). Fitting of the resulting spectra was done using the Spectra software (Bruker Nano GmbH) in the super byas mode (maximum stripping cycles of 2000).

Density Functional Theory. Density functional theory (DFT) calculations were performed within the Abinit software package (v. 10).[56] The Perdew−Burke−Ernzerhof exchange−correlation functional[57] was used with the vdw-DFT-D3(BJ) dispersion correction of Grimme.[58] Monkhorst−Pack grids of k-points were chosen with minimum real-space spacing between grid points of 30 Å.[59] Plane-wave calculations were performed using the projector augmented wave (PAW) method[60] with an energy cutoff of 24 Ha outside the

https://doi.org/10.1021/acs.inorgchem.4c02896
Inorg. Chem. 2024, 63, 19717−19727

PAW spheres and a 120 Ha cutoff within them. These computational parameters were chosen following convergence studies, with convergence of the internal pressure within 1% being the criterion. The Hubbard U parameters[50] were chosen as U = 5 eV and J = 0.5 eV on the Ta sites, yielding $U_{eff} = U - J$ = 4.5 eV, in accordance with previous literature results.[61] Calculations performed with the Hubbard U also included spin−orbit coupling and noncollinear antiferromagnetism.

Magnetic Measurements. The magnetization measurement was performed using the magnetic property measurement system (MPMS) by Quantum Design Inc. The sample in powder form (53.9 mg) was fixed in capsule and placed to the MPMS. Diamagnetic contributions from sample holder and capsule were subtracted from observed data.

■ ASSOCIATED CONTENT

Supporting Information

The Supporting Information is available free of charge at https://pubs.acs.org/doi/10.1021/acs.inorgchem.4c02896.

Additional X-ray diffraction data, figures, photographs of single crystal, band structures, Fermi surfaces, DRIFT analysis, and conductivity measurements (PDF)

Accession Codes

CCDC 2181179, 2327955, and 2352652 contain the supplementary crystallographic data for this paper. These data can be obtained free of charge via www.ccdc.cam.ac.uk/data_request/cif, or by emailing data_request@ccdc.cam.ac.uk, or by contacting The Cambridge Crystallographic Data Centre, 12 Union Road, Cambridge CB2 1EZ, UK; fax: +44 1223 336033.

■ AUTHOR INFORMATION

Corresponding Authors

Carl P. Romao − *Department of Materials, ETH Zürich, Zürich 8093, Switzerland;* orcid.org/0000-0002-5519-2519; Email: carl.romao@mat.ethz.ch

Hans-Jürgen Meyer − *Section for Solid State and Theoretical Inorganic Chemistry, Institute of Inorganic Chemistry, Eberhard Karls Universität Tübingen, Tübingen D-72076, Germany;* orcid.org/0000-0003-2450-4011; Email: juergen.meyer@uni-tuebingen.de

Authors

Fabian Grahlow − *Section for Solid State and Theoretical Inorganic Chemistry, Institute of Inorganic Chemistry, Eberhard Karls Universität Tübingen, Tübingen D-72076, Germany;* orcid.org/0000-0002-1308-4819

Fabian Strauß − *Institute of Physical and Theoretical Chemistry, Eberhard Karls Universität Tübingen, Tübingen D-72076, Germany*

Patrick Schmidt − *Section for Solid State and Theoretical Inorganic Chemistry, Institute of Inorganic Chemistry, Eberhard Karls Universität Tübingen, Tübingen D-72076, Germany;* orcid.org/0000-0001-6556-2088

Jaroslav Valenta − *International Center for Materials Nanoarchitectonics (WPI-MANA), National Institute for Materials Science, Tsukuba, Ibaraki 305-0047, Japan;* orcid.org/0000-0002-2268-7187

Markus Ströbele − *Section for Solid State and Theoretical Inorganic Chemistry, Institute of Inorganic Chemistry, Eberhard Karls Universität Tübingen, Tübingen D-72076, Germany;* orcid.org/0000-0002-5147-5677

Marcus Scheele − *Institute of Physical and Theoretical Chemistry, Eberhard Karls Universität Tübingen, Tübingen D-72076, Germany;* orcid.org/0000-0002-2704-3591

Complete contact information is available at: https://pubs.acs.org/10.1021/acs.inorgchem.4c02896

Author Contributions

The manuscript was written through contributions of all authors. All authors have given approval to the final version of the manuscript.

Funding

DFG grant ME 914/32-1, SCHE1905-9-1

Notes

The authors declare no competing financial interest.

■ ACKNOWLEDGMENTS

Funding by the Deutsche Forschungsgemeinschaft through grant ME 914/32-1 and SCHE1905/9-1 is gratefully acknowledged. We like to thank Prof. Takao Mori, Dr. Jaroslav Valenta, and Dr. Naohito Tsujii, (Research Center for Materials Nanoarchitectonics (MANA), National Institute for Materials Science (NIMS), Tsukuba, Japan) for performing magnetic measurements, and Dr. Jochen Glaser (Univ. Tübingen) for helpful discussions and suggestions. C. P. R. was supported by ETH Zurich and by the European Union and Horizon 2020 through Grant No. 810451. Computational resources were provided by the Swiss National Supercomputing Center (CSCS) under project ID s1128. The authors thank Ms. Elke Nadler and Prof. Dr. Thomas Chassé (University Tübingen) for recording SEM images and EDX data.

■ REFERENCES

(1) Lemoine, P.; Halet, J.-F.; Cordier, S. Inorganic Niobium and Tantalum Octahedral Cluster Halide Compounds with Three-Dimensional Frameworks: A Review on Their Crystallographic and Electronic Structures. In *Ligated Transition Metal Clusters in Solid-state Chemistry: The legacy of Marcel Sergent*, Halet, J.-F., Ed.; Springer International Publishing, 2019; pp 143−190.

(2) Kuhn, P. J.; McCarley, R. E. Chemistry of polynuclear metal halides. I. preparation of the polynuclear tantalum halides Ta_6X_{14}. *Inorg. Chem.* **1965**, *4* (10), 1482−1486.

(3) Simon, A.; Schnering, H. G.; Wöhrle, H.; Schäfer, H. Beiträge zur Chemie der Elemente Niob und Tantal. 44. Nb_6Cl_{14} Synthese, Eigenschaften, Struktur. *Struktur. Z. Anorg. Allg. Chem.* **1965**, *339*, 155−170.

(4) Bauer, D.; Schnering, H.-G. Beiträge zur Chemie der Elemente Niob und Tantal. LXVII. Die Struktur der Tantalhalogenide Ta_6Cl_{15} und Ta_6Br_{15}. *Z. Anorg. Allg. Chem.* **1968**, *361* (5−6), 259−276.

(5) Blight, D. G.; Kepert, D. L. Electrical Properties of Niobium Tetrachloride. *Phys. Rev. Lett.* **1971**, *27* (8), 504−504.

(6) Tremel, W. $NbTe_4I$ und $TaTe_4I$, zwei neue Tellurid-Iodide mit Kettenstruktur. *Chem. Ber.* **1992**, *125* (10), 2165−2170.

(7) Gressier, P.; Guemas, L.; Meerschaut, A. Preparation and structure of ditantalum iodide octaselenide, Ta_2ISe_8. *Acta Crystallogr. Sect. B* **1982**, *38* (11), 2877−2879.

(8) Gressier, P.; Meerschaut, A.; Guemas, L.; Rouxel, J.; Monceau, P. Characterization of the new series of quasi one-dimensional compounds $(MX_4)_nY$ (M = Nb, Ta; X = S, Se; Y = Br, I). *J. Solid State Chem.* **1984**, *51* (2), 141−151.

(9) Schmidt, P. J.; Thiele, G. A New Structural Variation of Nb_3YX_7 Compounds: Monoclinic Nb_3SI_7. *Acta Crystallogr. Sect. C* **1997**, *53* (12), 1743−1745.

(10) Smith, M. D.; Miller, G. J. Tantalum-Niobium Mixing in $Ta_{3-x}Nb_xTeI_7$ ($0 \le x \le 3$). *Z. Anorg. Allg. Chem.* **2000**, *626* (1), 94−102.

(11) Smith, M.; Miller, G. J. Ta_3SBr_7 — A New Structure Type in the M_3QX_7 Family (M=Nb, Ta; Q=S, Se, Te; X=Cl, Br, I). *J. Solid State Chem.* **1998**, *140* (2), 226−232.
(12) Khvorykh, G. V.; Shevelkov, A. V.; Dolgikh, V. A.; Popovkin, B. A. Niobium thiobromide, Nb_3SBr_7, with triangle Nb_3 cluster: structure and bonding. *J. Solid State Chem.* **1995**, *120* (2), 311−315.
(13) Ströbele, M.; Glaser, J.; Lachgar, A.; Meyer, H.-J. Struktur und elektrochemische Untersuchung von Nb_3Cl_8. *Z. Anorg. Allg. Chem.* **2001**, *627* (8), 2002−2004.
(14) Haraguchi, Y.; Michioka, C.; Ishikawa, M.; Nakano, Y.; Yamochi, H.; Ueda, H.; Yoshimura, K. Magnetic−Nonmagnetic Phase Transition with Interlayer Charge Disproportionation of Nb_3 Trimers in the Cluster Compound Nb_3Cl_8. *Inorg. Chem.* **2017**, *56* (6), 3483−3488.
(15) Pasco, C. M.; El Baggari, I.; Bianco, E.; Kourkoutis, L. F.; McQueen, T. M. Tunable Magnetic Transition to a Singlet Ground State in a 2D van der Waals Layered Trimerized Kagomé Magnet. *ACS Nano* **2019**, *13* (8), 9457−9463.
(16) Sheckelton, J. P.; Plumb, K. W.; Trump, B. A.; Broholm, C. L.; McQueen, T. M. Rearrangement of van der Waals stacking and formation of a singlet state at T = 90 K in a cluster magnet. *Inorg. Chem. Front.* **2017**, *4* (3), 481−490.
(17) Grytsiuk, S.; Katsnelson, M. I.; Loon, E. G. C. P. v.; Rösner, M. Nb_3Cl_8: a prototypical layered Mott-Hubbard insulator. *npj Quantum Mater.* **2024**, *9* (1), 8.
(18) Hu, J.; Zhang, X.; Hu, C.; Sun, J.; Wang, X.; Lin, H.-Q.; Li, G. Correlated flat bands and quantum spin liquid state in a cluster Mott insulator. *Commun. Phys.* **2023**, *6* (1), 172.
(19) Meyer, H.-J. $CsNb_3Br_7S$: Synthese, Struktur und Bindungsverhältnisse. *Z. Anorg. Allg. Chem.* **1994**, *620* (5), 863−866.
(20) Grahlow, F.; Strauß, F.; Scheele, M.; Ströbele, M.; Carta, A.; Weber, S. F.; Kroeker, S.; Romao, C. P.; Meyer, H.-J. Electronic structure and transport in the potential Luttinger liquids $CsNb_3Br_7S$ and $RbNb_3Br_7S$. *Phys. Chem. Chem. Phys.* **2024**, *26* (15), 11789−11797.
(21) Ströbele, M.; Oeckler, O.; Thelen, M.; Fink, R. F.; Krishnamurthy, A.; Kroeker, S.; Meyer, H.-J. Pnictide-Capped Butterfly Cluster in the Crystal Structure of Nb_4PnX_{11} (Pn = N, P; X = Cl, Br, I). *Inorg. Chem.* **2022**, *61*, 17599.
(22) Magnaterra, M.; Attig, J.; Peterlini, L.; Hermanns, M.; Upton, M.; Kim, J.; Prodan, L.; Tsurkan, V.; Kézsmárki, I.; van Loosdrecht, P H. M.; Grüninger, M. Quasimolecular J_{tet}= 3/2 moments in the cluster Mott insulator $GaTa_4Se_8$. *Phys. Rev. Lett.* **2024**, No. 046501.
(23) Lee, J.; Jin, K.-H.; Catuneanu, A.; Go, A.; Jung, J.; Won, C.; Cheong, S.-W.; Kim, J.; Liu, F.; Kee, H.-Y.; Yeom, H. W. Honeycomb-Lattice Mott Insulator on Tantalum Disulphide. *Phys. Rev. Lett.* **2020**, *125* (9), No. 096403.
(24) Grahlow, F.; Ströbele, M.; Meyer, H.-J. CSD 2208516: Experimental Crystal Structure Determination of $CsTaBr_6$. *ICSD Commun.* **2022**.
(25) Grahlow, F.; Ströbele, M.; Meyer, H.-J. CSD 2327955: Experimental Crystal Structure Determination of Cs_2TaBr_6. *ICSD Commun.* **2024**.
(26) Yun, H.; Jang, G.-J. Dicaesium hexachlorotantalate(IV), Cs_2TaCl_6. *Acta Crystallogr. Sec. E* **2007**, *63* (1), i22−i23.
(27) Tan, P. H.; Han, W. P.; Zhao, W. J.; Wu, Z. H.; Chang, K.; Wang, H.; Wang, Y. F.; Bonini, N.; Marzari, N.; Pugno, N.; Savini, G.; Lombardo, A.; Ferrari, A. C. The shear mode of multilayer graphene. *Nat. Mater.* **2012**, *11* (4), 294−300.
(28) Zhang, L.; Wang, H.; Zong, X.; Zhou, Y.; Wang, T.; Wang, L.; Chen, X. Probing interlayer shear thermal deformation in atomically-thin van der Waals layered materials. *Nat. Commun.* **2022**, *13* (1), 3996.
(29) Sheehan, P. E.; Lieber, C. M. Friction between van der Waals Solids during Lattice Directed Sliding. *Nano Lett.* **2017**, *17* (7), 4116−4121.
(30) Grahlow, F.; Ströbele, M.; Meyer, H.-J. CSD 2202624: Experimental Crystal Structure Determination of $TaBr_4$. *ICSD Commun.* **2022**.
(31) Ströbele, M.; Meyer, H.-J. Low-temperature preparation of tungsten halide clusters: Crystal structure of the adduct $W_5Br_{12} \cdot SbBr_3$. *Russ. J. Coord. Chem.* **2012**, *38* (3), 178−182.
(32) Wendlandt, W. W.; Hecht, H. G.*Reflectance spectroscopy*; Interscience, 1966.
(33) Kubelka, P. New Contributions to the Optics of Intensely Light-Scattering Materials. *Part I. J. Opt. Soc. Am.* **1948**, *38* (5), 448−457.
(34) Kubelka, P.; Munk, F. An article on optics of paint layers. *Z. Technol. Phys.* **1931**, *12* (593−601), 259−274.
(35) Kortüm, G.; Koffer, H. Diffuse Reflexionsspektren von adsorbiertem Jod. *Ber. Bunsenges. Phys. Chem.* **1963**, *67* (1), 67−75.
(36) Kortum, G.; Lohr, J. E.*Reflectance Spectroscopy*; Springer My Copy UK, 1969.
(37) Murphy, A. B. Band-gap determination from diffuse reflectance measurements of semiconductor films, and application to photoelectrochemical water-splitting. *Sol. Energy Mater. Sol. Cells* **2007**, *91* (14), 1326−1337.
(38) López, R.; Gómez, R. Band-gap energy estimation from diffuse reflectance measurements on sol−gel and commercial TiO_2: a comparative study. *J. Sol-Gel Sci. Technol.* **2012**, *61* (1), 1−7.
(39) Zanatta, A. R. Revisiting the optical bandgap of semiconductors and the proposal of a unified methodology to its determination. *Sci. Rep.* **2019**, *9* (1), 11225.
(40) Pankove, J. I.*Optical Processes in Semiconductors*; Prentice-Hall, 1971.
(41) Hadi, M. A.; Islam, M. N.; Podder, J. Indirect to direct band gap transition through order to disorder transformation of $Cs_2AgBiBr_6$ via creating antisite defects for optoelectronic and photovoltaic applications. *RSC Adv.* **2022**, *12* (24), 15461−15469.
(42) Imran, M. M. A.; Lafi, O. A. Electrical conductivity, density of states and optical band gap in $Se_{90}Te_6Sn_4$ glassy semiconductor. *Phys. B* **2013**, *410*, 201−205.
(43) Al-Fa'ouri, A. M.; Lafi, O. A.; Abu-Safe, H. H.; Abu-Kharma, M. Investigation of optical and electrical properties of copper oxide - polyvinyl alcohol nanocomposites for solar cell applications. *Arabian J. Chem.* **2023**, *16* (4), No. 104535.
(44) Kiran Kumar, K.; Ravi, M.; Pavani, Y.; Bhavani, S.; Sharma, A. K.; Narasimha Rao, V. V. R. Investigations on the effect of complexation of NaF salt with polymer blend (PEO/PVP) electrolytes on ionic conductivity and optical energy band gaps. *Phys. B* **2011**, *406* (9), 1706−1712.
(45) Hassanien, A. S.; Akl, A. A. Electrical transport properties and Mott's parameters of chalcogenide cadmium sulphoselenide bulk glasses. *J. Non-Cryst. Solids* **2016**, *432*, 471−479.
(46) Redmer, R.; Holst, B.; Hensel, F.*Metal-to-nonmetal Transitions*; Springer, 2010.
(47) Moore, J. E. The birth of topological insulators. *Nature* **2010**, *464* (7286), 194−198.
(48) Jha, G.; Heine, T. DFTB Parameters for the Periodic Table: Part III. *Spin-Orbit Coupling. J. Chem. Theory Comput.* **2022**, *18* (7), 4472−4481.
(49) Roy, S. B.Mott insulators and related phenomena: a basic introduction. In *Mott Insulators*; IOP Publishing Ltd, 2019; pp 3−1 3−35. DOI: .
(50) Amadon, B.; Jollet, F.; Torrent, M. γ and β cerium: LDA+U calculations of ground-state parameters. *Phys. Rev. B* **2008**, *77* (15), No. 155104.
(51) Dey, M.; Singh, A.; Singh, A. K. Formation of a Small Electron Polaron in Tantalum Oxynitride: Origin of Low Mobility. *J. Phys. Chem. C* **2021**, *125* (21), 11548−11554.
(52) Hinuma, Y.; Pizzi, G.; Kumagai, Y.; Oba, F.; Tanaka, I. Band structure diagram paths based on crystallography. *Comput. Mater. Sci.* **2017**, *128*, 140−184.
(53) Lisi, S.; Lu, X.; Benschop, T.; de Jong, T. A.; Stepanov, P.; Duran, J. R.; Margot, F.; Cucchi, I.; Cappelli, E.; Hunter, A.; Tamai, A.; Kandyba, V.; Giampietri, A.; Barinov, A.; Jobst, J.; Stalman, V.; Leeuwenhoek, M.; Watanabe, K.; Taniguchi, T.; Rademaker, L.; van der Molen, S. J.; Allan, M. P.; Efetov, D. K.; Baumberger, F.

https://doi.org/10.1021/acs.inorgchem.4c02896
Inorg. Chem. 2024, 63, 19717−19727

Observation of flat bands in twisted bilayer graphene. *Nat. Phys.* **2021**, *17* (2), 189−193.
(54) Han, G. H.; Duong, D. L.; Keum, D. H.; Yun, S. J.; Lee, Y. H. van der Waals Metallic Transition Metal Dichalcogenides. *Chem. Rev.* **2018**, *118* (13), 6297−6336.
(55) Schmidt, P.; Schneiderhan, P.; Ströbele, M.; Romao, C. P.; Meyer, H.-J. Reversible Iodine Intercalation into Tungsten Ditelluride. *Inorg. Chem.* **2021**, *60* (3), 1411−1418.
(56) Gonze, X.; Amadon, B.; Antonius, G.; Arnardi, F.; Baguet, L.; Beuken, J.-M.; Bieder, J.; Bottin, F.; Bouchet, J.; Bousquet, E.; Brouwer, N.; Bruneval, F.; Brunin, G.; Cavignac, T.; Charraud, J.-B.; Chen, W.; Côté, M.; Cottenier, S.; Denier, J.; Geneste, G.; Ghosez, P.; Giantomassi, M.; Gillet, Y.; Gingras, O.; Hamann, D. R.; Hautier, G.; He, X.; Helbig, N.; Holzwarth, N.; Jia, Y.; Jollet, F.; Lafargue-Dit-Hauret, W.; Lejaeghere, K.; Marques, M. A. L.; Martin, A.; Martins, C.; Miranda, H. P. C.; Naccarato, F.; Persson, K.; Petretto, G.; Planes, V.; Pouillon, Y.; Prokhorenko, S.; Ricci, F.; Rignanese, G.-M.; Romero, A. H.; Schmitt, M. M.; Torrent, M.; van Setten, M. J.; Van Troeye, B.; Verstraete, M. J.; Zérah, G.; Zwanziger, J. W. The Abinitproject: Impact, environment and recent developments. *Comput. Phys. Commun.* **2020**, *248*, No. 107042.
(57) Perdew, J. P.; Burke, K.; Ernzerhof, M. Generalized gradient approximation made simple. *Phys. Rev. Lett.* **1996**, *77* (18), 3865.
(58) Grimme, S.; Antony, J.; Ehrlich, S.; Krieg, H. A consistent and accurate ab initio parametrization of density functional dispersion correction (DFT-D) for the 94 elements H-Pu. *J. Chem. Phys.* **2010**, *132* (15), 154104.
(59) Monkhorst, H. J.; Pack, J. D. Special points for Brillouin-zone integrations. *Phys. Rev. B* **1976**, *13* (12), 5188.
(60) Torrent, M.; Holzwarth, N. A. W.; Jollet, F.; Harris, D.; Lepley, N.; Xu, X. Electronic structure packages: Two implementations of the projector augmented wave (PAW) formalism. *Comput. Phys. Commun.* **2010**, *181* (11), 1862−1867.
(61) Hernández, J. S.; Guevara, D.; Shamshurin, M.; Benassi, E.; Sokolov, M. N.; Feliz, M. Octahedral Tantalum Bromide Clusters as Catalysts for Light-Driven Hydrogen Evolution. *Inorg. Chem.* **2023**, *62* (46), 19060−19069.

https://doi.org/10.1021/acs.inorgchem.4c02896
Inorg. Chem. 2024, 63, 19717−19727

Supplementary Information

Ta_4SBr_{11}: A cluster Mott insulator with a corrugated, van der Waals layered structure

Fabian Grahlow,[a] Fabian Strauß,[b] Patrick Schmidt,[a] Jaroslav Valenta,[c] Markus Ströbele,[a] Marcus Scheele,[b] Carl P. Romao,[d] and Hans-Jürgen Meyer[a]*

[a] Section for Solid State and Theoretical Inorganic Chemistry, Institute of Inorganic Chemistry, Auf der Morgenstelle 18, Eberhard Karls Universität Tübingen, D-72076 Tübingen, Germany

[b] Institute for Physical and Theoretical Chemistry, Auf der Morgenstelle 18, Eberhard Karls Universität Tübingen, D-72076 Tübingen, Germany

[c] International Center for Materials Nanoarchitectonics (WPI-MANA), National Institute for Materials Science, 1-2-1, Sengen, Tsukuba, Ibaraki 305-0047, Japan

[d] Department of Materials, ETH Zürich, Wolfgang-Pauli-Str. 27, 8093 Zürich, Switzerland

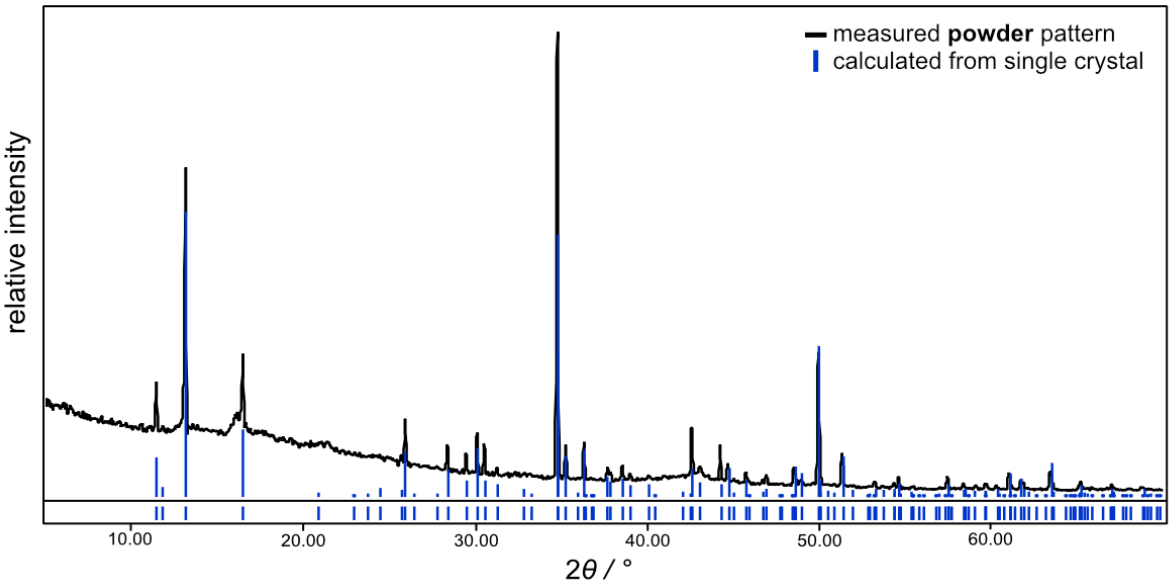

Figure S1: Powder X-Ray diffraction pattern (Cu-$K_{\alpha 1}$) of Ta_4SBr_{11}.

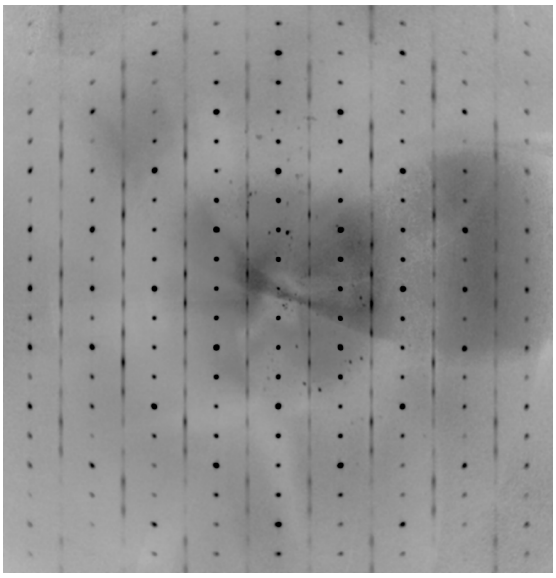

Figure S2: X-ray diffraction pattern of reciprocal lattice along the (010) direction of a Ta_4SBr_{11} single crystal, showing diffuse streaks perpendicular to (100), thereby doubling the *a* axis locally, but not in a long-range ordered way.

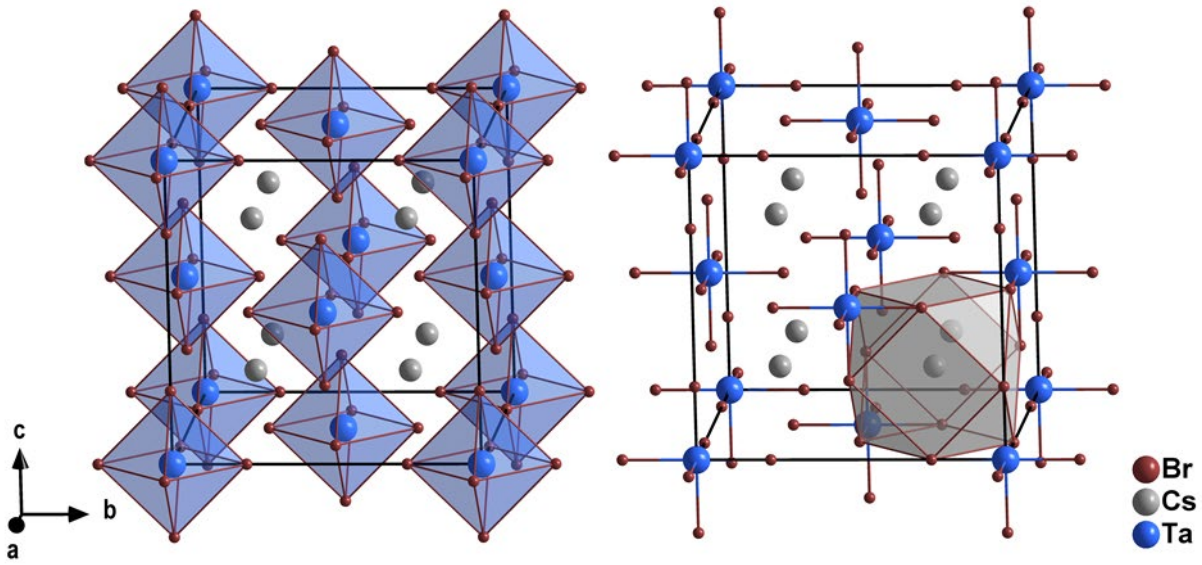

Figure S3: Unit cell of Cs_2TaBr_6. CCDC identification code: 2327955.

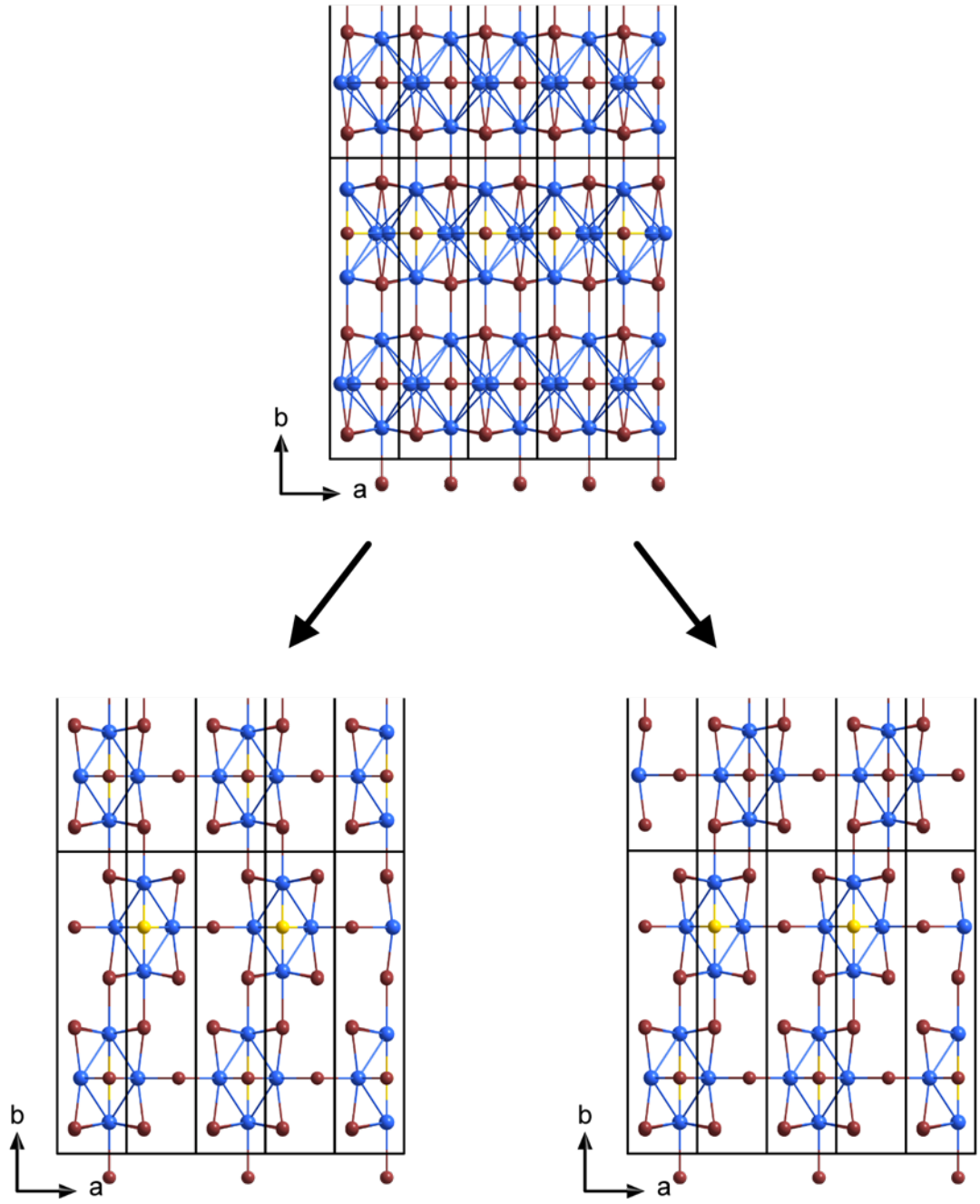

Figure S4: Two connectivity patterns (bottom left and right) within layers of Ta_4SBr_{11}, to resemble the average structure (top). Black lines emphasize the unit cell, with the original latter parameter *a* that is to be changed to 2*a*. Tantalum atoms are depicted in blue, bromine in brown and sulfur in yellow.

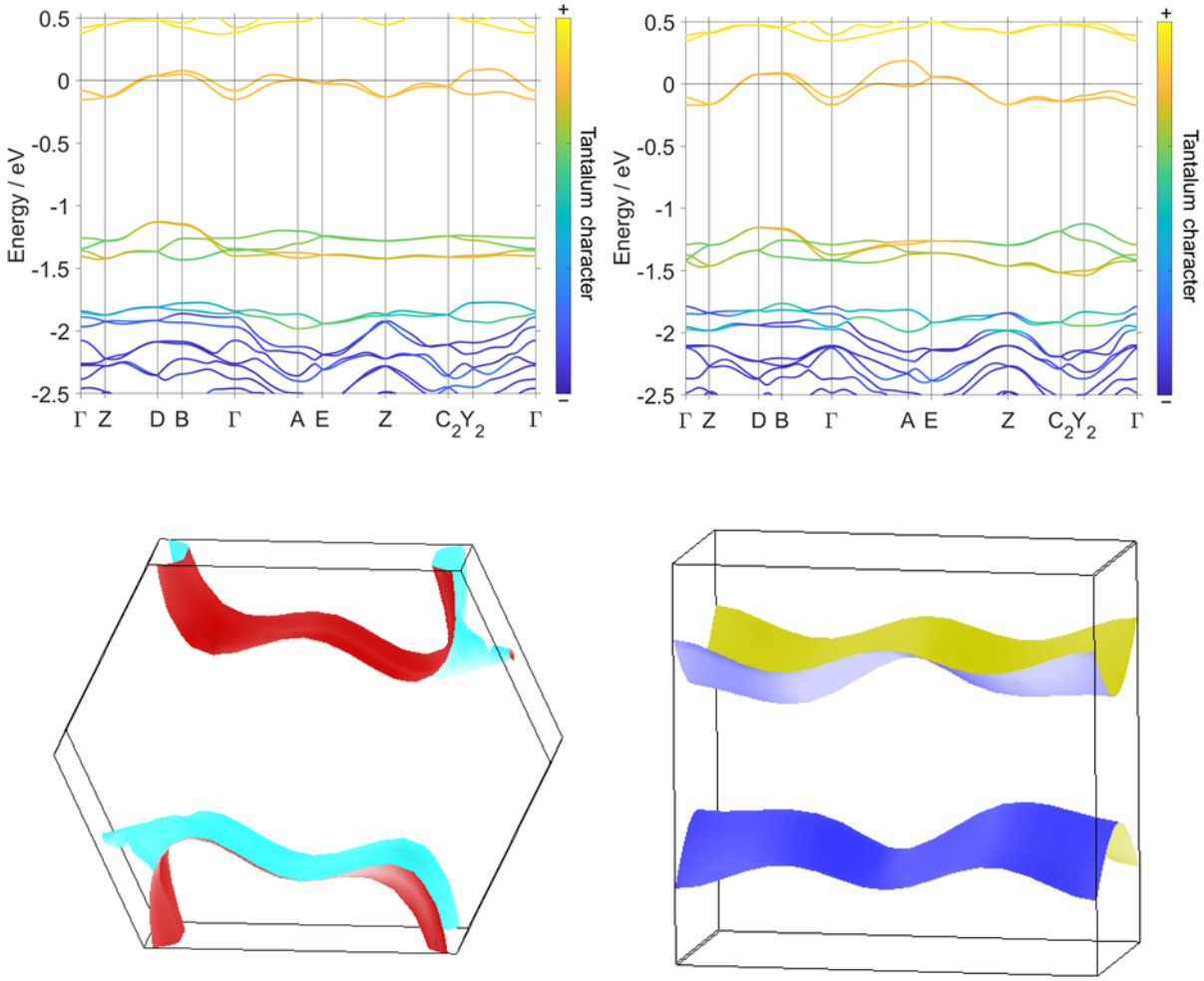

Figure S5: Electronic band structures (top) and single-band portions of the Fermi surfaces (bottom) of the staggered (left) and eclipsed (right) inter-layer arrangements of Ta_4SBr_{11}, with the kinked intra-layer arrangement. The displayed Fermi surfaces were calculated without spin-orbit coupling.

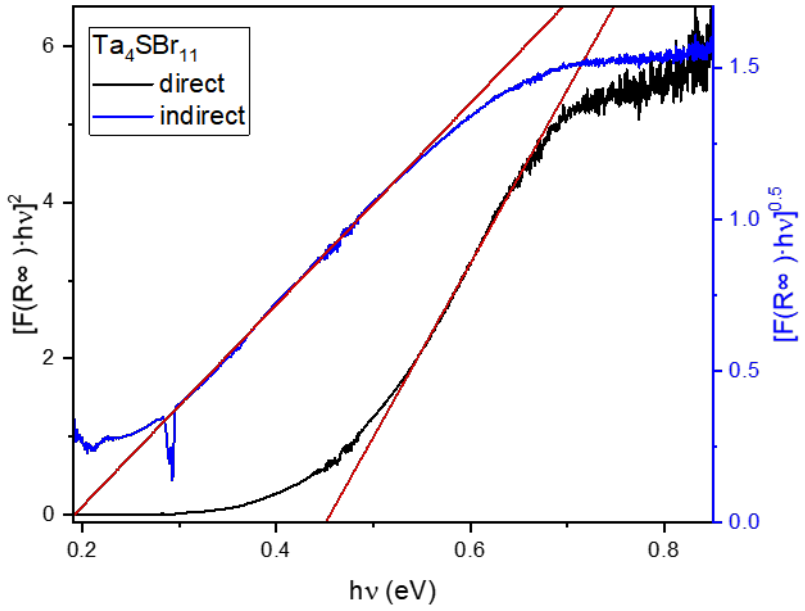

Figure S6: Tauc plot using $F(R_\infty)$ of Ta_4SBr_{11} for direct (black) and indirect (blue) gap fitting along with the linear extrapolation (red) to obtain the optical band gap (signals around 0.29 eV can be assigned to atmospheric absorption bands of CO_2).

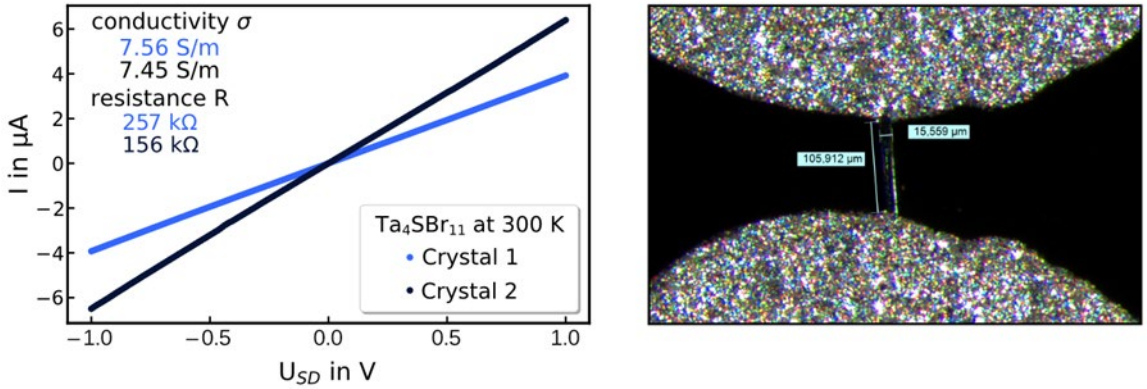

Figure S7: (left) Dark currents of Ta_4SBr_{11} Crystals on silicon with 770 nm dioxide layer at 300 K. (right) Optical micrograph of one of the contacted crystals.

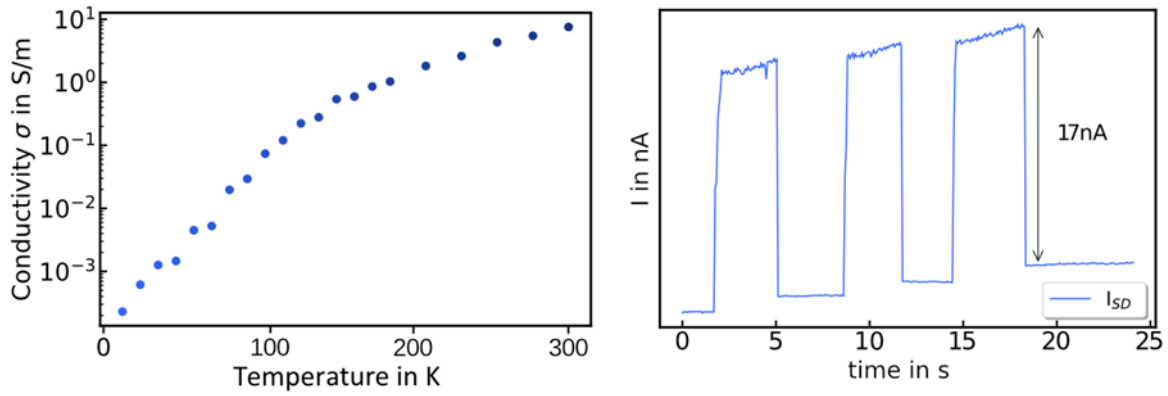

Figure S8: (left) Electrical conductivity of Ta_4SBr_{11} versus set temperature in a range of 20 K to 300 K. (right) Photoresponse of a Ta_4SBr_{11} crystal toward a 779 nm laser at 200 K (crystal 1).

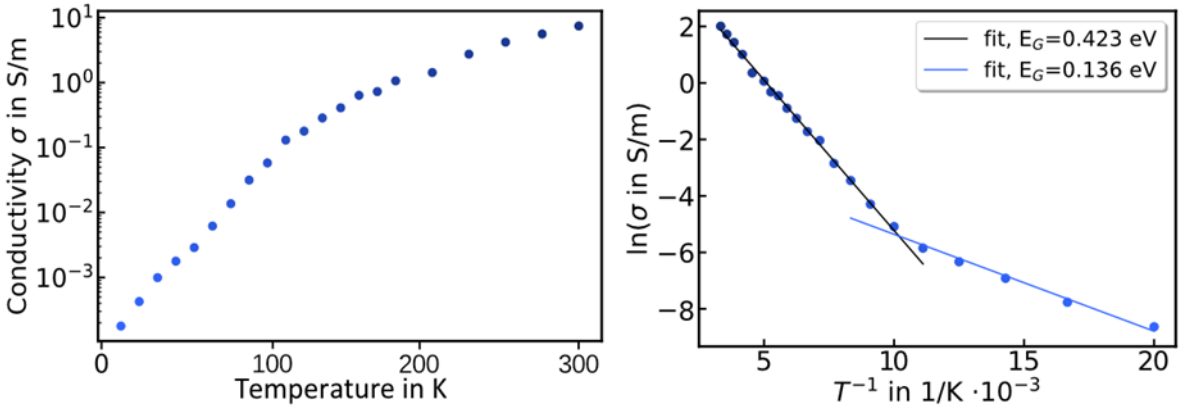

(left) Electrical conductivity of Ta_4SBr_{11} versus set temperature in a range of 20 K to 300 K. (right) Arrhenius-plot of the temperature dependent conductivity (crystal 2).

Table S1: Crystal data and structure refinement for Ta_4SBr_{11}.

Temperature	**149.9 (1) K**	**80.1 (1) K**
CCDC Identification code	2181179	2352652
Formula weight	1634.87	1634.87
Wavelength	71.073 pm	154.184 pm
Crystal system	Orthorhombic	Orthorhombic
Space group	*Pmmn*	*Pmmn*
Unit cell dimensions	a = 3.5507(1) pm b = 15.4690(4) pm c = 7.4842(3) pm	a = 3.5452(3) pm b = 15.452(1) pm c = 7.4796(4) pm
Volume	411.08(2) $Å^3$	409.74(5) $Å^3$
Z	1	1
Density (calculated)	6.604 g/cm^3	6.626
Absorption coefficient	53.356 mm^{-1}	80.239 mm^{-1}
Crystal size	0.09 × 0.01 × 0.01 mm^3	0.10 × 0.01 × 0.01 mm^3
Theta range for data collection	2.633 to 33.128°	5.727 to 77.902°
Reflections collected	21086	2824
Independent reflections	921 [R_{int} = 0.0329]	495 [R_{int} = 0.0286]
Completeness	100 % to theta = 33.128°	97.8 % to theta = 135.4°
Absorption correction	Analytical	Analytical
Refinement method	Full-matrix least-squares on F^2	
Data / restraints / parameters	921 / 0 / 37	495 / 6 / 39
Goodness-of-fit on F2	1.139	1.068
Final R indices [I > 2σ(I)]	R_1 = 0.0180, wR_2 = 0.0343	R_1 = 0.0324, wR_2 = 0.0874
R indices (all data)	R_1 = 0.0202, wR_2 = 0.0349	R_1 = 0.0343, wR_2 = 0.0887
Largest diff. peak and hole	2.043 and -2.165 $e.Å^{-3}$	1.603 and -1.796 $e.Å^{-3}$

Table S2: Atomic coordinates and equivalent isotropic displacement parameters (pm2) for Ta_4SBr_{11}. Free refinement of the site occupancy factors (SOF) of the disordered atoms was allowed. U(eq) is defined as one third of the trace of the orthogonalized U_{ij} tensor.

	SOF	x	y	z	U(eq)
Ta1	0.5	¼	0.60399(2)	0.38585(4)	8.72(7)
Ta2	0.5	0.33952(8)	¼	0.81816(4)	6.39(6)
Br1	1	¼	0.08541(3)	0.85987(5)	9.15(8)
Br2	1	¼	0.42105(3)	0.37504(6)	12.91(8)
Br3	1	¼	¾	0.92245(11)	19.23(14)
Br4	0.5	¼	¾	0.4020(3)	7.7(4)
S1	0.5	¼	¾	0.4508(7)	7.0(10)

Publication 3

Hubbard Dimer Physics and the Magnetostructural Transition in the Correlated Cluster Material Nb_3Cl_8

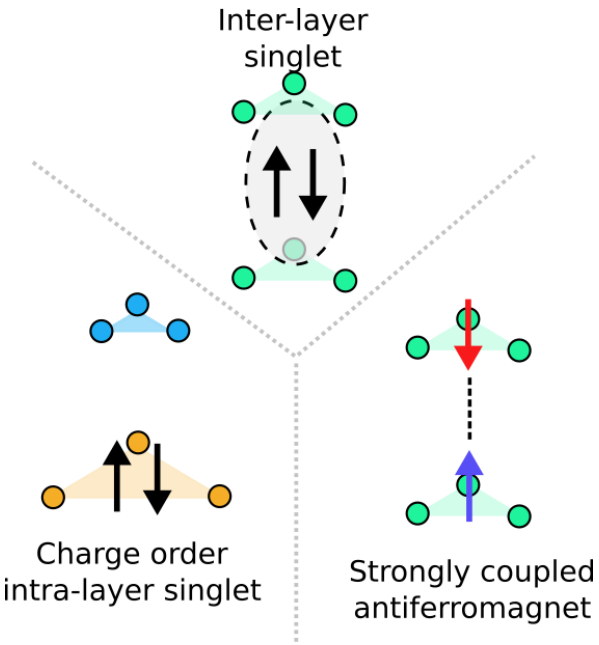

DOI: 10.48550/arXiv.2509.03988

Reproduced from

arXiv:2509.03988, **2025**, [cond-mat.str-el]

Hubbard dimer physics and the magnetostructural transition in the correlated cluster material Nb_3Cl_8

Alberto Carta,[*,†,‡,‖] Peter Mlkvik,[‡,‖] Fabian Grahlow,[¶] Markus Ströbele,[¶] H.-Jürgen Meyer,[¶] Carl P. Romao,[§] Nicola A. Spaldin,[‡] and Claude Ederer[‡]

†*PSI Center for Scientific Computing, Theory, and Data, 5232 Villigen PSI, Switzerland*
‡*Materials Theory, ETH Zürich, Wolfgang-Pauli-Strasse 27, 8093 Zürich, Switzerland*
¶*Section for Solid State and Theoretical Inorganic Chemistry, Institute of Inorganic Chemistry, Eberhard-Karls-Universität Tübingen, Auf der Morgenstelle 18, 72076 Tübingen, Germany*
§*Department of Materials, Faculty of Nuclear Sciences and Physical Engineering, Czech Technical University in Prague, Trojanova 13, Prague 120 00, Czech Republic*
‖*These authors contributed equally to this work.*

E-mail: alberto.carta@psi.ch

Abstract

We present a combined computational and experimental study of Nb_3Cl_8, a correlated layered material containing Nb trimers, through the lens of competing intra- and intercluster interactions. Different proposed explanations for its magnetostructural transition such as charge disproportionation, antiferromagnetic quenching, and interlayer singlet formation are investigated in light of the various reported low-temperature structures. Our findings rule out the previously proposed charge-disproportionation, suggest an intricate interplay between Mott physics and the formation of interlayer singlets, and also hint at a possible explanation of the observed intratrimer scissoring distortion. We suggest that the physics of Nb_3Cl_8 should be understood in the context of weakly coupled Hubbard dimers.

TOC Graphic

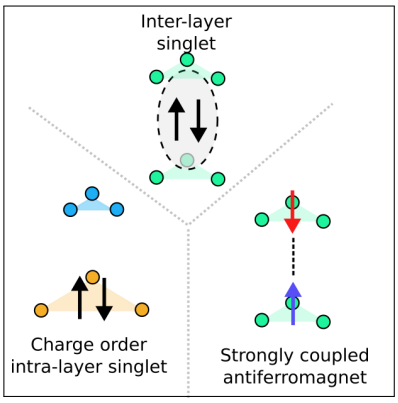

Introduction

Cluster Mott insulators are strongly correlated materials for which the traditional definition of sites on which electrons interact [1] is extended to include clusters of atoms [2–7]. The interplay of charge and spin degrees of freedom, combined with the complexity introduced by the crystal field of the cluster, makes these materials an exciting playground to explore and engineer the physics of strongly correlated systems.

Among these, Kagome cluster magnets [8] have garnered considerable interest due to the interplay between magnetism and correlation effects. In this work, we focus on Nb_3Cl_8, part of the triniobium octahalide Nb_3X_8 (X = Cl, Br, I) family. These compounds have recently been recognized as possible spin-liquid candidates [9, 10] and as obstructed-atomic-insulator candidates [11]; they exhibit thickness-dependent conductivity [12], display the anomalous valley Hall effect [13, 14], and have been showcased in Josephson diodes [15] and infrared sensors [16].

Nb_3Cl_8 is a layered 2D material consisting of Nb_3Cl_{13} cluster units [circled in Fig. 1(a)] arranged in a breathing Kagome lattice [17–19] with short intratrimer bond distances of $d_{\text{Nb-Nb}} \cong 2.8\,\text{Å}$. The nominal electronic filling of each trimer is 7 electrons and due to the octahedral coordination of the Nb ions in the cluster crystal field, the energy levels are split, leaving a lone electron in the $2a_1$ orbital [as shown in Fig. 1(d)]. In both the monolayer and bulk forms, these a_1 orbitals form narrow bands close to the Fermi level which are well separated from the rest of the electronic bands as shown in Fig. 1(e). Wannier functions corresponding to these a_1 states can be constructed as triangular molecular orbitals of mixed Nb-halogen character which are extended over the whole trimer [20] as seen in Fig. 1(f).

While the free-standing monolayer Nb_3Cl_8 has been characterized as a 2D Mott insulator both experimentally [21–23] and theoretically [9, 20, 21, 24, 25], the nature of the bulk material remains less explored. At high-temperature (HT), bulk Nb_3Cl_8 is found in the α-phase with space group $P\bar{3}m1$, with two consecutive layers stacked in an AB-staggered pattern [12, 15, 19, 26–28]. The interlayer distance is $\sim 6.8\,\text{Å}$ while the intertrimer distance (distance between centers of adjacent Nb_3 trimers in the stacking direction) is $d_{\text{HT}} \cong 7.8\,\text{Å}$ [27] [Fig. 1(b), left].

As the temperature is lowered below $T_c \cong 100\,\text{K}$, the material remains insulating but undergoes a magnetostructural transition to the low-temperature (LT) β-phase which exhibits a significant change in the stacking pattern to an -AA'-BB'-CC'- arrangement [27, 29, 30]. This results in a "dimerization" of nearest-neighbor trimers along the stacking direction [Fig. 1(b), right] [27, 30]. The newly formed pairs' intertrimer distance decreases significantly to $d_{\text{LT}} \cong 6.1\,\text{Å}$, and the calculated intertrimer hopping integral increases from 0.01 eV to $t_{\text{LT}} \cong 0.15\,\text{eV}$ [20].

The space group of the LT β-Nb_3Cl_8 is still a matter of debate, with several different candidate structures proposed. Kim *et al.* [31], for instance, report $R\bar{3}m$ symmetry corresponding to the ideal version of this stacking, which has also been observed in other members of the extended Nb_3X_8 family: $Nb_3Cl_4Br_4$ [29], Nb_3Br_8 [32], and Nb_3I_8 [31]. In the literature, lower symmetry structures such as $R3$ [27, 33] and $C2/m$ [30] have also been proposed.

The different LT phases reported in the literature could plausibly be ascribed to differing experimental conditions used to synthesize and characterize Nb_3Cl_8 and related phases. The $R3$ and $C2/m$ phases have been observed using single crystal diffraction techniques [27, 30], which are generally highly sensitive to crystallographic symmetry, whereas $R\bar{3}m$ was assigned to the LT phase using a combination of experimental and theoretical vibrational spectroscopy [31], which is a less reliable method of determining the space group. $Nb_3Cl_4Br_4$ was also observed to adopt an $R\bar{3}m$ structure at low temperature using single crystal diffraction [29].

In all cases, the structural transition is accompanied by a significant drop in the magnetic susceptibility [27, 29, 30, 33], indicating a strong quenching of the local trimer moments. Several interpretations have been proposed to explain the observed drop in magnetic suscepti-

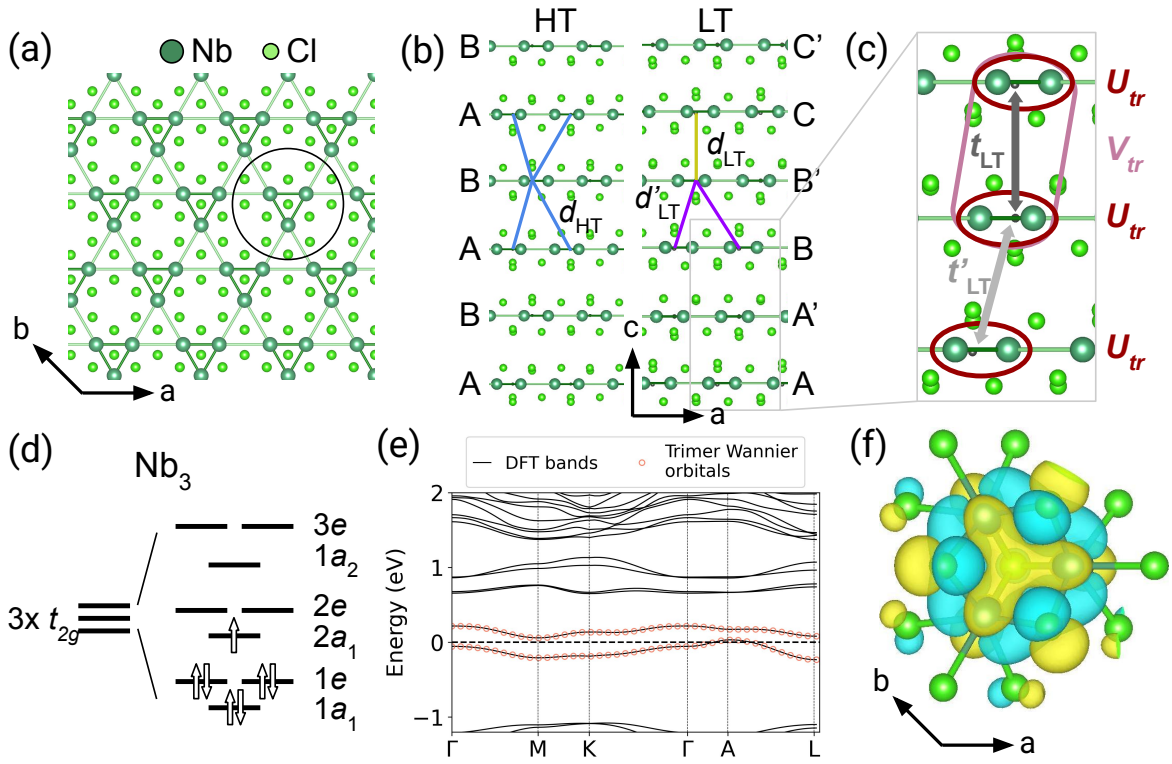

Figure 1: (a) Top view of the monolayer Nb_3Cl_8 with a trimer unit circled. (b) Side view of the bulk Nb_3Cl_8 in its HT and LT structures, showcasing the stacking and the change in distances between closest trimer centers across adjacent layers. (c) Closeup of the LT structure with the two relevant interlayer hoppings t_{LT} and t'_{LT} indicated. U_{tr} and V_{tr} represent the intra- and inter-trimer interactions considered in our calculations. (d) Energy level diagram of the Nb_3Cl_8 trimer. (e) DFT Band structure of LT bulk Nb_3Cl_8 with the Wannier bands superimposed. (f) Top view of the corresponding Wannier function for one of the trimers within an LT unit cell.

bility. Haraguchi *et al.* [27, 33] report a "breathing" effect in the Nb_3 trimers, with alternating layers of shorter and longer Nb-Nb bond lengths in the $R3$ structure from single-crystal X-ray diffraction (XRD). The authors propose charge disproportionation, $2[Nb_3]^7 \rightarrow [Nb_3]^8 + [Nb_3]^6$, leading to a formation of a singlet on the larger Nb trimers and causing a drop in the magnetic susceptibility [27].

When comparing Nb_3Cl_8 to other materials that exhibit singlet formation or charge disproportionation and subsequent structural distortions, several issues arise with the charge disproportionation model. Haraguchi *et al.* [27, 33] report bond lengths of $d_{\text{Nb1-Nb1}} = 2.801(3)$ Å and $d_{\text{Nb2-Nb2}} = 2.821(2)$ Å for the two inequivalent trimers, resulting in a notably small Nb-Nb bond-length difference of just 0.02 Å. We can compare these small distortions with other materials where metal-metal bonding is important. Vanadium dioxide (VO_2), for instance, is a material undergoing a similar paramagnetic-to-nonmagnetic transition associated with a formation of a V-V singlet state [34, 35]. VO_2 features a magnetostructural transition (coupled to a metal-insulator transition) contracting the original V-V bond by almost 10% or ~ 0.3 Å [36], roughly 15 times that observed in [27] for Nb_3Cl_8.

Moreover, using neutron diffraction, Sheckelton *et al.* [30] observe a different LT Nb_3Cl_8 structure which still exhibits the same magnetic-to-nonmagnetic transition, but has the $C2/m$ space group. This phase is characterized by an isosceles triangle geometry within the Nb_3 trimers leading to bond distances of $d_{\text{Nb1'-Nb2'}} = 2.86(2)$ Å and $d_{\text{Nb2'-Nb2'}} = 2.72(1)$ Å [30]. However, the authors ascribe the

change of intratrimer distances to secondary effects and speculate that it is the stacking of the β phase that drives a formation of singlets between different layers, causing the observed drop in susceptibility [30].

Computationally, due to the small bandwidth and thus the potential importance of local electron-electron interactions, Nb_3Cl_8 has largely been studied using a combination of density-functional theory (DFT) and dynamical mean-field theory (DMFT) [20, 21, 24, 37] or similar beyond-DFT methods [9, 38]. The bulk HT α-Nb_3Cl_8 has been labeled as a cluster-Mott insulator with many similarities to the 2D precursor material [9, 20, 21, 24], consistent with the isolated local moments of the experimentally observed HT Curie-Weiss susceptibility. For the LT β-Nb_3Cl_8 phase, most works agree on the important role of the increase in interlayer coupling [t_{LT} versus t'_{LT} in Fig. 1(c)], even though the specific proposals for the relevant physics vary.

By evaluating the role of an intratrimer Coulomb interaction correction U_{tr}, studies in bilayer LT β-Nb_3Cl_8 [21, 24] conclude that it is the competition between the interlayer hopping, t_{LT}, and intratrimer Coulomb interaction that determines whether the system is an interlayer singlet insulator or a Mott insulator, with strong interlayer antiferromagnetic fluctuations. This conclusion has been bolstered by the studies on bulk systems from Grytsiuk, Aretz *et al.* [20, 37]. The same authors also report a change from a Mott insulating hypothetical Nb_3F_8 to a weakly correlated Nb_3I_8, due to the decreasing onsite Coulomb interaction U_{tr} and the increasing interlayer hopping. Although the authors perform calculations of the experimentally observed $R3$ and the $C2/m$ structures [20], the origin and stability of the β Nb_3Cl_8 low symmetry phases with respect to the $R\bar{3}m$ phase remains unclear.

In our work, we employ both DFT+U+V [39] and DFT+DMFT [40] to assess and analyze the different mechanisms proposed for the observed magnetostructural transition using a basis of trimer-centered Wannier orbitals. The larger spatial extent of such molecular trimer orbitals in comparison to more localized atomic-like orbitals leads to a non-negligible intertrimer Coulomb repulsion V_{tr} [37]. We hence consider both types of interactions, U_{tr} and V_{tr}, and, in particular, focus on analyzing their influence on the physics of the bulk structure.

Our investigation of the different gap opening mechanism due to intra- and intercluster interactions shows a clear disagreement with the charge disproportionation picture [27, 33]. Instead, we obtain a continuous crossover between a Mott-insulating regime with strong antiferromagnetic intertrimer correlations and a band-insulator corresponding to the formation of intertrimer singlets [21, 24, 30, 37]. We conclude that the physics of Nb_3Cl_8 is well described within a picture of weakly coupled Hubbard dimers. Additionally, we also suggest a possible origin of the scissoring distortion reported in Sheckelton *et al.* [30] resulting from atomic level interactions within the trimer. We corroborate our theoretical results with an experimental investigation of the structure and properties of Nb_3Cl_8 and $Nb_3Cl_4Br_4$, and suggest that synthesis conditions influence the LT phases of $Nb_3Br_{4-x}Cl_{4+x}$ materials.

Results and discussion

Stability of the $R3$ charge ordered phase

We begin by investigating the stability of the proposed trimer breathing mode coupling to charge order as described by Haraguchi *et al.* [27, 33].

To do so, we construct molecular trimer Wannier functions from the $2a_1$ bands that lie close to the Fermi level [Fig. 1(e)] following Ref. [20]. We then perform a series of DFT+U+V calculations using these trimer orbitals as the basis, treating both the Coulomb interactions on one trimer (U_{tr}) and between adjacent trimers (V_{tr}). This is made possible by a recently developed extension of the QUANTUM ESPRESSO code [41].

The proposed breathing mode [see inset graphic in Fig. 2(c)] breaks the symmetry between the two trimers in the unit cell, leading to a difference in their onsite single-particle en-

ergies. Specifically, the energy of the long-edge trimer is lowered, while that of the short-edge trimer is raised.

In this section, we focus on spin unpolarized calculations, where the onsite occupation for spin up equals the onsite occupation for spin down, $n_{ii}^{\uparrow} = n_{ii}^{\downarrow} := n_{ii}$. The spin polarized case will be treated in the next section. In this case, the Hubbard contribution to the Kohn-Sham potential due to the onsite interaction parameter reads:

$$\Delta v_{ii}^{\sigma} = U_{\mathrm{tr}} \left(\frac{1}{2} - n_{ii} \right). \tag{1}$$

In the high-symmetry $R\bar{3}m$ structure, the two trimers are equivalent, leading to an onsite occupation of exactly $n_{ii} = 0.5$ for each one. Consequently, the potential correction from Eq. (1) is zero. A structural distortion, such as the trimer breathing mode that lowers the symmetry to $R3$, breaks this equivalence. This splitting of the trimer orbital energy levels creates a small initial occupation difference, Δn. The Hubbard U term then acts to amplify this imbalance: for the more occupied trimer ($n_{ii} > 0.5$), Δv_{ii}^{σ} is negative, favoring further filling, while for the less occupied one ($n_{ii} < 0.5$), Δv_{ii}^{σ} is positive, promoting emptying. Following the charge disproportionation model proposed by Haraguchi *et al.* [27], a sufficiently strong Hubbard U can be expected to drive this system towards a larger occupation difference, potentially approaching the limit of two electrons, thereby forming a singlet state on one trimer while completely emptying the other. However, our calculations reveal that this amplification effect is rather weak.

Our results are presented in Fig. 2(a, b) where we plot the occupation difference and the energy as a function of the trimer breathing mode amplitude which is defined as the edge difference between long-edge and short-edge trimers, for values around the calculated constrained random-phase approximation (cRPA) values $[(U_{\mathrm{tr}}, V_{\mathrm{tr}}) = (1.46, 0.38)\,\mathrm{eV}$, see Table S1]. We remark that the absolute value of the energy difference between calculations with different U_{tr} and V_{tr} is not physically meaning-

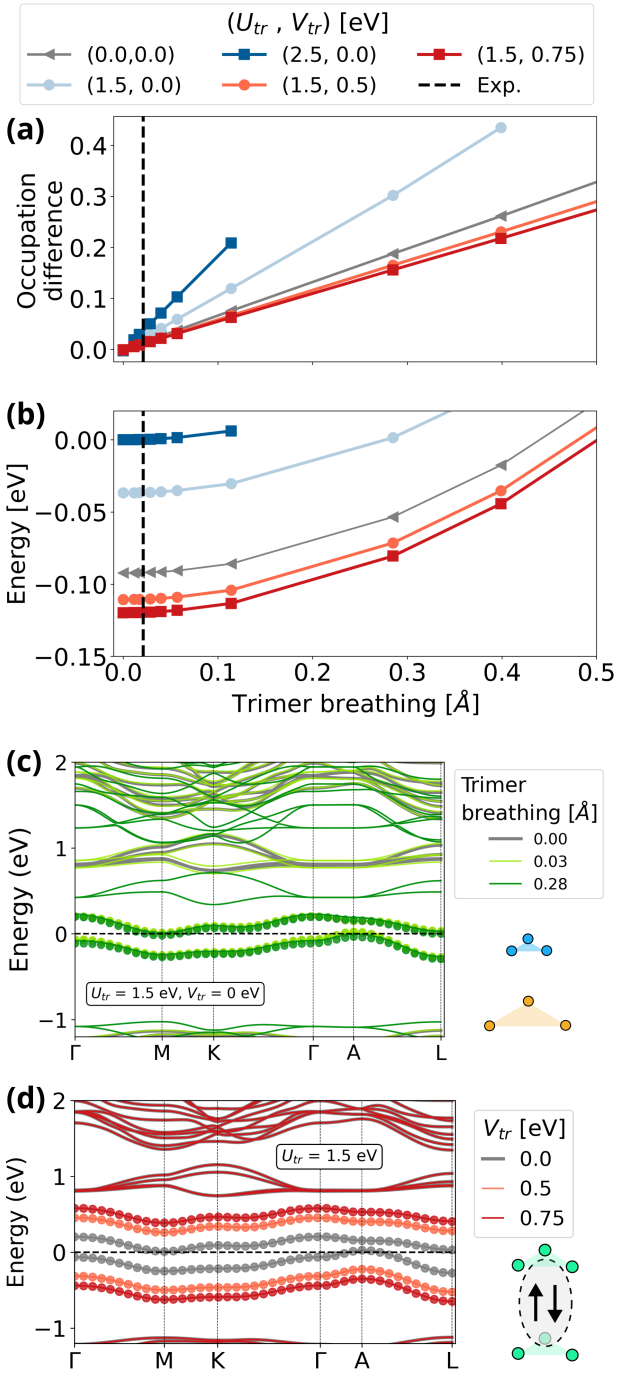

Figure 2: (a) Occupation difference between trimers and (b) total energy per unit cell as a function of the breathing mode for different values of U_{tr} and V_{tr}. The vertical dashed line indicates the experimentally reported amplitude of the breathing mode from Ref. [27]. Band structure plots for (c) three breathing mode values at $(U_{\mathrm{tr}}, V_{\mathrm{tr}}) = (1.5, 0)\,\mathrm{eV}$ and for (d) zero breathing mode ($R\bar{3}m$ structure) at three V_{tr} values for $U_{\mathrm{tr}} = 1.5$ eV. The trimer bands are highlighted with full circles.

ful, and it is only shown in Fig. 2(b) for visual clarity.

We find that for $(U_{\rm tr}, V_{\rm tr}) = (1.5, 0)$ eV, the reported $R3$ structure [27, 33] corresponds to an occupation difference of only 0.03 electrons [see vertical dashed line in Fig. 2(a)]. We observe that even at $U_{\rm tr} = 2.5$ eV (60% higher than the computed cRPA value) and at a breathing mode amplitude of 0.4 Å (20 times the experimental value), the occupation difference remains smaller than 0.4 electrons. Furthermore, we observe that the energy minimum consistently occurs at zero breathing mode, which corresponds to the higher symmetry $R\bar{3}m$ structure [Fig. 2(b)].

By examining the band structure at different breathing mode amplitudes [Fig. 2(c)], we observe minimal changes in the bands near the Fermi level as the breathing mode amplitude increases, and the material remains metallic. This finding is not consistent with the experimentally observed insulating behavior.

To investigate this point further we perform calculations where in addition to the $+U$ correction we include an intersite term $V_{\rm tr}$. The $+V$ correction essentially modifies the effective hopping between neighboring sites by adding an intersite potential [39]:

$$\Delta v_{ij}^{\sigma} = -V_{\rm tr} n_{ji}^{\sigma} \quad . \tag{2}$$

Here n_{ji}^{σ} is the off-diagonal intertrimer component of the density matrix which is a measure of the intersite hybridization.

Upon including $V_{\rm tr}$ [light red and red lines in Fig. 2(a, b)], we observe a further suppression of the occupation difference between trimers. This is accompanied by an opening of a band gap [Fig. 2(d)], the nature of which will be discussed more in detail in the next section.

Consequently, based on our DFT+U+V calculations, the charge-ordered phase accompanied by a trimer breathing mode as proposed by Haraguchi *et al.* [27] appears to be energetically unfavorable. We therefore rule out the charge disproportionation mechanism as explanation for the observed magnetic-nonmagnetic transition in Nb_3Cl_8.

Origin of the quenched magnetism in the $R\bar{3}m$ phase

We now consider different possible explanations of the low susceptibility observed in β-Nb_3Cl_8. In this section, we study separately the effects of the interaction terms $U_{\rm tr}$ and $V_{\rm tr}$, allowing for spin-polarization in the system.

As previously mentioned, with no spin-polarization, one would expect the $+U$ correction to promote charge polarization in one of the trimer orbitals. In spin-polarized calculations instead, the $+U$ correction can favor the formation of an onsite magnetic moment on the Nb_3 molecular orbital. This is because the potential shift $\Delta v_{ii}^{\sigma} = U_{\rm tr}\left(\frac{1}{2} - n_{ii}^{\sigma}\right)$ for site i and spin σ, promotes either fully occupied or completely empty spin channels on each orbital. So, at strong U, one would expect for one trimer orbital one spin channel σ to be completely occupied $n_{ii}^{\sigma} \sim 1$ and the opposite spin channel $\bar{\sigma}$ to be empty $n_{ii}^{\bar{\sigma}} \sim 0$, which corresponds to the formation of a local magnetic moment on the trimer.

In Fig. 3(a, b), we show the average onsite trimer moment $|n_{ii}^{\uparrow} - n_{ii}^{\downarrow}|$ and the magnitude of the off-diagonal occupation matrix element n_{ij}^{σ}, respectively, as a function of $U_{\rm tr}$ and $V_{\rm tr}$. In Fig. 3(c), we show the band structure for fixed $V_{\rm tr}$ and changing $U_{\rm tr}$.

Two competing tendencies emerge: a strong onsite Coulomb interaction $U_{\rm tr}$ favors the development of antiferromagnetically aligned local magnetic moments on the Nb_3 sites [Fig. 3(a)], suppressing any intersite bonding [$n_{ij}^{\sigma} \to 0$ in Fig. 3(b)].

This local moment formation leads to a band gap opening [Fig. 3(c)] and the strong antiferromagnetic correlations between adjacent trimers could be responsible for the suppression of the magnetic susceptibility [20]. We underline that we are not arguing for the presence of long-range antiferromagnetic order in the material. Rather, we argue that in the strong $U_{\rm tr}$ regime nearest neighboring trimer orbitals could show strong antiferromagnetic correlations, as schematically depicted in the inset in Fig. 3(c). Conversely, a dominant intersite Coulomb interaction $V_{\rm tr}$ promotes the for-

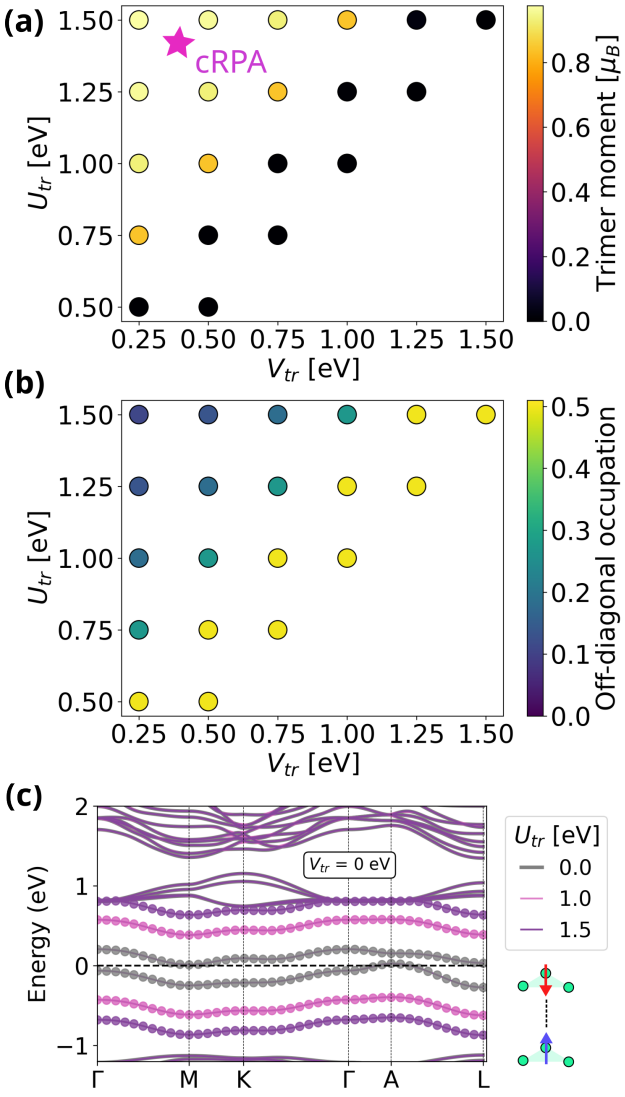

Figure 3: (a) Absolute value of the trimer moment and (b) intertrimer occupation as a function of U_{tr} and V_{tr}. Star indicates the cRPA values. (c) Band structure within spin-polarized DFT+U+V with antiferromagnetically aligned trimer magnetic moments for three U_{tr} values for $V_{\mathrm{tr}} = 0$. Bands corresponding to the trimer orbitals are highlighted with circles. All calculations are performed for the $R\bar{3}m$ structure (no trimer breathing mode).

mation of bonding-antibonding states between trimers ($n^{\sigma}_{ij} = 0.5$) [Fig. 3(b)] and also leads to the formation of a band gap [as was previously shown in Fig. 2(d)], which in this case is related to the large bonding-antibonding splitting. Since two electrons per dimer would then occupy the lower-lying bonding state, forming a nonmagnetic singlet [inset in Fig. 2(d)], this scenario would also be compatible with a drop in magnetic susceptibility.

Our cRPA calculations for the trimer molecular orbitals, in good agreement with the findings of Grytsiuk, Aretz *et al.* [20, 37], suggest that Nb_3Cl_8 lies closer to the strong U_{tr} regime.

To summarize, our calculations indicate that a change in stacking from $P\bar{3}m1$ to $R\bar{3}m$ is sufficient to explain the low magnetic susceptibility observed in β-Nb_3Cl_8, without the need to introduce any further symmetry-lowering distortions, in agreement with previous works [20, 37].

Dynamical effects in the $R\bar{3}m$ phase

So far, our treatment of the physics in Nb_3Cl_8 has been based on a static mean-field treatment of interaction effects, which highlights the crucial role of both onsite and intersite interactions, particularly within dimerized units of Nb_3 molecular orbitals. To move beyond this static mean-field approximation and capture dynamical effects, we now employ DFT+DMFT.

We construct a DMFT impurity problem for the $R\bar{3}m$ structure using a cluster of two neighboring molecular trimer orbitals, as first introduced in Aretz *et al.* [37], and explore the behavior of the system under a variety of interaction parameters, in particular exploring the nature of the insulating state.

This approach is well suited for systems like Nb_3Cl_8 due to the strong onsite and intersite interactions U_{tr} and V_{tr}, a significant intertrimer hopping along the stacking direction ($t_{\mathrm{LT}} = 0.13\,\mathrm{eV}$), and comparatively weaker hybridization between the dimerized cluster and the rest of the Nb_3 molecular orbitals ($t_{\text{in-plane}} = 0.02\,\mathrm{eV}$). These considerations allow us to draw significant analogies between the physics of the Nb_3X_8 family and the so-called *Hubbard dimer*, a model system consisting of two interacting sites with one orbital each.

For two electrons in the Hubbard dimer model (*i.e.* at half filling), the gap, E_g, in the excitation spectrum between the highest occupied and lowest unoccupied states of the Hubbard

dimer, is dependent on the three parameters that define the model, the intersite hopping t, the onsite U and the intersite V interaction parameters [42]:

$$E_g = -2t + V + \sqrt{(U-V)^2 + 16t^2}. \quad (3)$$

In general the (unnormalized) ground state of such a model system $|\psi_0^{\text{dimer}}\rangle$ can be written as:

$$\begin{aligned} |\psi_0^{\text{dimer}}\rangle = A(|\uparrow,\downarrow\rangle - |\downarrow,\uparrow\rangle) \\ +(|\uparrow\downarrow,0\rangle + |0,\uparrow\downarrow\rangle), \end{aligned} \quad (4)$$

where $A = 4t/[\sqrt{(U-V)^2+16t^2} - (U-V)]$. Here, $|\uparrow,\downarrow\rangle$ corresponds to a state with an up-spin electron on the first and a down spin electron on the second site, whereas $|\uparrow\downarrow,0\rangle$ corresponds to double occupation of the first site, and analogous for the other states in Eq. (4).

For $U = V$, $A = 1$ the ground state can be described by a single Slater determinant expressed in the bonding-antibonding basis, and corresponds to the bonded state of two trimer sites. The opposite limit, $U \gg V$, $A \to \infty$, corresponds to the suppression of double occupancies and the maximally correlated state, the Heitler-London limit.

In Fig. 4(a-d), we depict the dependence of various properties of β-Nb_3Cl_8 on both U_{tr} and V_{tr}. We show the band gap [Fig. 4(a)] obtained from the spectral function, and the quasiparticle weight [Fig. 4(b)] defined from the frequency dependence of the self-energy. In addition, we also show the off-diagonal occupation matrix element [Fig. 4(c)], and the probability of double occupancy on one of the Nb_3 molecular orbitals [Fig. 4(d)]. The latter is obtained from analyzing the probability of the various multiplet states occurring in the two site cluster, based on the statistics from the employed quantum Monte Carlo solver.

We obtain an insulating solution for any value of the tested U_{tr} and V_{tr} parameters, except in the vicinity of $U_{\text{tr}} = V_{\text{tr}} = 0$ [Fig. 4(a)], with the size of the band gap depending on both U_{tr} and V_{tr}. At high U_{tr} and small V_{tr}, the insulator exhibits hallmark features of a Mott state, such as a vanishing quasiparticle weight [Fig. 4(b)]. By increasing $V_{\text{tr}}/U_{\text{tr}}$, the quasiparticle weight rises, reaching $Z = 1$ at $U_{\text{tr}} = V_{\text{tr}}$, where the system is a band insulator. This is accompanied by a gradual increase in the off-diagonal occupation from $V_{\text{tr}} = 0$ to the maximum 0.5 at $U_{\text{tr}} = V_{\text{tr}}$, with the double occupation probability changing in a similar way [Fig. 4(c, d)]. At small $V_{\text{tr}}/U_{\text{tr}}$, our results show a marked suppression of double occupancies highlighting the localization of a single electron per Nb_3 site. The multiplet analysis can also clarify the relative spin orientation of the Nb_3 sites. Even at small $V_{\text{tr}}/U_{\text{tr}}$, configurations with spins aligning in opposite directions between trimers have high probability, while configurations where spins point in the same direction on both trimers are suppressed.

The analogies to the Hubbard dimer are thereby particularly evident. We can identify the band insulator observed on the diagonal in Fig. 4(a-d) with the $A = 1$ bonding regime and the Mott insulator at low $V_{\text{tr}}/U_{\text{tr}}$ with the correlated high A regime. Importantly, our results indicate a continuous crossover between the two different insulating states, which is reflected in all observables examined.

Finally, we further exemplify this evolution by showing the spectral function at a fixed value of U_{tr} and different values of V_{tr}, projected on suitably constructed bonding and antibonding dimer orbitals [Fig. 4(e, f)]. We observe that the two peaks change their character with increasing V_{tr}. The lower peak becomes predominantly bonding, while the upper peak becomes more antibonding as V_{tr} increases. Due to inherent difficulties in the analytic continuation and the large size of the gap, the spectral function shows smooth peaks across the spectrum, and we are not able to resolve finer spectral details such as the splitting of the Hubbard peaks that was observed, e.g., in the work of Aretz *et al.* [37].

These results provide evidence that the physics of the $R\bar{3}m$ phase of Nb_3Cl_8 and the Nb_3X_8 family in general can be described by dimers of Nb_3 molecular units, which are weakly coupled to each other. These findings support the results from the previous sections and indicate the presence of strong local antiferromagnetic correlations which could be

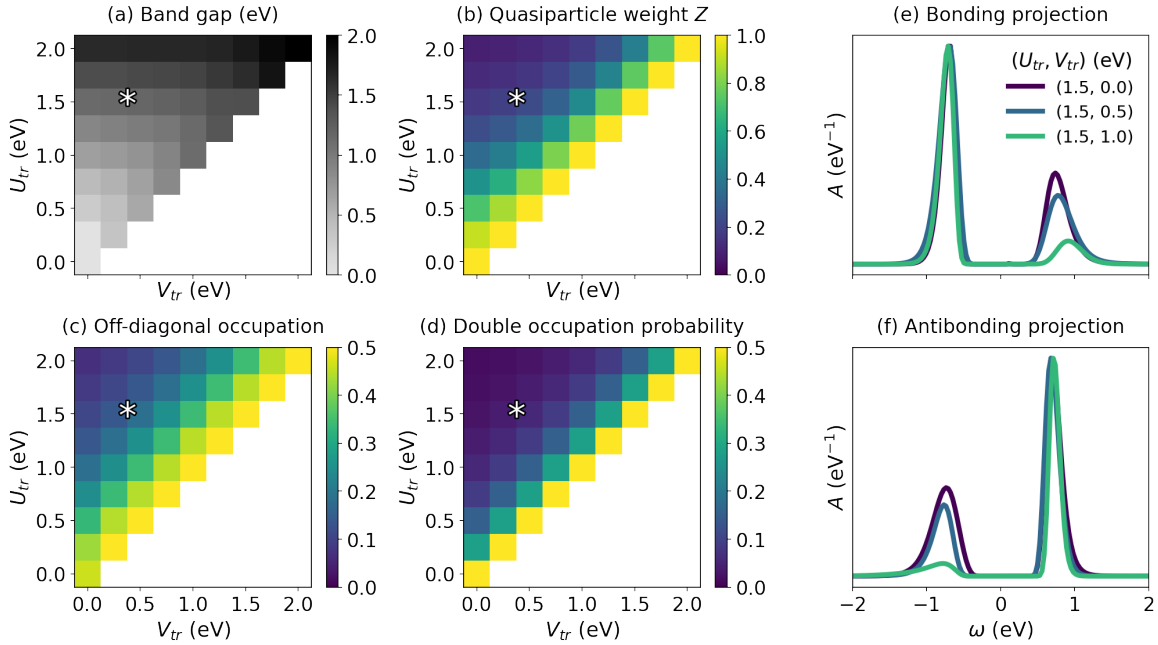

Figure 4: Observables of the $R\bar{3}m$ Nb_3Cl_8 cluster from DFT+DMFT as a function of U_{tr} and V_{tr}. The cRPA values for Nb_3Cl_8 are shown with a star. (a) Band gap. (b) Quasiparticle weight, Z. (c) Off-diagonal occupation. (d) Double occupation probability. (e) Spectral function projected onto the bonding and (f) antibonding combination of the individual trimer orbitals across the (U_{tr}, V_{tr}) spectrum.

ultimately responsible for the suppression of the magnetic susceptibility in β-Nb_3Cl_8, as has been suggested previously [37]. The additional analysis of the U and V dependence sheds light on the evolution of this state under stronger electronic correlation effects. Moreover, we explicitly demonstrate a continuous crossover between the Mott and singlet (band) insulating states, in line with recent theoretical proposals [24, 43, 44]. The cRPA calculations indicate that Nb_3Cl_8 itself lies closer to the Mott limit, while the rest of the family lies closer to the singlet (band) insulating limit [see Table S1 and Fig. S1 for the rest of the family].

Further symmetry lowering in the β-Nb_3Cl_8 phase

We will now consider the case of a system very close to the Mott regime, with relatively little intertrimer hybridization as a starting point to understand further symmetry lowering effects, analyzing the physics within the Nb_3 unit. By incorporating all six bands between 1.2 eV and -0.5 eV [as shown in Fig. 5(b), corresponding to the $2a_1$ and $2e$ levels in Fig. 1(d)] in the wannierization, we construct a basis set consisting of one d atomic orbital per Nb atom, yielding a total of three d orbitals per Nb_3 trimer [as shown in Fig. 5(a)] and six d orbitals per unit cell [45].

Using cRPA, we calculated the relevant, now atomic, interaction parameters [Table S2]: the onsite interaction on a single Nb atom, $U_{\mathrm{at}} = 2.3$ eV, the intratrimer interaction between two different Nb atoms inside the same trimer, $V_{\mathrm{at}}^{\mathrm{intra}} = 1.36$ eV, and the intertrimer interaction between neighboring trimers, $V_{\mathrm{at}}^{\mathrm{inter}} = 0.39$ eV.

Leveraging our previous finding that the intertrimer occupation is small in the Mott regime, leading to electron localization on the trimer, we neglect the interaction across trimers ($V_{\mathrm{at}}^{\mathrm{inter}}$) for simplicity. We then perform DFT+DMFT calculations considering two separate impurity problems, with each impurity containing the three Nb d orbitals, including U_{at} and $V_{\mathrm{at}}^{\mathrm{intra}}$ in the interaction Hamiltonian [see Eq. (S4) for further details].

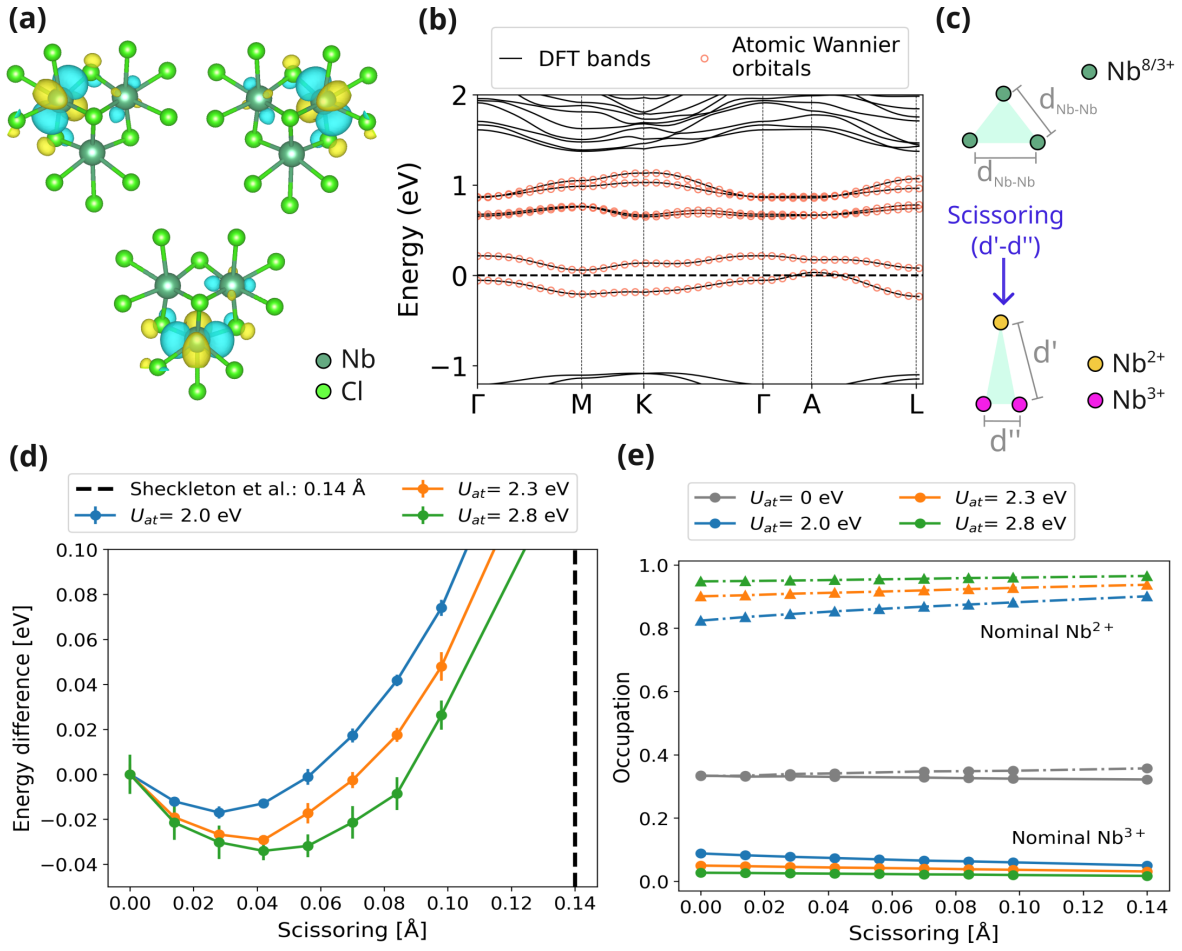

Figure 5: (a) Top view of the three atomic Wannier functions per trimer. (b) DFT band structure with the bands recalculated from the atomic Wannier model. (c) Schematic of the scissoring distortion within one trimer, connecting the $R\bar{3}m$ structure to the $C2/m$. (d) Energy difference per unit cell as a function of the scissoring amplitude. The black dashed line corresponds to the scissoring amplitude reported in Ref. [30]. (e) Occupation of the inequivalent Nb atoms inside one trimer. The solid lines correspond to the symmetry-equivalent nominal Nb^{3+} sites, while the dash-dotted line corresponds to the nominal Nb^{2+} site.

While DFT calculations distribute the single electron per each trimer equally among the Nb atoms, leading to an oxidation state of $Nb^{8/3+}$, in our charge self-consistent DFT+DMFT calculations we observe that for realistic values of $(U_{\mathrm{at}}, V_{\mathrm{at}}^{\mathrm{intra}})$ most of the charge concentrates on one of the Nb atoms [see Fig. 5(e) for 0.0 Å scissoring]. This charge ordering within the trimer changes the nominal oxidation states of the three Nb atoms and renders them inequivalent: for every Nb_3 trimer we obtain one nominal Nb^{2+} site and two empty Nb^{3+} sites.

Our results also indicate that the structure accommodates this change in oxidation state within each trimer by elongating the bond length d' between the nominal Nb^{3+} and Nb^{2+} atoms and contracting the bond length d'' between the two Nb^{3+} atoms [see Fig. 5(c)]. The difference, $d' - d''$, is termed *scissoring*. This scissoring distortion lowers the symmetry from $R\bar{3}m$ to $C2/m$, precisely matching both our own (see next section) and previous experimental work by Sheckelton *et al.* [30].

This can be seen from Fig. 5(d, e), where we show the energy per unit cell and the occupation of the nominal Nb^{2+} and Nb^{3+} as a function of the scissoring mode. We consider various values of U_{at}, while maintaining a constant ratio of $V_{\mathrm{at}}^{\mathrm{intra}}/U_{\mathrm{at}} = 0.24$ (corresponding to our cRPA results). However, it is worth not-

ing that our results exhibit weak dependence on the value of $V_{\mathrm{at}}^{\mathrm{intra}}$, and similar outcomes can be obtained by setting $V_{\mathrm{at}}^{\mathrm{intra}} = 0$.

For $U_{\mathrm{at}} = 0\,\mathrm{eV}$, the scissoring changes the occupation of the Nb atoms only slightly [Fig. 5(e), gray line], and the system always relaxes back to $R\bar{3}m$ symmetry. For all finite values of U_{at} considered, the system shows strong electron charge concentration on the nominal Nb^{2+} atom [Fig. 5(e), colored lines], and an energy minimum at a finite scissoring distortion [Fig. 5(d)]. As U_{at} increases, the energy minimum deepens and shifts towards a larger scissoring amplitude, while the occupation of the Nb^{2+} atom becomes closer to 1.

Compared to the results of Sheckelton *et al.* [30], our calculated equilibrium scissoring amplitude is markedly smaller. For $U_{\mathrm{at}} = 2.3$ eV [orange solid line in Fig. 5(d)], we find ∼0.04 Å, versus 0.14 Å reported in Ref. [30] [indicated by the vertical black line in Fig. 5(d)].

We also note that comparable results can be obtained through simpler DFT+U calculations, utilizing standard orthonormalized atomic orbitals as implemented in QUANTUM ESPRESSO [46]. If one starts an atomic relaxation with a small scissoring distortion and initializes the entire magnetic moment on a single Nb atom per Nb_3 trimer (and ensuring that the two magnetic Nb atoms in a unit cell containing two trimers are initialized with opposite magnetization), then for realistic values of the Hubbard U parameter, the system relaxes to $C2/m$ symmetry. This $C2/m$ phase is lower in energy than the antiferromagnetic $R\bar{3}m$ phase, where the magnetization is uniformly spread over the trimer, and it exhibits a scissoring mode amplitude similar to that found in our DFT+DMFT calculations, with most of the trimer's magnetization concentrated on the nominal Nb^{2+} atom.

In this section, we have demonstrated the possibility of additional ordering in β-Nb_3Cl_8 arising from the internal structure of the Nb_3 unit. Since the amplitude of the scissoring distortion is dependent on the value of U_{at}, and given that intertrimer bonding components become more relevant for other members of the Nb_3X_8 family, the approximation of being deep in the Mott state may break down in those cases. We would then expect this scissoring tendency to be less pronounced across the rest of the series, which aligns with experimental observations, having previously found the $C2/m$ phase only in Nb_3Cl_8. Hence, we now turn to our experimental results for Nb_3Cl_8 and the mixed $Nb_3Cl_4Br_4$ compound.

Experimental

Crystallography. In order to validate the results of our computational investigation of Nb_3Cl_8, and to attempt to understand the origins of the differing LT phases reported in the literature, we have synthesized Nb_3Cl_8 and $Nb_3Cl_4Br_4$ and characterized their crystallographic structure and electronic properties. Our samples of Nb_3Cl_8 were determined by single crystal XRD to adopt the HT $P\bar{3}m1$ phase at 100 K, the lowest temperature at which we could perform these measurements. Magnetic susceptibility measurements (Fig. S5) on a single crystal show the phase transition to occur below 100 K on cooling and slightly above 100 K on heating, and our finding of the HT phase at 100 K is therefore ascribed to hysteresis of the phase transition.

Therefore, in order to observe the LT phase, we prepared $Nb_3Br_{4-x}Cl_{4+x}$, which was determined to have an increased phase transition temperature by Pasco *et al.* [29]. However, whereas the authors observed a LT $R\bar{3}m$ phase, we found the LT structure to adopt $C2/m$ (Table 1, Fig. 6), indicating that the space group of LT $Nb_3Cl_4Br_4$, like that of LT Nb_3Cl_8, possesses some ambiguity.

Notably, our synthetic method, which employed only elemental Nb, $NbCl_5$ and $NbBr_5$ as reagents, follows that of Sheckelton *et al.* [30], who found the $C2/m$ phase in Nb_3Cl_8 at low temperatures. In contrast, synthesis using a transport agent such as NH_4Cl or $TeCl_4$ were reported to yield a LT $R\bar{3}m$ phase [29, 31], whereas reports of the $R3$ phase are associated with flux growth in $PbCl_3$ followed by soaking in hot water [27, 33]. These associations suggest that the precise LT phase adopted by Nb_3Cl_8 and $Nb_3Br_{4-x}Cl_{4+x}$ could be determined by the synthetic conditions. In particular, tellurium

Table 1: Selected crystallographic data of $Nb_3Br_{4-x}Cl_{4+x}$ above and below the transition temperature.

Formula*	$Nb_3Br_{3.7}Cl_{4.3}$	$Nb_3Br_{3.8}Cl_{4.2}$
CCDC number	2364410	2365009
Temperature	270.0(1) K	100.0(1) K
Crystal system	trigonal	monoclinic
Space group	$P\bar{3}m$	$C2/m$
Wavelength	154.184 pm	71.037 pm
Radiation type	Cu-K_α	Mo-K_α
Residual factor (R_1)	0.0350	0.0350
Residual factor (wR_2)	0.0903	0.0909

*The composition variation is within the synthesis and refinement error margin, and is considered as $Nb_3Br_4Cl_4$.

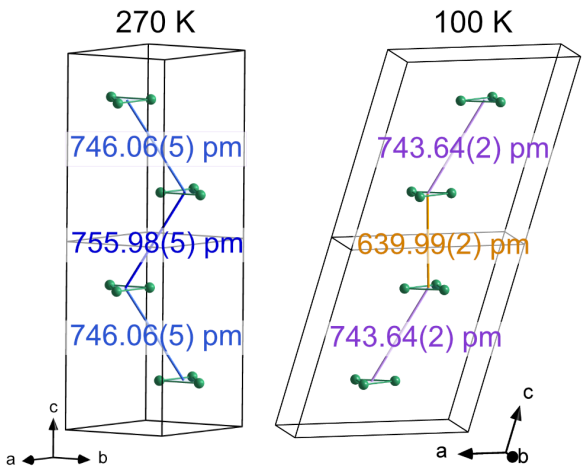

Figure 6: Stacking arrangement and distances of Nb_3 clusters (green triangles) in $Nb_3Br_{4-x}Cl_{4+x}$ as determined from single crystal X-ray diffraction data at 270 K (left) and 100 K (right). Chloride and bromide ions are omitted for clarity.

has been reported to incorporate itself into the Nb_3Cl_8 structure by capping Nb_3 triangles [47], and the introduction of defects has been suggested to trap Nb_3Br_8 in its HT phase [29]; a similar effect related to the introduction of impurities from the transport agent could push the material into the $R\bar{3}m$ phase, which is more closely related to the HT $P\bar{3}m1$ phase than the $C2/m$ is.

The changes between trimers in adjacent layers in $Nb_3Cl_4Br_4$ following the phase transition can be readily seen in the single-crystal XRD refinements. At 270 K, the intertrimer distances are at 755.98(5) pm and 746.06(5) pm (Fig. 6, left). In the low temperature structure (at 100 K), these distances alternate between 639.99(2) pm and 743.64(2) pm (Fig. 6, right), leading to the stacking shift (Fig. 1b) which modifies the intercluster interactions (Fig. 1c).

At 270 K, in the $P\bar{3}m1$ phase, the Nb–Nb distances within a cluster form equilateral triangles with bond lengths of 284.97(6) pm (Fig. 7, top). In the low-temperature $C2/m$ phase at 100 K, the clusters adopt an isosceles triangular arrangement, with one Nb–Nb bond measuring 284.61(8) pm and the other two at 284.45(8) pm (Fig. 7, bottom). The asymmetry arises due to the unambiguous loss of 3-fold rotational symmetry upon cooling, but the overall change in bond lengths remains very small, to the point where one short and two long Nb–Nb bonds is possible within the experimental uncertainty. The difference in Nb–Nb bond lengths is much smaller in $Nb_3Cl_4Br_4$ than was reported by Sheckelton *et al.* in Nb_3Cl_8 [30]. According to our computational results discussed in the previous section, the change in the stacking sequence observed in Fig. 6 is driven by intertrimer interaction, while the symmetry reduction to $C2/m$, which removes the 3-fold rotation axis and allows the Nb–Nb bond lengths to differ, is likely a secondary effect driven by intratrimer interactions.

Magnetic measurements. We conducted magnetic measurements on Nb_3Cl_8 to observe the phase transition, as this occured below the minumum temperature at which we could perfom crystallographic measurements. We see a similar phase transition temperature (*ca.* 100 K) and degree of hysteresis (Fig. S5) to previous reports of single crystals of Nb_3Cl_8 [27, 30, 31]. However, unlike Haraguchi *et al.* [27],

who observed this transition only in single crystals, we were able to detect a magnetic phase transition in both single crystal and powder samples (Fig. S6). In comparison to the single crystal sample, the powder sample displays an increased hysteresis, and a stronger temperature dependence of the paramagnetic response below the transition temperature. This temperature dependence leads to suppression of the paramagnetism near the transition temperature upon heating, a phenomenon also observed in assemblages of single crystals [29], suggesting that inter-grain interactions affect the magnetic properties of Nb_3Cl_8.

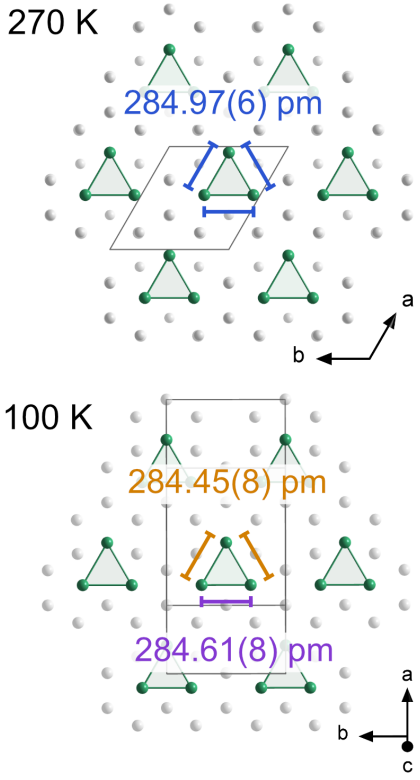

Figure 7: Nb–Nb distances within Nb_3 clusters in $Nb_3Br_{4-x}Cl_{4+x}$ as determined from single crystal X-ray diffraction data at 270 K (top) and 100 K (bottom). Niobium atoms are depicted in green, chloride and bromide ions are gray. The unit cell vectors are shown as grey lines.

Optical Band Gaps. Optical measurements were performed above the structural transition temperature at room temperature. For both Nb_3Cl_8 and $Nb_3Cl_4Br_4$, we observe similar direct and indirect optical band gaps (see Table 2), based on measurements on bulk samples consisting of small crystallites. This result indicates similar electronic properties of Nb_3Cl_8 and $Nb_3Cl_4Br_4$, validating our use of $Nb_3Cl_4Br_4$ as a proxy for low-temperature structural measurements. The values are consistent with literature reports [12, 48] but are smaller compared to our DFT+DFMT results.

Table 2: Direct and indirect optical band gaps for Nb_3Cl_8 and $Nb_3Br_4Cl_4$ at room temperature, determined by DRIFT Spectroscopy. (See Fig. S2 and Fig. S3 for full optical spectra)

Nb_3Cl_8	direct	0.510 eV
	indirect	0.344 eV
$Nb_3Br_4Cl_4$	direct	0.537 eV
	indirect	0.311 eV

Electrical conductivity. We investigated the temperature-dependent conductivity of bulk crystals and observed semiconducting behavior (Fig. S4) for the high temperature modification above 100 K. The conductivity ranges from approximately 2×10^{-3} S·m^{-1} at 300 K to 8×10^{-8} S·m^{-1} at 100 K. Below 100 K, the conductivity fell below the detection limit. No hysteresis was observed during cooling and heating cycles, which is consistent with the measurements being conducted above the structural transition temperature. As the magnetic susceptibility shows some hysteresis above 100 K (Fig. S5), our experimental results suggest that the electrical conductivity is not strongly affected by the magnetic transition, further indicating that the magnetic transition is not driven by charge disproportionation. Our results algin with the earlier measurements by Yoon *et al.* [12] at higher temperatures.

Conclusion

In this work, we performed a DFT+U+V, DFT+DMFT, and experimental study of the bulk LT β-Nb_3Cl_8 phase. Particularly, we studied the different proposed mechanisms of the

observed magnetostructural transition, with a focus on the effects of intra- and intertrimer Coulomb interactions.

We showed that it is the dimerization of the layers due to the change in stacking that is the primary driver of the magnetic transition in these compounds and that the charge disproportionation model [27, 33] is not consistent with our calculations. In particular, through a DFT+DMFT analysis we show that Nb_3Cl_8 behaves as a system of weakly-coupled Hubbard dimers, and that two of the proposed explanations for the physics of Nb_3Cl_8, the Mott-like strongly antiferromagnetically coupled system, and the singlet-like band insulator are smoothly connected, with the intertrimer interaction dictating their crossover. Additionally, the analysis of the intratrimer behavior suggests a possible mechanism for the experimentally observed scissoring of the trimer units.

The important role of the intertrimer interaction manifests itself also in the other members of the Nb_3X_8 family [see Table S1] where a smaller U/t ratio leads to a larger proximity to the band insulator solution rather than a Mott-like behavior.

In line with the theoretical findings, single-crystal X-ray diffraction reveals a structural phase transition in $Nb_3Br_4Cl_4$ from $P\bar{3}m1$ to $C2/m$, accompanied by a pronounced reduction in the distances between adjacent clusters. The bond lengths within the Nb_3 clusters slightly decrease upon cooling across the transition. Symmetry breaking leads to a slight distortion of the equilateral Nb_3 triangles into isosceles ones. However, the difference between the shorter and longer Nb–Nb bond lengths remains small and experimentally does not indicate a clear preference regarding whether the one inequivalent bond is longer or shorter than the others. The primary structural effect detected by our X-ray diffraction study is therefore a rearrangement of clusters of adjacent layers relative to one another, rather than significant changes within the clusters themselves. Magnetic measurements on Nb_3Cl_8 confirm the expected magnetic-to-nonmagnetic transition around 90 K, with clear hysteresis observed in both single crystals and powder samples. Temperature-dependent conductivity measurements showed a gradual decrease upon cooling to the transition temperature, without significant hysteresis. Below 100 K, no current could be detected within the sensitivity of the measurement setup. The differing hysteresis behavior of the magnetic and electric properties is consistent with our computational results, in particular the absence of interlayer charge disproportionation.

In conclusion, our work provides further evidence that the magnetostructural transition in β-Nb_3Cl_8 is driven primarily by a change in crystal stacking to the $R\bar{3}m$ phase. The physics of this interlayer dimerization can be understood in terms of weakly-coupled Hubbard dimers formed from pairs of Nb trimers. The subtle competition between intratrimer and intertrimer interactions tunes the system across a crossover between the limits of a Mott insulator and a band insulator. Concurrently, Coulomb interactions within a trimer drive a secondary, more subtle scissoring distortion within the Nb_3 trimer units.

This mechanism highlights the general importance of interlayer coupling in determining the electronic and magnetic properties of the Nb_3X_8 family of materials. Our calculations suggest that targeted control of external parameters such as pressure, chemical substitution, or strain, might allow systematic exploration of the crossover from Mott to band insulator and engineering of new functionalities in this and related cluster Mott systems.

Acknowledgement The authors thank S. Grytsiuk, J. Aretz, M. Rösner, and M. I. Katsnelson for valuable discussions and initial input files. P.M. and N.A.S. acknowledge funding from the Swiss National Science Foundation (Grant number 209454) and from ETH Zürich. Calculations were performed on the "Euler" cluster of ETH Zürich and the Swiss National Supercomputing Center Eiger cluster under Project ID s1304. C.P.R. acknowledges support from the project FerrMion of the Ministry of Education, Youth and Sports, Czech Republic, co-funded by the European Union (CZ.02.01.01/00/22_008/0004591). We would

like to thank Dr. F. Strauß for conducting and analyzing the conductivity measurements and Prof. M. Scheele for providing access to the necessary equipment. We also thank Dr. J. Glaser for conducting and analyzing the magnetic measurements.

Supporting Information Available

The Supporting Information for this article is available at ...

Supporting Information

Theoretical and computational details

DFT+U+V calculations

We perform DFT+U+V calculations using the QUANTUM ESPRESSO package (v6.6) [46, 49] within the generalized gradient approximation with the Perdew-Burke-Ernzerhof [50] exchange-correlation functional, utilizing the semiempirical DFT-D3 correction [51] to account for the van der Waals effects. We use the scalar-relativistic ultrasoft pseudopotentials from the GBRV library [52] with semicore $4s$ and $4p$ states included as valence for the Nb atoms.

We construct a localized set of orbitals using WANNIER90 (v3.1.0) [53, 54]. Starting from a conventional non-spin-polarized DFT calculations, we consider the two bands in close proximity to the Fermi level with dominant Nb contributions and with no entanglement with the surrounding bands [see Fig. 1(e)]. Following Grytsiuk *et al.* [20], our basis set consists of two trimer-centered Wannier functions computed by projecting the Kohn-Sham (KS) states around the Fermi level onto initial guesses of d_{z^2} orbitals and performing subsequent orthonormalization to finally obtain the molecular trimer orbitals shown in Fig. 1(f).

We then employ these trimer orbitals in both spin-unpolarized and spin-polarized DFT+U+V calculations using the implementation from Ref. [41]. We consider both onsite (intratrimer) and intersite (intertrimer) interactions described by parameters U_{tr} and V_{tr}, respectively [see Fig. 1(c)].

DFT+DMFT calculations

The trimer basis set for the DFT+DFMT calculations is described by the same Wannier functions obtained in the previous section. We consider an impurity problem composed of two adjacent trimer orbitals, a "dimer of trimers", for which the Hamiltonian reads:

$$H = H_0 + H_{\mathrm{int}} - H_{\mathrm{DC}}, \tag{S1}$$

where H_0 corresponds to the effective single-particle DFT Hamiltonian as obtained in the wannierization procedure and H_{int} is the interaction Hamiltonian:

$$H_{\mathrm{int}} = U_{\mathrm{tr}} \sum_i \hat{n}_i^{\uparrow} \hat{n}_i^{\downarrow} + V_{\mathrm{tr}} \sum_{\langle ij \rangle, \sigma\sigma'} \hat{n}_i^{\sigma} \hat{n}_j^{\sigma'}, \tag{S2}$$

where $\hat{n}_i^{\sigma}$ is the spin resolved number operator for trimer site i and spin σ. The meaning of U_{tr} and V_{tr} corresponds to the same as in the DFT+U+V case, that of an onsite (intratrimer) and intersite (intertrimer) interaction, respectively.

H_{DC} is the double-counting (DC) term, which cancels out the part of local interaction already included in the H_0 term [39]. Here, we employ the standard fully-localized limit for the expression of the energy of the double counting correction [55], which in this basis set, translates to a constant shift of the trimer orbital energies:

$$\Sigma_{\mathrm{DC}}^{tr} = U \sum_{i,\sigma} \left(N_i^{\mathrm{tr}} - \frac{1}{2} \right) \hat{n}_i^{\sigma}. \tag{S3}$$

Here, $N_i^{\mathrm{tr}} = \sum_{\sigma} \langle n_i^{\sigma} \rangle$ is the occupation of the trimer orbitals. In the presence of a difference in occupation between the two trimers, this term could in principle favor the localization of two electrons on one trimer. However, similarly to DFT+U+V calculations, we find no trace of this tendency in our DFT+DMFT calculations and both trimers remain equally occupied. We note that we have not included an intersite contribution to the double-counting potential. The approach outlined in Ref. [39] and used in the DFT+U+V calculations, effectively removes the double counting of the Hartree contribution stemming from intersite interactions, which would further suppress charge-disproportionation in the present case. However, given that our DFT+DMFT calculations already show no tendency for charge order and maintain equally occupied trimers, we do not anticipate that including this term would sig-

nificantly alter our results.

In the atomic basis, we construct Wannier functions including all 6 bands in the energy range between −0.5 eV and 1.5 eV around the Fermi level. This results in one d orbital per Nb site oriented towards the center of the trimer. We then perform DFT+DMFT calculations with 2 impurity models, each one including the 3 atomic orbitals belonging to one Nb_3 unit. The resulting Hamiltonian has the same form as described in Eq. (S1), however, the H_0 term this time represents the tight binding model described by the atomic Wannier basis set, and $H_{\rm int}$ reads:

$$H_{\rm int} = U_{\rm at} \sum_i \hat{m}_i^{\uparrow} \hat{m}_i^{\downarrow} + V_{\rm at}^{\rm intra} \sum_{\langle ij \rangle, \sigma\sigma'} \hat{m}_i^{\sigma} \hat{m}_j^{\sigma'}, \tag{S4}$$

where now $\hat{m}_i^{\sigma}$ is the number operator for an atomic orbital on Nb site i and spin channel sigma σ, and $V_{\rm at}^{\rm intra}$ is the Nb-Nb interaction inside one trimer. For the DC correction we again employ the fully-localized limit, but this time in the atomic basis:

$$\Sigma_{\rm DC}^{at} = \sum_i U \left(M_i^{\rm at} - \frac{1}{2} \right) \hat{m}_i^{\sigma} \quad , \tag{S5}$$

where $M_i^{\rm at} = \sum_{\sigma} \langle m_i^{\sigma} \rangle$. This terms translates to a downward energetic shift of the occupied atoms and an upward shift of the unoccupied ones.

In our DMFT calculations for the three-atom clusters, we have again omitted the intersite contribution to the double-counting corrections. Given that the material is deep in the Mott regime, the strong Coulomb interaction enforces a local filling of exactly one electron per Nb_3 cluster. The subspace of relevant electronic configurations is therefore composed almost exclusively of states with a single occupied atomic orbital per trimer. Within this subspace, the Hamiltonian term for the intersite interaction, $V_{at}^{\rm intra} \sum_{ij} m_i^{\sigma} m_j^{\sigma'}$, always acts as the zero operator and, in fact, we see an extremely weak dependence of our results on the value of $V_{\rm at}^{\rm intra}$, which makes application of a double counting correction unnecessary.

All our DFT+DMFT calculations are fully charge self-consistent and were performed using `solid_dmft` [56], which is part of the TRIQS library [57]. We solve all the DMFT impurity problems with the continuous-time quantum Monte Carlo solver CT-HYB [58–60] at the inverse electronic temperature close to room temperature of $\beta = (k_B T)^{-1} = 40 {\rm eV}^{-1}$. We use 10^4 warm-up steps and 2×10^8 Monte Carlo cycles with 120 steps each. We average over both spin channels to ensure a paramagnetic solution.

From the local Green's function, $G_{\nu\nu'}(\tau)$, where ν, ν' correspond to different orbitals and τ is the imaginary time, we obtain the local occupations on a given site (trimer), $n_{\nu\nu'} = G_{\nu\nu'}(\tau = 0^-)$, as well as the averaged spectral weight around the Fermi level, $\bar{A}(\omega = 0) = -(\beta/\pi) {\rm Tr} G(\tau = \beta/2)$. Additionally, we calculate the quasiparticle weight, $Z = [1 - \partial {\rm Im}\Sigma(i\omega)/\partial(i\omega)|_{i\omega \to 0}]^{-1}$, from the imaginary part of the local self-energy, Σ, by fitting a third-order polynomial to the lowest five Matsubara frequencies and interpolating to zero frequency. Finally, we use the maximum-entropy method [61, 62] to obtain the k-averaged spectral functions on the real frequency axis.

cRPA calculations

For the cRPA calculations, norm-conserving pseudopotentials from PSEUDODOJO [63, 64] are used to perform the initial DFT calculations. For these, we use a kinetic energy cutoff of 52 Ry (∼700 eV) and 12×52 Ry for the charge density. We converge the total energies to 10^{-3} Ry using a 6×6×3 k-point, smearing the occupations with the Marzari-Vanderbilt scheme [65] with smearing parameter of 0.001 Ry.

Screened Coulomb interaction parameters are obtained using the cRPA code RESPACK [66], using the WAN2RESPACK interface to QUANTUM ESPRESSO [67]. We set the polarization function cutoff to 15 Ry and we use a total of 300 bands, setting the upper limit of the highest possible excitations to 25 eV above the Fermi energy.

cRPA results for the Nb_3X_8 family

The calculated Coulomb interaction parameters using cRPA [68, 69] are given in Table S1 and Table S2. We give both the screened and unscreened values for U and V parameters in the $R\bar{3}m$ phase of Nb_3X_8 compounds in both the trimer and atomic basis sets used in the text.

In the trimer basis (Table S1), the values of $U_{\rm tr}$ and $V_{\rm tr}$ change monotonically throughout the series, with increasing $V_{\rm tr}/U_{\rm tr}$ ratio from 1/4 to approximately 1/3. Both the U and the V parameters are strongly screened with increasing ratio of screening across the compounds – 76% to 83% screening for U.

Table S2 presents the calculated intratrimer onsite ($U_{\rm at}$) and intratrimer ($V_{\rm at}^{\rm intra}$) and intertrimer ($V_{\rm at}^{\rm inter}$) intersite interactions in the atomic basis. Similarly to the trimer basis, $U_{\rm at}$ and $V_{\rm at}$ decrease monotonically across the entire series. Notably, the intertrimer $V_{\rm at}^{\rm inter}$ interaction remains quite large in the atomic basis, being practically identical to the $V_{\rm tr}$ values reported in Table S1 for the trimer basis.

Our cRPA results for the trimer basis show good agreement with previous works [20, 37] performed for the $R\bar{3}m$ and $R3$ structures. As expected, since the underlying structures do not differ except for a slight symmetry-breaking, the results remain comparable. Calculations for the atomic basis have so far been only performed in the monolayer [20], where all the interaction parameters are understandably larger than the ones shown here due to the lack of screening in a 2D structure.

In Fig. S1 we show the off-diagonal occupation in analogy to Fig. 4(c), indicating the positions of the cRPA-calculated interaction parameters of the Nb_3X_8 compounds in the trimer basis from Table S1 (shown as star, square, and triangle, respectively). As we move further down the series, the ratio of $U_{\rm tr}/V_{\rm tr}$ changes, and we get closer to the singlet insulating regime edge of the diagram, aided by the marked change in $t_{\rm LT}$ [not shown in Fig. S1]. The increasing proximity to the band insulator is also the reason why the other compounds in the series, Nb_3Br_8 and Nb_3I_8, both feature a band gap already with conventional DFT.

Table S1: The screened and unscreened interaction parameter values in eV as obtained from cRPA for Nb_3Cl_8, Nb_3Br_8, and Nb_3I_8 in the trimer basis.

	(All in eV)	$U_{\rm tr}$	$V_{\rm tr}$
Nb_3Cl_8	Screened	1.46	0.38
	Unscreened	6.00	2.20
	Ratio	0.24	0.17
Nb_3Br_8	Screened	1.21	0.36
	Unscreened	5.73	2.11
	Ratio	0.21	0.17
Nb_3I_8	Screened	0.85	0.28
	Unscreened	5.10	1.99
	Ratio	0.17	0.14

Table S2: The screened and unscreened interaction parameter values in eV as obtained from cRPA for Nb_3Cl_8, Nb_3Br_8, and Nb_3I_8 in the atomic basis.

	(All in eV)	$U_{\rm at}$	$V_{\rm at}^{\rm intra}$	$V_{\rm at}^{\rm inter}$
Nb_3Cl_8	Screened	2.33	1.36	0.39
	Unscreened	9.70	4.96	2.02
	Ratio	0.24	0.27	0.19
Nb_3Br_8	Screened	2.00	1.10	0.35
	Unscreened	9.39	4.78	1.98
	Ratio	0.21	0.23	0.18
Nb_3I_8	Screened	1.52	0.78	0.27
	Unscreened	8.62	4.44	1.87
	Ratio	0.18	0.18	0.14

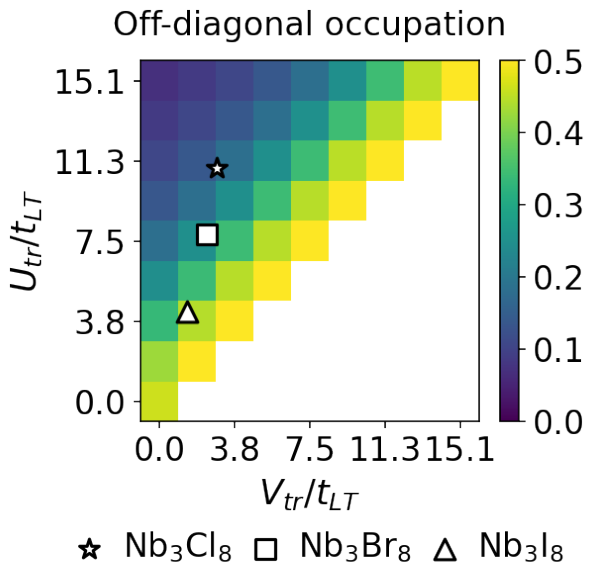

Figure S1: The off-diagonal occupation of the Nb_3X_8 cluster from DFT+DMFT as a function of $U_{\mathrm{tr}}/t_{\mathrm{LT}}$ and $V_{\mathrm{tr}}/t_{\mathrm{LT}}$. The cRPA values for Nb_3Cl_8, Nb_3Br_8, and Nb_3I_8 are shown with a circle, square, and triangle, respectively.

Experimental details

Synthesis of Nb_3Cl_8. A mixture of $NbCl_5$ (76.9 mg, 28.4 mmol ABCR GmbH, 99.9%) and Nb (23.1 mg, 24.9 mmol, ABCR GmbH, 99.9%), fused into an evacuated silica tube, was heated with 0.5 K/min in a Simon-Müller furnace. After heating at 750 °C for 48 hours, Nb_3Cl_8 was obtained as plate-like crystals (yield: $> 95\,\%$).

Synthesis of $Nb_3Br_4Cl_4$. A mixture of $NbBr_5$ (79.8 mg, 16.2 mmol, ABCR GmbH, 99.9%), $NbCl_5$ (43.8 mg, 16.2 mmol ABCR GmbH, 99.9%) and Nb (26.4 mg, 28.4 mmol, ABCR GmbH, 99.9%), fused into an evacuated silica tube, was heated with 0.5 K/min in a Simon-Müller furnace. After heating at 750 °C for 48 hours, $Nb_3Br_4Cl_4$ was obtained as plate-like crystals (yield: $> 90\,\%$).

Single-Crystal X-ray Diffraction. To maintain crystal integrity, separate single crystals were selected for each measurement and gradually cooled to the target temperature at a rate of 2 K/min. Data collection was performed on a Rigaku XtaLAB Synergy-S single-crystal X-ray diffractometer equipped with HyPix-6000HE detector and monochromated Mo-K_α radiation (λ = 71.037 pm) at 100 K and monocromated Cu-K_α radiation (λ = 154.184 pm) at 270 K. X-ray intensities were corrected for absorption with a numerical method (crystal faces) using CrysAlisPro 1.171.43.121a (Rigaku Oxford Diffraction, 2024). Structures were solved by direct methods (SHELXT) and refined by full-matrix least squares methods performed with SHELXL-2019/3 [70] as implemented in Olex2 1.5 [71]. Detailed crystallographic data can be obtained free of charge via www.ccdc.cam.ac.uk and the CCDC numbers.

Electrical Conductivity Conductivity measurements were performed in a Lake Shore Cryotronics CRX-6.5K probe station with a Keithley 2636B source meter unit. Plate-like crystals of Nb_3Cl_8 were transferred into the chamber under protective gas and contacted with silver paste on a silicon substrate with 770 nm oxide layer. The conductive silver pads at each end of the crystals were connected to the circuit with gold coated tungsten tips. The chamber was kept under vacuum ($> 5 \cdot 10^{-5}$ mbar) and the temperature was varied between 20 K and 300 K (Fig. S4 blue: cooling; red: heating). Before each measurement, sufficient time was allowed for the sample to reach the chosen temperature. Two-point conductivity measurements were performed by varying the applied source–drain voltage from -1 V to 1 V while detecting the current.

DRIFT (Diffuse Reflectance Infrared Fourier Transformation) Spectroscopy. Samples were measured at room temperature under inert conditions in diffuse reflectance with a Harrick Praying Mantis attachment using a Bruker Vertex 70 infrared spectrophotometer with a deuterated triglycine sulfate (DTGS) detector and KBr beamsplitter. The background spectra were collected using pure dried KI in powder form.

Magnetic Studies. Magnetic susceptibility measurements of crystalline powders and single crystals were performed in gelatine capsules between 5 K and 300 K with a Quantum design SQUID magnetometer equipped with a 1802

R/G bridge and a 1822 MDMS controller.

Optical band gap determination from DRIFTS (diffuse reflectance infrared fourier transform spectroscopy)

The absorption coefficient F was obtained using Kubelka–Munk analysis following:

$$F(R_\infty) = \frac{\alpha}{S} = \frac{(1-R_\infty)^2}{2R_\infty}, \qquad \text{(S6)}$$

where $R_\infty = \frac{R_{\text{sample}}}{R_{\text{standard}}}$ is the reflectance of an infinitely thick specimen, α is the absorption coefficient, and S is the scattering coefficient. For particle sizes greater than the light wavelengths measured, the scattering coefficient is understood to be approximately independent of frequency ($F(R_\infty) \sim \alpha$) and therefore $F(R_\infty)$ could be understood as a "pseudo-absorbance" coefficient [72–74].

The band gap determination was performed on the DRIFTS data according to Zanata *et al.* [75]. The energy is plotted against the absorption coefficient α and fitted with a sigmoid-Boltzmann function:

$$\alpha(E) = \alpha_{\text{max}} + \frac{\alpha_{\text{min}} - \alpha_{\text{max}}}{1 + \exp\left(\frac{E - E_0^{\text{Boltz}}}{\delta E}\right)}, \qquad \text{(S7)}$$

where α_{min} (α_{max}) stands for the minimum (maximum) absorption coefficient; E_0^{Boltz} is the energy coordinate at which the absorption coefficient is halfway between α_{min} and α_{max}; and δE is associated with the slope of the sigmoid, indicating the energy range over which most optical transitions occur [75].

The band gap can then be calculated by the following equation with $n_{\text{dir}}^{\text{Boltz}} = 0.3$ and $n_{\text{indir}}^{\text{Boltz}} = 4.3$:

$$E_g^{\text{Boltz}} = E_0^{\text{Boltz}} - n_{(\text{dir/indir})}^{\text{Boltz}} \cdot \delta E. \qquad \text{(S8)}$$

Magnetic measurements

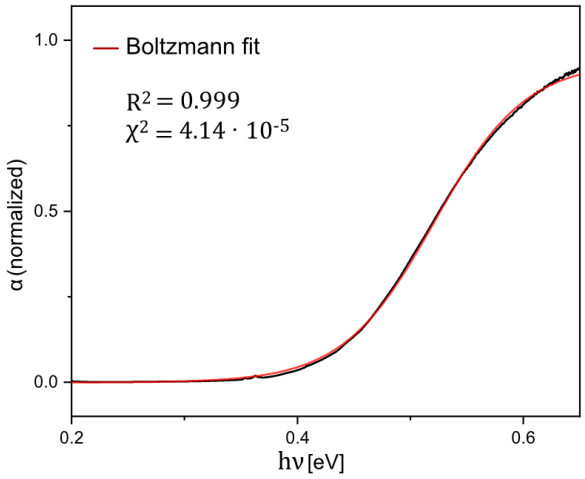

Figure S2: Optical absorption coefficient spectra of Nb_3Cl_8 with the Boltzmann function used to fit α (normalized).

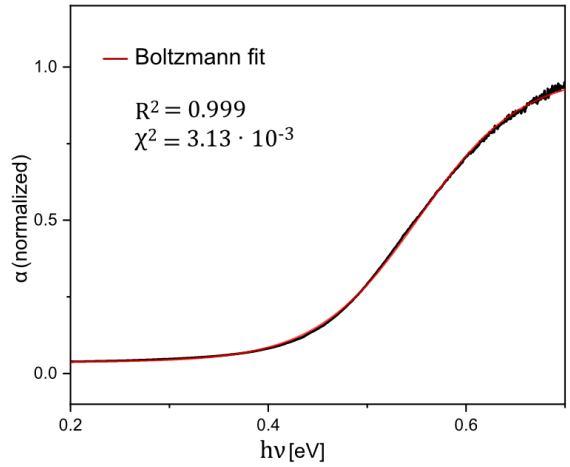

Figure S3: Optical absorption coefficient spectra of $Nb_3Br_4Cl_4$ with the Boltzmann function used to fit α (normalized).

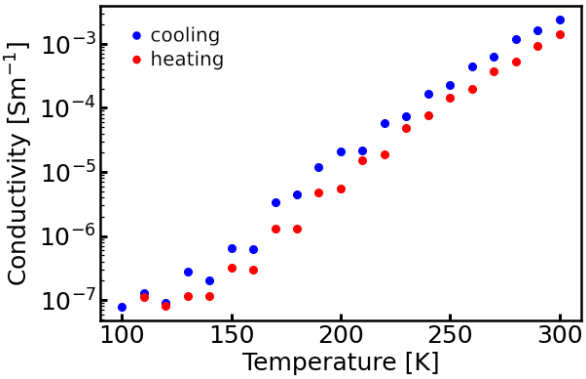

Figure S4: Electrical conductivity of Nb_3Cl_8 versus set temperature in a range of 100 K to 300 K. red: cooling; blue: heating

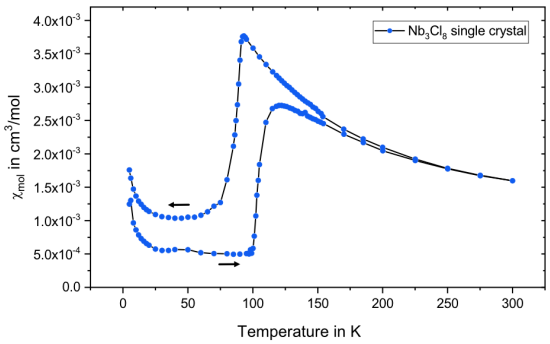

Figure S5: Magnetic susceptibility of single crystals of Nb_3Cl_8 versus set temperature in a range of 5 K to 300 K.

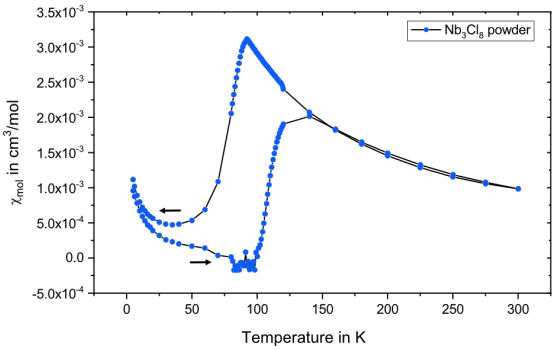

Figure S6: Magnetic susceptibility of a powdered sample of Nb_3Cl_8 versus set temperature in a range of 5 K to 300 K.

References

(1) Roy, S. B. *Mott Insulators: Physics and Applications*; IOP Publishing, 2019.

(2) Müller, H.; Kockelmann, W.; Johrendt, D. The Magnetic Structure and Electronic Ground States of Mott Insulators GeV_4S_8 and GaV_4S_8. *Chem. Mater.* **2006**, *18*, 2174–2180.

(3) Kimber, S. A. J.; Senn, M. S.; Fratini, S.; Wu, H.; Hill, A. H.; Manuel, P.; Attfield, J. P.; Argyriou, D. N.; Henry, Paul. F. Charge Order at the Frontier between the Molecular and Solid States in $Ba_3NaRu_2O_9$. *Phys. Rev. Lett.* **2012**, *108*, 217205.

(4) Nag, A.; Middey, S.; Bhowal, S.; Panda, S. K.; Mathieu, R.; Orain, J. C.; Bert, F.; Mendels, P.; Freeman, P. G.; Mansson, M. et al. Origin of the Spin-Orbital Liquid State in a Nearly J=0 Iridate $Ba_3ZnIr_2O_9$. *Phys. Rev. Lett.* **2016**, *116*, 097205.

(5) Streltsov, S. V.; Cao, G.; Khomskii, D. I. Suppression of Magnetism in $Ba_5AlIr_2O_{11}$: Interplay of Hund's Coupling, Molecular Orbitals, and Spin-Orbit Interaction. *Phys. Rev. B* **2017**, *96*, 014434.

(6) Jayakumar, V.; Hickey, C. Elementary Building Blocks for Cluster Mott Insulators. 2023.

(7) Grahlow, F.; Strauß, F.; Schmidt, P.; Valenta, J.; Ströbele, M.; Scheele, M.; Romao, C. P.; Meyer, H.-J. Ta_4SBr_{11}: A Cluster Mott Insulator with a Corrugated, Van Der Waals Layered Structure. *Inorg. Chem.* **2024**, *63*, 19717–19727.

(8) Nikolaev, S. A.; Solovyev, I. V.; Streltsov, S. V. Quantum Spin Liquid and Cluster Mott Insulator Phases in the Mo_3O_8magnets. *npj Quantum Mater.* **2021**, *6*, 1–8.

(9) Hu, J.; Zhang, X.; Hu, C.; Sun, J.; Wang, X.; Lin, H.-Q.; Li, G. Correlated Flat Bands and Quantum Spin Liquid State in a Cluster Mott Insulator. *Commun. Phys.* **2023**, *6*, 1–8.

(10) Liu, B.; Zhang, Y.; Han, X.; Sun, J.; Zhou, H.; Li, C.; Cheng, J.; Yan, S.; Lei, H.; Shi, Y. et al. Possible Quantum-Spin-Liquid State in van Der Waals Cluster Magnet Nb_3Cl_8. *J. Phys.: Condens. Matter* **2024**, *36*, 155602.

(11) Xu, Y.; Elcoro, L.; Song, Z.-D.; Vergniory, M. G.; Felser, C.; Parkin, S. S. P.; Regnault, N.; Mañes, J. L.; Bernevig, B. A. Filling-Enforced Obstructed Atomic Insulators. *Phys. Rev. B* **2024**, *109*, 165139.

(12) Yoon, J.; Lesne, E.; Sklarek, K.; Sheckelton, J.; Pasco, C.; Parkin, S. S. P.; McQueen, T. M.; Ali, M. N. Anomalous Thickness-Dependent Electrical Conductivity in van Der Waals Layered Transition Metal Halide, Nb_3Cl_8. *J. Phys.: Condens. Matter* **2020**, *32*, 304004.

(13) Peng, R.; Ma, Y.; Xu, X.; He, Z.; Huang, B.; Dai, Y. Intrinsic Anomalous Valley Hall Effect in Single-Layer Nb_3I_8. *Phys. Rev. B* **2020**, *102*, 035412.

(14) Feng, Y.; Yang, Q. Enabling Triferroics Coupling in Breathing Kagome Lattice Nb_3X_8 (X = Cl, Br, I) Monolayers. *J. Mater. Chem. C* **2023**, *11*, 5762–5769.

(15) Wu, H.; Wang, Y.; Xu, Y.; Sivakumar, P. K.; Pasco, C.; Filippozzi, U.; Parkin, S. S. P.; Zeng, Y.-J.; McQueen, T.; Ali, M. N. The Field-Free Josephson Diode in a van Der Waals Heterostructure. *Nature* **2022**, *604*, 653–656.

(16) Oh, S.; Choi, K. H.; Chae, S.; Kim, B. J.; Jeong, B. J.; Lee, S. H.; Jeon, J.; Kim, Y.; Nanda, S. S.; Shi, L. et al. Large-Area Synthesis of van Der Waals Two-Dimensional Material Nb_3I_8 and Its Infrared Detection Applications. *J. Alloy Compd.* **2020**, *831*, 154877.

(17) Schäfer, H.; Schnering, H. G. Metall-Metall-Bindungen bei niederen Halogeniden, Oxyden und Oxydhalogeniden schwerer Übergangsmetalle Thermochemische und strukturelle Prinzipien. *Angew. Chem.* **1964**, *76*, 833–849.

(18) Magonov, S. N.; Zoennchen, P.; Rotter, H.; Cantow, H. J.; Thiele, G.; Ren, J.; Whangbo, M. H. Scanning Tunneling and Atomic Force Microscopy Study of Layered Transition Metal Halides Nb_3X_8 (X = Cl, Br, I). *J. Am. Chem. Soc.* **1993**, *115*, 2495–2503.

(19) Ströbele, M.; Glaser, J.; Lachgar, A.; Meyer, H.-J. Struktur und elektrochemische Untersuchung von Nb_3Cl_8. *ZAAC* **2001**, *627*, 2002–2004.

(20) Grytsiuk, S.; Katsnelson, M. I.; van Loon, E. G. C. P.; Rösner, M. Nb_3Cl_8: A Prototypical Layered Mott-Hubbard Insulator. *npj Quantum Mater.* **2024**, *9*, 1–13.

(21) Gao, S.; Zhang, S.; Wang, C.; Yan, S.; Han, X.; Ji, X.; Tao, W.; Liu, J.; Wang, T.; Yuan, S. et al. Discovery of a Single-Band Mott Insulator in a van Der Waals Flat-Band Compound. *Phys. Rev. X* **2023**, *13*, 041049.

(22) Shan, P. F.; Han, X.; Li, X.; Liu, Z. Y.; Yang, P. T.; Wang, B. S.; Wang, J. F.; Liu, H. Y.; Shi, Y. G.; Sun, J. P. et al. Pressure-Induced Metallic State in a van Der Waals Cluster Mott Insulator Nb_3Cl_8. *Mater. Today Phys.* **2023**, *38*, 101267.

(23) Nakamura, R.; Takegami, D.; Fujinuma, K.; Nakamura, M.; Ferreira-Carvalho, M.; Melendez-Sans, A.; Yoshimura, M.; Tsuei, K.-D.; Haraguchi, Y.; Aruga Katori, H. et al. Charge Fluctuations in a Cluster Mott State: Hard x-Ray Photoemission Study on a Breathing Kagome Magnet Nb_3Cl_8. *Phys. Rev. B* **2024**, *110*, L081109.

(24) Zhang, Y.; Gu, Y.; Weng, H.; Jiang, K.; Hu, J. Mottness in Two-Dimensional van Der Waals Nb_3X_8 Monolayers (X=Cl, Br, and I). *Phys. Rev. B* **2023**, *107*, 035126.

(25) Stepanov, E. A. Signatures of a Charge Ice State in the Doped Mott Insulator Nb_3Cl_8. 2024.

(26) Kennedy, J. R.; Adler, P.; Dronskowski, R.; Simon, A. Experimental and Theoretical Electronic Structure Investigations on α-Nb_3Cl_8 and the Intercalated Phase β'-$NaNb_3Cl_8$. *Inorg. Chem.* **1996**, *35*, 2276–2282.

(27) Haraguchi, Y.; Michioka, C.; Ishikawa, M.; Nakano, Y.; Yamochi, H.; Ueda, H.; Yoshimura, K. Magnetic–Nonmagnetic Phase Transition with Interlayer Charge Disproportionation of Nb_3 Trimers in the Cluster Compound Nb_3Cl_8. *Inorg. Chem.* **2017**, *56*, 3483–3488.

(28) Jiang, Z.; Jiang, D.; Wang, Y.; Li, C.; Liu, K.; Wen, T.; Liu, F.; Zhou, Z.; Wang, Y. Pressure-Driven Symmetry Breaking and Electron Disproportionation of the Trigonal Nb_3 Cluster in Nb_3Cl_8. *Sci. China Phys. Mech. Astron.* **2022**, *65*, 278211.

(29) Pasco, C. M.; El Baggari, I.; Bianco, E.; Kourkoutis, L. F.; McQueen, T. M. Tunable Magnetic Transition to a Singlet Ground State in a 2D van Der Waals Layered Trimerized Kagomé Magnet. *ACS Nano* **2019**, *13*, 9457–9463.

(30) Sheckelton, J. P.; Plumb, K. W.; Trump, B. A.; Broholm, C. L.; McQueen, T. M. Rearrangement of van Der Waals Stacking and Formation of a Singlet State at T = 90 K in a Cluster Magnet. *Inorg. Chem. Front.* **2017**, *4*, 481–490.

(31) Kim, J.; Lee, Y.; Choi, Y. W.; Jung, T. S.; Son, S.; Kim, J.; Choi, H. J.; Park, J.-G.; Kim, J. H. Terahertz Spectroscopy and DFT Analysis of Phonon Dynamics of the Layered Van Der Waals Semiconductor Nb_3X_8 (X = Cl, I). *ACS Omega* **2023**, *8*, 14190–14196.

(32) Regmi, S. Observation of Flat and Weakly Dispersing Bands in the van Der Waals Semiconductor Nb_3Br_8 with Breathing Kagome Lattice. *Phys. Rev. B* **2023**, *108*.

(33) Haraguchi, Y.; Yoshimura, K. Molecular Orbital Electronic Instability in the van Der Waals Kagomé Semiconductor Nb_3Cl_8: Exploring Future Directions. *J. Phys. Soc. Jpn.* **2024**, *93*, 111002.

(34) Morin, F. J. Oxides Which Show a Metal-to-Insulator Transition at the Néel Temperature. *Phys. Rev. Lett.* **1959**, *3*, 34–36.

(35) Goodenough, J. B. The Two Components of the Crystallographic Transition in VO_2. *J. Solid State Chem.* **1971**, *3*, 490–500.

(36) Eyert, V. The Metal-Insulator Transitions of VO_2: A Band Theoretical Approach. *Ann. Phys.* **2002**, *11*, 650–704.

(37) Aretz, J.; Grytsiuk, S.; Liu, X.; Feraco, G.; Knekna, C.; Waseem, M.; Dan, Z.; Bianchi, M.; Hofmann, P.; Ali, M. N. et al. From Strong to Weak Correlations in Breathing-Mode Kagome van Der Waals Materials: $Nb_3(F,Cl,Br,I)_8$ as a Robust and Versatile Platform for Many-Body Engineering. 2025.

(38) Xiong, J.-X.; Zhang, X.; Zunger, A. Role of Magnetic and Structural Symmetry Breaking in Forming the Mott Insulating Gap in Nb_3Cl_8. *Phys. Rev. B* **2025**, *111*, 155122.

(39) Leiria Campo Jr, V.; Cococcioni, M. Extended DFT+U+V Method with On-Site and Inter-Site Electronic Interactions. *J. Phys.: Condens. Matter* **2010**, *22*, 055602.

(40) Kotliar, G.; Savrasov, S. Y.; Haule, K.; Oudovenko, V. S.; Parcollet, O.; Marianetti, C. A. Electronic Structure Calculations with Dynamical Mean-Field Theory. *Rev. Mod. Phys.* **2006**, *78*, 865–951.

(41) Carta, A.; Timrov, I.; Mlkvik, P.; Hampel, A.; Ederer, C. Explicit Demonstration of the Equivalence between DFT+U and the Hartree-Fock Limit of DFT+DMFT. *Phys. Rev. Res.* **2025**, *7*, 013289.

(42) Pavarini, E., Koch, E., Scalettar, R., Martin, R., Institute for Advanced Simulation, German Research School for Simulation Sciences, Eds. *The Physics of Correlated Insulators, Metals, and Superconductors: Lecture Notes of the Autumn School on Correlated Electrons 2017*; Schriften Des Forschungszentrums Jülich. Reihe Modeling and Simulation Band 7; Forschungszentrum, Zentralbibliothek: Jülich, 2017.

(43) Nájera, O.; Civelli, M.; Dobrosavljević, V.; Rozenberg, M. J. Multiple Crossovers and Coherent States in a Mott-Peierls Insulator. *Phys. Rev. B* **2018**, *97*, 045108.

(44) Jiang, K.; Qi, Z.; Weng, H.; Hu, J. Mottness in Obstructed Atomic Insulators without Mott Transition. *Phys. Rev. B* **2023**, *108*, 195102.

(45) Streltsov, S. V.; Takegami, D.; Nakamura, R.; Kovaleva, P. P.; Poteryaev, A. I.; Nikolaev, S. A.; Xu, H.-H.; Sui, Y.; Yoshimura, M.; Tsuei, K.-D. et al. Beyond a Cluster-Mott State in the Breathing Kagome Lattice of $LiZn_2Mo_3O_8$. *Phys. Rev. B* **2025**, *111*, 085124.

(46) Giannozzi, P.; Andreussi, O.; Brumme, T.; Bunau, O.; Buongiorno Nardelli, M.; Calandra, M.; Car, R.; Cavazzoni, C.; Ceresoli, D.; Cococcioni, M. et al. Advanced Capabilities for Materials Modelling with Quantum ESPRESSO. *J. Phys.: Condens. Matter* **2017**, *29*, 465901.

(47) Miller, G. J. Solid State Chemistry of Nb_3Cl_8: Nb_3TeCl_7, Mixed Crystal Formation, and Intercalation. *J. Alloys Compd.* **1995**, *217*, 5–12.

(48) Date, M.; Petocchi, F.; Yen, Y.; Krieger, J. A.; Pal, B.; Hasse, V.; McFar-

lane, E. C.; Körner, C.; Yoon, J.; Watson, M. D. et al. Momentum-Resolved Fingerprint of Mottness in Layer-Dimerized Nb_3Br_8. *Nat. Commun.* **2025**, *16*, 4037.

(49) Giannozzi, P.; Baroni, S.; Bonini, N.; Calandra, M.; Car, R.; Cavazzoni, C.; Ceresoli, D.; Chiarotti, G. L.; Cococcioni, M.; Dabo, I. et al. QUANTUM ESPRESSO: A Modular and Open-Source Software Project for Quantum Simulations of Materials. *J. Phys.: Condens. Matter* **2009**, *21*, 395502.

(50) Perdew, J. P.; Burke, K.; Ernzerhof, M. Generalized Gradient Approximation Made Simple. *Phys. Rev. Lett.* **1996**, *77*, 3865–3868.

(51) Grimme, S.; Antony, J.; Ehrlich, S.; Krieg, H. A Consistent and Accurate Ab Initio Parametrization of Density Functional Dispersion Correction (DFT-D) for the 94 Elements H-Pu. *J. Chem. Phys.* **2010**, *132*, 154104.

(52) Garrity, K. F.; Bennett, J. W.; Rabe, K. M.; Vanderbilt, D. Pseudopotentials for High-Throughput DFT Calculations. *Comput. Mater. Sci.* **2014**, *81*, 446–452.

(53) Mostofi, A. A.; Yates, J. R.; Lee, Y.-S.; Souza, I.; Vanderbilt, D.; Marzari, N. Wannier90: A Tool for Obtaining Maximally-Localised Wannier Functions. *Comput. Phys. Commun.* **2008**, *178*, 685–699.

(54) Pizzi, G.; Vitale, V.; Arita, R.; Blügel, S.; Freimuth, F.; Géranton, G.; Gibertini, M.; Gresch, D.; Johnson, C.; Koretsune, T. et al. Wannier90 as a Community Code: New Features and Applications. *J. Phys.: Condens. Matter* **2020**, *32*, 165902.

(55) Anisimov, V. I.; Solovyev, I. V.; Korotin, M. A.; Czyżyk, M. T.; Sawatzky, G. A. Density-Functional Theory and NiO Photoemission Spectra. *Phys. Rev. B* **1993**, *48*, 16929–16934.

(56) Merkel, M. E.; Carta, A.; Beck, S.; Hampel, A. Solid_dmft: Gray-Boxing DFT+DMFT Materials Simulations with TRIQS. *JOSS* **2022**, *7*, 4623.

(57) Parcollet, O.; Ferrero, M.; Ayral, T.; Hafermann, H.; Krivenko, I.; Messio, L.; Seth, P. TRIQS: A Toolbox for Research on Interacting Quantum Systems. *Comput. Phys. Commun.* **2015**, *196*, 398–415.

(58) Werner, P.; Millis, A. J. Hybridization Expansion Impurity Solver: General Formulation and Application to Kondo Lattice and Two-Orbital Models. *Phys. Rev. B* **2006**, *74*, 155107.

(59) Gull, E.; Millis, A. J.; Lichtenstein, A. I.; Rubtsov, A. N.; Troyer, M.; Werner, P. Continuous-Time Monte Carlo Methods for Quantum Impurity Models. *Rev. Mod. Phys.* **2011**, *83*, 349–404.

(60) Seth, P.; Krivenko, I.; Ferrero, M.; Parcollet, O. TRIQS/CTHYB: A Continuous-Time Quantum Monte Carlo Hybridisation Expansion Solver for Quantum Impurity Problems. *Comput. Phys. Commun.* **2016**, *200*, 274–284.

(61) Jarrell, M.; Gubernatis, J. E. Bayesian Inference and the Analytic Continuation of Imaginary-Time Quantum Monte Carlo Data. *Phys. Rep.* **1996**, *269*, 133–195.

(62) Kraberger, G. J.; Triebl, R.; Zingl, M.; Aichhorn, M. Maximum Entropy Formalism for the Analytic Continuation of Matrix-Valued Green's Functions. *Phys. Rev. B* **2017**, *96*, 155128.

(63) Hamann, D. R. Optimized Norm-Conserving Vanderbilt Pseudopotentials. *Phys. Rev. B* **2013**, *88*, 085117.

(64) van Setten, M. J.; Giantomassi, M.; Bousquet, E.; Verstraete, M. J.; Hamann, D. R.; Gonze, X.; Rignanese, G. M. The PseudoDojo: Training and Grading a 85 Element Optimized Norm-Conserving Pseudopotential Table.

Comput. Phys. Commun. **2018**, *226*, 39–54.

(65) Marzari, N.; Vanderbilt, D.; De Vita, A.; Payne, M. C. Thermal Contraction and Disordering of the Al(110) Surface. *Phys. Rev. Lett.* **1999**, *82*, 3296–3299.

(66) Nakamura, K.; Yoshimoto, Y.; Nomura, Y.; Tadano, T.; Kawamura, M.; Kosugi, T.; Yoshimi, K.; Misawa, T.; Motoyama, Y. RESPACK: An Ab Initio Tool for Derivation of Effective Low-Energy Model of Material. *Comput. Phys. Commun.* **2021**, *261*, 107781.

(67) Kurita, K.; Misawa, T.; Yoshimi, K.; Ido, K.; Koretsune, T. Interface Tool from Wannier90 to RESPACK: Wan2respack. *Comput. Phys. Commun.* **2023**, *292*, 108854.

(68) Aryasetiawan, F.; Imada, M.; Georges, A.; Kotliar, G.; Biermann, S.; Lichtenstein, A. I. Frequency-Dependent Local Interactions and Low-Energy Effective Models from Electronic Structure Calculations. *Phys. Rev. B* **2004**, *70*, 195104.

(69) Miyake, T.; Aryasetiawan, F. Screened Coulomb Interaction in the Maximally Localized Wannier Basis. *Phys. Rev. B* **2008**, *77*, 085122.

(70) Sheldrick, G. M. Crystal Structure Refinement with SHELXL. *Acta Cryst. C* **2015**, *71*, 3–8.

(71) Dolomanov, O. V.; Bourhis, L. J.; Gildea, R. J.; Howard, J. a. K.; Puschmann, H. OLEX2: A Complete Structure Solution, Refinement and Analysis Program. *J. Appl. Cryst.* **2009**, *42*, 339–341.

(72) Wendlandt, W. W.; Hecht, H. G. *Reflectance Spectroscopy*; Interscience Publishers, 1966.

(73) Kubelka, P.; Munk, F. An Article on Optics of Paint Layers. *Z. Tech. Phys* **1931**, *12*, 259–274.

(74) Kubelka, P. New Contributions to the Optics of Intensely Light-Scattering Materials. Part I. *J. Opt. Soc. Am.* **1948**, *38*, 448–457.

(75) Zanatta, A. R. Revisiting the Optical Bandgap of Semiconductors and the Proposal of a Unified Methodology to Its Determination. *Sci. Rep.* **2019**, *9*, 11225.

Publication 4

Structural Modifications of $M_5O_4I_{11}$ (M = Nb, Ta) Cluster Networks from Heterogeneous Solid-State Reactions

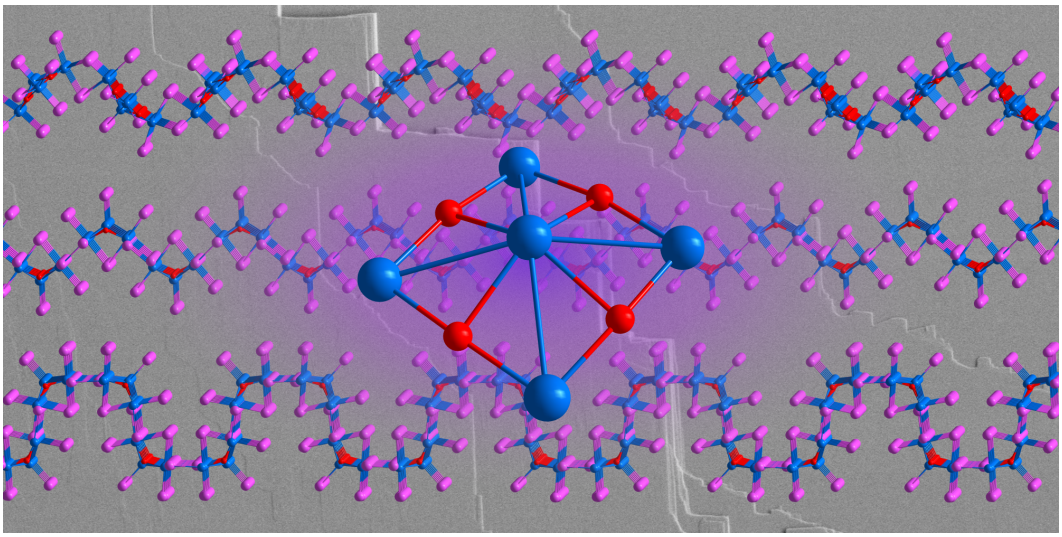

DOI: 10.1039/D5DT02097B

Reproduced from

Dalton Trans., **2025**, 54, 16593-16604

Dalton Transactions

ROYAL SOCIETY OF CHEMISTRY

PAPER

View Article Online
View Journal | View Issue

Cite this: *Dalton Trans.*, 2025, **54**, 16593

Structural modifications of $M_5O_4I_{11}$ (M = Nb, Ta) cluster networks from heterogeneous solid-state reactions

Fabian Grahlow, [a] Jan Beitlberger,[a] Mario Martin,[b] Eric Juriatti,[b] Heiko Peisert, [b] Marcus Scheele, [b] Markus Ströbele, [a] Carl P. Romao[c] and Hans-Jürgen Meyer *[a]

The cluster compounds $M_5O_4I_{11}$ (M = Nb, Ta) and $Ta_5O_4I_{11}(TaI_5)$ were obtained from heterogeneous solid-state reactions and structurally characterised by single-crystal X-ray diffraction. Their crystal structures are based on the novel $[M_5O_4]$ cluster core with metal (M) atoms arranged following the motif of a square pyramid. Iodide ligands contribute to different connectivities in the structures, resulting in (van der Waals type) waved layer structures. Two structural modifications exist for $Ta_5O_4I_{11}$, denoted as o-$Ta_5O_4I_{11}$ and m-$Ta_5O_4I_{11}$, and the compound $Ta_5O_4I_{11}(TaI_5)$ encloses $[TaI_5]$ molecules within voids of the structure. The two-dimensional nature of the structures and the presence of metal-to-metal bonding motivated investigations of the electronic properties through optical band-gap measurements, electrical conductivity studies, electronic band structure calculations, and X-ray photoelectron spectroscopy.

Received 1st September 2025,
Accepted 17th October 2025

DOI: 10.1039/d5dt02097b

rsc.li/dalton

Introduction

The chemistry of reduced niobium and tantalum halides is characterised by metal cluster compounds that are usually achieved through solid-state synthesis at elevated temperatures.[1] These compounds display a wide range of structural motifs and oxidation states, with a pronounced tendency to form clusters featuring octahedral M_6 (M = Nb, Ta) cores.[2] Many transition metal (M) halide (X) clusters crystallise in either the $[M_6X_{12}]$- or $[M_6X_8]$-structural types.[3–6] The $[M_6X_{12}]$ structure consists of twelve halide ligands bridging the edges of an M_6 octahedron which generally favours combinations of larger metal atoms with smaller halides. In contrast, $[M_6X_8]$ clusters, in which eight halides cap the faces of the octahedron, tend to form when smaller metal atoms are paired with larger halide ions. Due to the spatial separation of adjacent clusters by outer ligands, these crystalline materials typically exhibit semiconducting behaviour with poor electrical conductivity.[7,8] The chemistry of binary niobium halide clusters is further enriched by triangular Nb_3 clusters present in Nb_3X_8 (X = Cl, Br, I), as well as Peierls-distorted NbX_4.[9,10] Metal-rich tantalum halides exist as Ta_6X_{14}, Ta_6X_{15} and TaX_4.[5,11–15]

Beyond these well-established binary systems, the range of cluster compounds and structural diversity expands significantly in heteroanionic halides of niobium and tantalum. Among the most common examples are chalcohalides, which include M_3 clusters, such as Ta_3SBr_7 and ANb_3SBr_7 (A = Rb, Cs),[16–18] as well as M_4 clusters exhibiting planar, butterfly or tetrahedral geometries (*e.g.* Nb_4OI_{10}; $Ta_4S_9Br_8$; Ta_4SBr_{11}; $Nb_4Se_4I_4$)[19–26] Octahedral M_6 clusters are also observed, as in Nb_6I_9S.[27] A notable characteristic of these compounds is the presence of bridging halides along with the interstitial or capping atoms, which are most often chalcogenides, and rarely pnictides (Nb_4PnX_{11}, Pn = N, P; X = Cl, Br, I).[25]

Occasionally, molecular MX_5 units are found to be incorporated into a cluster network. A notable example is $Nb_7S_2I_{19}$ which can be represented as $(Nb_3SI_7)_2(NbI_5)$, emphasising the stabilisation of thermodynamically unstable NbI_5 monomers within the inorganic framework of Nb_3SI_7. This structure exemplifies a form of structural synergism, where the enclosed molecule influences the topology of the surrounding cluster framework.[28] Similarly, space-filling $[ZrCl_5]^-$ units are observed in the compound described as $Cs_3Zr_7Cl_{20}Mn$ and $[TaBr_6]^-$ units in $(Ta_6Br_{12})Br_3(TaBr_6)_{0.86}$.[29,30]

Less common is the occurrence of pentanuclear M_5 clusters. Reported examples generally fall into two categories: those composed of two different metals, which give rise to a

[a]*Section for Solid State and Theoretical Inorganic Chemistry, Institute of Inorganic Chemistry, Eberhard Karls Universität Tübingen, Auf der Morgenstelle 18, D-72076 Tübingen, Germany. E-mail: juergen.meyer@uni-tuebingen.de*
[b]*Institute of Physical and Theoretical Chemistry, Eberhard Karls Universität Tübingen, Auf der Morgenstelle 18, D-72076 Tübingen, Germany*
[c]*Department of Materials, Faculty of Nuclear Sciences and Physical Engineering, Czech Technical University in Prague, Trojanova 13, 120 00 Prague, Czech Republic*

variety of geometries, and metal halide clusters that typically adopt a square-pyramidal cluster core. The latter is commonly observed in compounds with the general formula $[M_5X_{13}]^{n-}$ (M = Mo, W, Tc; X = Cl, Br, I; n = 0, 1, 2, 3).[31–33]

Oxyiodides of niobium and tantalum are reported as MO_2I, MOI_2 and $NbOI_3$.[34–36] More recently there has been some progress in the development of metal-rich oxyiodides.[19,37] In the course of this progress, we present a new class of metal-rich oxyiodides based on a distinctive M_5 cluster motif, observed for both niobium and tantalum.

These clusters, of the general formula $M_5O_4I_{11}$ with M = Nb and Ta, are shown to exist in two polymorphic forms for tantalum (*o*-$Ta_5O_4I_{11}$, *m*-$Ta_5O_4I_{11}$), as well as in the compound $Ta_5O_4I_{11}(TaI_5)$, containing molecular $[TaI_5]$ in its structure. The syntheses and crystal structures of the compounds are reported, and their electrical conductivities and electronic structures are analysed through a combination of experimental measurements and theoretical calculations.

Experimental

Preparations

Manipulations of starting materials, such as charging the silica ampoules (estimated volume 5 cm^3) with starting materials were performed in an argon-filled glovebox (MBraun, labmaster 130, O_2 < 1 ppm, H_2O < 1 ppm).

o-$Ta_5O_4I_{11}$, *m*-$Ta_5O_4I_{11}$ and $Ta_5O_4I_{11}(TaI_5)$

A mixture of TaI_5 (144.8 mg, 0.178 mmol), Ta (6.1 mg, 0.03 mmol, Merck, 99.9%), Li_2O (5.1 mg, 0.169 mmol, ABCR, 96%) and Li_2CN_2 (4.6 mg, 0.085 mmol) was fused into an evacuated silica tube and heated with 0.5 K min^{-1} to 500 °C in a Simon–Müller furnace. After heating at 500 °C for 48 hours, *o*-$Ta_5O_4I_{11}$ and *m*-$Ta_5O_4I_{11}$ were obtained as black, plate-like (*o*-$Ta_5O_4I_{11}$) and rod-shaped (*m*-$Ta_5O_4I_{11}$) crystals, which are sensitive to moisture (estimated yield: ~30% (*o*-$Ta_5O_4I_{11}$); ~10% (*m*-$Ta_5O_4I_{11}$); a powder X-ray diffraction pattern is shown in Fig. S1, top). Reactions at 500 °C with a shorter reaction time of 12 hours resulted in a few black crystals of $Ta_5O_4I_{11}(TaI_5)$. Additional side phases were red TaO_2I and black, fibrous $TaOI_2$, as well as $Ta_2O_3I_4$ and $LiTa_3O_2I_{12}$ which are reported in this study.

$Nb_5O_4I_{11}$

NbI_4 (160.8 mg, 0.268 mmol), Li_2O (2 mg, 0.067 mmol) and $Li_2(CN_2)$ (7.2 mg, 0.135 mmol) were fused into a silica ampoule and heated to 400 °C with a rate of 0.1 K min^{-1}. The holding time was 24 hours before the reaction was cooled down to room temperature with a rate of 0.1 K min^{-1}. Black, plate-like crystals of $Nb_5O_4I_{11}$ were obtained at the walls of the ampoule (yield: ~10%); $NbOI_2$ and NbI_5 were sublimed to the cooler part of the ampoule, while LiI, $Li_3Nb_7O_5I_{15}$[38] and an amorphous phase were found in the hotter part at the bottom. Crystals behave sensitive in moist air. A powder X-ray diffraction pattern is shown in Fig. S1, bottom.

NbI_4 and TaI_5

NbI_4 and TaI_5 were synthesised according to literature by reacting appropriate amounts of niobium or tantalum (Merck, 99.9%) with resublimed iodine (Merck, 99.999%) at 400–450 °C in evacuated quartz ampoules.[39]

$Li_2(CN_2)$

$Li_2(CN_2)$ was synthesised as described before,[40] by reacting LiH (99.4%, Alfa Aesar) with melamine (≥99%) in a 6 : 1 molar ratio under argon.

Powder X-ray diffraction

All reaction products were investigated by powder X-ray diffraction (PXRD) using a StadiP diffractometer (Stoe, Darmstadt) with Ge-monochromated Cu-$K_{\alpha1}$ radiation, and a Mythen1 Detector.

Single-crystal X-ray diffraction

Data collections were performed on a Rigaku XtaLAB Synergy-S single-crystal X-ray diffractometer equipped with HyPix-6000HE detector and monochromated Mo-K_α radiation (λ = 0.71073 Å) and Cu-K_α radiation (λ = 1.54184 Å) at 150 K. X-ray intensities were corrected for absorption with a numerical method (crystal faces) using CrysAlisPro 1.171.43.121a (Rigaku Oxford Diffraction, 2024). The structures were solved by direct methods (SHELXT) and refined by full-matrix least–squares methods performed with SHELXL–2019/3 as implemented in Olex2 1.5.

EDX and SEM

Energy dispersive X-ray spectroscopy (EDX) and scanning electron microscopy (SEM) were performed on a HITACHI SU8030 scanning electron microscope with a Bruker QUANTAX 6G EDX-detector. Single crystals of *o*- and *m*-$Ta_5O_4I_{11}$ were mounted onto carbon tape under an argon atmosphere during sample preparation. For inert transfer, a vacuum transfer device, similar to the one reported by Yao *et al.*, was used.[41] In our adapted design, it consists of a steel lid with an O-ring seal (Fig. S2a). The lid is placed on top of the sample holder and evacuated within the glovebox airlock. It is then rapidly flooded with argon to create a reduced-pressure environment, ensuring an airtight seal *via* the O-ring (Fig. S2b and c). Once inserted into the SEM transfer chamber and evacuated, the internal pressure becomes equal to, or slightly higher than, the external pressure. This allows the magnetic lid to be lifted using neodymium magnets from outside the chamber (Fig. S2d).

Electrical conductivity

Conductivity measurements were performed in a Lake Shore Cryotronics CRX-6.5K probe station with a Keithley 2636B source meter unit. Rod-shaped crystals of *o*- and *m*-$Ta_5O_4I_{11}$ were contacted on a silicon substrate with 770 nm oxide layer using silver paste (Fig. S3, right) and transferred into the measuring chamber under protective gas. The conductive silver pads at each end of the crystals were connected to the circuit with gold coated tungsten tips. The chamber was kept under vacuum (<5 × 10^{-5} mbar) and the temperature was varied between 140 K and 350 K. Before each measurement,

sufficient time was allowed for the sample to reach the chosen temperature. Two-point conductivity measurements were performed by varying the applied source–drain voltage from −2 V to 2 V while detecting the current. For time-resolved photocurrent measurements, using a picosecond pulsed laser driver (Taiko PDL M1, PicoQuant) together with a laser head 779 nm (pulse length < 500 ps) the crystals were illuminated at ~55 mW cm^{-2} laser output power using the continuous wave mode under a constant bias of 1 V. The electrical measurements shown in this work had crystal dimensions (length L; width W; height H) of *o*-$Ta_5O_4I_{11}$: L = 205 μm; W = 124 μm; H = 75 μm and *m*-$Ta_5O_4I_{11}$: L = 119.4 μm; W = 32.4 μm; H = 27.3 μm.

DRIFT (diffuse reflectance infrared fourier transformation) spectroscopy

Samples were measured at room temperature under inert conditions in diffuse reflectance with a Harrick Praying Mantis attachment using a Bruker Vertex 70 infrared spectrophotometer with a deuterated triglycine sulfate (DTGS) detector and KBr beamsplitter. The background spectra were collected using pure dried KBr in powder form.

TXRF (total internal reflection X-ray fluorescence) spectroscopy

TXRF studies were performed using a S2 Picofox (Bruker AXS Microanalysis, Berlin, Germany) equipped with a Mo X-ray tube, which was operated at 50 kV and 600 μA. The measurement period for each sample was 1000 s (live time). Fitting of the resulting spectra was done using the Spectra software (Bruker Nano GmbH) in the super bias mode (maximum stripping cycles of 2000).

XPS (X-ray photoelectron spectroscopy)

XPS measurements were performed under ultra-high vacuum (UHV) conditions (8×10^{-10} mbar) using an XR50 Al-K_α standard source equipped with a PHOIBOS 100 hemispherical analyser (SPECS GmbH, Berlin, Germany). Since *o*-$Ta_5O_4I_{11}$ represents the major phase of the synthesis, the crystals used for XPS measurements were carefully selected under the optical microscope. To avoid exposure to air and prevent oxidation, the synthesised samples were mounted on a double-sided conductive carbon tape under argon atmosphere. For inert transfer into the spectrometer, a custom-built vacuum transfer device (an enlarged version of the design used for SEM/EDX) was employed. This device consists of an aluminium lid with an O-ring that seals the sample holder under reduced pressure within the glovebox airlock (Fig. S4, SI). Upon evacuation of the XPS transfer chamber, the external pressure drops below the internal pressure, causing the lid to detach and fall off, thereby revealing the sample without contact to air. The chamber is then further evacuated to UHV before transferring the sample into the measurement chamber (see Fig. S5, SI for details).

The binding energy scale was calibrated to the signal positions of Au $4f_{7/2}$ (84.0 eV), Ag $3d_{5/2}$ (368.2 eV) and Cu $2p_{3/2}$ (932.6 eV). To take charging effects into account, the acquired Ta 4f spectrum was referenced by setting the I $3d_{5/2}$ peak to a binding energy of 619 eV. Peak fitting of XPS spectra was performed using the software Unifit 2018 (Unifit Scientific Software GmbH, Leipzig, Germany).

DFT (Density functional theory)

DFT calculations were performed in the software package Abinit (v. 10).[42] The Perdew–Burke–Ernzerhof exchange–correlation functional was used with the dispersion correction of Grimme.[43,44] Calculations were performed using a plane wave basis set and the PAW formalism,[45] with an energy cut-off of 100 Ha inside the PAW spheres and 24 Ha outside. A 4 × 2 × 2 (*o*-$Ta_5O_4I_{11}$) or 3 × 2 × 2 (*m*-$Ta_5O_4I_{11}$) Monkhorst–Pack grid[46] of k-points was used to sample reciprocal space. These quantities were chosen following convergence studies. Methfessel–Paxton smearing was used to determine band occupation.[47] PAW data files were used as received from the Abinit library. The structures were relaxed to an internal pressure of 2 MPa prior to calculations of the electronic band structure.

Results and discussion

Synthesis and crystal structure

The two most stable compounds reported in the Ta–O–I system appear to be TaO_2I and $TaOI_2$, both of which were synthesised *via* transport reactions involving Ta, I_2 and Ta_2O_5 in temperature gradients of 450–550 °C.[34,35,48] In our study, we aimed to access more metal-rich compounds in this system by further reducing tantalum below the Ta(IV) oxidation state in $TaOI_2$. For this purpose we have explored Li_2CN_2 as an unconventional reduction agent, which has previously been shown its reducing nature, as demonstrated in metathesis reactions of $NiCl_2$ with Li_2CN_2, yielding elemental Ni, along with LiCl, C_3N_4 and N_2.[49]

The employment of Li_2CN_2 into the Ta–O–I system triggers reduction reactions likely above 300 °C, marked by the emergence of a violet gas phase. As the temperature exceeded 400 °C, this gas phase darkened significantly. Upon cooling, crystalline iodine was found deposited on the cooler part of the ampoule, indicating that molecular iodine is present in the gas phase, likely along with reactive precursors that contribute to the observed cluster formation.

Additionally, slightly increased pressure was observed in the ampoules, indicating the formation of N_2. Amorphous C_3N_4 was identified as a side product *via* infrared spectroscopy (see Fig. S6, SI). These findings further confirm that Li_2CN_2 acts as a reducing agent in our system, consistent with its previously reported behaviour in the reduction of $NiCl_2$ to elemental Ni.

Thermal analysis of reactions aimed to investigate the impact of Li_2CN_2 on the Ta–O–I system proved to be complex, as the reaction pathways are intricate. In addition to the observed cluster compounds (discussed in detail in this study), various crystalline and amorphous by-products were detected.

Each experiment resulted in the formation of multiple products, indicating that several reactions occurred simultaneously. The spatial distributions of these products within the reaction container suggests the occurrence of partial transport reactions along a narrow temperature gradient.

Among the consistently identified side products were LiI, $TaOI_2$ and TaO_2I, as well as two previously unreported compounds: $LiTa_3O_2I_{12}$ and $Ta_2O_3I_4$. While these compounds are not the focus of this study, their structures have been characterised by us and are briefly described as follows. Both compounds feature Ta^{5+} ions in distorted octahedral coordination environments. The structure of $LiTa_3O_2I_{12}$ forms kinked strands of $[Ta_3O_2I_{10}I_{4/2}]^-$ units which are separated by disordered lithium ions (Fig. 1 left). In $Ta_2O_3I_4$, each Ta^{5+} ion is coordinated by three oxygen and three iodide ions, forming octahedra that connect *via* corner-sharing oxygen atoms and edge-sharing iodides, with one terminal iodide per octahedra. This connectivity results in zig-zag layers (Fig. 1 right).

Efforts to minimise the amount of these side products by adjusting reactant ratios frequently resulted in lower yields of the desired cluster compounds. Likewise, prolonging the reaction duration to steer the system toward thermodynamic equilibrium did not improve reaction selectivity or reproducibility. This suggests that the cluster formation may proceed under kinetic control, potentially influenced by the side phases. Notably, the cluster compounds were consistently found in close proximity to TaO_2I, implying that this phase could serve as a precursor in the cluster-forming process.

Comparable unconventional reduction methods with Li_2CN_2 were recently reported in the Nb–O–I system, resulting in several novel niobium oxyiodides, such as the oxygen centred Nb_4OI_{12-x} clusters with $x = 0, 1, 2$.[19,37]

In extension of these findings, analogous reactions were also performed in the Ta–O–I system, yielding distinct cluster networks, referred to as *o*-$M_5O_4I_{11}$ (M = Nb, Ta), *m*-$Ta_5O_4I_{11}$, and $Ta_5O_4I_{11}(TaI_5)$, where *o* and *m* denote the orthorhombic and monoclinic polymorphs, respectively.

The crystal structure of *o*-$Ta_5O_4I_{11}$ was solved and refined from single-crystal X-ray diffraction data in the orthorhombic space group $Pmc2_1$ (No. 26). The characteristic motif of *o*-$Ta_5O_4I_{11}$ is depicted in Fig. 2: The Ta_5 cluster core adopts the motif of a distorted square pyramid. At the base of the pyramid, four μ_3-oxygen atoms bridge the edges between the metal atoms. Each of the four outer metal atoms exhibits distorted octahedral coordination by oxygen and iodide atoms with additional metal-to-metal bonding with the central metal atom on top of the pyramid (Fig. 2) with intermetallic distances given in Table 1.

The connectivity within and between clusters can be described using the notation $[(Ta_5O_4)I^i_2I^{a1}_4I^{a-a}_{10/2}]$ where two inner (i) iodide ligands cap the edges at the apex of the distorted square-pyramidal cluster core, and four outer (a) iodides are terminally coordinated, one positioned above and three below the base of the pyramid. Additionally, ten iodide ligands are shared (10/2) between adjacent clusters, referred to as bridging outer (a–a) iodides. This notation follows the convention originally developed for describing octahedral cluster compounds.[1,7,50]

Each cluster is connected to four neighbouring clusters at its corners through bridging iodide ligands, forming extended layers expanding into the *ac*-plane. Along the *a*-axis, the Ta(2)

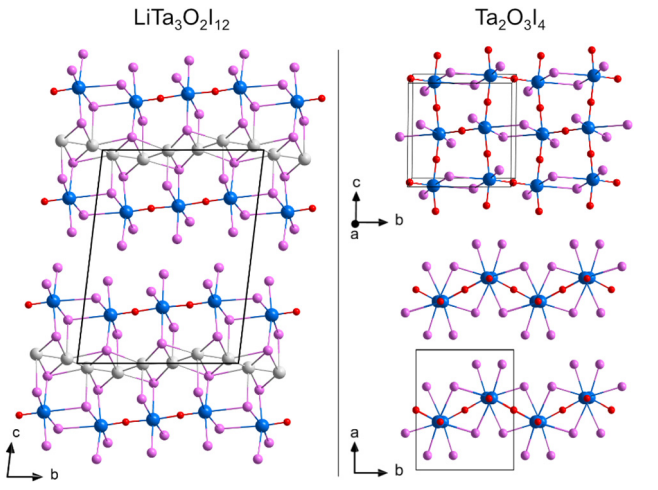

Fig. 1 Sections of the crystal structures of $LiTa_3O_2I_{12}$ (left) and $Ta_2O_3I_4$ (right). Tantalum atoms are depicted in blue, iodine pink, oxygen red and lithium grey.

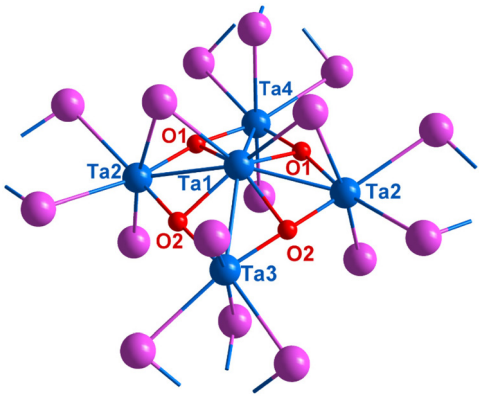

Fig. 2 Building block of isotypic $M_5O_4I_{11}$ structures (M = Nb, Ta), with the $[M_5O_4]$ cluster core displayed for M = Ta, corresponding to *o*-$Ta_5O_4I_{11}$ (iodide atoms are shown in pink).

Table 1 Comparison of selected interatomic distances and bond angles in *o*-$Ta_5O_4I_{11}$ and $Nb_5O_4I_{11}$. For atom labelling, see Fig. 2

Distance/pm; ∠/°	*o*-$Ta_5O_4I_{11}$	$Nb_5O_4I_{11}$
Intra cluster		
$M(1)$–$M(2)$	283.2(1)	285.2(1)
$M(1)$–$M(3)$	288.7(1)	287.8(4)
$M(1)$–$M(4)$	290.7(1)	290.4(4)
∠$M(2)$–$M(1)$–$M(2)$	149.3(1)	148.9(1)
∠$M(3)$–$M(1)$–$M(4)$	136.9(1)	131.3(1)
Inter cluster		
$M(2)$–$M(2)$	435.7(1)	430.1(3)
$M(3)$–$M(4)$	388.4(1)	377.5(4)

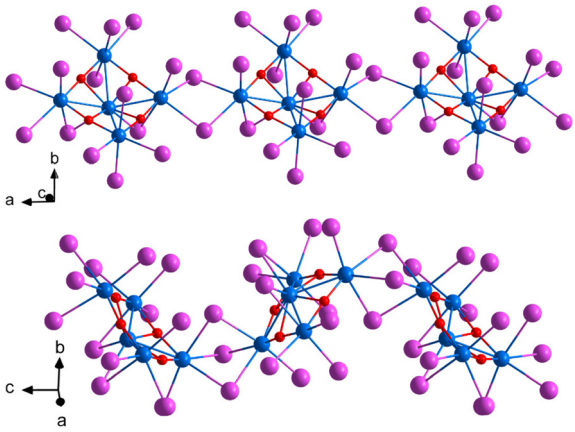

Fig. 3 Cluster connectivities in the structure of $M_5O_4I_{11}$ along *a* (top) and *c* (bottom), corresponding to *o*-$Ta_5O_4I_{11}$. *M* atoms are depicted in blue, oxygen in red and iodine in pink.

atoms are linked by two bridging iodides positioned perpendicular to an (m_x) mirror plane (Fig. 3 top). Ta(3) and Ta(4) are connected by three iodide bridges along a (2_1) screw axis that runs parallel to the *c*-axis, creating a tilted arrangement of clusters, as illustrated in Fig. 3, bottom. In the extended crystal structure, this leads to the formation of undulating layers which are separated by a van der Waals gap (Fig. 4).

A comparison of selected interatomic distances and bond angles in *o*-$Ta_5O_4I_{11}$ and the isostructural $Nb_5O_4I_{11}$ is given in Table 1. As expected, given the similarity of ionic radii of niobium and tantalum,[51] the shortest *M*–*M* bond lengths for both compounds fall within the same rang. However, the ∠*M*(3)–*M*(1)–*M*(4) bond angle, which traces the undulation of the layers along the *c*-axis, differs by around 6°. Furthermore, the inter cluster *M*(3)–*M*′(4) distance in this direction is 11 pm shorter in $Nb_5O_4I_{11}$, resulting in a slightly more pronounced corrugation of the layers.

The crystal structure of the monoclinic *m*-$Ta_5O_4I_{11}$ contains a [Ta_5O_4] cluster core similar to that found in *o*-$Ta_5O_4I_{11}$. However, the core in *m*-$Ta_5O_4I_{11}$ is less distorted due to a

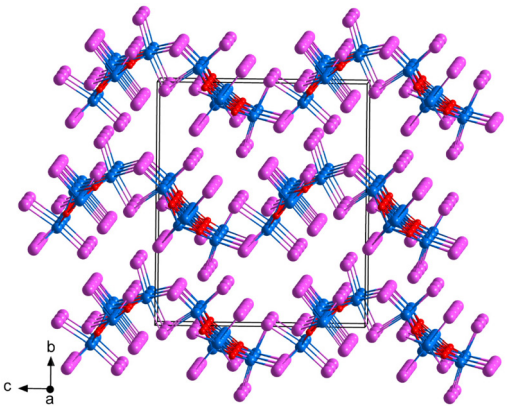

Fig. 4 Waved layer structure of $M_5O_4I_{11}$, corresponding to *o*-$Ta_5O_4I_{11}$. *M* atoms are depicted in blue, oxygen in red and iodine in pink.

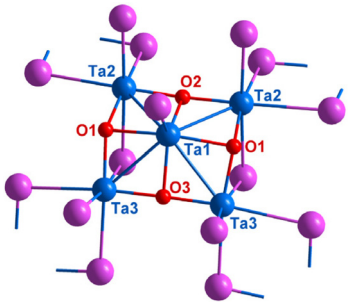

Fig. 5 Building block of the *m*-$Ta_5O_4I_{11}$ structure. Tantalum atoms are depicted in blue, oxygen atoms in red and iodine atoms in pink.

different spatial arrangement of the iodine atoms, leading to variations in how the cluster interconnect (Fig. 5). Each [$(Ta_5O_4)I^i_2I^a_5I^{a-a}_{8/2}$] cluster includes two inner (i) μ_2-bridging iodides located at the base of the pyramid, five terminal outer (a) iodides each bonded to one of the five tantalum atoms towards the pyramid's apex, and eight outer (a–a) iodides that are shared between two clusters (8/2) (see Table S1 in SI for comparison of interatomic distances).

Each cluster is interconnected with four neighbouring clusters at all four corners through two iodide bridges, forming an extended layered network. In this structure, the surrounding cluster pyramids are oriented oppositely to the central one: when the central cluster points upwards, the adjacent clusters point downwards, and *vice versa* (Fig. 6); this alternating orientation results in a sinusoidal layering pattern. These undulating layers are further separated by a van der Waals gap (Fig. 7).

The cluster network of $Ta_5O_4I_{11}(TaI_5)$ is closely related to that of *m*-$Ta_5O_4I_{11}$, but with the additional incorporation of molecular [TaI_5] units. This leads to a significant transformation of the overall structural architecture. Fig. 8 shows a section of the $Ta_5O_4I_{11}(TaI_5)$ structure (top) along with the arrangement of [$Ta_5O_4I_{11}$] layers (bottom left) and [TaI_5] units (bottom right). A closer comparison of the layer formation and

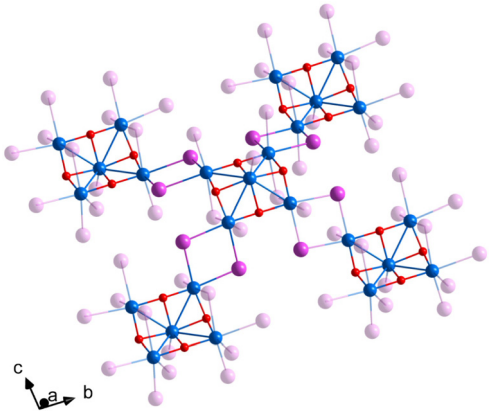

Fig. 6 Section of the *m*-$Ta_5O_4I_{11}$ structure depicting the inter-cluster connectivity within one layer. Tantalum atoms are depicted in blue, oxygen in red and iodine in pink.

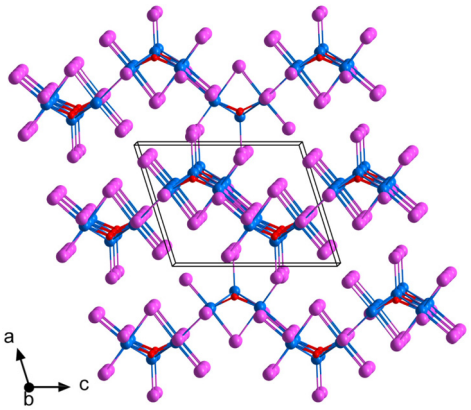

Fig. 7 Sinusoidal connectivity of clusters in the layered structure of *m*-$Ta_5O_4I_{11}$. Note that there is no connectivity between adjacent layers. Tantalum atoms are depicted in blue, oxygen in red and iodine in pink.

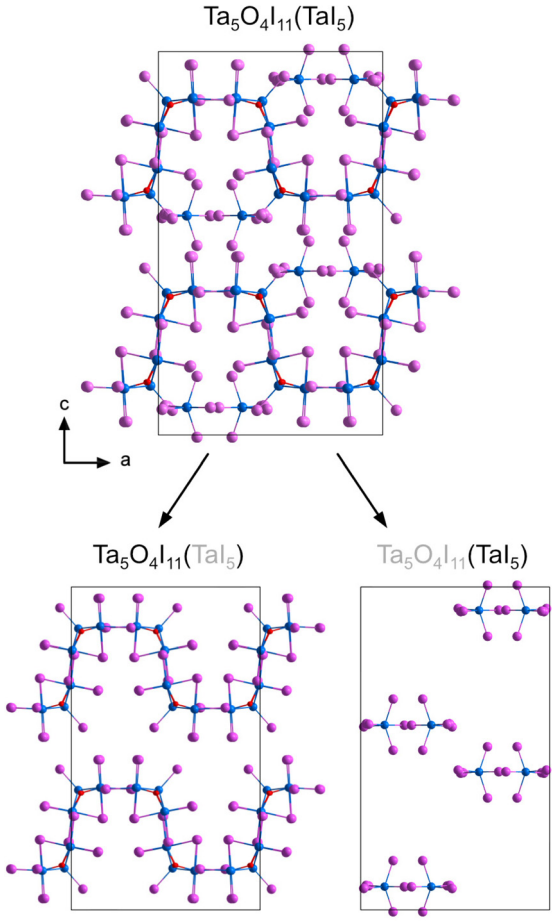

Fig. 8 Projected crystal structure of $Ta_5O_4I_{11}(TaI_5)$ (top) and segmentation of the structure into $[Ta_5O_4I_{11}]$ (left) and $[TaI_5]$, appearing as two superimposed TaI_5 units (right).

organisation in $Ta_5O_4I_{11}(TaI_5)$ (Fig. 8) and *m*-$Ta_5O_4I_{11}$ (Fig. 7) reveals clear structural differences, even though the cluster connectivity pattern $[(Ta_5O_4)I^i_2I^a_5I^{a-a}_{8/2}]$ remains the same in both structures.

Notable differences between both structures are observed in the amplitude of the sinusoidal waves of the layers and by the directional shift of these waves relative to one another. In *m*-$Ta_5O_4I_{11}$, the clusters alternate in an up-and-down fashion, whereas in $Ta_5O_4I_{11}(TaI_5)$, for each directional shift of the wave, two of the four adjacent clusters point in the same direction as the central cluster and two are inverted and point the other direction (compare Fig. 7 and Fig. 8). This more pronounced corrugation creates voids that accommodate $[TaI_5]$ molecules, which contribute to the stabilisation of the structure of $Ta_5O_4I_{11}(TaI_5)$.

This finding aligns with the observations made for the compound $Nb_7S_2I_{19} \triangleq (Nb_3SI_7)_2(NbI_5)$, which Miller and Lin described as exhibiting a synergistic relationship between the extended framework and the enclosed $[NbI_5]$ molecule.[28] In this structure, $[NbI_5]$ molecules are packed within hexagonal channels formed between the $[Nb_3SI_7]$. In contrast, when $[NbI_5]$ molecules are absent, Nb_3SI_7 adopts a van der Waals layered structure that lacks these hexagonal voids.[17]

As with the $[NbI_5]$ units in $Nb_7S_2I_{19}$, the $[TaI_5]$ molecules in $Ta_5O_4I_{11}(TaI_5)$ are incorporated as trigonal bipyramidal monomers (see Fig. 9) similar to the geometries reported for $TaCl_5$ and $TaBr_5$ in the vapour phase.[52,53] However, in the solid state, TaI_5 typically crystallises as $(TaI_5)_2$ dimers composed of edge-sharing bioctahedra.[54]

The Ta–I bond lengths of molecular $[TaI_5]$ in the structure of $Ta_5O_4I_{11}(TaI_5)$ range from 260(1) pm to 271(1) pm, with an average of 266(1) pm. This closely matches the average Nb–I distance of 267(1) pm of the NbI_5 monomers in $Nb_7S_2I_{19}$, as well as the average Ta–I distance of 267(1) pm in Ta_2I_{10}, not considering edge-sharing iodides.[54]

Although all $M_5O_4I_{11}$-based compounds share a similar penta-nuclear cluster core, they display distinct structural frameworks. These differences arise from variations in the inner (i) and outer (a) iodine ligand environments, the presence of incorporated $[TaI_5]$ molecules, as well as the cluster connectivity (a–a).

In particular, *o*-$Ta_5O_4I_{11}$ features clusters interconnected by two and three μ_2-bridging iodides at the corners (Fig. 3), resulting in shorter inter cluster Ta–Ta distances and potentially stronger electronic interactions, since *m*-$Ta_5O_4I_{11}$ clusters are only connected by two iodide bridges at all four corners (Fig. 6). This difference is expected to influence the electronic properties of the material, particularly electrical conductivity, which is discussed later in this study.

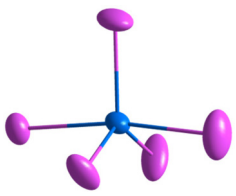

Fig. 9 Molecular $[TaI_5]$ in the structure of $Ta_5O_4I_{11}(TaI_5)$ with 80% displacement ellipsoids. Blue: Ta, pink: I.

The $[Ta_5O_4]$ cluster motive demonstrates both structural stability and geometric flexibility, as it persists across different environments and tolerates considerable distortions. However, despite these characteristics, the *o*- and *m*-modifications of $Ta_5O_4I_{11}$ are not interconvertible by thermal treatment. Heating beyond 650 °C results in decomposition and the formation of $TaOI_2$, rather than phase transition between the two forms.

For *o*-$M_5O_4I_{11}$, the structures with niobium and tantalum are isotypic. However, no analogues of *m*-$Ta_5O_4I_{11}$ or $Ta_5O_4I_{11}(TaI_5)$ could be observed for niobium. Instead, niobium forms distinct cluster types such as Nb_4OI_{12-x}, reflecting differences in cluster stability and connectivity between the two elements.[19,37]

$Ta_5O_4I_{11}$ carries six cluster electrons, but their distribution across the four short Ta–Ta bonds is not straightforward. From a formal oxidation state perspective, the four basal tantalum atoms can be assigned to Ta^{4+}, while the apical atom is considered more reduced, with an oxidation state of Ta^{3+}. To further probe this, XPS measurements are employed in the next section.

Analysis of Ta–Ta distances provide additional insights into the presence of metal–metal bonding in *o*-$Ta_5O_4I_{11}$. The average Ta–Ta bond length is approximately 286 pm, which is slightly shorter than in other tantalum halide clusters such as Ta_6I_{14} (~292 pm), Ta_3SeI_7 (~295 pm) or Ta_4SBr_{11} (~305 pm). This comparison supports the presence of bonding interactions between the tantalum atoms. Additional insight into electron distribution and bonding can be gained through ELF (Electron Localisation Function) analysis.

Scanning electron microscopy (SEM), energy dispersive X-ray spectroscopy (EDX) and total reflection X-ray fluorescence (TXRF)

When in contact with moist air, samples of $Ta_5O_4I_{11}$ show pronounced surface degradation and partial delamination (Fig. S7 in SI). To prevent this, a custom-designed vacuum transfer device was developed, enabling inert handling and transfer of samples. Details of the vessel design and operation are provided in the Experimental section and illustrated in Fig. S2 of the SI.

The scanning electron micrographs in Fig. 10 were obtained from samples transferred under inert conditions. Fig. 10 shows crystal agglomerates and surfaces morphologies of *o*-$Ta_5O_4I_{11}$ (Fig. 10a–c) and *m*-$Ta_5O_4I_{11}$ (Fig. 10d–f). The two compounds clearly exhibit different morphologies: *o*-$Ta_5O_4I_{11}$ frequently shows well defined individual layers (Fig. 10c), suggesting weaker interlayer interactions. In contrast, *m*-$Ta_5O_4I_{11}$ displays more compact, block-like surface features (Fig. 10f), indicating stronger interactions between adjacent layers.

To verify the composition, determined by X-ray diffraction, EDX measurements of multiple crystals were performed, resulting in an average Ta : O : I ratio of 5 : 4.3(5) : 10.9(3). TXRF measurements verified the Ta : I ratio to be 5 : 11.3(2).

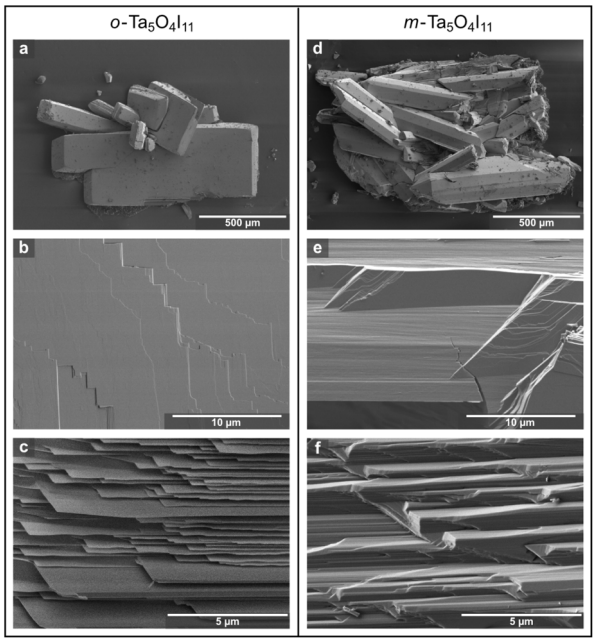

Fig. 10 Scanning electron micrographs of *o*-$Ta_5O_4I_{11}$ crystals (a–c) and *m*-$Ta_5O_4I_{11}$ crystals (d–f), showing a layered morphology.

X-ray photoelectron spectroscopy (XPS)

Further insights on the oxidation state of tantalum in *o*-$Ta_5O_4I_{11}$ were achieved using X-ray photoelectron spectroscopy (XPS).

The Ta 4f spectrum shown in Fig. 11 can be described by two doublets (Ta $4f_{7/2}$ and Ta $4f_{5/2}$), which are assigned to the oxidation states of Ta^{4+} and Ta^{3+}.[55,56] The fit parameters are summarised in Table S2 (SI). The intensity ratio of Ta^{4+} and Ta^{3+} components of 4.14 : 1 is in good agreement with the proposition of a Ta^{3+} at the central position on top of the dis-

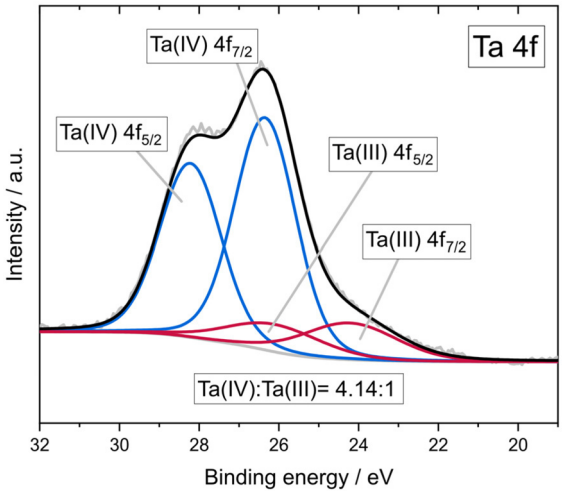

Fig. 11 XPS spectrum of Ta 4f depicting Ta(IV) and Ta(III) oxidation states in a ratio of 4.14 : 1.

torted pyramid and four Ta^{4+} at the corners of the pyramid base.

The survey spectrum in Fig. S8 (SI) reveals the presence of iodine and oxygen (notably, the additional carbon and silicon signals can be attributed to the carbon tape substrate) giving further evidence for the proposed structure.

Optical band gap determination from DRIFTS (Diffuse reflectance infrared fourier transform spectroscopy)

The absorption coefficient F was obtained using Kubelka–Munk analysis following:

$$F(R_\infty) = \frac{\alpha}{S} = \frac{(1-R_\infty)^2}{2R_\infty},$$

where

$$R_\infty = \frac{R_{\text{sample}}}{R_{\text{standard}}}$$

is the reflectance of an infinitely thick specimen, α is the absorption and S is the scattering coefficient. For particle sizes greater than the light wavelengths measured, the scattering coefficient is understood to be approximately independent of frequency ($F(R_\infty) \sim \alpha$) and therefor $F(R_\infty)$ could be understood as a "pseudo-absorbance" coefficient.[57–63]

The band gap determination was performed on the DRIFTS data according to Zanata *et al.*[64] The energy is plotted against the absorption coefficient α and fitted with a sigmoid-Boltzmann function:

$$\alpha(E) = \alpha_{\max} + \frac{\alpha_{\min} - \alpha_{\max}}{1 + \exp\left(\frac{E - E_0^{\text{Boltz}}}{\delta E}\right)}$$

where $\alpha_{\min}$ ($\alpha_{\max}$) stands for the minimum (maximum) absorption coefficient; E_0^{Boltz} is the energy coordinate at which the absorption coefficient is halfway between $\alpha_{\min}$ and $\alpha_{\max}$; and δE is associated with the slope of the sigmoid, indicating the energy range over which most optical transitions occur.[64]

The band gap can then be calculated by following equation with $n_{\text{dir}}^{\text{Boltz}} = 0.3$ and $n_{\text{indir}}^{\text{Boltz}} = 4.3$:

$$E_g^{\text{Boltz}} = E_0^{\text{Boltz}} - n_{\text{dir/indir}}^{\text{Boltz}} \cdot \delta E$$

The optical band gaps of o-$Ta_5O_4I_{11}$ were determined to be 0.241 eV (direct) and 0.226 eV (indirect) indicating semiconducting behaviour (see Fig. S9, SI). The band gap of m-$Ta_5O_4I_{11}$ could not be measured within the detectable range of the DRIFTS setup. To further assess the electronic properties, conductivity measurement were subsequently performed.

Electrical properties

We reasoned that the structural differences in o-$Ta_5O_4I_{11}$ *vs.* m-$Ta_5O_4I_{11}$ as well as their distinct ligand environments should manifest in different electrical properties. Hence, two-point current–voltage scans of both modifications (o and m) were carried out at varying temperatures. Exemplarily results, obtained at 300 K are displayed in Fig. S3 (SI).[19,65] The measurements revealed that o-$Ta_5O_4I_{11}$ is roughly one order of magnitude more conductive than m-$Ta_5O_4I_{11}$ with typical values of 5×10^{-5} S m^{-1} to 2×10^{-4} S m^{-1} for o-$Ta_5O_4I_{11}$ *vs.* 4×10^{-6} S m^{-1} to 2×10^{-5} S m^{-1} for m-$Ta_5O_4I_{11}$.

Using the two-point conductivities obtained at different temperatures, we arrive at the Arrhenius plot in Fig. 12, indicating temperature-activated, Arrhenius type transport for both phases, which is typical for semiconductors.[66,67] From the slopes of both plots, we calculate activation energies of E_A = 0.10 eV for o-$Ta_5O_4I_{11}$ and E_A = 0.40 eV for m-$Ta_5O_4I_{11}$, respectively. Due to the poor signal strength from m-$Ta_5O_4I_{11}$ at temperatures below 240 K, additional conductivities were measured above 300 K up to 350 K to improve the fit confidence. o-$Ta_5O_4I_{11}$ was measured between 140 K–300 K.

To a first order approximation, the electrical band gap of an intrinsic semiconductor can be gauged as two times the activation energy, hence 0.2 eV for o-$Ta_5O_4I_{11}$ and 0.8 eV for m-$Ta_5O_4I_{11}$, respectively.

Both crystal species exhibit low photocurrents toward optical excitation at 779 nm illuminated with 40 mW output power. o-$Ta_5O_4I_{11}$ showed higher photocurrents around 1 nA while m-$Ta_5O_4I_{11}$ exhibited around 15 pA at 300 K (Fig. S10, SI). At lower temperatures, the photocurrent decreases gradually until it is below the noise level at ~0.1 pA.

Band structure

The spin-unpolarised electronic band structures of o-$Ta_5O_4I_{11}$ and m-$Ta_5O_4I_{11}$ were calculated using density functional theory (DFT). At the DFT level, o-$Ta_5O_4I_{11}$ is a band metal (Fig. 13), unlike the small-gap semiconductor observed in our optical and electrical measurements. Since the experimental gap of o-$Ta_5O_4I_{11}$ is small, the DFT calculations were performed with spin orbit coupling, as this could plausibly open a small gap, however this was not observed. The opening of the gap could therefore be due to electronic correlations and magnetic interactions between Ta atoms, as was determined in the related Mott insulating material Ta_4SBr_{11}.[22] However, due to the large size of the unit cell of o-$Ta_5O_4I_{11}$, computational

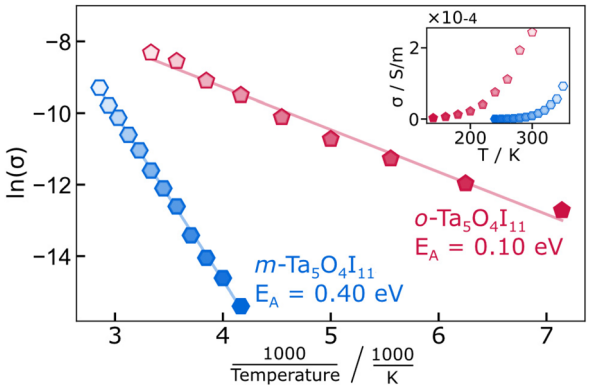

Fig. 12 Arrhenius-plot of the temperature-dependent conductivity between 140 K–300 K for o-$Ta_5O_4I_{11}$ (red) and 240 K–350 K for m-$Ta_5O_4I_{11}$ (blue). The inset shows the linear plot of conductivity *versus* temperature.

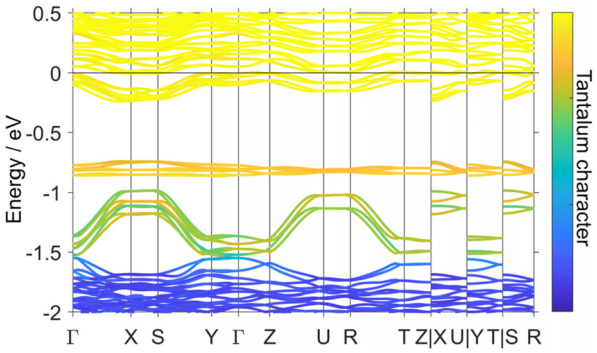

Fig. 13 Calculated electronic band structure of *o*-$Ta_5O_4I_{11}$, with bands coloured by their Ta character. Spin–orbit coupling was included in the calculation. Special points in and paths through reciprocal space were chosen following the literature.[68]

exploration of potential Mott behaviour was not possible in this case.

In contrast, DFT calculations showed *m*-$Ta_5O_4I_{11}$ to be a semiconductor with a gap of 0.4 eV (Fig. 14), in accordance with experiments. The existence of a band gap in *m*-$Ta_5O_4I_{11}$ is therefore most likely not due to magnetic interactions or spin–orbit coupling. Significant differences in the electronic structure and chemical bonding between *o*-$Ta_5O_4I_{11}$ and *m*-$Ta_5O_4I_{11}$ can be seen. In *o*-$Ta_5O_4I_{11}$, the states near the Fermi energy have predominantly Ta d character, with several distinct band manifolds being visible. The upper manifolds are nearly flat, indicating localised electrons. In *m*-$Ta_5O_4I_{11}$, a much greater degree of hybridisation can be seen near the Fermi level, with the valence electrons having some O and I character in addition to Ta character (see Fig. S11–S14 in the SI for details). The formation of a band gap in *m*-$Ta_5O_4I_{11}$ could then be ascribed to the formation of covalent bonds between Ta and other cluster atoms, whereas Ta atoms in *o*-$Ta_5O_4I_{11}$ are more ionic. In *o*-$Ta_5O_4I_{11}$, the Ta atoms would therefore be expected to behave closer to idealised Ta^{3+} and Ta^{4+}, which contain unpaired d electrons, leading to partially filled bands at the DFT level.

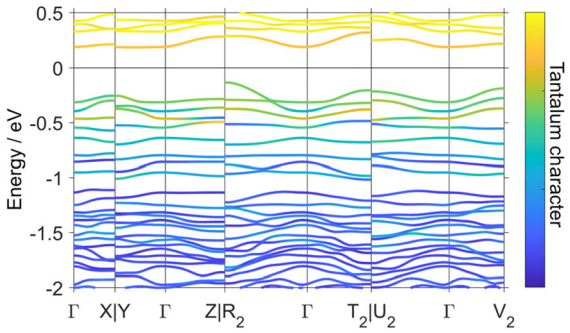

Fig. 14 Calculated electronic band structure of *m*-$Ta_5O_4I_{11}$, with bands coloured by their Ta character. Spin–orbit coupling was not included in the calculation. Special points in and paths through reciprocal space were chosen following the literature.[68]

Electron localisation function (ELF)

We have also calculated from DFT the electron localisation function (ELF) of *o*-$Ta_5O_4I_{11}$ and *m*-$Ta_5O_4I_{11}$, further elucidating the electronic structure and chemical bonding in these materials.[69,70] Like the band structures, the ELFs of the two polymorphs are strikingly different. The ELFs around the Ta and O atoms in *o*-$Ta_5O_4I_{11}$ are largely spherical, indicating ionic bonding (Fig. 15). The monoclinic modification shows

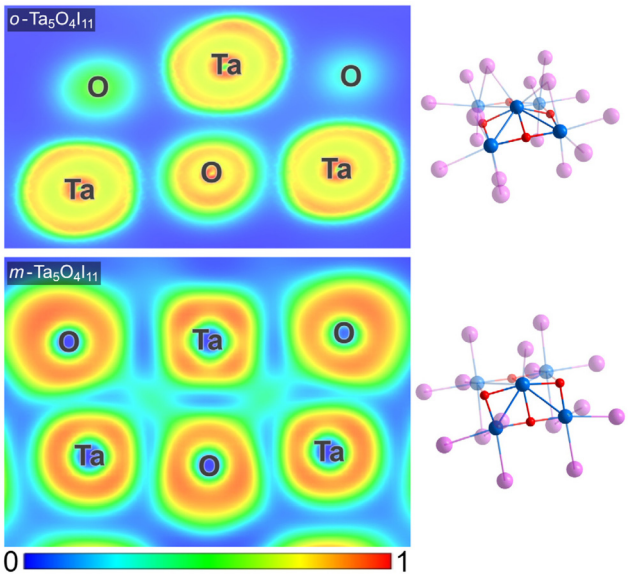

Fig. 15 Calculated ELF of *o*-$Ta_5O_4I_{11}$ (top) and *m*-$Ta_5O_4I_{11}$ (bottom), showing the presence of increased covalent bonding between Ta and O in the monoclinic phase, as demonstrated by the deviation of the shapes of the ELFs from idealised ionic spheres.

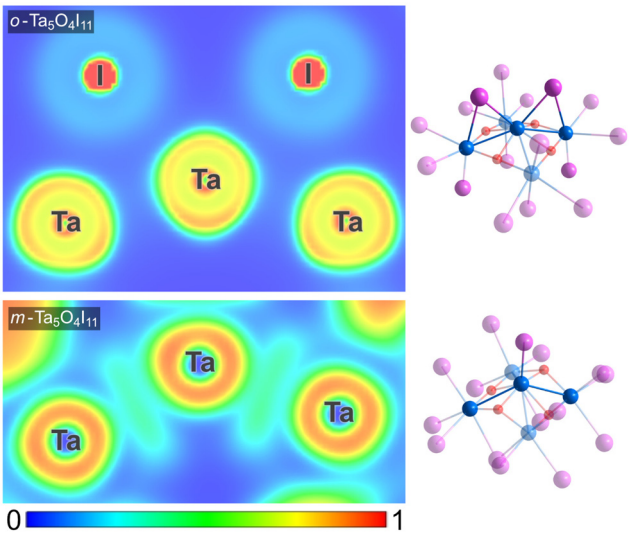

Fig. 16 Calculated ELF of *o*-$Ta_5O_4I_{11}$ (top) and *m*-$Ta_5O_4I_{11}$ (bottom), showing the presence of interstitial localised electrons in the monoclinic phase, corresponding to Ta–Ta bonds. No similar feature can be seen in the orthorhombic phase.

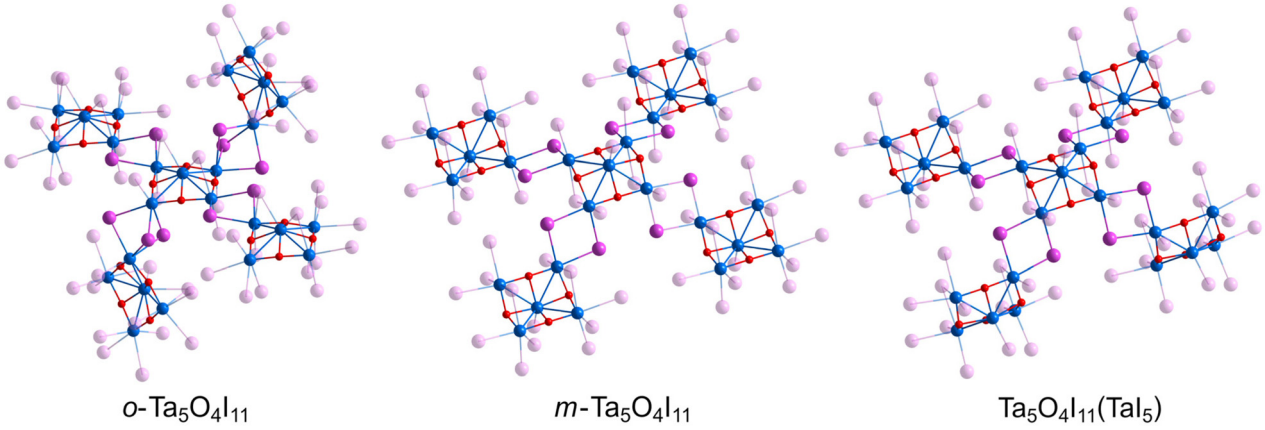

Fig. 17 Comparison of the inter cluster connectivity of *o*-$Ta_5O_4I_{11}$, *m*-$Ta_5O_4I_{11}$ and $Ta_5O_4I_{11}(TaI_5)$.

the ELFs of the atoms to be more distorted, as well as the presence of some interstitial electron density, which are indicators of covalent bonding. As Fig. 16 shows, this extra electron density lies in the planes between pairs of Ta atoms, corresponding to the formation of Ta–Ta bonds. This feature is absent in *o*-$Ta_5O_4I_{11}$, where there are instead nodal planes between the Ta atoms, again indicative of ionic interactions (compare Fig. S15 in SI).

Charge-disproportionated Ta^{3+} and Ta^{4+} ions, as seen in the XPS measurements of *o*-$Ta_5O_4I_{11}$ (Fig. 11), do not appear in our DFT calculations, where the ELFs and electron counts around the Ta atoms are nearly identical at each site. Therefore, this disproportionation could be driven by whichever factors which lead to the opening of the band gap and are not accounted for in our DFT calculations.[71]

Conclusions

Heterogeneous solid-state reactions involving an unidentified gas phase have led to the formation of the compounds $Nb_5O_4I_{11}$, *o*-$Ta_5O_4I_{11}$, *m*-$Ta_5O_4I_{11}$, and $Ta_5O_4I_{11}(TaI_5)$, all featuring an $[M_5O_4]$ cluster core. In these structures, each cluster is connected to four neighbouring clusters at the corners *via* two or three bridging iodide ligands, creating distinct extended layered networks. These connectivity patterns are summarised in Fig. 17. A common structural characteristic among these compounds is a sinusoidal layering pattern within the crystal lattice, with layers separated by van der Waals gaps. The presence of bridging outer ligands spatially separates adjacent clusters, resulting in semiconducting behaviour with low electrical conductivity primarily confined to the layers, particularly evident in both forms of $Ta_5O_4I_{11}$.

In all compounds, the $[Ta_5O_4]$ cluster core possesses six cluster electrons involved in metal–metal bonding, that could likely be localised along the four shorter metal–metal contacts between the pyramidal base and apex. According to a localised bonding model, the metal atoms in the basal plane may be assigned to Ta^{4+}, while the apical metal atom corresponds to Ta^{3+} in *o*-$Ta_5O_4I_{11}$, ensuring charge neutrality. This interpretation is supported by XPS, and it is partially consistent with charge distribution predicted by DFT calculations.

Conflicts of interest

There are no conflicts to declare.

Data availability

Data are available within the article.

The data that support the findings of this study are available on request from the corresponding author, H.-J. Meyer. Computational data are availiable from DOI: 10.5281/zenodo.17424860.

Supplementary information (SI): See DOI: https://doi.org/10.1039/d5dt02097b.

CCDC 2351105 ($Ta_5O_4I_{11}(TaI_5)$), 2380271 (*o*-$Ta_5O_4I_{11}$), 2389419 ($Ta_2O_3I_4$), 2390289 ($LiTa_3O_2I_{12}$), 2400835 ($Nb_5O_4I_{11}$) and 2424946 (*m*-$Ta_5O_4I_{11}$) and contain the supplementary crystallographic data for this paper.[72a–f]

Acknowledgements

Funding by the Deutsche Forschungsgemeinschaft through grant ME 914/32-1 and SCHE1905/9-1 is gratefully acknowledged. Computational resources were provided by the state of Baden-Württemberg through bwHPC and the DFG through grant no INST 40/467-1 FUGG (JUSTUS cluster). C. P. R. acknowledges support from the project FerrMion of the Ministry of Education, Youth and Sports, Czech Republic, co-funded by the European Union (CZ.02.01.01/00/22_008/0004591). The authors thank Ms. Elke Nadler (University Tübingen) for recording SEM images and EDX data.

References

1 H. Schäfer and H.-G. v. Schnering, *Angew. Chem.*, 1964, **76**, 833–849.
2 F. A. Cotton, *Q. Rev., Chem. Soc.*, 1966, **20**, 389–401.
3 P. Lemoine, J.-F. Halet and S. Cordier, in *Ligated Transition Metal Clusters in Solid-state Chemistry : The legacy of Marcel Sergent*, ed. J.-F. Halet, Springer International Publishing, Cham, 2019, pp. 143–190, DOI: 10.1007/430_2019_39.
4 L. Pauling, *The nature of the chemical bond and the structure of molecules and crystals*, Cornell University Press, 1949.
5 D. Bauer and H.-G. Schnering, *Z. Anorg. Allg. Chem.*, 1968, **361**, 259–276.
6 R. E. McCarley, J. Lewis and M. L. H. Green, *Philos. Trans. R. Soc. London, Ser. A*, 1982, **308**, 141–157.
7 A. Simon, H.-G. Schnering, H. Wöhrle and H. Schäfer, *Z. Anorg. Allg. Chem.*, 1965, **339**, 155–170.
8 D. G. Blight and D. L. Kepert, *Phys. Rev. Lett.*, 1971, **27**, 504–504.
9 S. L. Benjamin, Y.-P. Chang, A. L. Hector, M. Jura, W. Levason, G. Reid and G. Stenning, *Dalton Trans.*, 2016, **45**, 8192–8200.
10 D. R. Taylor, J. C. Calabrese and E. M. Larsen, *Inorg. Chem.*, 1977, **16**, 721–722.
11 P. J. Kuhn and R. E. McCarley, *Inorg. Chem.*, 1965, **4**, 1482–1486.
12 H.-G. v. Schnering, D. Vu, S.-L. Jin and K. Peters, *Z. Kristallogr. - New Cryst. Struct.*, 1999, **214**, 15–16.
13 G. Meyer, R. Wiglusz, I. Pantenburg and A.-V. Mudring, *Z. Anorg. Allg. Chem.*, 2008, **634**, 825–828.
14 F. Grahlow, M. Ströbele and H.-J. Meyer, *ICSD Commun.*, 2022, DOI: 10.25505/fiz.icsd.cc2cy0dr.
15 B. Bajan and H.-J. Meyer, *Z. Kristallogr. – Cryst. Mater.*, 1996, **211**, 818–818.
16 M. Smith and G. J. Miller, *J. Solid State Chem.*, 1998, **140**, 226–232.
17 G. V. Khvorykh, A. V. Shevelkov, V. A. Dolgikh and B. A. Popovkin, *J. Solid State Chem.*, 1995, **120**, 311–315.
18 F. Grahlow, F. Strauß, M. Scheele, M. Ströbele, A. Carta, S. F. Weber, S. Kroeker, C. P. Romao and H.-J. Meyer, *Phys. Chem. Chem. Phys.*, 2024, **26**, 11789–11797.
19 J. Beitlberger, M. Ströbele, F. Strauß, M. Scheele, C. P. Romao and H.-J. Meyer, *Eur. J. Inorg. Chem.*, 2024, **27**, e202400329.
20 H. B. Yaich, J. C. Jegaden, M. Potel, M. Sergent, A. K. Rastogi and R. Tournier, *J. Less-Common Met.*, 1984, **102**, 9–22.
21 M. N. Sokolov, A. L. Gushchin, P. A. Abramov, A. V. Virovets, E. V. Peresypkina, S. G. Kozlova, B. A. Kolesov, C. Vicent and V. P. Fedin, *Inorg. Chem.*, 2005, **44**, 8756–8761.
22 F. Grahlow, F. Strauß, P. Schmidt, J. Valenta, M. Ströbele, M. Scheele, C. P. Romao and H.-J. Meyer, *Inorg. Chem.*, 2024, **63**, 19717–19727.
23 F. A. Cotton and M. Shang, *J. Am. Chem. Soc.*, 1990, **112**, 1584–1590.
24 J. L. Seela, J. C. Huffman and G. Christou, *J. Chem. Soc., Chem. Commun.*, 1987, 1258–1260.
25 M. Ströbele, O. Oeckler, M. Thelen, R. F. Fink, A. Krishnamurthy, S. Kroeker and H.-J. Meyer, *Inorg. Chem.*, 2022, **61**, 17599–17608.
26 A. Broll, A. Simon, H.-G. von Schnering and H. Schäfer, *Z. Anorg. Allg. Chem.*, 1969, **367**, 1–18.
27 G. J. Miller, *J. Alloys Compd.*, 1995, **217**, 5–12.
28 G. J. Miller and J. Lin, *Angew. Chem., Int. Ed. Engl.*, 1994, **33**, 334–336.
29 J. Zhang and J. D. Corbett, *Inorg. Chem.*, 1995, **34**, 1652–1656.
30 K. Habermehl, A.-V. Mudring and G. Meyer, *Eur. J. Inorg. Chem.*, 2010, **2010**, 4075–4078.
31 T. C. Zietlow and H. B. Gray, *Inorg. Chem.*, 1986, **25**, 631–634.
32 J. D. Franolic, J. R. Long and R. Holm, *J. Am. Chem. Soc.*, 1995, **117**, 8139–8153.
33 M. Ströbele and H.-J. Meyer, *Dalton Trans.*, 2019, **48**, 1547–1561.
34 S. Hartwig and H. Hillebrecht, *Z. Naturforsch., B:J. Chem. Sci.*, 2007, **62**, 1543–1548.
35 M. Ruck, *Acta Crystallogr., Sect. C:Cryst. Struct. Commun.*, 1995, **51**, 1960–1962.
36 S. Hartwig and H. Hillebrecht, *Z. Anorg. Allg. Chem.*, 2008, **634**, 115–120.
37 J. Beitlberger, M. Martin, M. Scheele, P. Schmidt, M. Stroebele and H.-J. Meyer, *Dalton Trans.*, 2025, **54**, 5486–5493.
38 J. Beitlberger, M. Ströbele, P. Schmidt, C. P. Romao and H.-J. Meyer, *Dalton Trans.*, 2025, **54**, 14376–14383.
39 G. Brauer, *Handbuch der präparativen anorganischen Chemie*, Enke, 1975.
40 M. Ströbele, E. Bayat and H.-J. Meyer, *Inorg. Chem.*, 2024, **63**, 16565–16572.
41 Y. Yao, J. Liu, Z. Wang, S. Yao and F. Du, *Micron*, 2024, **187**, 103720.
42 M. J. Verstraete, J. Abreu, G. E. Allemand, B. Amadon, G. Antonius, M. Azizi, L. Baguet, C. Barat, L. Bastogne and R. Bejaud, arXiv, 2025, preprint, arXiv:2507.08578, DOI: 10.48550/arXiv.2507.08578.
43 J. P. Perdew, K. Burke and M. Ernzerhof, *Phys. Rev. Lett.*, 1996, **77**, 3865.
44 S. Grimme, J. Antony, S. Ehrlich and H. Krieg, *J. Phys. Chem.*, 2010, **132**(15), 154104.
45 M. Torrent, N. A. W. Holzwarth, F. Jollet, D. Harris, N. Lepley and X. Xu, *Comput. Phys. Commun.*, 2010, **181**(11), 1862–1867.
46 H. J. Monkhorst and J. D. Pack, *Phys. Rev. B*, 1976, **13**, 5188.
47 M. Methfessel and A. Paxton, *Phys. Rev. B:Condens. Matter Mater. Phys.*, 1989, **40**, 3616.
48 G. Brauer and A. Simon, *Handbook of Inorganic Synthesis*, 1985, vol. 5, pp. 1563–1564.
49 K. Gibson, M. Ströbele, B. Blaschkowski, J. Glaser, M. Weisser, R. Srinivasan, H.-J. Kolb and H.-J. Meyer, *Z. Anorg. Allg. Chem.*, 2003, **629**, 1863–1870.
50 B. Baján and H.-J. Meyer, *Z. Naturforsch., B:J. Chem. Sci.*, 1995, **50**, 1373–1376.
51 R. Shannon, *Acta Crystallogr., Sect. A*, 1976, **32**, 751–767.

52 H. A. Skinner and L. E. Sutton, *Trans. Faraday Soc.*, 1940, **35**, 668–680.
53 G. L. Carlson, *Spectrochim. Acta*, 1963, **19**, 1291–1307.
54 K. Habermehl, I. Pantenburg, P. Held and G. Meyer, *Z. Anorg. Allg. Chem.*, 2008, **634**, 829–831.
55 I. Perez, V. Sosa, F. G. Perera, J. T. E. Galindo, J. L. Enríquez-Carrejo and P. G. Mani-González, *Vacuum*, 2019, **165**, 274–282.
56 Y. Abbas, Y.-R. Jeon, A. S. Sokolov, S. Kim, B. Ku and C. Choi, *Sci. Rep.*, 2018, **8**, 1228.
57 W. W. Wendlandt and H. G. Hecht, *Reflectance spectroscopy*, Interscience, New York, 1966.
58 P. Kubelka, *J. Opt. Soc. Am.*, 1948, **38**, 448–457.
59 P. Kubelka and F. Munk, *Z. Tech. Phys.*, 1931, **12**, 259–274.
60 G. Kortüm and H. Koffer, *Ber. Bunsen-Ges.*, 1963, **67**, 67–75.
61 G. Kortum and J. E. Lohr, *Reflectance Spectroscopy*, Springer My Copy, UK, 1969.
62 A. B. Murphy, *Sol. Energy Mater. Sol. Cells*, 2007, **91**, 1326–1337.
63 R. López and R. Gómez, *J. Sol-Gel Sci. Technol.*, 2012, **61**, 1–7.
64 A. R. Zanatta, *Sci. Rep.*, 2019, **9**, 11225.
65 F. Fetzer, A. Maier, M. Hodas, O. Geladari, K. Braun, A. J. Meixner, F. Schreiber, A. Schnepf and M. Scheele, *Nat. Commun.*, 2020, **11**, 6188.
66 A. M. Al-Fa'ouri, O. A. Lafi, H. H. Abu-Safe and M. Abu-Kharma, *Arabian J. Chem.*, 2023, **16**, 104535.
67 M. M. A. Imran and O. A. Lafi, *Phys. B*, 2013, **410**, 201–205.
68 Y. Hinuma, G. Pizzi, Y. Kumagai, F. Oba and I. Tanaka, *Comput. Mater. Sci.*, 2017, **128**, 140–184.
69 A. D. Becke and K. E. Edgecombe, *J. Phys. Chem.*, 1990, **92**, 5397–5403.
70 A. Savin, R. Nesper, S. Wengert and T. F. Fässler, *Angew. Chem., Int. Ed. Engl.*, 1997, **36**, 1808–1832.
71 A. Walsh, A. A. Sokol, J. Buckeridge, D. O. Scanlon and C. R. A. Catlow, *J. Phys. Chem. Lett.*, 2017, **8**, 2074–2075.
72 (*a*) CCDC 2351105: Experimental Crystal Structure Determination, 2025, DOI: 10.5517/ccdc.csd.cc2jxj33; (*b*) CCDC 2380271: Experimental Crystal Structure Determination, 2025, DOI: 10.5517/ccdc.csd.cc2kwvy8; (*c*) CCDC 2389419: Experimental Crystal Structure Determination, 2025, DOI: 10.5517/ccdc.csd.cc2l6d18; (*d*) CCDC 2390289: Experimental Crystal Structure Determination, 2025, DOI: 10.5517/ccdc.csd.cc2l7938; (*e*) CCDC 2400835: Experimental Crystal Structure Determination, 2025, DOI: 10.5517/ccdc.csd.cc2ll89s; (*f*) CCDC 2424946: Experimental Crystal Structure Determination, 2025, DOI: 10.5517/ccdc.csd.cc2mdc2h.

Supporting Information

Structural Modifications of $M_5O_4I_{11}$ (M = Nb, Ta) Cluster Networks from Heterogeneous Solid-State Reactions

Fabian Grahlow, Jan Beitlberger, Mario Martin, Eric Juriatti, Heiko Peisert, Marcus Scheele, Markus Ströbele, Carl P. Romao, and Hans-Jürgen Meyer

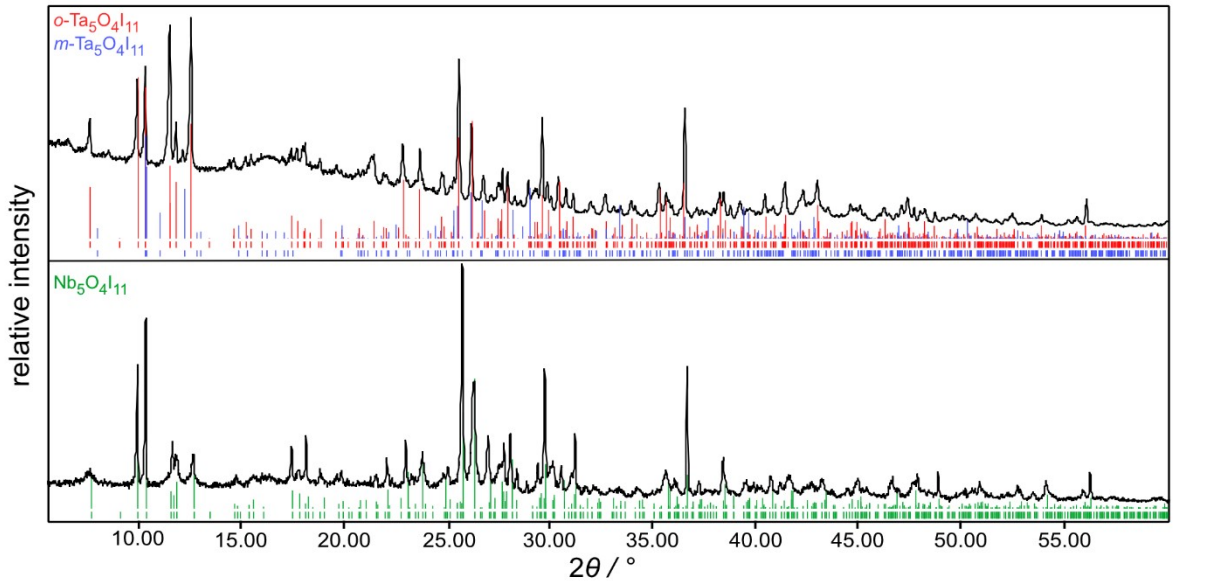

Figure S1. Powder X-ray diffraction patterns of $Ta_5O_4I_{11}$ (orthorhombic and monoclinic) and $Nb_5O_4I_{11}$ with the corresponding Bragg positions, calculated from the single-crystal X-ray diffraction measurements.

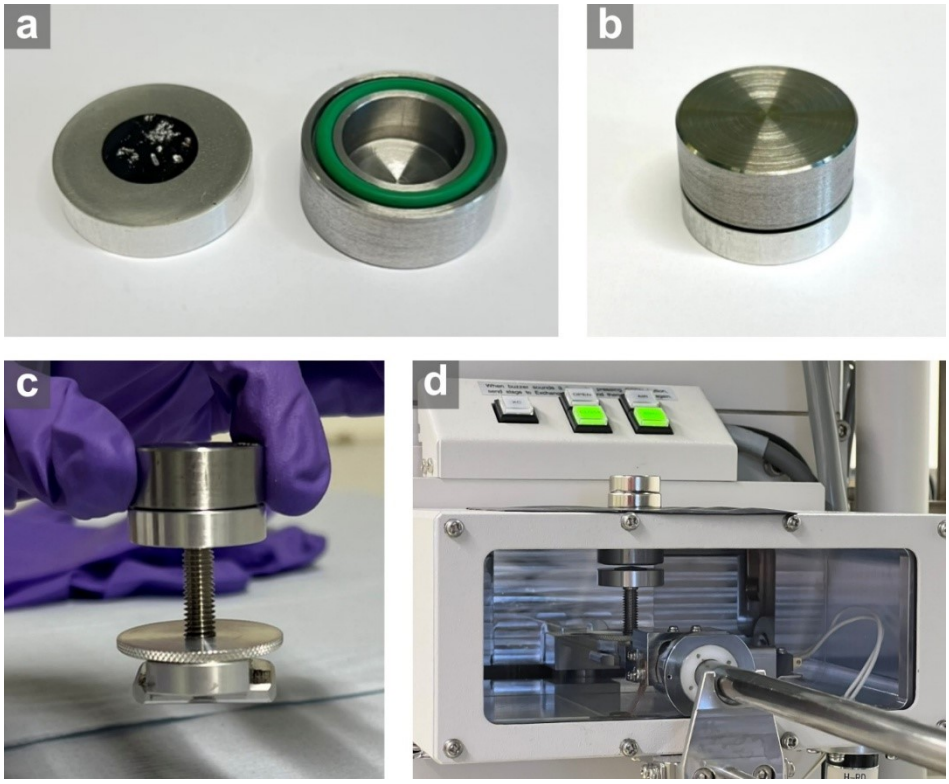

Figure S2. Procedure for inert transfer of samples into the scanning electron microscope. (a) The sample is fixed onto the sample holder using carbon tape. (b) The lid is placed on top of the sample holder, evacuated within the glovebox airlock, and then rapidly flooded with argon to ensure airtight seal. (c) The sealed sample is screwed on the transfer holder and transferred into the SEM airlock, while the reduced-pressure environment maintains the seal. (d) Once the SEM chamber is evacuated, the transfer chamber lid can be lifted using an external magnet.

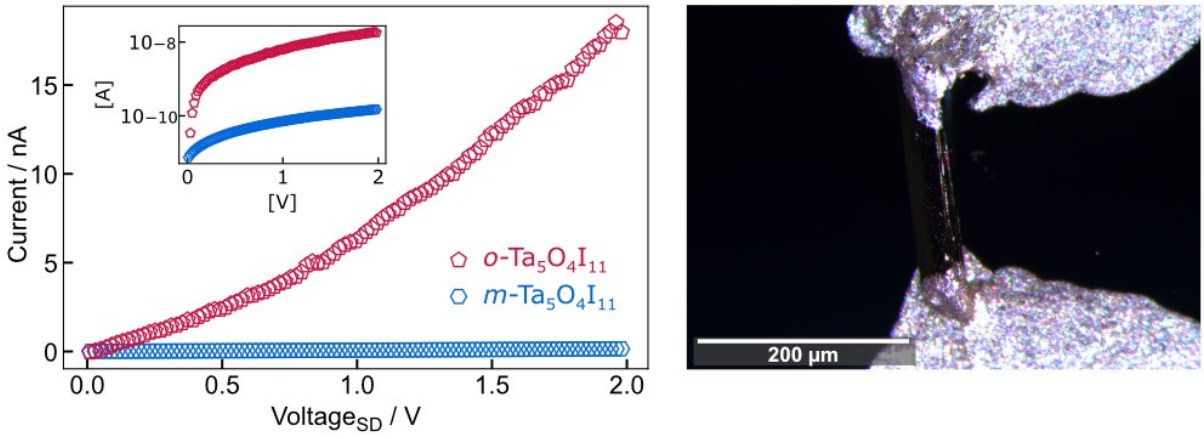

Figure S3. *I*-*U*-sweeps of an *o*-$Ta_5O_4I_{11}$ crystal (red) and a *m*-$Ta_5O_4I_{11}$ crystal (blue) at a temperature of 300 K (left). The inset shows the same data on a logarithmic scale to see the increase of current of *m*-$Ta_5O_4I_{11}$ (left). Single crystals are fixed onto Si/SiO_2 using conductive silver paste (right).

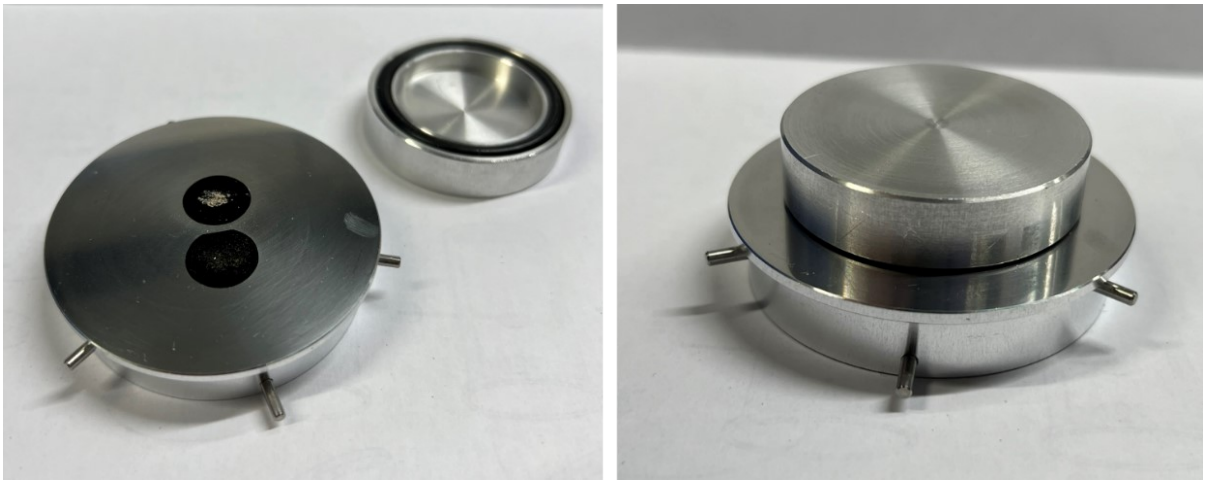

Figure S4. Sample holder and lid for inert transfer for XPS measurements. The sample is fixed onto the sample holder using carbon tape (left). The lid is placed on top of the sample holder, evacuated within the glovebox airlock, and then rapidly flooded with argon to ensure airtight seal (right).

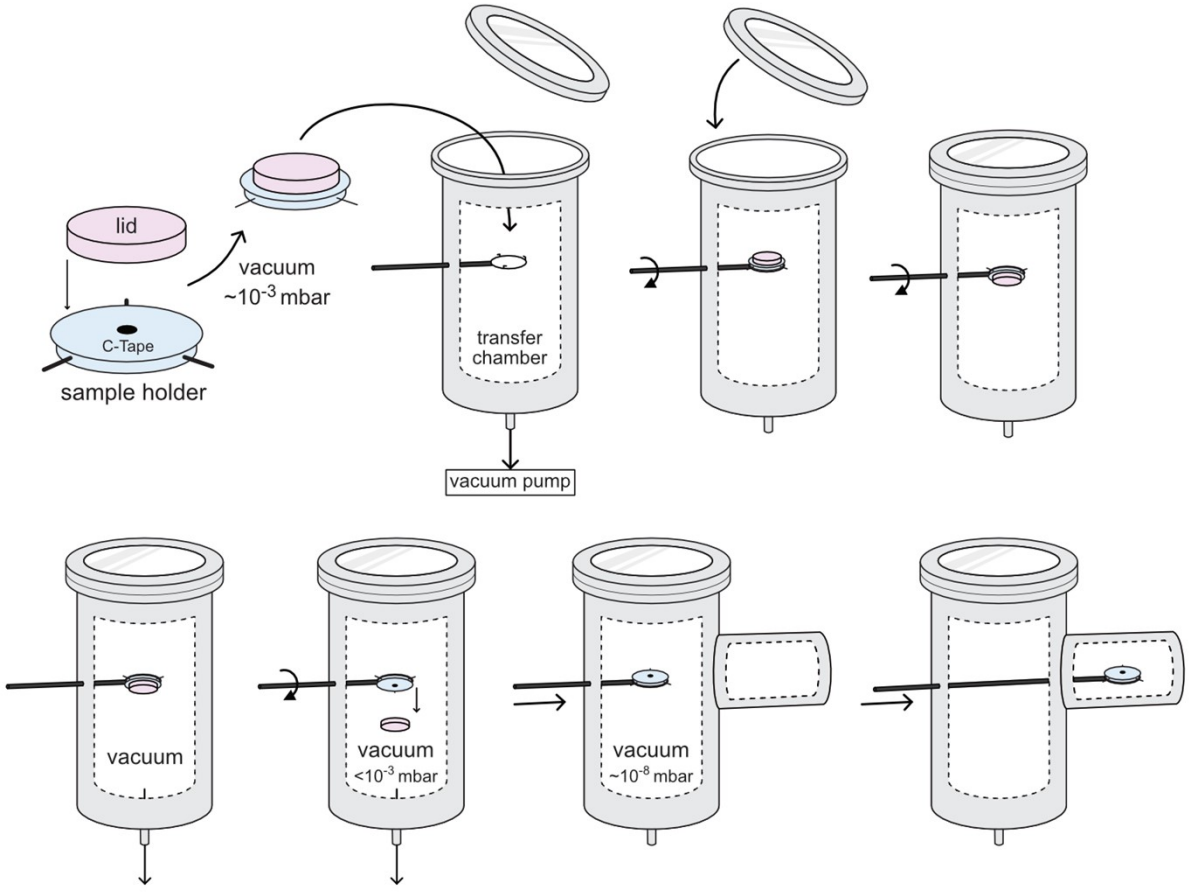

Figure S5. Schematic illustration of the inert transfer procedure for XPS measurements. The sample is mounted on a holder using carbon tape and sealed with a lid under reduces pressure (~10^{-3} mbar) inside a glovebox airlock (compare Figure S4). The sealed holder is then placed into the XPS transfer chamber, which is subsequently closed. From outside the chamber, the sample holder is inverted. As the chamber is evacuated, the internal pressure of the sealed holder becomes higher than the chamber pressure (<10^{-3} mbar), causing the lid to detach and fall to the bottom of the chamber. The pressure is further reduced to ~10^{-8} mbar before the sample is transferred into the XPS measurement chamber.

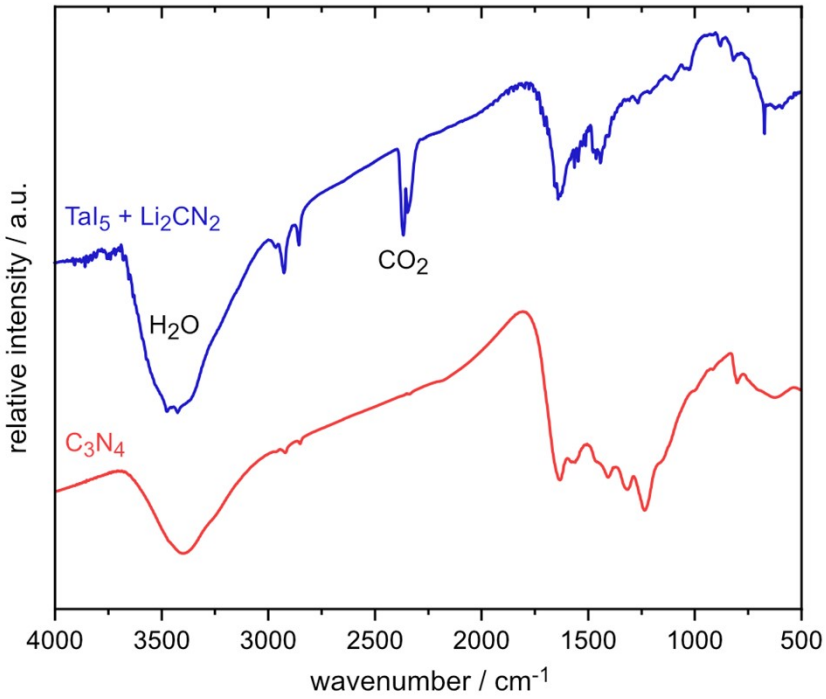

Figure S6. IR spectrum of the product from the reaction of TaI_5 and Li_2CN_2 (blue, top) compared to the IR spectrum of amorphous C_3N_4, synthesized according to literature procedure (red, bottom).[1]

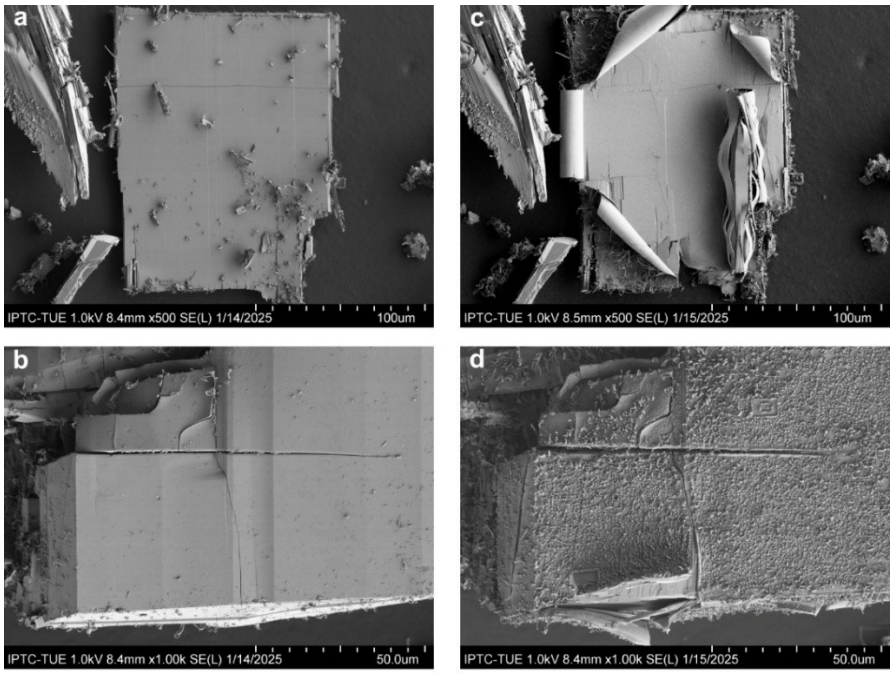

Figure S7. SEM images of two $Ta_5O_4I_{11}$ crystals after inert transfer into the device (a, b), and the corresponding crystals after being exposed to air for five minutes before being re-examined in the SEM (c, d).

[1] H. Zhao, X. Chen, C. Jia, T. Zhou, X. Qu, J. Jian, Y. Xu, T. Zhou, *Materials Science and Engineering: B* **2005**, *122*, 90-93.

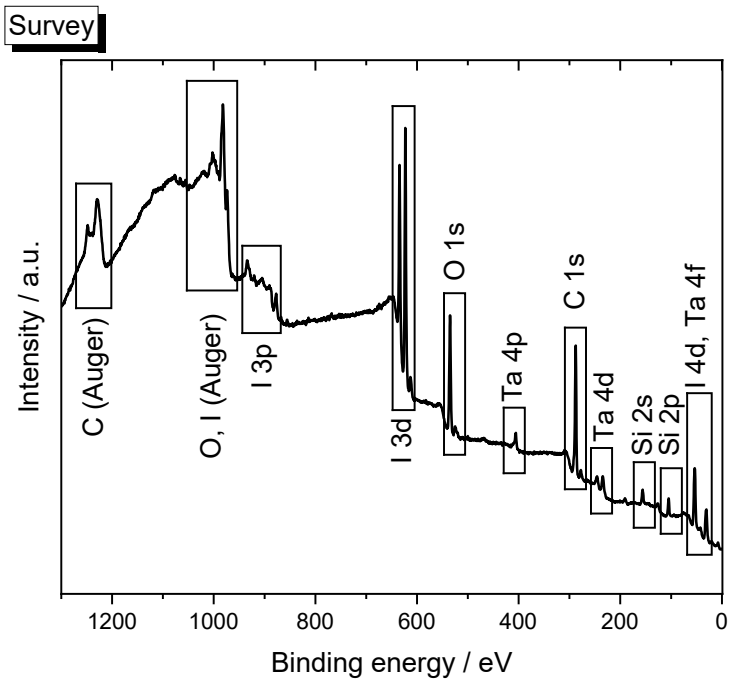

Figure S8. XPS survey spectrum for binding energies of 1300-0 eV showing Ta, I and O signals from the sample and C, Si and O signals from the conductive carbon tape.

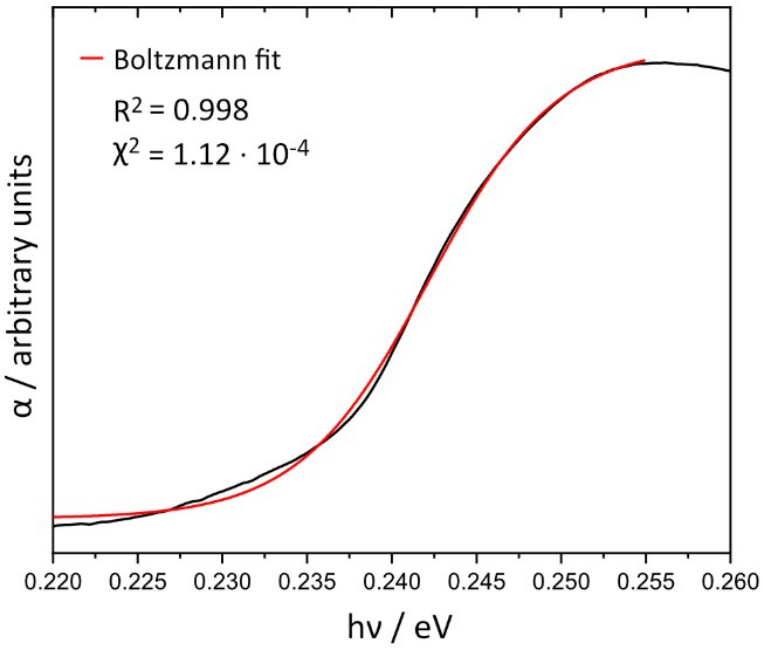

Figure S9. Optical absorption spectrum of *o*-$Ta_5O_4I_{11}$ with the Boltzmann function used to fit *α*.

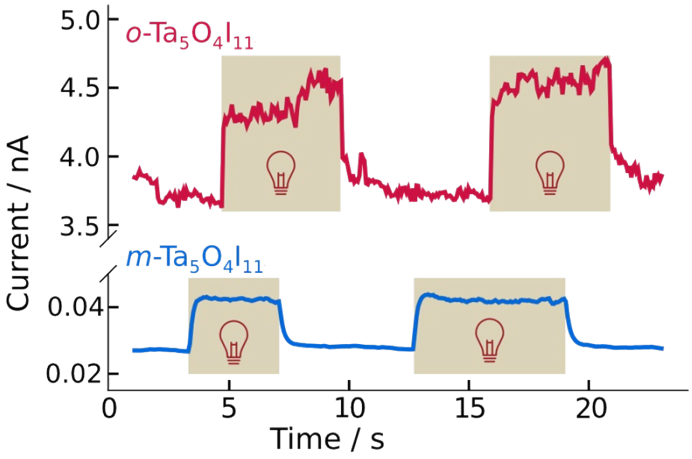

Figure S10. Photoresponse of an *o*-$Ta_5O_4I_{11}$ crystal (top, red) and a *m*-$Ta_5O_4I_{11}$ crystal (bottom, blue) toward a 779 nm laser at 300 K.

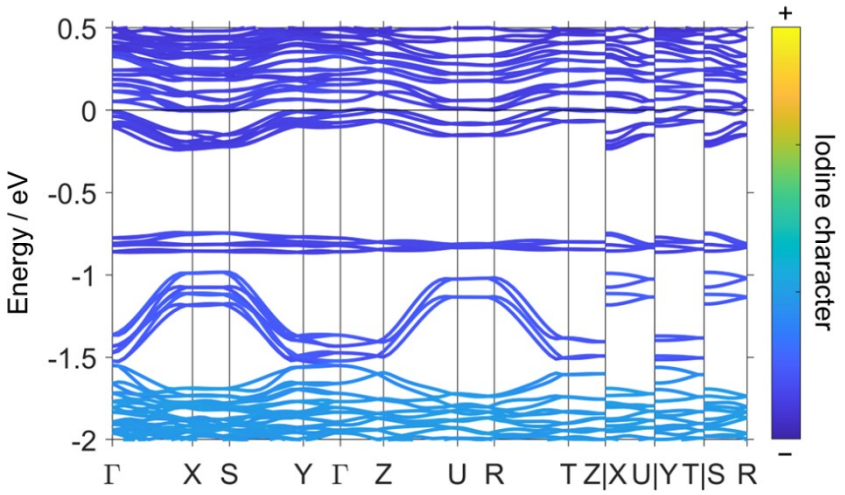

Figure S11. Calculated electronic band structure of *o*-$Ta_5O_4I_{11}$, with bands coloured by their I character. Spin-orbit coupling was included in the calculation. Special points in and paths through reciprocal space were chosen following the literature.[1]

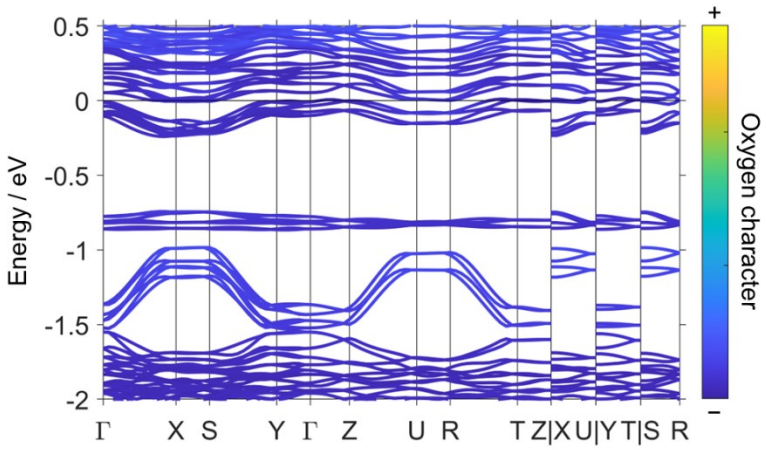

Figure S12. Calculated electronic band structure of *o*-$Ta_5O_4I_{11}$, with bands coloured by their O character. Spin-orbit coupling was included in the calculation. Special points in and paths through reciprocal space were chosen following the literature.[1]

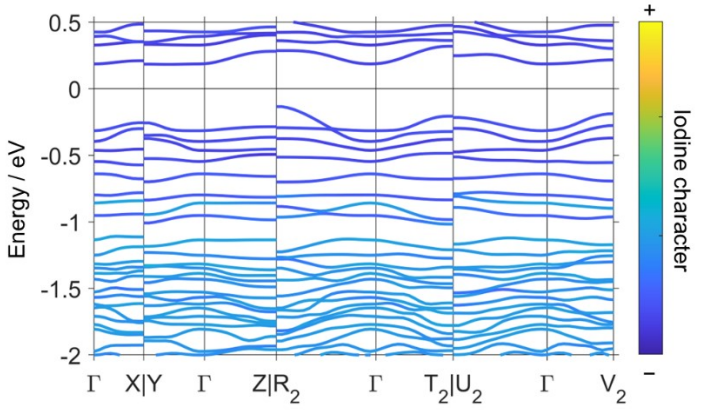

Figure S13. Calculated electronic band structure of *m*-$Ta_5O_4I_{11}$, with bands coloured by their I character. Spin-orbit coupling was included in the calculation. Special points in and paths through reciprocal space were chosen following the literature.[1]

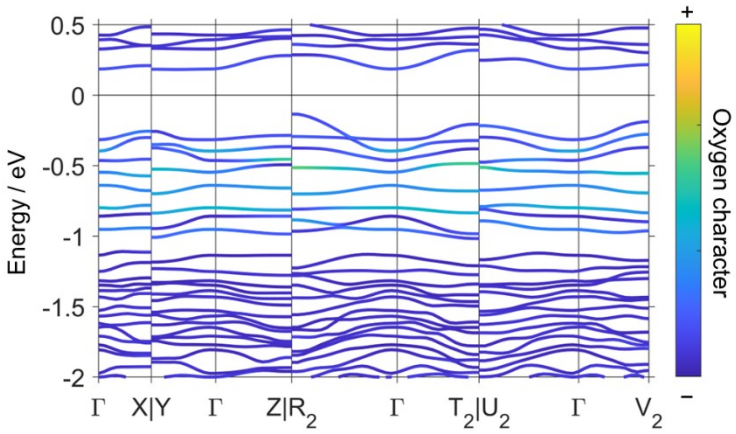

Figure S14. Calculated electronic band structure of *m*-$Ta_5O_4I_{11}$, with bands coloured by their O character. Spin-orbit coupling was included in the calculation. Special points in and paths through reciprocal space were chosen following the literature.[1]

1. Y. Hinuma; G. Pizzi; Y. Kumagai; F. Oba; I. Tanaka. Band structure diagram paths based on crystallography. *Comput. Mater. Sci.* **2017**, *128*, 140-184.

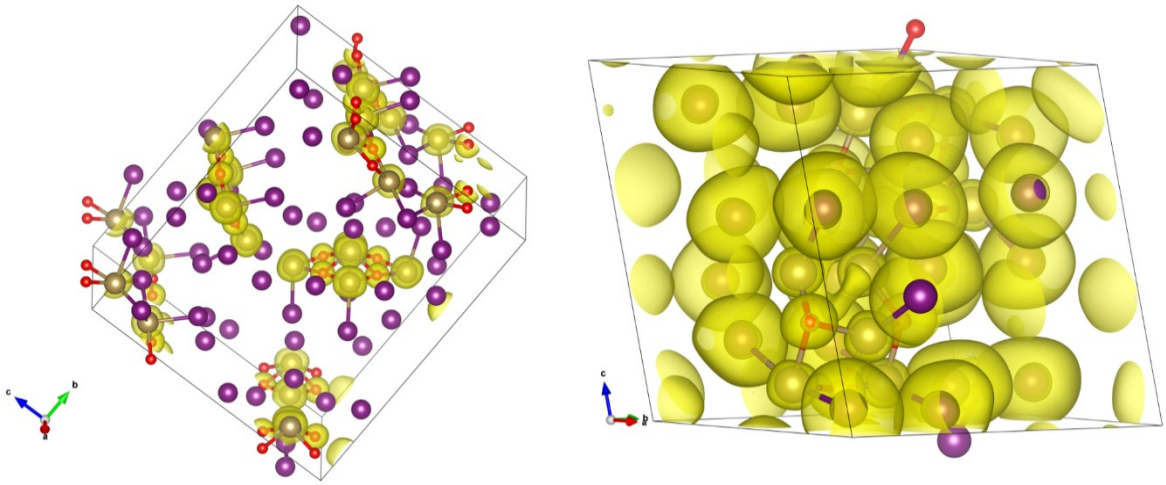

Figure S15. Three-dimensional ELF images of orthorhombic (left) and monoclinic (right) $Ta_5O_4I_{11}$ with isosurfaces at the 0.65 level.

Table S1. Comparison of selected interatomic distances (pm) and bond angles (°) in *m*-$Ta_5O_4I_{11}$ and $Ta_5O_4I_{11}(TaI_5)$.

distance / pm ; ∠ / °	***m*-$Ta_5O_4I_{11}$**	**distance / pm ; ∠ / °**	**$Ta_5O_4I_{11}(TaI_5)$**
intra cluster		**intra cluster**	
Ta(1) – Ta(2)	286.34(3)	Ta(1) – Ta(5)	286.91(4)
Ta(1) – Ta(3)	286.97(3)	Ta(1) – Ta(2)	287.66(4)
		Ta(1) – Ta(3)	287.17(4)
		Ta(1) – Ta(4)	287.57(4)
∠ Ta(2) – Ta(1) – Ta(3)	132.21(1)	∠ Ta(3) – Ta(1) – Ta(5)	131.33(1)
		∠ Ta(2) – Ta(1) – Ta(4)	130.57(1)
inter cluster		**inter cluster**	
Ta(2) – Ta(3)	443.17(4)	Ta(2) – Ta(3)	439.06(5)
Ta(4) – Ta(5)	434.12(3)	Ta(4) – Ta(5)	433.71(7)

Table S2. XPS-fit parameters for the Ta 4f spectrum depicted in Figure 11.

	Position (eV)	Gaussian width (eV)	Lorentzian width (eV)	rel. area (%)
Ta^{4+} $4f_{7/2}$	26.35	1.65	0.30	46.1
Ta^{4+} $4f_{5/2}$	28.23	1.65	0.30	34.5
Ta^{3+} $4f_{7/2}$	24.23	2.50	0.50	11.1
Ta^{3+} $4f_{5/2}$	26.10	2.50	0.50	8.3

Table S3. Crystallographic data of $M_5O_4I_{11}$ (M = Nb, Ta) cluster compounds.

	$Nb_5O_4I_{11}$	*o*-$Ta_5O_4I_{11}$	*m*-$Ta_5O_4I_{11}$	$Ta_5O_4I_{11}(TaI_5)$
CCDC Identification code	2400835	2380271	2424946	2351105
Formula weight	1924.45	2364.65	2364.65	3180.10
Radiation type	Cu K_α	Mo K_α	Mo K_α	Mo K_α
Wavelength / pm	154.184	71.073	71.073	71.073
Crystal system	orthorhombic	orthorhombic	monoclinic	orthorhombic
Space group	$Pmc2_1$	$Pmc2_1$	$P2_1/m$	$Pbca$
Unit cell dimensions / Å	a = 9.7963(2) b = 17.8082(3) c = 15.2052(2)	a = 9.8198(1) b = 17.8539(1) c = 15.3672(1)	a = 8.9594(1) b = 13.6077(1) c = 15.3672(1) β = 107.500(2)	a = 17.7586(3) b = 13.4107(4) c = 30.4660(6)
Volume / Å^3	2652.61(8)	2694.20(4)	1351.20(3)	7255.6(3)
Z	4	4	2	8
Density (calculated) / g cm^{-3}	4.819	5.830	5.812	5.822
Absorption coefficient / mm^{-1}	117.683	32.835	32.735	31.645
Crystal size / mm^3	0.09×0.05×0.01	0.36×0.04×0.04	0.18×0.09×0.03	0.14×0.02×0.01
Theta range for data collection	3.823° to 68.216°	2.074° to 30.507°	2.370° to 25.344°	2.017° to 25.350°
Reflections collected	10180	128478	39410	53383
Independent reflections	4407	8650	2583	6642
R_{int}	0.0339	0.0403	0.0303	0.0507
restraints / parameters	1 / 208	1 / 206	0 / 98	0 / 245
Goodness-of-fit on F^2	1.025	1.102	1.479	1.015
Final R indices [$I > 2\sigma(I)$]	R_1 = 0.0485 wR_2 = 0.1254	R_1 = 0.0215 wR_2 = 0.0560	R_1 = 0.0154 wR_2 = 0.0342	R_1 = 0.0226 wR_2 = 0.0443
R indices (all data)	R_1 = 0.0515 wR_2 = 0.1270	R_1 = 0.0218 wR_2 = 0.0561	R_1 = 0.0154 wR_2 = 0.0343	R_1 = 0.0305 wR_2 = 0.0464
Largest diff. peak and hole	1.205 and -0.493 e·Å^{-3}	1.509 and -1.157 e·Å^{-3}	0.759 and -0.731 e·Å^{-3}	1.946 and -1.789 e·Å^{-3}

7 Unpublished Manuscripts

Manuscript 1

A Complete Cathode Recovery Cycle of an Exhausted and Dismantled Lithium Battery Material

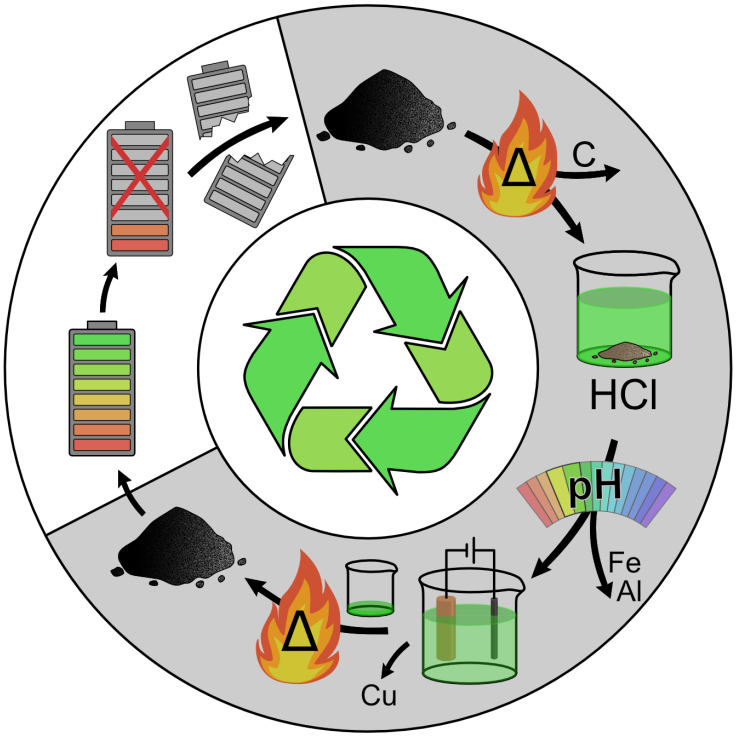

A complete cathode recovery cycle of an exhausted and dismantled lithium battery material

Fabian Grahlow,[a] Patrick Schmidt,[a] and Hans-Jürgen Meyer*[a]

Abstract: One of the most important Li-ion cathode materials developed to date is lithium nickel manganese cobalt oxide ($Li(Ni,Mn,Co)O_2$), abbreviated as Li-NMC battery. Cathode materials of this type can refer to a variety of blends, where lower cobalt contents such as NMC 6:2:2 ($LiNi_{0.6}Mn_{0.2}Co_{0.2}O_2$) or NMC 5:3:2 are preferred to reduce material costs and environmental impact. A simple and cost-effective recycling process for spent graphitic NMC Li-ion battery materials is reported for a material obtained from a commercial thermomechanical battery segmentation process. Thermo-analytical studies carried out on genuine Li-NMC/graphite material show the successive loss of electrolyte and graphite with increasing temperature. Subsequent laboratory-scale heating experiments of genuine Li-NMC/graphite materials in air confirm these findings. Impurities are removed by pH-controlled precipitation followed by electrolysis to remove and recover copper. An aqueous sol-gel process was chosen to synthesize fresh NMC cathode material. Depending on the processing conditions, the products obtained relate to an average NMC composition of 6:2:2 and 5:3:2, as shown by powder XRD measurements, structure refinement and chemical analyses.

Introduction

Following the discovery of the remarkable cathode material $LiCoO_2$ for lithium-ion batteries (LIBs) by Goodenough and co-workers,[1] several developments have been undertaken for everyday application.[2] Especially for mobile use, several requirements have to be considered: In addition to high energy densities, such as cost, safety, long-term stability and performance are important. Therefore, mixed metal oxides containing Ni, Mn and Co instead of Co alone have been developed, such as $LiNi_{0.6}Mn_{0.2}Co_{0.2}O_2$ (referenced as NMC 622).[2-3]

As more and more electric vehicles are sold in recent and coming years, these rechargeable batteries will play an increasingly important role in everyday transport.[4] While there is a need to produce more and more new batteries, it is important to keep an eye on used battery materials and recycle them in order to conserve natural resources and be sustainable.[5] As battery manufacturers develop a wide variety of compositions, it is likely that several different types of batteries will be used in the automotive industry, requiring an elaborate recycling process.[6] To date, there are several recycling methods, clearly summarised by Pinegar & Smith.[7] Methods used to separate anode from cathode material are flotation, assisted by ultra-sonification and pyrolysis.[8] Recovery of graphite requires complex laboratory installations, several intermediate treatment steps and large quantities of surfactants and waste water. Recent developments for alternative anode materials are moving towards nanostructured silicon, reducing the importance of recovering graphite in high yields, while retaining conventional cathodes.[9] Two prominent recycling methods for NMC LIBs involve acid leaching and the pyrometallurgical processing:

Acid leaching is a well-established method for recycling battery materials on a laboratory scale.[10] It can be carried out using both inorganic and organic acids, usually in the presence of hydrogen peroxide. Suitable organic acids reported for NMC LIBs are malic acid and acetic acid.[11] An advantage here is the direct complexation required in the subsequent sol-gel synthesis in the case of a direct resynthesis. However, the addition of stronger acids such as sulphuric or nitric acid with H_2O_2 have been reported to result in a faster and more efficient leaching.[7b, 11b, 12] To separate the metals from the leach solution, several extracting agents and organic solvents are necessary. The extracted metals in solution can then be successively precipitated by slowly increasing the pH of the solution.[7b, 12b]

Pyrometallurgical processes are the most used commercial LIB recycling method. They are primarily used to recover cobalt and nickel alloys. An advantage is that LIB sorting and pre-treatment is not always required. However, parts of the battery material such as graphite and lithium are not recovered and are lost in the process. Separating metals like Co, Ni, Cu and Fe from a pyrometallurgical process generally require subsequent leaching and solvent extracting processes are required, combined with high temperature treatments.[7a]

Thermal treatments have been reported to improve the recovery of cathode material, as a pre-treatment to remove organic binders and some of the conductive carbon, and a complete thermal removal of the carbon material in spent NMC LIBs in one step is desirable and involves a significant simplification of the whole recycling process.[13]

Here we investigate a full recycling and recovery process by a simple combination of thermal, leaching, electrochemical and sol-gel treatment of a graphitic NMC LIB material which was obtained

[a] F. Grahlow, P.Schmidt, Prof. Dr. H.-J. Meyer
Section for Solid State and Theoretical Inorganic Chemistry
Institute of Inorganic Chemistry
Auf der Morgenstelle 18, Eberhard Karls Universität Tübingen
D-72076 Tübingen, Germany
E-mail; juergen.meyer@uni-tuebingen.de

from a commercial mechanical battery segmentation process. The thermal treatment involves the removal of (residual) electrolyte, organic binders and graphite at moderate temperatures. Removal of iron, aluminium impurities removed by pH-dependent precipitation and copper is recovered by electrolysis. The subsequent aqueous sol-gel treatment yields fresh Li(Ni,Mn,Co)O_2 without the need for NMC metal separation as an intermediate recycling step.

Results and Discussion

The spent Li-NMC battery material (Figure 1) used in this study originates from a commercial recycling process. In this process, the batteries have been completely discharged and disassembled. The subsequent steps include shredding and an initial vacuum-drying of the spent battery material. The purpose of this treatment is to separate volatile constituents such as the electrolyte, a process that is not always complete, as will be shown later.
The resulting so called 'blackmass' shown in Figure 1, is supposed to consist of a mixture of graphite, Li-NMC and lithium salts. It is important to note, that individual batteries that are being processed in a commercial recycling process might differ in terms of electrolytes, graphite content and the cathode composition, as they come from different battery manufacturers. The individual nature of these battery materials is an exclusive knowledge of the manufacturers.

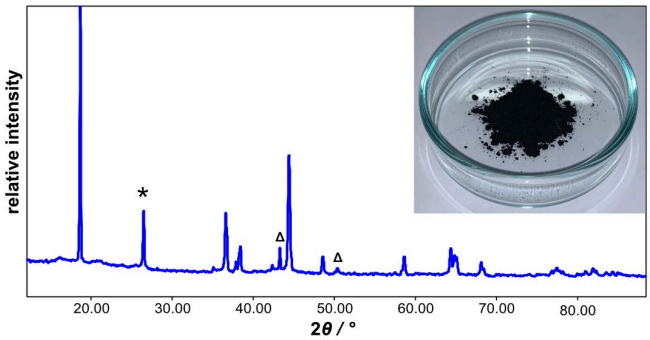

Figure 1. Powder XRD pattern (Cu-$K_{\alpha1}$) of spent graphitic Li-NMC battery material with a picture of the so-called "black mass" in the inset. Marked are the peaks corresponding to * graphite and Δ copper.[15] The unlabelled peaks correspond to NMC cathode material.[16]

Overview of the recycling process

Figure 2 illustrates the recycling scheme developed in this work, which consists of seven processing steps labelled from one to seven. In the first step a thermal treatment (500-550 °C) of the crude 'blackmass' removes all organic compounds without alteration of the NMC material and its composition. Some aluminium and iron compounds formed in this first step do not dissolve in the following leaching step (Step 2) with chloric acid / H_2O_2 (see PXRD pattern in Figure S1). Hydrochloric acid was chosen because it is superior in dissolving the NMC material compared to the commonly used nitric acid leaching, which in combination with H_2O_2 precipitates insoluble MnO_2, requiring additional sulfuric or hydrochloric acid.[14] In order to precipitate all the remaining iron and aluminium from the filtrate, the acidity of the solution was adjusted to pH = 4.3 using lithium hydroxide in step 3. Due to the lithium deficiency in the given Li_x(Ni,Mn,Co)O_2 (with x<1) material obtained from the commercial recycling process, the use of lithium hydroxide also ensures the formation of the desired Li(Ni,Mn,Co)O_2 cathode material. In step 4, a voltage of 1.6 V is applied between a graphite anode and a copper cathode for 4 hours, resulting in the complete recovery of copper from solution. The remaining solution is then dried and complexated with citric acid via an aqueous sol-gel process and then calcined to yield a new Li-NMC cathode material (Step 5 and 6). Excess Li, introduced by the titration with LiOH can be recovered by washing the product with water (Step 7). Detailed procedures can be found in the Experimental Section.

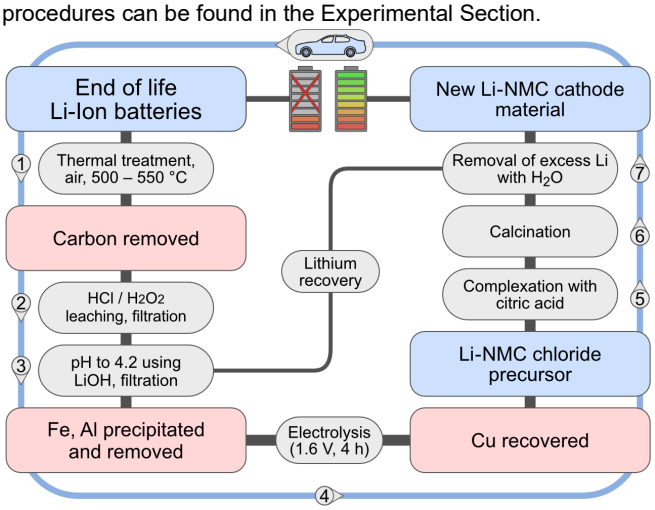

Figure 2. Recycling scheme for end of life lithium battery, departing from heat treatment for the removal of carbon, followed by acid leaching, pH dependent precipitation of impurities and electrolysis, sol-gel synthesis, involving complexation and calcination as structuring procedure for new Li-NMC cathode material.

Starting material (End of life battery material)

The TXRF analysis of the raw black mass used in this study showed a fairly consistent cathode composition with an average ratio of Ni:Mn:Co ratio of 2.80(5):1.00(4):1, which is close to the ratio of conventional NMC 622 batteries.[3a] This indicates a reasonable sorting of the battery type in the commercial process. Additionally, multiple samples revealed iron contents between 0.9 and 3.2 wt.% (2.0 ±0.8 wt.% on average), copper contents between 5.0 and 7.1 wt.% (6.0 ±1.0 wt.% on average) and aluminium contents between 2.8 and 7.2 wt.% (3.6 ±1.8 wt.% on average). These results indicate an inhomogeneity of the original material, which is due to macroscopic flakes of elemental copper and aluminium, which might be removed mechanically with improved disassembly and sorting processes.

Thermal study of the spent graphitic Li-NMC battery material

The thermal behaviour of the given spent battery material was investigated by thermogravimetric (TG) and differential thermogravimetric (DTG) analyses between room temperature and 1000 °C. Within this temperature range a total mass loss of approximately 40 % compared to the raw material is obtained. The thermolysis can be divided into three main steps, shown by the TG (blue) and DTG (red) curves in Figure 3. In the range from room temperature to 150 °C, there is a mass loss of 7.5 % and above this temperature, in the range from 150 to 400 °C the mass loss is 8.0 %. The most significant mass loss of 23.5 % occurs between 400 and 800 °C.

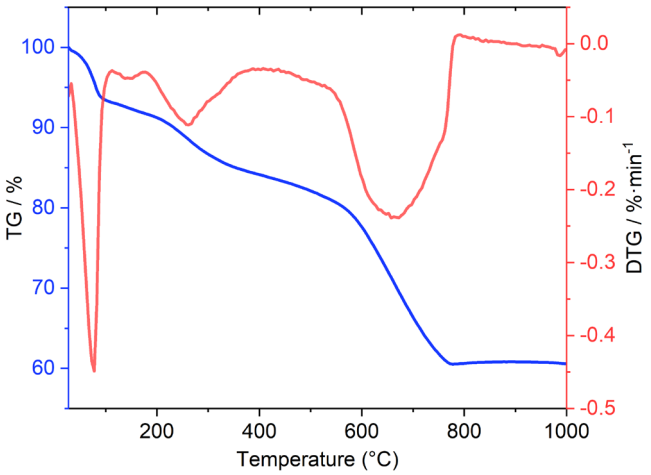

Figure 3. Thermal analysis of spent graphitic NMC LIB material heated to 1000 °C in an open corundum crucible with an airflow of 60 ml/min and a heating rate of 2 K/min (blue = thermo gravimetry; red = differential thermo gravimetry).

The mass losses obtained at lower temperatures suggest that several volatile fractions are released between 50 °C and 400 °C. These can be attributed to the volatilization of the residual electrolyte and other organic compounds, as previously described by other groups.[8a] For our given material, different types of electrolyte have to be considered, due to different battery manufacturers. The total mass loss in this temperature range is approximately 16 %.

However, this figure should only be considered as characteristic for the given powder, which was subjected to a mechanical-vacuum-thermo pre-treatment. Multiple, separate reactions in an argon atmosphere resulted in a similar mass loss of 15-25 %, indicating the loss of electrolyte, rather than an oxidation of the binder or carbon up to 550 °C.

The mass loss of 23.5 % in the temperature range of 400 to 800 °C in air corresponds to the oxidation of graphite and organic binder.[17] This gives a total mass loss of approximately 39 % for the thermolysis up to 800 °C. The mass loss in the region between 400 and 800 °C can be related to the loss of carbon, by oxidation in air.

Most of the organic binder is removed mechanically prior to this study, leaving only moderate amounts in the 'blackmass'. The decomposition of PVDF, the most commonly used binder, was not independently analysed in this study as it has been extensively studied by other groups. It has been shown that these compounds start decomposing at 300 °C, generating gaseous products such as HF, CO_2, H_2, and other hydrocarbon gases, which mostly react with the aluminium and lithium present in the spent battery material.[18]

From this experiment with a continuous heating ramp of 2 K/min, the carbon loss can be seen to occur approximately above 400 °C. Subsequent steady-state annealing studies were carried out to analyse the carbon loss in more detail, showing a significant loss in the temperature range between 500 and 550 °C within a few hours.

Step 1: Thermal removal of graphite

Continuous heating of spent NMC battery material in open corundum crucibles in air at temperatures between 500 and 550 °C results in a decreasing graphite content over time. Following this finding, samples were treated at 525 °C with successively increasing reaction times, from two hours to 20 hours, and the products were periodically analysed by powder XRD, with the results shown in Figure 4.

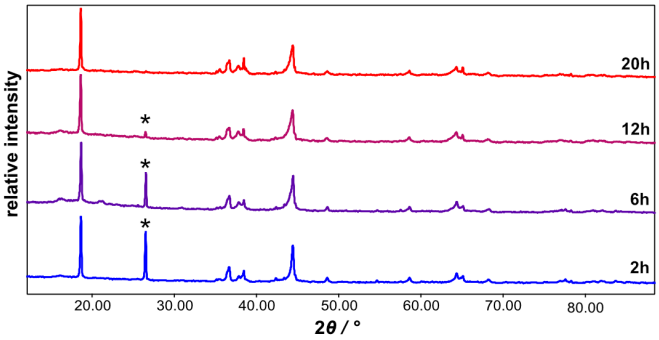

Figure 4. Powder XRD patterns (Cu-$K_{\alpha 1}$ radiation) of the 'blackmass' showing the decreasing graphite content over time (graphite (002)-reflection marked with *) after treatment at 525 °C at 2-20 hours.[15a]

The recorded XRD patterns of the thermally treated material show a clear signature of the original graphitic NMC material, plus the strongest PXRD (002)-reflection of graphite at 2θ = 26.62°.[15a] However, the intensity of this peak decreases and eventually disappears as the reaction time is prolonged from two hours (bottom) to 20 hours (top) of heating (see Figure 4).

Step 2: Acid leaching of thermally treated Li-NMC material

A simple method for acid leaching would be to use citric, malic or acetic acid, as these could directly help with the complexation required in the subsequent processing. Although the malic acid leaching has been reported for Li-NMC battery material,[19] it was not feasible for our material, which was obtained from a commercial recycling process. Supporting the leaching with extensive amounts of H_2O_2 without the use of leaching aids (like HCl or H_2SO_4) only resulted in its catalytic decomposition in the presence of manganese oxide and iron oxide as has been extensively investigated.[14] Due to the presence of iron oxides in the material used in this study, this issue is more significant compared to some other laboratory scale investigations, where batteries are neatly disassembled by hand.[8c, 10c, 17, 20]
Reasonable conventional leaching procedures are to dissolve powders in aqueous solutions of stronger acids such as HNO_3 or HCl and H_2O_2, followed by citrate complexation and pyrolysis to obtain fresh Li-NMC battery material.[21] The combination of 2 M HCl and a small quantity of H_2O_2 proved to be an effective leaching solution for the genuine, thermally treated 'blackmass' material used in this study (see experimental section for details). TXRF measurements of the solid residues (<10 % of starting mass) from the first filtration indicate that the mixture contains approximately 82 wt.% Al, Fe and Cu impurities and approximately 6 wt.% Ni, Mn, Co material, with the remainder being trace elements (Table S1).

Step 3: pH-controlled precipitation

A well-established metal separation method is the pH-controlled precipitation. We tested the feasibility of removing the aluminium, iron and copper contaminants in the obtained mixture by slowly adding LiOH to the acidic solution until the required acidity is reached. Ideally, the pH would be set to promote the precipitation of the impurities and leave the NMC-ions in solution. In practice, this method will inevitably result in some loss of nickel, manganese or cobalt, leading to a change in composition, which is affected by the acidity during precipitation. Depending on the further use of the cathode material, it is possible either to aim for a different composition or to add components to the mixture in the subsequent precursor process to obtain the desired product.
For our material, we still found 1.6 wt.% copper when precipitating at pH = 5.3 while we recorded significant loss of mainly nickel, followed by iron (Table S1). TXRF measurements of the product obtained after subsequent processing and washing revealed an Ni:Mn:Co ratio of 4.86:3.09:2.06.
Figure 5 shows PXRD patterns of new Li-NMC cathode material (bottom) which is in good accordance with $Li(Ni_{0.5}Mn_{0.3}Ni_{0.2})O_2$ and the recovered $LiCl{\cdot}H_2O$ and Li_2CO_3 (top).[22-23] in terms of iron and aluminium it is therefore a fresh Li-NMC 532 product with 1.6 wt.% copper impurities. As the 'blackmass' contains copper in the form of macroscopic flakes, well-established mechanical separation methods might reduce the content even more.

The impact of specific contaminants on the functionality of NMC materials has been investigated, demonstrating that impurities such as aluminium exert a more pronounced influence than other contaminants. [24] This understanding enables the development of an optimised recycling process, with a particular focus on targeted impurity removal.

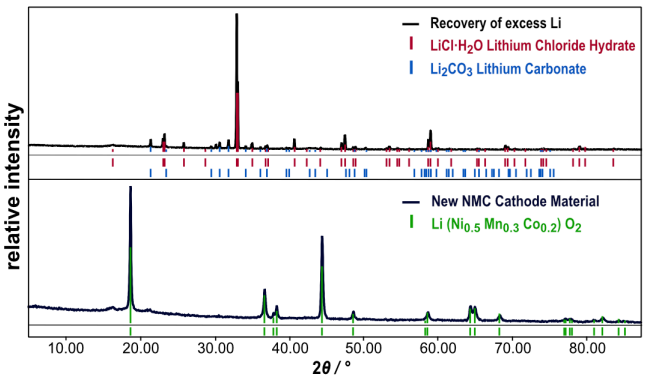

Figure 5. Recorded powder XRD patterns (Cu-$K_{\alpha 1}$ radiation) of the washed Li-NMC material after the sol-gel processing (bottom) and recovered lithium compounds (top).[22] The Bragg positions (in corresponding colours) are in good accordance to corresponding reference phases.[23]

In attempt to remove the contaminants while preserving the NMC 622 composition, we optimized the pH-controlled precipitation and filtration to a pH value of 4.2 and combined it with an electrochemical processing step. The precipitation conditions are sufficient to completely remove iron and aluminium without affecting copper and NMC. TXRF measurements were conducted on the evaporated solution, which yielded an NMC ratio of 6.00:2.03:1.97. The copper content was found to be 5.8 wt.%, and no traces of aluminium or iron were detected (see Table S1). Subsequently, copper can be removed electrochemically from the filtrate leaving only NMC in the solution.

Step 4: Electrochemical removal and recovery of copper

By applying a voltage of 1.6 V between a graphite anode and copper cathode in solution, copper could be removed completely over the course of four hours of electrolysis. TXRF analysis of the obtained final product revealed an Ni:Mn:Co ratio of 6.01:2.1:1.9 which is very close to the desired 622 composition.

Step 5-7: Synthesis of fresh Li-NMC material

In general, the particle size and morphology of the as-obtained carbon-free Li-NMC 622 material can be conditioned in a subsequent process to produce a ready-to-use cathode material. Several methods have been described for the synthesis of $Li(Ni,Mn,Co)O_2$.[1, 21, 25] A commonly used method for the synthesis of metal oxides such as garnets ($Y_3Fe_5O_{12}$)[26] or $Li(Ni,Mn,Co)O_2$[7b, 27] is the aqueous sol-gel method, as this

method is known to allow precise control of the composition and morphology of these materials.

The crystalline Li-NMC material obtained from the sol-gel processing (Step 7) is compared with a Li-NMC 622 material prepared under similar conditions, but starting from pure metal nitrates solvated in H_2O, followed by citrate complexation and pyrolysis to obtain fresh Li-NMC battery material. The product of the calcination (Step 6) is washed to remove and recover excess lithium in the form of LiCl and Li_2CO_3 (Step 7, compare Figure 5). A comparison of the powder patterns of both materials after sol-gel synthesis is presented in Figure 6 and shows almost identical patterns, with Bragg positions in good agreement with the corresponding reference phases.[16]

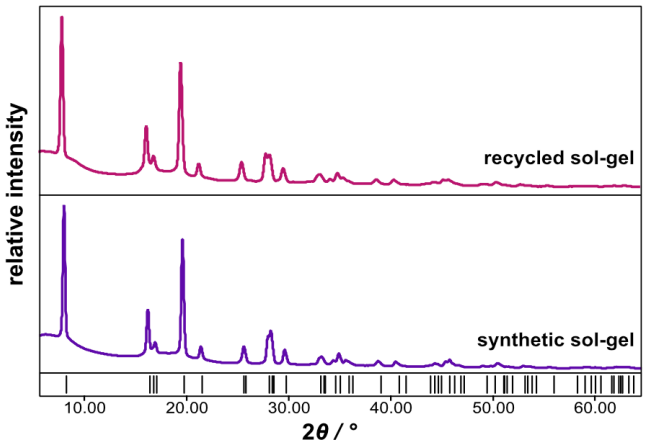

Figure 6. Recorded powder XRD patterns (Mo-K_α radiation) of Li-NMC material after the sol-gel processing, departing from recycled material (top) and from metal nitrates (bottom). The Bragg positions (black) are in good accordance to corresponding reference phases.[16]

Crystal structure refinement of graphite-free Li-NMC material

In order to evaluate the structural identity of our recycled Li-NMC 622 material (and Li-NMC 532 material, Figure S4) a full refinement with the FullProfSuite[28] was performed on the recorded XRD pattern of the recycled material using the crystallographic data of $LiNiO_2$, space group $R\bar{3}m$,[29] as starting values. The ratios of nickel, manganese and cobalt were fixed to the refined TXRF ratios. The fit between the observed (red) and calculated (black) pattern, shown in Figure 7, reveals an excellent congruence without any significant side phases being detectable. Thus, we can conclude, that the elements nickel, manganese and cobalt are still fully present in the $LiNiO_2$ type structure. The small particle size was considered using a spherical harmonic correction implemented in the FullProfSuite. The isotropic refinement converged in good agreement (R_{Bragg} = 0.3802; X^2 = 1.10; R_P = 1.1232, and wR_P = 1.4175) with around 5.8 % Ni^{2+} ions in Li^+ sites and therefore the observed habitus (SEM, see Figure 8) is more cubic/octahedral-like compared to the ideal 2D layered structure (expected for Li^+/Ni^{2+} mixed site <3.8 %).

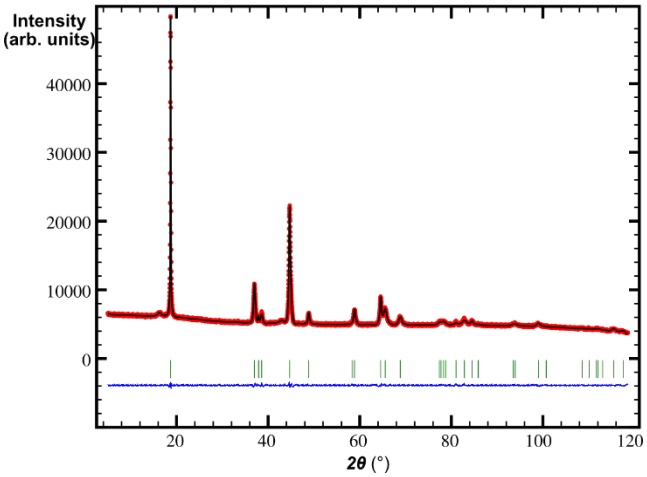

Figure 7. Rietveld fit of the Cu-$K_{\alpha 1}$ PXRD pattern of the fresh Li-NMC material. The observed pattern (red dots) is superimposed with the calculated pattern (black line). Green ticks mark the Bragg reflections of the calcined Li-NMC 622 material. The difference curve between the observed and calculated pattern is shown in the lower part of the graph (blue line). Broad reflections at 2θ values 16.2° and 43.1° emerge from the sample carrier foil.

Scanning electron microscopy (SEM) analysis of the obtained material

SEM images of the new Li-NMC 622 product are shown in Figure 8, ranging from 100x to 50.000x magnification. Homogeneous particles with high crystallinity are well distributed. The particle size ranges from 50 to 250 nm, suggesting a high surface area and short lithium diffusion lengths.

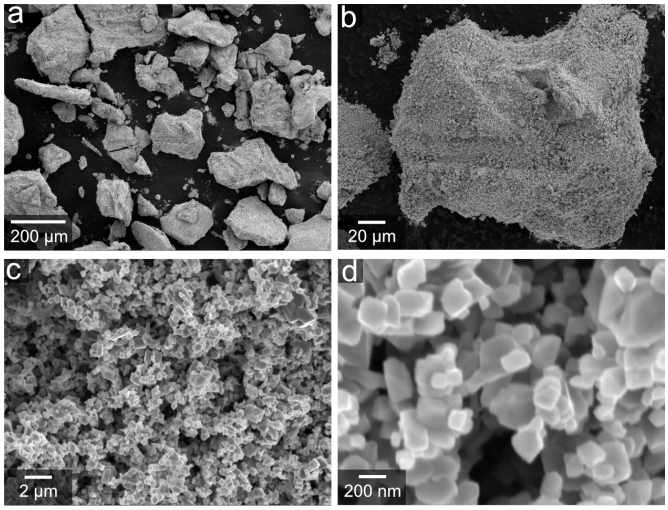

Figure 8. Electron micrographs of the obtained NMC 622 material from (a) 100 times to (d) 50000 times magnification.

Conclusions

Recycling of lithium-ion battery materials is an important process for sustainability and resource conservation. There have been several methods reported in the literature for recycling these materials, such as pyrometallurgical processes, hydrometallurgical processes, and direct recycling methods. Each method has its own advantages and challenges.

Our aim is to develop a simple and cost-efficient methodology, departing from a commercially recycled battery material that would not require a separation of the relevant elements lithium, nickel, manganese and cobalt.

The so-called 'blackmass' used in this study is a powdered mixture obtained from a commercial battery shredding process, containing the graphite anode, the Li-NMC cathode and several impurities originating from all kinds of battery components (aluminium, copper, iron, binder, etc.).

The carbon components (graphite, binder etc.) were completely removed in a moderate heating process at 550 °C. Iron and aluminium impurities were removed by precipitation at pH 4.2, and the residual copper was removed and recovered electrochemically.

The purified Li-NMC precursor solution was subjected to an aqueous sol-gel route using citric acid. After calcination and washing, fresh Li-NMC material was obtained with an unchanged initial composition. We note here, that the Li-NMC precursor solution can be used in other established synthesis routes, such as NaOH precipitation to control the morphology,[30] or to tailor the composition for a specific application by adding nickel, manganese or cobalt.

The crystal structure of the obtained recycled crystalline $Li(Ni_{0.6}Mn_{0.2}Co_{0.2})O_2$ material was confirmed by X-ray and elemental analysis and its homogeneous crystallinity verified by scanning electron microscopy. However, its feasibility for the use as a new cathode material is not yet demonstrated. We suggest coin cell electrochemical performance measurements using the recycled Li-NMC cathode material to validate the performance.

It is obvious that mechanical separation and shredding of spent batteries is the first step in an industrial recycling process. However, the diverse construction of lithium batteries does make the disassembly and recycling a challenging process. We emphasise the importance of thorough battery construction to make subsequent treatments and recycling steps as lucrative as possible.

Experimental Section

Thermogravimetric analysis (TG, DTG) was performed with a Netzsch Jupiter, STA 449 F3 apparatus between room temperature and 1000 °C with a heating and cooling rate of 2 $K \cdot min^{-1}$ in a corundum crucible.

Thermal treatment of the spent Li-NMC battery material was performed in a corundum boat which was inserted in a quartz tube. The quartz tube was then inserted in a tube oven which was positioned away from the horizontal plane with an angle (ca. 10°) to allow a natural convection of the surrounding air. Reactions were performed at 500-550 °C and reaction times between 6 and 48 h. The best conditions for the removal of graphite from the Li-NMC 622 battery material were 525 °C and 20 hours.

Precursor method to process thermally treated Li-NMC battery material. The battery material, recycled via dry carbon removal was dissolved (25 g/l) in 5 M HCl and 1/10 volume equivalents of concentrated H_2O_2 (30 %). The mixture was stirred over night at room temperature and then increased to 80 °C for an hour. Insoluble components were then filtrated off. By adding 2 M LiOH the pH was slowly adjusted to 4.2 (5.3 for NMC 532), resulting in the precipitation of mostly aluminium and iron impurities. These were filtered off and the remaining solution was electrochemically treated for four hours with an applied voltage of 1.6 V using a graphite anode and a copper cathode. The solution was then dried using a citrate sol-gel method (the amount of citric acid used was four times the initial quantity of black mass, corresponding to approximately five molar equivalents of citric acid). The resulting powder was then thermally treated in a Carbolite CWF1300 oven. Hereby, it was first heated at 460 °C for 6 hours and then at 775 °C for 10 hours. All heating and cooling rates were at 5 K/min. To remove LiCl and Li_2CO_3, the powder was washed with H_2O.

A reference Li-NMC 532 cathode material was synthesised from the chlorides (735.66 mg of $NiCl_2 \cdot 6H_20$; 167.00 mg of $MnCl_2 \cdot 2H_2O$; 245.47 mg of $CoCl_2 \cdot 6H_2O$; 555.92 mg of LiOH; 3.5 g citric acid) using a similar citrate sol-gel method.

Additionally, a NMC 622 material was synthesized following a nitrate-route (294 mg of $LiNO_3 \cdot 3H_20$; 510 mg of $Ni(NO_3)2 \cdot 6H_2O$; 111 mg of $Mn(NO_3)2 \cdot 6H_2O$; 126 mg of $Co(NO_3)2 \cdot 6H_2O$), which were dissolved in water together with 5 g of citric acid and then dried. The obtained powder was then heated at 460 °C for 6 hours followed by a step at 775 °C for 10 hours. All heating and cooling rates were at 2 K/min.

Powder X-ray diffraction (PXRD). Diffraction data for PXRD studies and refinement on $Li(Ni,Mn,Co)O_2$ were collected using a StadiP diffractometer (Stoe, Darmstadt) with Ge monochromated Cu-$K_{\alpha 1}$ radiation (λ = 1.54140 Å) with a Mythen1 Detector and a Rigaku XtaLab Synergy-S diffractometer with Mo-K_α radiation (λ = 0.71073 Å) and a graphite mirror. Measurements were performed with small amounts of crystalline powder, fixed to a micro loop using perfluoropolyalkylether.

Total Reflection X-ray Fluorescence spectroscopy (TXRF) studies. TXRF studies were performed using a S2 Picofox (Bruker AXS Microanalysis, Berlin, Germany) equipped with a Mo X-ray tube, which was operated at 50 kV and 600 µA. The measurement period for each sample was 1000 s (live time). Fitting of the resulting spectra was done using the Spectra software (Bruker Nano GmbH) in the super bias mode (maximum stripping cycles of 2000).

Scanning Electron Microscopy (SEM) studies. The sample surfaces were investigated with the scanning electron microscope JEOL JSM-6500F.

Acknowledgements

We like to express our gratitude to Priv.-Doz. Dr. Michael Marks (FB Geowissenschaften, Univ. Tübingen) for the TXRF measurements and helpful discussions, and Dr. Ronny Löffler (Center for Light-Matter-Interaction, Sensors and Analytics, LISA$^+$, Univ. Tübingen) for scanning electron micrographs. Tim Werz performed electrochemical experiments during his lab course.

Keywords: Li-NMC 622 recycling • industry battery waste • pH-dependant precipitation • electrolysis • sol-gel synthesis

[1] a) K. Mizushima, P. C. Jones, P. J. Wiseman, J. B. Goodenough, *Mater. Res. Bull.* **1980**, *15*, 783-789; b) K. Mizushima, P. C. Jones, P. J. Wiseman, J. B. Goodenough, *Solid State Ionics* **1981**, *3-4*, 171-174.

[2] M. Winter, B. Barnett, K. Xu, *Chem. Rev.* **2018**, *118*, 11433-11456.

[3] a) X. Chen, W. Shen, T. T. Vo, Z. Cao, A. Kapoor, in *2012 10th International Power & Energy Conference (IPEC)*, **2012**, pp. 230-235; b) F. H. Gandoman, J. Jaguemont, S. Goutam, R. Gopalakrishnan, Y. Firouz, T. Kalogiannis, N. Omar, J. Van Mierlo, *Appl. Energy* **2019**, *251*, 113343.

[4] a) C. Pillot, in *36th Annual International Battery Seminar & Exhibit. Avicenne Energy*, **2019**; b) J. Neumann, M. Petranikova, M. Meeus, J. D. Gamarra, R. Younesi, M. Winter, S. Nowak, *Adv. Energy Mater.* **2022**, *12*, 2102917.

[5] a) H. Chen, J. Shen, *PLOS ONE* **2017**, *12*, e0185922; b) T. Elwert, D. Goldmann, F. Römer, M. Buchert, C. Merz, D. Schueler, J. Sutter, *Recycling* **2016**, *1*, 25-60; c) G. Harper, R. Sommerville, E. Kendrick, L. Driscoll, P. Slater, R. Stolkin, A. Walton, P. Christensen, O. Heidrich, S. Lambert, A. Abbott, K. Ryder, L. Gaines, P. Anderson, *Nature* **2019**, *575*, 75-86.

[6] a) Y. Zhao, O. Pohl, A. I. Bhatt, G. E. Collis, P. J. Mahon, T. Rüther, A. F. Hollenkamp, *Sustain. Chem.* **2021**, *2*, 167-205; b) R. E. Ciez, J. Whitacre, *Nat. Sustain.* **2019**, *2*, 148-156; c) N. Nitta, F. Wu, J. T. Lee, G. Yushin, *Mater. Today* **2015**, *18*, 252-264.

[7] a) H. Pinegar, Y. R. Smith, *J. Sustain. Met.* **2019**, *5*, 402-416; b) H. Pinegar, Y. R. Smith, *J. Sustain. Met.* **2020**, *6*, 142-160.

[8] a) G. Zhang, Y. He, Y. Feng, H. Wang, X. Zhu, *ACS Sustainable Chem. Eng.* **2018**, *6*, 10896-10904; b) G. Zhang, Y. He, H. Wang, Y. Feng, W. Xie, X. Zhu, *J. Cleaner Prod.* **2019**, *231*, 1418-1427; c) L. Sun, K. Qiu, *J. Hazard. Mater.* **2011**, *194*, 378-384; d) Y. He, T. Zhang, F. Wang, G. Zhang, W. Zhang, J. Wang, *J. Cleaner Prod.* **2017**, *143*, 319-325; e) J. Yu, Y. He, Z. Ge, H. Li, W. Xie, S. Wang, *Sep. Purif. Technol.* **2018**, *190*, 45-52.

[9] a) L. Sun, Y. Liu, R. Shao, J. Wu, R. Jiang, Z. Jin, *Energy Storage Mater.* **2022**, *46*, 482-502; b) M. A. Rahman, G. Song, A. I. Bhatt, Y. C. Wong, C. Wen, *Adv. Funct. Mater.* **2016**, *26*, 647-678; c) Y. Cui, *Nat. Energy* **2021**, *6*, 995-996.

[10] a) J. Li, P. Shi, Z. Wang, Y. Chen, C.-C. Chang, *Chemosphere* **2009**, *77*, 1132-1136; b) J. Guan, Y. Li, Y. Guo, R. Su, G. Gao, H. Song, H. Yuan, B. Liang, Z. Guo, *ACS Sustainable Chem. Eng.* **2017**, *5*, 1026-1032; c) L. Li, J. Ge, F. Wu, R. Chen, S. Chen, B. Wu, *J. Hazard. Mater.* **2010**, *176*, 288-293; d) Y. M. Park, H. Lim, J.-H. Moon, H.-N. Lee, S. H. Son, H. Kim, H.-J. Kim, *Metals* **2017**, *7*, 303.

[11] a) R. Gao, C. Sun, T. Zhou, L. Zhuang, H. Xie, *ChemistrySelect* **2020**, *5*, 6482-6490; b) P. Ning, Q. Meng, P. Dong, J. Duan, M. Xu, Y. Lin, Y. Zhang, *Waste Manage. (Oxford)* **2020**, *103*, 52-60; c) K. Wang, G. Zhang, M. Luo, M. Zeng, *J. Environ. Chem. Eng.* **2022**, *10*, 108250.

[12] a) M. Esmaeili, S. O. Rastegar, R. Beigzadeh, T. Gu, *Chemosphere* **2020**, *254*, 126670; b) T. Or, S. W. Gourley, K. Kaliyappan, A. Yu, Z. Chen, *Carbon Energy* **2020**, *2*, 6-43.

[13] G. Zhang, Z. Du, Y. He, H. Wang, W. Xie, T. Zhang, *Sustainability* **2019**, *11*, 2363.

[14] a) F. Haber, J. Weiss, W. J. Pope, *Proc. R. Soc. London, Ser. A* **1934**, *147*, 332-351; b) S.-S. Lin, M. D. Gurol, *Environ. Sci. Technol.* **1998**, *32*, 1417-1423; c) M. A. Hasan, M. I. Zaki, L. Pasupulety, K. Kumari, *Appl. Catal., A* **1999**, *181*, 171-179; d) D. Broughton, R. Wentworth, *J. Am. Chem. Soc.* **1947**, *69*, 741-744; e) D. Broughton, R. Wentworth, M. Laing, *J. Am. Chem. Soc.* **1947**, *69*, 744-747.

[15] a) P. H. Gamlen, J. W. White, *J. Chem. Soc., Faraday Trans. 2* **1976**, *72*, 446-455; b) H. M. Otte, *J. Appl. Phys.* **1961**, *32*, 1536-1546.

[16] a) Y.-J. Gu, Y.-B. Chen, H.-Q. Liu, Y.-M. Wang, C.-L. Wang, H.-K. Wu, *J. Alloys Compd.* **2011**, *509*, 7915-7921; b) S. C. Yin, Y. H. Rho, I. Swainson, L. F. Nazar, *Chem. Mater.* **2006**, *18*, 1901-1910.

[17] F. Wang, T. Zhang, Y. He, Y. Zhao, S. Wang, G. Zhang, Y. Zhang, Y. Feng, *J. Cleaner Prod.* **2018**, *185*, 646-652.

[18] a) Y. Ji, C. T. Jafvert, N. N. Zyaykina, F. Zhao, *J. Cleaner Prod.* **2022**, *367*, 133112; b) M. Wang, Q. Tan, L. Liu, J. Li, *ACS Sustainable Chem. Eng.* **2019**, *7*, 12799-12806; c) C. Hanisch, T. Loellhoeffel, J. Diekmann, K. J. Markley, W. Haselrieder, A. Kwade, *J. Cleaner Prod.* **2015**, *108*, 301-311; d) D. Song, X. Wang, E. Zhou, P. Hou, F. Guo, L. Zhang, *J. Power Sources* **2013**, *232*, 348-352; e) X. X. Zhang, Q. Xue, L. Li, E. Fan, F. Wu, R. J. Chen, *ACS Sustainable Chem. Eng.* **2016**, *4*, 7041-7049; f) Y. Chen, N. Liu, Y. Jie, F. Hu, Y. Li, B. P. Wilson, Y. Xi, Y. Lai, S. Yang, *ACS Sustainable Chem. Eng.* **2019**, *7*, 18228-18235; g) J. B. DeLisio, X. Hu, T. Wu, G. C. Egan, G. Young, M. R. Zachariah, *J. Phys. Chem. B* **2016**, *120*, 5534-5542.

[19] L. Yao, H. Yao, G. Xi, Y. Feng, *RSC Adv.* **2016**, *6*, 17947-17954.

[20] L. Li, X. Zhang, M. Li, R. Chen, F. Wu, K. Amine, J. Lu, *Electrochem. Energy Rev.* **2018**, *1*, 461-482.

[21] S. Laubach, S. Laubach, P. C. Schmidt, D. Ensling, S. Schmid, W. Jaegermann, A. Thißen, K. Nikolowski, H. Ehrenberg, *Phys. Chem. Chem. Phys.* **2009**, *11*, 3278-3289.

[22] a) Y. Idemoto, J. W. Richardson, N. Koura, S. Kohara, C.-K. Loong, *J. Phys. Chem. Solids* **1998**, *59*, 363-376; b) E. Weiss, H. Hensel, H. Kühr, *Chem. Ber.* **1969**, *102*, 632-642.

[23] Y.-J. Gu, Q.-G. Zhang, Y.-B. Chen, H.-Q. Liu, J.-X. Ding, Y.-M. Wang, H.-F. Wang, L. Chen, M. Wang, S.-W. Fan, Q.-F. Zang, X.-L. Yang, *J. Alloys Compd.* **2015**, *630*, 316-322.

[24] S. Krüger, C. Hanisch, A. Kwade, M. Winter, S. Nowak, *J. Electroanal. Chem.* **2014**, *726*, 91-96.

[25] J. Yu, Z. Han, X. Hu, H. Zhan, Y. Zhou, X. Liu, *J. Power Sources* **2013**, *225*, 34-39.

[26] E. Garskaite, K. Gibson, A. Leleckaite, J. Glaser, D. Niznansky, A. Kareiva, H. J. Meyer, *Chem. Phys.* **2006**, *323*, 204-210.

[27] C. K. Lee, K.-I. Rhee, *J. Power Sources* **2002**, *109*, 17-21.

[28] a) J. Rodriguez-Carvajal, *Abstracts of the Satellite Meeting on Powder Diffraction of the XV Congress of the IUCr,* **1990**, 127; b) J. Rodriguez-Carvajal, T. Roisnel, *IUCr-Newsl.* **1998**, *20*, 35–36.

[29] W. Li, J. N. Reimers, J. R. Dahn, *Phys. Rev. B* **1992**, *46*, 3236-3246.

[30] T. Entwistle, E. Sanchez-Perez, G. J. Murray, N. Anthonisamy, S. A. Cussen, *Energy Rep.* **2022**, *8*, 67-73.

Supporting Information

A complete cathode recovery cycle of an exhausted and dismantled lithium battery material

Fabian Grahlow [a], Patrick Schmidt [a], Hans-Jürgen Meyer *[a]

[a] Section for Solid State and Theoretical Inorganic Chemistry, Institute of Inorganic Chemistry, Auf der Morgenstelle 18, Eberhard Karls Universität Tübingen, D-72076 Tübingen, Germany, juergen.meyer@uni-tuebingen.de

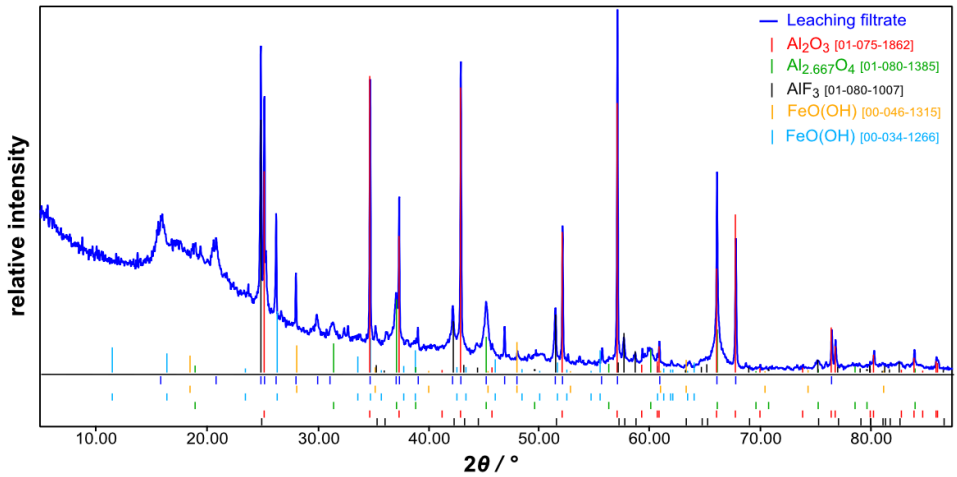

Figure S1: Powder XRD pattern (Cu-$K_{\alpha1}$ radiation) of the leaching filtrate containing mostly unsoluable aluminium and iron compounds.

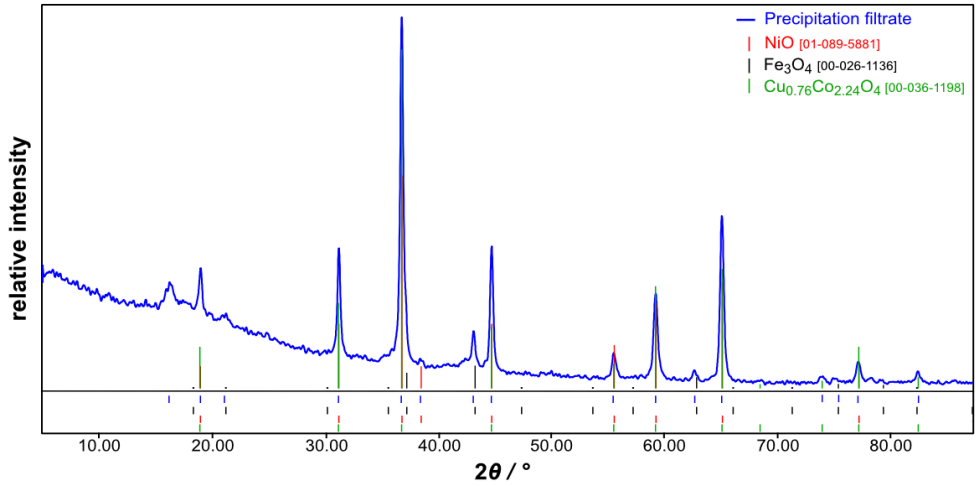

Figure S2: Powder XRD pattern (Cu-$K_{\alpha1}$ radiation) of the filtrate after pH-controlled precipitation of impurities.

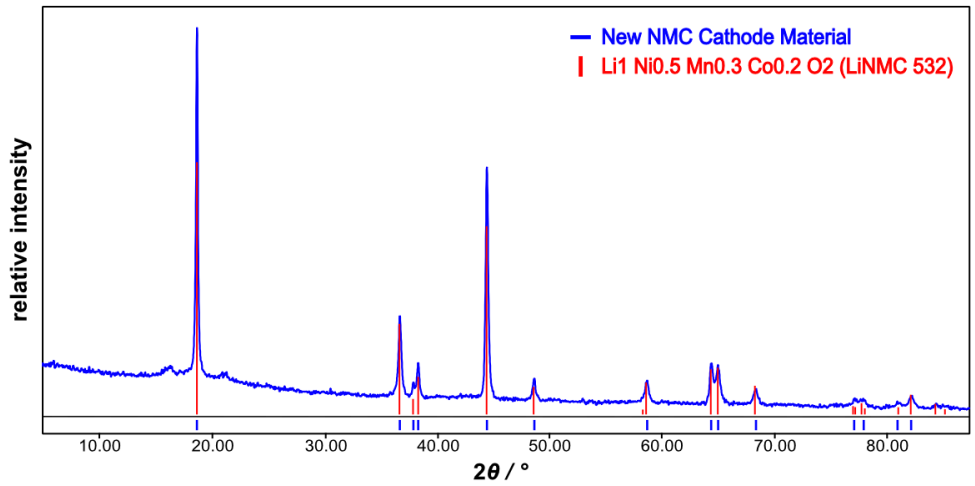

Figure S3: Powder XRD pattern (Cu-$K_{\alpha 1}$ radiation) of the fresh NMC 532 material.

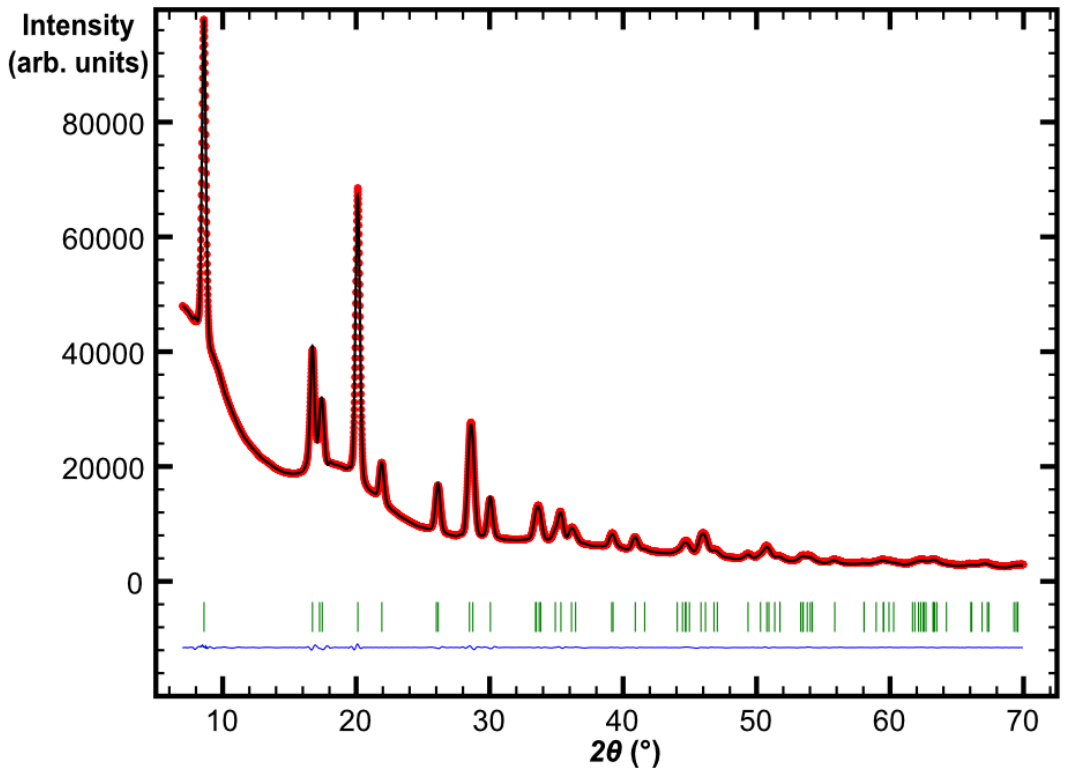

Figure S4. Rietveld fit of the Mo-K_{α} XRD pattern of the as-obtained, graphite-free NMC LIB material. The observed pattern (red dots) is superimposed with the calculated pattern (black line). Green ticks mark the Bragg reflections of the calcined NMC 532 LIB material. The difference curve between the observed and calculated pattern is shown in the lower part of the graph (blue line).

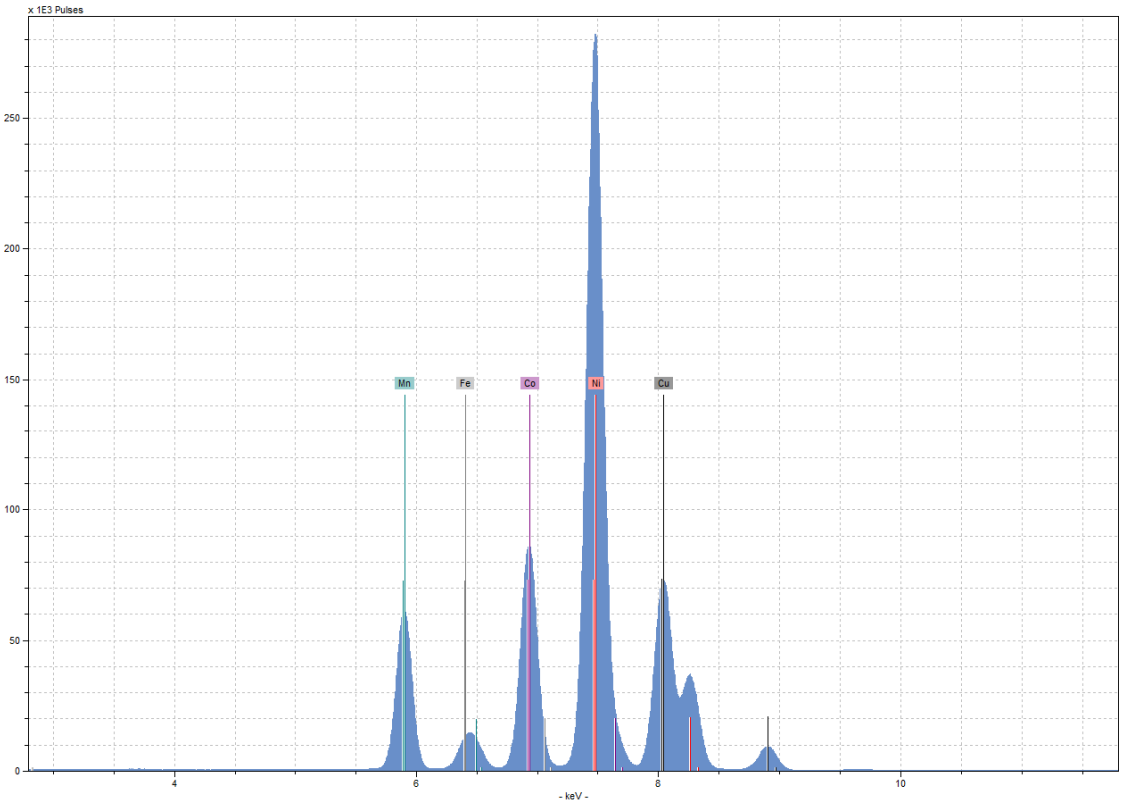

Figure S5. Section of the TXRF spectrum (Mo-K_α) of the calcinated blackmass, showing copper and iron impurities.

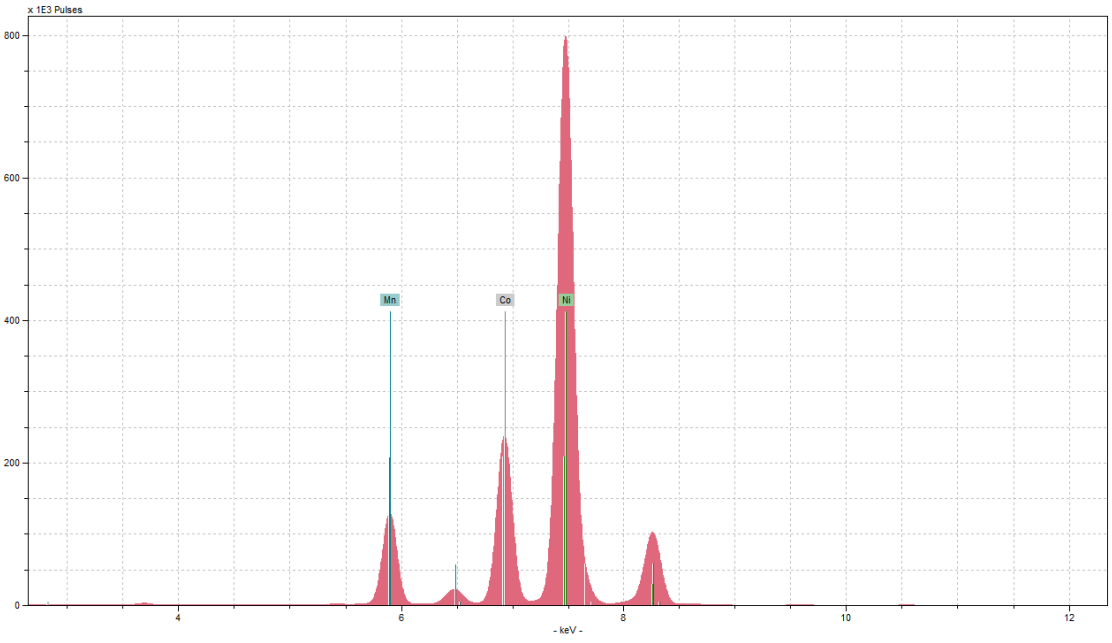

Figure S6. Section of the TXRF spectrum (Mo-K_α) of the purified, fresh Li-NMC cathode material.

Table S1: Total Internal Reflection X-Ray Fluorescence (TXRF) measurements of the battery material at each step of the recycling process. The element contents are given as Mass-% of each sample.

	Raw Material	Thermally treated	Leaching Filtrate	pH = 4.2 solution	pH = 4.2 + electrolysis (NMC 622)	pH = 5.3 Precipitation Filtrate	pH = 5.3 (NMC 532)
Step		1	2	3	4-6		
Ni	52.7	52.2	3.5	57.1	60.7	38.7	48.7
Mn	18.3	20.4	0.6	18.2	17.5	5.7	29.0
Co	18.8	19.3	2.0	18.9	21.7	12.0	20.7
Fe	2.9	1.7	10.7	0.0	0.0	33.1	0.0
Cu	6.3	5.8	3.9	5.8	0.0	22.5	1.6
Al	2.1	3.2	67.5	0.0	0.0	7.1	0.0